Semiconductors, Vol. 37, No. 10, 2003, pp. 1127–1150. Translated from Fizika i Tekhnika Poluprovodnikov, Vol. 37, No. 10, 2003, pp. 1153–1178.
Original Russian Text Copyright © 2003 by Mynbaev, Ivanov-Omskiĭ.

REVIEW

Modification of $Hg_{1-x}Cd_xTe$ Properties by Low-Energy Ions

K. D. Mynbaev* and V. I. Ivanov-Omskiĭ

Ioffe Physicotechnical Institute, Russian Academy of Sciences, St. Petersburg, 194021 Russia
**e-mail: mynkad@mail.ioffe.ru*

Submitted July 24, 2002; accepted for publication October 30, 2002

Abstract—We present an overview concerning the modification of properties of HgCdTe solid solutions and related Hg-containing materials under surface treatment with low-energy (60–2000 eV) ion beams. The conditions for conductivity-type conversion in *p*-material, dose, and time dependences of the depth of the conversion layer are analyzed. The modification of electrical properties of *n*-type material subjected to ion-beam treatment is discussed. The suggested mechanisms of conductivity-type conversion under low-energy ion treatment of HgCdTe doped with vacancies or acceptor impurities are regarded. Properties of *p*–*n* junctions produced by this technique are reviewed, and electrical and photoelectric parameters of HgCdTe IR photodetectors fabricated by low-energy ion treatment are analyzed. Several examples of novel device structures developed with the use of the method are presented. © *2003 MAIK "Nauka/Interperiodica".*

1. INTRODUCTION

Owing to their unique physical properties, mercury cadmium telluride (MCT) solid solutions $Hg_{1-x}Cd_xTe$ are currently the leading material in IR optoelectronics [1, 2]. The variation of the solid solution composition, x, allows one to obtain HgCdTe with the energy gap E_g in the range from 0 to 1.6 eV, while the lattice mismatch between CdTe ($E_g = 1.6$ eV) and $Hg_{1-x}Cd_xTe$ with $x = 0.2$ ($E_g = 0.1$ eV) is only 0.2%. It is evident that such a possibility for E_g control makes possible the design of multiwavelength detectors of IR radiation based on a single material. High electron mobility in MCT makes it possible to produce high-speed devices.

Up to now, technology remains the major problem of MCT alloys. Naturally, the lattice parameter independence of the composition is a serious advantage of MCT over any other material. However, the production of high-quality MCT meets serious problems and is very expensive. A weak Hg–Te chemical bond is responsible for a large number of intrinsic defects affecting the material properties. The small value of E_g, which is necessary for the fabrication of far-IR detectors, creates problems in the stability of the material surface and interfaces in device structures. Further, a significant contribution of nonradiative recombination transitions is typical of narrow-gap semiconductors, such as MCT alloys with small x; this effect significantly deteriorates the device parameters if the source materials are insufficiently pure. Modern technology resolves these problems, at least partially, but the cost of high-quality material increases drastically. In this context, strong competition has lately been observed between MCT and III–V semiconductors [3], the technology of growth and postgrowth treatment being better derived for the latter materials. In particular, an alternative to narrow-gap MCT IR photodetectors, where incident photons are detected via the excitation of interband optical transitions, is presented by devices based on quantum wells (QW) in III–V semiconductors, e.g., GaAs/AlGaAs, where optical transitions between the QW subbands are used. Another version of III–V IR detectors are devices with quantum dots (QD) in (In,Ga)As/GaAs compounds, which rely upon optical transitions between the bound states in QDs [4]. Further, IR detectors are produced using strained InAs/GaInSb type II superlattices.

Nevertheless, now as before, MCT remains the material of choice for photon detectors in many areas of IR technique [5]. This stimulates a continuous search for new MCT device technologies, and the competition with III–V materials only stimulates this process.

On the one hand, a low energy threshold for the intrinsic defect formation in HgCdTe hinders the application of standard methods to obtain the prescribed electrical properties. On the other hand, easy generation of intrinsic defects opens the way to control the MCT electrical properties by varying the density of these defects only, without impurity doping. It is commonly accepted nowadays that the electrical properties of undoped MCT crystals and epitaxial layers (epilayers) are defined by Hg vacancies (acceptors) and residual donor impurities [6]. For example, *p*-type conductivity in undoped MCT is due to Hg vacancies V_{Hg}, and their concentration can be varied widely, from 10^{15} to 10^{18} cm^{-3}, by thermal treatment (this material is known as vacancy-doped). This makes MCT alloys attractive for defect engineering, an area currently in progress in the technology of semiconductor devices.

Low-energy ion treatment (LEIT) is widely used in semiconductor device technology. The term "low-energy" here refers to ions with energies of $E = 2000$ eV, and, as a rule, their effect on the material differs from

Table 1. Parameters of ion-beam etching in the studies of the conductivity type conversion in MCT

Ion energy, eV	Current density, mA cm^{-2}	Time, min	Temperature of a sample holder	Reference
500–2000	0.2–1		Water cooling	[16]
100–150	0.5–0.8		50°C	[17]
1200–1800	0.06–0.32	1–30	Uncooled	[18]
60–800	0.05–0.20	20	Uncooled	[19]
750	0.3–1	30	50°C	[20]
700	0.14, 0.54	0.25–10	Water cooling	[21, 22]
1800	0.05	2		[23]

the effect of irradiation with high-energy ions (ion implantation, radiation stimulated diffusion, etc.). In particular, LEIT is used in ion-beam etching and reactive ion etching (RIE). These etching modes are more technologically effective than ordinary chemical etching. Furthermore, dry ion etching is anisotropic. It is used for the formation of device structures on MCT [7–9] and for the cleaning of the material surface [10, 11]. At the early stages of LEIT application for MCT etching, it turned out, however, that LEIT can stimulate conversion from *p*- to *n*-type conductivity [12].

2. CONDUCTIVITY TYPE CONVERSION AND FORMATION OF *P–N* JUNCTIONS

2.1. Ion-Beam Etching of MCT

It has been found that ion-beam etching can produce a conversion layer on the surface of *p*-type MCT. At first, it was regarded only as a side effect complicating the application of LEIT in MCT technology. However, in 1981 this “side effect” was patented as a method for *p–n* junction formation [13]. The dependences of the conversion-region depth on the ion energy, current density, and the irradiation time were studied, and it was established that this depth exceeds manyfold the range of ions and may be as long as hundreds of micrometers. The dependence of the conversion-region depth on the ion current density was nearly square-root type, and that on the irradiation time was nearly linear. The formation of a *p–n* junction (i.e., the fact of conversion) was confirmed by the appearance of typical diode current–voltage (*I–V*) characteristic.

In 1985, the method was further derived in the patent [14], where simultaneous effects of ion etching and the conductivity-type conversion were used in the fabrication of MCT photodiodes coupled with a silicon device for signal reading.

A more detailed study of conversion in MCT under ion-beam etching was published in 1987 [15]. This article discussed the formation of *p–n* junctions under bombardment of MCT with 1-keV Ar ions with doses from 10^{12} to 10^{14} cm^{-2}. The experimental dependence of the number of annihilating vacancies (acceptors), V_mN_a, on the irradiation dose was linear (here V_m is the volume of the converted material, and N_a, the acceptor concentration). The formation of *p–n* junctions was confirmed by the data of electron microscopy, in the electron beam induced current (EBIC) mode.

In [16], the conductivity-type conversion was investigated not only in MCT single crystals and epilayers, but also in HgMnTe and HgZnTe crystals (the substitution of Mn and Zn for Cd in the lattice is aimed at strengthening a weak Hg–Te chemical bond and obtaining a stabler material). The parameters of the Ar ion beam used in these experiments are listed in Table 1. It was established that the depth of the conversion region decreases in the order HgCdTe–HgMnTe–HgZnTe, and also with the acceptor concentration in the initial increase in material. It was noted that the conversion in HgZnTe occurred only in the material with a relatively low initial concentration of acceptors ($<5 \times 10^{16}$ cm^{-3}). The material parameters after ion-beam etching were similar to those obtained after thermal annealing (e.g., the electron density after ion-beam etching was 3×10^{15} cm^{-3} at $T = 77$ K, irrespective of the sample history).

Similar conclusions were made in [24], where the effect of ion-beam etching on $Hg_{1-x}Zn_xTe$ ($x = 0.15$) solid solution was studied. The properties of the treated material were virtually independent of the process parameters. The converted regions in HgZnTe appeared to be thinner than in MCT under the same conditions; in the authors’ opinion, this is indicative of higher stability of bonds in the Zn-containing solid solution.

A thorough investigation of the conversion in MCT subjected to ion-beam etching was reported in [17]. Under study was the effect of the collimated beam of neutralized Ar ions (the parameters are listed in Table 1) on MCT single crystals produced by solid-state recrystallization. The crystals with $0.2 < x < 0.3$ were either of *p*-type (with a hole density of $p = (0.6–5) \times 10^{16}$ cm^{-3} and a mobility of $\mu_p = 400–800$ cm^2 V^{-1} s^{-1} at $T = 77$ K) or *n*-type conductivity. In the latter case, samples with standard parameters (at $T = 77$ K, the electron density $n = (0.5–2) \times 10^{15}$ cm^{-3}, mobility $\mu_n = (1–2) \times 10^5$ cm^2 V^{-1} s^{-1}) were treated, as well as specially selected crystals with a high degree of compensation ($\mu_n < 6 \times 10^4$ cm^2 V^{-1} s^{-1}).

It appeared that ion-beam etching of p-type samples results in the formation of an n-layer with a thickness of more than 10 μm. The layer parameters were nonuniform: the electron density n in the 1–2-μm-thick surface layer was nearly, an order of magnitude higher than in the depth of the converted layer, where the density was $(1–4) \times 10^{15}$ cm^{-3}. This led to the conclusion that the n-layer formed by ion-beam etching contains (i) a surface region, where the effects of radiation impact of ions dominate and (ii) a "bulk" region, where the conversion effect is manifested in its "pure" form.

The conductivity-type conversion in p-type MCT epilayers subjected to ion-beam etching was studied in [25]. The epilayers were grown by liquid-phase epitaxy (LPE) from Te-rich solutions, their composition was x = 0.2–0.6, the concentration of uncompensated acceptors was $N_a - N_d = (5–400) \times 10^{15}$ cm^{-3}, and the thickness was ~30 μm. They were subjected to ion-beam etching with Ar^+ ions with an energy of 1.2 keV and doses from 10^{16} to 10^{18} cm^{-2}.

In the samples with $x \approx 0.2$, ion-beam etching caused the conversion of the surface layer conductivity to n-type to a depth of up to several tens of micrometers. The depth of the p–n junction position, h, increased nonlinearly with increasing irradiation dose, and decreased with increasing $N_a - N_d$. As determined from the study of the profile of the electron density distribution over the epilayer thickness d, the n-type conversion layer produced by ion-beam etching was nonuniform across its thickness. Figure 1 shows typical distribution profiles of the electron (n) and hole (p) density for two samples differing in initial values of $N_a - N_d$. These dependences were obtained by calculating "differential" (in the layer removed by etching) values of the Hall constant R_H from smooth curves approximating the experimental data. As seen, at first, n linearly decreases in the surface layer and then remains constant as far as the conversion front; i.e., the ion-beam etching results in the formation of an n^+–n–p structure. The surface transition region with decreasing n could be as thick as 2 μm. In the samples with $N_a - N_d \geq 4 \times 10^{17}$ cm^{-3}, the depth of the converted region did not exceed 0.5 μm, independent of the irradiation dose. A similarly thin (<0.5 μm) conversion region was formed by ion-beam etching in epilayers with $x > 0.2$ (the samples studied were x = 0.30, 0.45, 0.51, and 0.58, $N_a - N_d = (2–5) \times 10^{16}$ cm^{-3}); no conversion in deeper layers was observed in these alloys.

These results were later confirmed by the same authors [18]. In this work p-type samples were under ion-beam etching with the initial parameters similar to those listed above, and n-type samples with the initial electron density $n = (1–6) \times 10^{14}$ cm^{-3} at 77 K, obtained by postgrowth annealing in saturated Hg vapor at 250°C. Ion-beam etching was performed with a beam of Ar^+ ions with the parameters listed in Table 1.

Again, among all the compositions under study (x = 0.20–0.60), the conversion of the conductivity type was observed only in the samples with x = 0.20–0.24 and $N_a - N_d \leq 2 \times 10^{17}$ cm^{-3}. The depth of the converted region h was proportional to the square root of the processing time t and inversely proportional to $(N_a - N_d)^{1/2}$. These dependences are shown in Fig. 2 (points *1*) and Fig. 3, respectively. No dependence of h on the composition of solid solution was observed in this case.

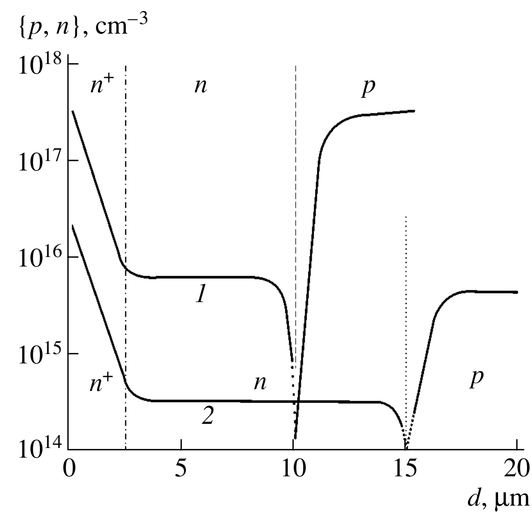

Fig. 1. Distribution of charge carriers over the thickness of ion-beam-milled MCT epilayers. $N_a - N_d$: (*1*) 2×10^{17}, (*2*) 5×10^{15} cm^{-3} [25]. The formation of the three-layer n^+–n–p structure is seen.

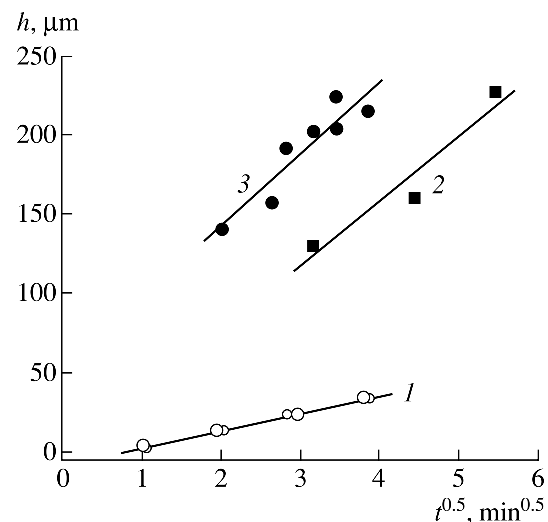

Fig. 2. Conversion-region depth, h, versus LEIT time, t: (*1*) ion-beam etching of MCT epilayers, $x = 0.22$, $N_a - N_d = 7.8 \times 10^{15}$ cm^{-3} [18]; (*2*) etching of MCT single crystals with $x = 0.22$, the h value is reduced to $N_a - N_d = 1.0 \times 10^{16}$ cm^{-3} [20]; (*3*) RIE of MCT single crystals with $x = 0.21$, $N_a - N_d = 1.0 \times 10^{16}$ cm^{-3} [26]. Solid lines: linear approximations of the experimental data.

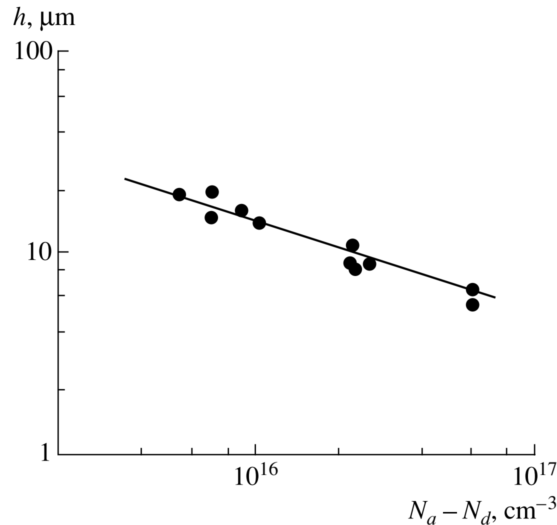

Fig. 3. The conversion region depth after ion-beam etching versus $N_a - N_d$ in the original samples [18].

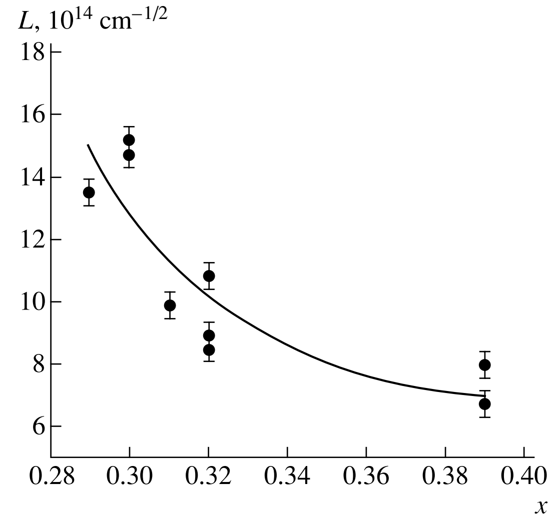

Fig. 4. The dependence of $L = h(N_a - N_d)^{1/2}$ on the MCT composition [19]. Solid line: fitting with relation (1).

However, the dependence on composition was found in an even later study by these authors [19]. The conductivity-type conversion was investigated in MCT epilayers with $0.28 \le x \le 0.55$ and $Zn_xCd_yHg_{1-x-y}Te$ of different compositions under etching with a beam of neutralized Ar ions with energies from 60 to 800 eV and the current density from 0.05 to 0.2 mA cm^{-2} (see Table 1). The processing time was 20 min. The conversion to n-type was observed only for the compositions with $x \le 0.39$. Figure 4 shows the dependence of h on the composition of the solid solution, x, for MCT samples ion-milled in one and the same mode. Since samples with different initial values of $N_a - N_d$ were studied, and, as shown in [18], h is inversely proportional to $(N_a - N_d)^{1/2}$, the product of h and $(N_a - N_d)^{1/2}$ is plotted along the ordinate axis. As seen in Fig. 4, the quantity $L = h(N_a - N_d)^{1/2}$ decreases with increasing x. For example, for $N_a - N_d = 1.0 \times 10^{16}$ cm^{-3}, the h-versus-x dependence is described by the empirical relation

$$h[\mu\text{m}] \approx 6.32 + 2.48 \times 10^4 \exp\left(-\frac{x}{0.036}\right). \qquad (1)$$

No pronounced dependence of h on x, y, or E_g was observed for $Zn_xCd_yHg_{1-x-y}Te$. For the above-mentioned treatment modes, h was in the range 7–15 μm.

Comparing their data with the data of their previous studies [18, 25], the authors of [19] came to the conclusion that the critical factor for the conversion effect in MCT with $x \ge 0.28$ is the charge transferred by ions. A charged layer is formed on the semiconductor surface under irradiation with charged ions. In a narrow-gap semiconductor, such as an MCT solid solution with $x \approx 0.2$, this charge is neutralized by intrinsic carriers, their concentration n_i being very high in these materials at the treatment temperature. In the material with high x, and, correspondingly, large E_g, the n_i density is significantly less, insufficient for neutralization of the surface charge. The accumulated charge prevents further sputtering of the surface and hinders the processes responsible for the conductivity-type conversion. At $x > 0.5$, the reduced Hg content in the material results in the situation when the treatment even with a beam of neutralized ions, when the surface charge is absent, does not cause conversion.

To determine the exact form of a p–n junction produced by ion-beam etching, which might reveal the mechanisms of the junction formation, a detailed EBIC study of the p–n junctions was performed in [20]. MCT single crystals with $x = 0.21$ grown by the modified Bridgman technique were studied. Crystals with a hole density of (1–5) × 10^{16} cm^{-3} and mobility of 250–700 cm^2 V^{-1} s^{-1} were milled with a beam of neutralized Ar ions, with the parameters listed in Table 1.

The EBIC data have revealed the “diffusion-type” form of p–n junctions produced by ion-beam etching, with the n-region formed also under the edges of the mask used. The long (tens of minutes) irradiation time made possible the conductivity-type conversion to a large depth, thus producing ultradeep p–n junctions. For example, Fig. 2 (points *2*) shows the data [20] concerning the formation of p–n junctions in MCT with $x = 0.22$ under ion-beam etching with a current density of 0.6 mA cm^{-2}. The initial hole density in this sample was $p = 3.5 \times 10^{15}$ cm^{-3}; for clarity, the depths of p–n junctions in this figure are reduced to the initial hole density $p = 1 \times 10^{16}$ cm^{-3}, following the method used in [19]. The real depth of the p–n junction in this sample after 30-min ion-beam etching was 385 μm. Study of electrical parameters of converted layers has shown that the electron density in the ~10-μm-thick surface layer was by a factor of ~3 higher than the “bulk” density, which

remained uniform until the *p–n* junction was reached by means of layer-by-layer etching. Study of degradation of the produced *p–n* junctions has demonstrated that the position and shape of the junctions did not change for several months at least.

Detailed studies of the depth and lateral extension of the *p–n* junction formed by ion-beam etching were performed also in [21, 22]. In this case, MCT epilayers with $x = 0.21$–0.33 were grown by molecular-beam epitaxy (MBE) on CdZnTe substrates at the temperature of 195°C. After termination of the layer growth, a passivating CdTe layer was grown *in situ* at 250°C on top of the epilayer. The structures were then annealed in vacuum at 250°C for 24 h and 325°C for 1.5 h to obtain layers with different concentrations of vacancies (acceptors). The concentrations obtained were in the range $(1–11) \times 10^{16}$ cm^{-3}. Further, 3-mm-long and 40- to 60-μm-wide stripes were produced on these samples by ion-beam etching. The irradiation parameters are listed in Table 1. The angle of ion incidence onto the sample surface was 45°.

The position of the *p–n* junction and its lateral extension were determined by the EBIC method. It was established that in the case of a conversion region depth of less than 10 μm, its size was proportional to the ion current and the treatment time, and inversely proportional to the concentration of vacancies in the starting samples. Comparison of the conversion regions in samples with $x \approx 0.21$ and 0.31 has shown that in the latter case, the conversion layer was deeper [21]. The ratio of the lateral size to the depth of the *p–n* junction was 0.5 in all the samples.

The conductivity-type conversion in MBE-grown MCT epilayers was studied also in [27]. The layers with $x = 0.23$ were grown on GaAs substrates with a 4.5-μm-thick CdTe buffer layer. The specific feature of these layers was the presence of a wide-band-gap region on their surface, with a graded increase in Cd content up to $x = 0.35$ at the surface. The samples were milled with Ar ions with an energy of $E = 500$ eV and a current density of $j = 0.3$ mA cm^{-2} for 12 min, resulting in the *p*- to *n*-conductivity-type conversion to a depth of 5 μm. If the wide-band-gap region was removed, the ion-beam etching caused the conversion through the entire thickness of the epilayer, which indicates that the conversion rate decreases with increasing *x*.

Of special interest is the study [23], where the temperature stability of *p–n*-structures formed by ion-beam etching was investigated. These results allow the estimation of the possibility of reverse conversion to *p*-type in MCT samples, earlier converted to *n*-type by LEIT. MCT single crystals with $x = 0.205$ and a hole density of $p = 5.8 \times 10^{15}$ cm^{-3} at $T = 77$ K were studied. The crystals were milled for 2 min with a beam of neutralized Ar ions with $E = 1.8$ keV and $j = 0.05$ mA cm^{-2}. After characterization of the converted material, the MCT wafers were cut into samples 1×1 cm^2 in size, which were further annealed at 85, 120, and 160°C for 1, 2, and 4 h. The variation of sample properties was monitored by measuring R_H at 77 K in magnetic field from 0.5 to 1.5 T.

The study has shown that ion-beam etching formed a three-layer n^+–n–p structure in the sample, with an overall *n*-layer thickness of ~10 μm. The top ~2-μm-thick surface layer was characterized by a relatively high density and low mobility of electrons. The electron density in the "bulk" of the *n*-layer was $(4–5) \times 10^{14}$ cm^{-3}. Annealing at 85°C for 4 h did not change the structural properties, but annealing at 160°C for 2 h not only resulted in disappearance of the *n*-layer, but also even modified the properties of the starting *p*-type crystal matrix. Annealing at an intermediate temperature of 120°C showed that the thickness of the *n*-layer formed by ion-beam etching decreased with increasing annealing time. This experiment demonstrated the reversibility of processes occurring in MCT under ion-beam etching, which was achieved by thermal annealing. An important factor was the difference in the time intervals necessary for the conductivity-type conversion to *n*-type under ion-beam etching and back to *p*-type under annealing. The second time was much longer, which is indicative of a substantially lower rate of processes under thermal annealing as compared with those under LEIT.

We may conclude that, in the general case, the ion-beam etching of MCT with $x \leq 0.39$ results in the conductivity-type conversion in the surface layer to a thickness defined by the composition of the solid solution and the concentration of uncompensated acceptors, and also by the ion current density and the processing time. For each sample, the absolute value of depth is apparently dependent on the sample history. None of the studies revealed a dependence of the conversion region depth on the ion energy. A material converted to *n*-type conductivity can be converted back to *p*-type by thermal annealing.

2.2. Reactive Ion Etching of MCT

Reactive ion etching (RIE) is an alternative to ion-beam etching. It is generally assumed that the effect of the former process is milder, because an ultralow energy of ions and electrons in a plasma (on the order of tens of electronvolts and lower) makes it possible to avoid the generation of radiation defects, and that chemically active gases in plasma can saturate the dangling bonds on the surface. Commonly, dry etching of MCT is performed in the plasma of inert gases (most frequently, Ar), hydrogen, or a hydrogen–methane mixture.

The effect of etching in hydrogen and Ar plasma on MCT properties was studied, e.g., in [28]. The *p*-type MCT single crystals with $x = 0.22$–0.25 and $N_a - N_d = (4–9) \times 10^{15}$ cm^{-3} were studied. Plasma treatment was performed in a high-vacuum chamber at 300 K for 5–60 min using rf discharge at 40.56 MHz with a current density of 4–10 μA cm^{-2}; no bias was applied to the

Table 2. Parameters of reactive ion etching in the studies of conductivity-type conversion in MCT

Type of plasma	Pressure in the chamber, Torr	Bias, kV	Temperature of a sample holder	Reference
Ar, H_2		0	Water cooling	[28]
Ar, H_2, CH_4	0.05	0.3	40°C	[26]
$H_2 + CH_4$	0.41	0.18	18°C	[29]
Hg	0.0008–0.003	0.6–3.0	50°C	[30]

samples under treatment (Table 2). The formation of a conversion layer with a thickness of 50–100 μm was observed. The profiles of the charge carrier distribution over depth were typical of an n^+–n–p structure. The "bulk" n-layer was characterized by low density and high mobility of electrons. In the case of a plasma current density less than 4 μA cm^{-2}, the n-layer was not formed.

The results obtained in studying the n-layer formation under treatment with hydrogen or Ar plasma were similar, which led the authors of [28] to the conclusion that the conductivity-type conversion is related only to radiation from plasma, and no effect of hydrogen as a chemically active impurity was exhibited under RIE of MCT.

RIE of MCT was studied also in [26]. Single crystals with x = 0.21 and 0.28 grown by the modified Bridgman technique were studied. The hole density p was (5–10) × 10^{15} cm^{-3}, with a mobility of 300–600 cm^2 V^{-1} s^{-1}. RIE was performed in a reactor operating at 13.56 MHz in Ar or a hydrogen–methane plasma. The RIE parameters used are listed in Table 2.

It was found that under the action of hydrogen and methane on the MCT surface, the conversion layer was formed independently of whether pure gases or a mixture of them, whatever the proportion, were used. However, the depth of the p–n junction was reduced with increasing methane partial pressure in the chamber.

When an Ar plasma was used, the thickness of the layer removed by etching increased linearly with increasing etching time t and rf discharge power, whereas the depth of the p–n junction was proportional to $t^{0.52}$ and virtually power-independent. Figure 2 (points *3*) shows the obtained $h(t)$ dependence for a sample with x = 0.21 and $p = 1.0 \times 10^{16}$ cm^{-3}. The RIE was performed with an Ar pressure of 0.05 Torr, a discharge power of 180 W, and a dc bias of 300 V.

Table 3. Results of reactive ion etching in the studies of MCT ($x \approx 0.21$) in pure argon, hydrogen, and methane plasmas [26]

Parameter	Ar	H_2	CH_4
Depth of etching, μm	5.2	2.5	0.8
Depth of p–n junction, μm	203	85	10

Note: Etching time 10 min, pressure 0.05 Torr, discharge power 180 W.

The thickness of layers removed by etching and p–n junction depths obtained with different gases are listed in Table 3. Based on these data, the authors of [26] made the conclusion that the formation of p–n junctions was related just to the physical effect on the MCT surface (collisions of plasma ions with lattice atoms); thus, the process was similar to that under ion-beam etching of MCT.

In [29], LPE-grown MCT layers were studied in RIE experiments. Samples with x = 0.31, $N_a - N_d = 8 \times 10^{15}$ cm^{-3}, ~20 μm in thickness, were etched in a hydrogen–methane mixture in the mode specified in Table 2. The formation of the converted layer was determined by measuring the laser-beam induced current (LBIC), with layer-by-layer chemical etching of the treated layers. In the mode used, a 1-min-long RIE removed ~0.2 μm of material from the surface and the p–n junction was formed at a depth of ~1.5 μm.

In similar conditions, RIE of layers with x = 0.30 and $N_a - N_d = 1.6 \times 10^{15}$ cm^{-3} was performed [31]. The formation of a p–n junction was studied by the LBIC on the cleaved surface of the sample. The depth and the lateral extension of the p–n junction were investigated. At RIE modes specified in [29], surface treatment for 90 s resulted in the removal of a 0.2-μm-thick layer from the surface and the p–n junction was formed at a depth of ~1.5 μm, with a lateral extension of less than 1 μm. Treatment for 1 h removed 10 μm of material from the surface, the p–n junction was located at the depth of 90 μm, and its lateral extension was ~33 μm.

RIE in a hydrogen–methane mixture was used also for the formation of p–n junctions in LPE-grown epilayers with x = 0.32 [32, 33].

Of interest are the data on RIE of MCT in an rf glow discharge in mercury plasma [30]. MCT single crystals with x = 0.20–0.22 and x = 0.27 were treated by RIE at a Hg vapor pressure of 8×10^{-4} to 3×10^{-3} Torr, under bias from 0.6 to 3 kV. A surface n^+-layer of up to 2.5 μm in thickness was formed by RIE both in p- and n-type samples. Further, conversion to a large depth was observed in initially p-type layers. For example, in MCT with x = 0.2 and $p = 5 \times 10^{15}$ cm^{-3}, the p–n junction was formed at a depth of ~250 μm after RIE for 5 min under 1.5-kV bias. The authors attribute so high a conversion rate, considerably exceeding the rate

under MCT etching with Ar ions, to additional oversaturation of the MCT surface with mercury from the plasma.

Thus, the effect of the conductivity-type conversion under RIE of MCT is similar to the effect observed under ion-beam etching. No influence of the chemical characteristics of the plasma was observed. The depth of the conversion region depends on the sample history and the process parameters (the type of plasma, time, pressure, power, etc.).

3. PROPERTIES OF CONVERTED LAYERS

To understand the mechanisms of the conductivity-type conversion and the potentiality of LEIT for the production of photodetectors, it is necessary to know the parameters of the material formed under treatment. The parameters of MCT subjected to LEIT were determined from the measurements of the Hall coefficient R_H and mobility under layer-by-layer chemical etching and of capacitance–voltage (C–V) characteristics of metal–insulator–semiconductor (MIS) structures formed on the converted layer, etc.

Generally, ion treatment of semiconductors produces radiation defects, which can be detrimental for the material parameters. For instance, ion implantation typically produces highly damaged surface layers with a very high carrier density, low mobility, and short lifetimes. The degradation of the material parameters was observed also in thin surface layers of MCT subjected to LEIT. In particular, the irradiation of *n*-type MCT single crystals with $x = 0.27$ by Ar ions with $E = 500$ eV at $j = 0.3$ mA cm^{-2} for 80 min caused the degradation of parameters to a depth of several micrometers [34]. The electron density in the 1-μm-thick surface layer increased from 7×10^{14} cm^{-3} in the original crystal to 4×10^{16} cm^{-3} after treatment. The carrier lifetime decreased by nearly an order of magnitude, and the surface-recombination rate increased by nearly a factor of 20.

However, the situation changed when moving away from the surface, deep into the converted layer. The first measurements of the electron density in the layers converted by LEIT have shown that the density was by several orders of magnitude smaller than that obtained when *p*–*n* junctions are produced by ion implantation. In MCT with $x \approx 0.2$, the electron density at 77 K was $n = 1.4 \times 10^{15}$ cm^{-3} and the mobility $\sim 9.6 \times 10^4$ cm^2 V^{-1} s^{-1} [13]. Similar material characteristics were observed in the study of C–V characteristics of MIS structures based on MCT single crystals with $0.2 < x < 0.3$ [17]. The structures were formed by growing a CdS layer 100–200 Å in thickness, with subsequent deposition of a 3000-Å-thick ZnS layer. C–V characteristics were recorded at $T = 77$ K at a frequency of 1 MHz. For both *p*- and *n*-type MCT, LEIT gave rise to *n*-layers with two sublayers. The electron density in the first (surface) *n*-layer 1–5 μm in thickness was $(2–5) \times 10^{16}$ cm^{-3}, which is higher by a factor of 2–10 than in the more deeply lying bulk layer. The carrier mobility in bulk layers, $\sim(1–4) \times 10^5$ cm^2 V^{-1} s^{-1}, and its temperature dependence were typical of an uncompensated material. In the case of crystals with initially *n*-type conductivity, it was found that weakly compensated samples subjected to ion-beam etching typically exhibit a slight increase in electron density n and mobility μ_n in the range were R_H levels off. Ion-beam etching of strongly compensated samples leads to a considerable increase in μ_n. It was stated also that low-temperature (75°C) annealing of samples after ion-beam etching made the surface layer characteristics similar to those of the bulk converted layer, presumably by “healing” the radiation defects.

Electrical properties of *p*- and *n*-type MCT epilayers with $x \approx 0.2$, subjected to ion-beam etching were studied in detail in [18, 25]. The measurements of R_H and conductivity σ at 77 K have shown that ion-beam etching causes the transition from “classical” *p*- to “classical” *n*-properties of the material (see Fig. 5). Figure 5 also illustrates the variations produced by ion-beam etching in initially *n*-type MCT. Figure 5b shows that, prior to ion-beam etching, the electron mobility in the studied sample was about $\mu_n \approx 1 \times 10^5$ cm^2 V^{-1} s^{-1}, and its temperature dependence had a maximum at 100 K. This means that the initial sample was strongly compensated. Ion-beam etching resulted in a sharp increase of μ_n up to 8×10^5 cm^2 V^{-1} s^{-1} at $T = 4.2$ K and the form of the μ_n temperature dependence returned to the “classical” one. In this case, n increased only by the factor of ~2. It indicates that ion-beam etching reduces the degree of compensation of the material.

The data concerning the changes in properties of initially *p*-type material caused by ion-beam etching are listed in Table 4. As seen, the *n*-type material formed under ion-beam etching demonstrated a low electron density at 77 K, $(3–15) \times 10^{14}$ cm^{-3}, and high mobility, no less than 10^5 cm^2 V^{-1} s^{-1}. The carrier lifetime τ, determined from the photoconductivity relaxation, was also rather high: the best sample with $x = 0.23$ has shown $\tau = 2.3$ μs at 77 K. It was found also in [18] that n in the converted material depended on $N_a - N_d$ in the starting samples. The correlation between these factors is shown in Fig. 6 (points *1*). Later, this interconnection was observed also in MCT epilayers with a high Cd content [19]. As an example, Table 5 presents some data on the electrical parameters of MCT epilayers with $0.28 \le x \le 0.55$, treated by ions with $E = 400$ eV at $j = 0.1$ mA cm^{-2}. Again, low density n and high mobility μ_n at 77 K indicated a high quality of the obtained *n*-layer. Evidently, the data in Table 5 (points *2* in Fig. 6) confirm the trend to interrelation between the electron density in the converted sample and $N_a - N_d$ in the original one.

Measurements of electrical parameters of $Zn_xCd_yHg_{1-x-y}Te$ epilayers in the same study [19] also showed low density and high mobility of carriers in layers converted to *n*-type. Typical density at 77 K was $\sim 1.1 \times 10^{15}$ cm^{-3}.

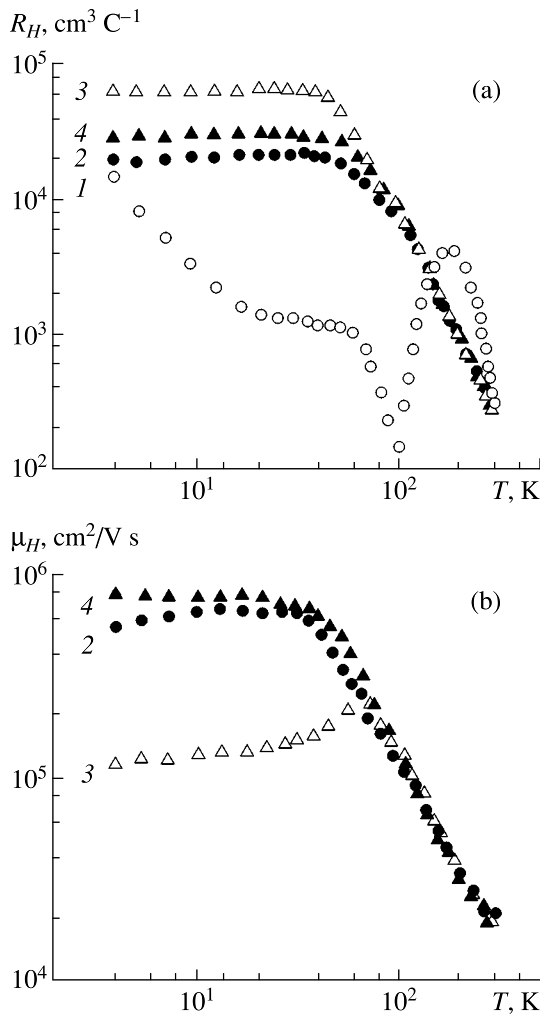

Fig. 5. Temperature dependences of (a) the Hall constant, R_H, and (b) the Hall mobility, μ_H, in MCT samples with the initially p-type conductivity: (*1*) before and (*2*) after ion-beam etching; and those with initially n-type: (*3*) before and (*4*) after etching [18]. The initial mobility in the p-type sample is not shown.

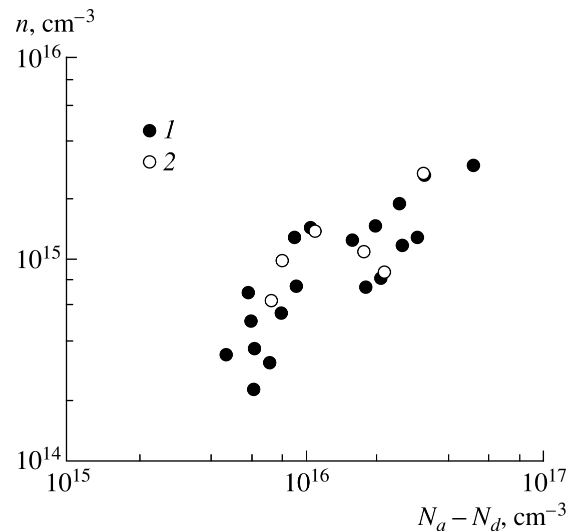

Fig. 6. The electron density n at 77 K in converted epilayers versus $N_a - N_d$ in initial samples of different compositions: (*1*) $x = 0.20$–0.24 [18], (*2*) $x > 0.24$ [19].

One might expect that the presence of two sublayers, surface and bulk, in the converted layer would be characteristic only of a material subjected to ion-beam etching, but not to RIE, in which the amount of radiation defects must be significantly smaller. However, two sublayers were found also after RIE, even in the case when no bias was applied to the sample during etching [28]. In this case, the electron density in the surface sublayer, as defined from R_H, was 10^{18} cm^{-3} (the value typical of layers subjected to ion implantation), and the mobility was $\mu_n \approx 10^4$ cm^2 V^{-1} s^{-1}. In the bulk layer, the carrier density was ~10^{15} cm^{-3} at a mobility of ~$(1–2) \times 10^5$ cm^2 V^{-1} s^{-1} and lifetimes of ~1 μs.

The application of ion-beam etching in the experiments where the p–n junction was located at the depth of several hundreds of micrometers [20] also produced structures with higher electron density in the surface layer and nearly three times smaller in the bulk of the converted layer, when the surface layer of about 10 μm thickness was removed. In MCT single crystals with $x = 0.23$, a similar bulk density in the n-layer was as high as ~9×10^{14} cm^{-3} at a mobility of 1×10^5 cm^2 V^{-1} s^{-1} at 77 K.

The authors of [20] also measured the diffusion length of minority carriers in p-type MCT with $x = 0.2$ and $N_a - N_d = (3–100) \times 10^{15}$ cm^{-3}, ion-beam-milled with Ar ions with $E = 750$ eV for 20 min [35]. The electron diffusion length was found to vary from 6 to 15 μm, and the lifetime from 2 to 6 ns, respectively. The diffusion length of holes was in the range 20–65 μm (with lifetimes of 1–10 μs), and in some samples it was close to the maximum theoretically possible values.

The carrier density in MCT layers converted by LEIT was also estimated by an LBIC study [29]. The LBIC intensity was measured in layer-by-layer chemical etching of RIE-treated MCT layer; the first step in chemical etching was 0.1 μm, and subsequent LBIC measurements were performed after every 0.5 μm. It appeared that the overall thickness of the n-layer was 1.6 μm. The intensity of the LBIC signal decreased nearly twofold after the first step of etching, which indicated the existence of a thin (less than 0.1 μm) layer with a high electron density on the RIE-treated surface of MCT. Further, the dependence of the LBIC signal intensity on the thickness of the layer removed by chemical etching was modeled. The best fit of the calculated curve to the experimental data was obtained under the assumption of uniform electron density distribution in the converted layer, with values $n = 1 \times 10^{15}$ cm^{-3} and $\mu_n = 5 \times 10^3$ cm^2 V^{-1} s^{-1}.

Table 4. Electrical properties (at 77 K) of ion-beam-etched MCT epilayers [18]

Sample	x	Sample parameters prior to etching		Sample parameters after etching		
		$N_a - N_d$, cm^{-3}	μ_p, cm^2 V^{-1} s^{-1}	n, cm^{-3}	μ_n, 10^5 cm^2 V^{-1} s^{-1}	τ, μs
1	0.21	2.1×10^{17}	200	1.2×10^{13}	2.1	0.49
2	0.23	5.9×10^{15}	490	3.5×10^{14}	1.5	1.80
3	0.22	5.9×10^{15}	510	8.3×10^{14}	1.3	0.40
4	0.22	4.8×10^{15}	440	6.7×10^{14}	2.2	0.55
5	0.22	9.2×10^{15}	400	9.6×10^{14}	1.7	0.63
6	0.21	2.6×10^{16}	240	1.2×10^{15}	2.1	0.49
7	0.23	2.0×10^{16}	470	5.0×10^{14}	2.1	2.30
8	0.23	1.0×10^{16}	320	1.5×10^{15}	1.2	0.55
9	0.20	4.5×10^{15}	550	1.6×10^{14}	1.7	1.00
10	0.23	6.0×10^{15}	500	3.5×10^{14}	1.8	1.20

Table 5. Parameters of MCT epilayers ($x > 0.24$) before and after ion-beam etching [19]

Sample	E_g, eV (300 K)	x	Parameters of original layers		Parameters of layers after etching	
			N_a–N_d, 10^{16} cm^{-3}	μ_p, cm^2 V^{-1} s^{-1}	n, 10^{15} cm^{-3}	μ_n, 10^4 cm^2 V^{-1} s^{-1}
C1	0.264	0.28	0.80	360	1.0	3.7
C2	0.291	0.30	1.1	420	1.4	6.2
C3	0.304	0.31	0.73	460	0.63	2.1
C4	0.318	0.32	3.2	420	2.7	0.49
C5	0.412	0.39	1.8	250	1.1	1.9
C6	0.412	0.39	2.2	260	0.88	2.0
C7	0.565	0.50	2.1	75	No conversion	
C8	0.594	0.52	2.4	120	No conversion	
C9	0.637	0.55	2.3	260	No conversion	

Note: Temperature of measurement: 77 K for samples C1–C6; 300 K for samples C7–C9.

A detailed study of the electrical parameters of RIE-treated MCT was reported in [36]. MCT epilayers with $x = 0.3$, 10 μm in thickness, were grown on CdZnTe substrates by LPE. The hole density in the as-grown epilayers was $p \approx 2 \times 10^{16}$ cm^{-3}. The layers were treated by RIE for 2 min in a hydrogen–methane mixture ($H_2 : CH_4 = 5 : 1$) under 500-mTorr pressure, with a discharge power of 100 W. The LBIC study revealed that the surface layer was converted to n-type to a depth of ~2 μm.

Temperature dependences of the Hall constant R_H and conductivity σ were measured in the temperature range 30–400 K in magnetic fields from 0 to 12 T, and the values of n and μ_n for separate layers were calculated from the data obtained. The n value in the bulk of the converted layer was ~$(1–3) \times 10^{15}$ cm^{-3}, and μ_n was about 4×10^4 cm^2 V^{-1} s^{-1} at 77 K. The temperature dependence of μ_n followed the $T^{3/2}$ law. In this case, the sheet density of electrons in the thin surface layer was rather high (~10^{13} cm^{-2}), which indicated a high density of defects typical of a distorted surface. These conclusions were confirmed later in [37] for samples with $x =$ 0.23 and 0.31; it was shown that n and μ_n values in the surface layers of RIE-treated MCT for the samples with different x are similar and they exhibit a very weak temperature dependence down to 20 K.

The properties of RIE-treated MCT were also studied on single crystals treated with a mercury plasma [30]. As mentioned above, the surface n^+-layer was formed in all cases. Study of the X-ray reflection intensity revealed substantial lattice distortions in the surface layer, whose thickness depended on the bias applied during RIE. The n^+-layer thickness was 2.2, 1.7, and 1.5 μm for 2.4, 1.2 and 0.6 kV biases, respectively. As concerns the bulk material, the samples with initial p-type conductivity usually demonstrated a rise in the lifetime τ after RIE, whereas the samples of initial n-type exhibited a slight increase in n and a significant rise in μ_n at 77 K, according to R_H and σ data. The lifetime of the minority carriers in these samples was

raised by RIE by nearly an order of magnitude. For instance, the mobility of ~8×10^4 cm^2 V^{-1} s^{-1} and the lifetime of ~12 μs at 77 K were reached in samples with $x = 0.27$.

Summarizing the data obtained, we may state that low electron density (at a level of 10^{15} cm^{-3} or lower) and high mobility are typical properties of n-type layers produced by LEIT in single crystals and in epilayers of vacancy-doped MCT. Temperature dependences of n and μ_n are typical of uncompensated material. In most cases, a radiation-distorted surface layer of 0.1–10 μm in thickness presumably exists, with higher n and lower μ_n.

4. LOW-ENERGY ION TREATMENT OF DOPED MCT

Specific attention must be paid to the data on LEIT of MCT, in which the p-type conductivity is defined not by mercury vacancies, but by acceptor impurities introduced into the material. If it is assumed, to a first approximation (as did the authors of the first studies devoted to LEIT of MCT), that the conductivity-type conversion in samples subjected to LEIT is due to the vacancy filling, then, in the case of acceptor-doped MCT, where the vacancy concentration is reduced almost to zero by special postgrowth annealing, no conversion should occur at all. It appeared, however, that this is not the case.

In particular, the RIE effect on As-doped MCT epilayers was studied in [31]. Layers with $x = 0.29$ were grown on CdTe substrates by vapor-phase epitaxy (VPE) at a temperature of 500°C, with elementary As added to the Hg source during growth. After growth, the samples were subjected to controlled cooling, activation of the As introduced, and low-temperature annealing for vacancy annihilation. As a result, p-type conductivity with $p = 1.6 \times 10^{16}$ cm^{-3} was obtained, and it was noted that, at the annealing temperature used, undoped MCT layers would be converted to layers with n-type conductivity, and, therefore, the p-type obtained was attributed specifically to the As introduced. Further, a 0.5-μm-thick layer was removed from the epilayer surface by chemical etching and windows of 300 × 300 μm^2 in size formed in the photoresist layer deposited on the surface. After this, the epilayers were treated by RIE in a hydrogen–methane mixture at a discharge power density of 0.4 W cm^{-2} and a bias of 180 V applied to the sample. A 3-μm-thick layer was removed from the surface after 60 min of such treatment.

The LBIC study has shown that the RIE of As-doped samples resulted in the formation of a p–n junction between the regions open to RIE and those that remained under the photoresist mask, with the n-region formed across the total thickness of the epilayer, as confirmed by the LBIC study during layer-by-layer chemical etching. To determine the parameters of the n-layer obtained, the temperature dependence of LBIC intensity in the range of 80–300 K was recorded. The calculated dependences were fitted to the obtained experimental data, with the electron density in the n-layer as a fitting parameter. The best fit was obtained for $n \approx 2 \times 10^{16}$ cm^{-3}, which was accepted as the sought density.

Similar experiments were performed with $x = 0.31$ epilayers grown using the same technique and also doped with As [38]. The hole density in the samples was 2×10^{16} cm^{-3}. The sample surface was chemically etched, and then windows of 400 × 400 μm^2 in size formed in the photoresist mask. RIE was performed for 30 min in a CH_4 + H_2 mixture at a pressure of 400 mTorr, with a discharge power of 90 W. As a result, a 0.75-μm-thick MCT layer was removed from the surface within the windows. The LBIC study revealed the formation of a p–n junction, with the conversion across all the epilayer thickness, i.e., to a depth exceeding 7 μm.

It is worth noting that one of the RIE-treated samples was later annealed in Hg vapor at a temperature of 200°C for 17 h. The LBIC study has shown that no p–n junction was found after this annealing, i.e., the annealing converted the conductivity back, from n- to p-type. To confirm this fact, R_H was measured in the sample that had undergone RIE and annealing in magnetic field up to 12 T. This study confirmed that the electrical parameters of the sample were uniform across its thickness and they coincided with those in the starting p-samples, $p = 2 \times 10^{16}$ cm^{-3}, and $\mu_p = 350$ cm^2 V^{-1} s^{-1}. Hence, the RIE effect (p–n junction formation) was completely compensated by low-temperature annealing in a Hg vapor.

The conversion of MCT conductivity from p- to n-type under RIE was studied also in samples doped with Au [36]. MCT epilayers with $x = 0.3$, 10 μm in thickness, were LPE-grown on CdZnTe substrates; the hole density after the epitaxy was $p \approx 2 \times 10^{16}$ cm^{-3}. RIE for 2 min in a (5 H_2 : 1 CH_4) mixture at a pressure of 500 mTorr with a discharge power of 100 W resulted in the formation of an n-layer of ~2 μm in thickness. In the bulk of the converted layer, the electron density was equal to that in vacancy-doped MCT converted to n-type by RIE, i.e., $(1–3) \times 10^{15}$ cm^{-3}. At the same time, the electron mobility at 77 K was at a level of 6×10^4 cm^2 V^{-1} s^{-1}, i.e., 50% higher than in the vacancy-doped samples.

The conversion of As-doped MCT under ion-beam etching was studied in [39]. Studied were graded-band-gap MCT epilayers autodoped with As, grown on (111) CdTe substrates by the vaporization–condensation–diffusion method at 873 K. After growth, the layers were subjected *in situ* to low-temperature isothermal annealing in an Hg vapor to minimize the concentration of Hg vacancies.

The data of secondary-ion mass spectrometry (SIMS) indicated that the cross-sectional distribution of the As concentration in the MCT epilayer could be considered uniform within 10 μm from the surface (that is, in the layer in which the composition was uniform and

corresponded to $x = 0.22$) and that the As concentration was 1.8×10^{16} cm^{-3}. The hole density in the layer was 1.9×10^{16} cm^{-3}, with a mobility of 410 cm^2 V^{-1} s^{-1}. Hence, it was concluded that p-type conductivity was a due precisely to As atoms with 100% electrical activity.

The ion-beam etching was performed by Ar^+ ions with $E = 500$ eV and $j = 0.1$ mA cm^{-2}, with a processing time of 5 min. The measurements of R_H and σ showed that this etching mode results in the conversion from p- to n-type to a depth of no less than 6 μm. In this case, the n value in the surface layer up to 2 μm thick was $\sim 6 \times 10^{16}$ cm^{-3}, and in the bulk of the converted layer it was $\sim 1 \times 10^{16}$ cm^{-3}. Within the experimental error it corresponded to the As concentration in the epilayer prior to ion-beam etching and, at the same time, was more than an order of magnitude higher than the electron density observed in vacancy-doped MCT after LEIT. On the whole, these results are in good agreement with the data on LEIT for As-doped MCT epilayers presented in [31].

Later, the authors performed a similar study of similar epilayers autodoped with Sb [40]. In this case, the electron density in a layer subjected to ion-beam etching was lower than the Sb concentration in the original sample. This was attributed by the authors to the specifics of the conversion mechanism in the materials doped with different impurities. It can be noted that the initial hole density of $(6–10) \times 10^{16}$ cm^{-3} in the sample autodoped with Sb was higher than in the As-doped samples, $(1.8–2) \times 10^{16}$ cm^{-3}. With due regard for this, the depth of the converted region, reduced to $N_a - N_d$ in the starting material, was the same in both cases and coincided with good precision with the dimensions of the converted regions produced by LEIT in vacancy-doped MCT [41].

As far as we know, up to now only one study [42] was devoted to LEIT of MCT preliminarily doped with a donor impurity. In the experiments described in [42], the ion treatment was applied, among others, to MCT samples with $0.20 \le x \le 0.22$ doped with In to $(5–50) \times 10^{14}$ cm^{-3}. Prior to ion-beam etching, the samples were thermally annealed and converted to p-type conductivity with $N_a - N_d$ in the range of 10^{15}–10^{16} cm^{-3}. Further, the samples were irradiated with a beam of neutralized Ar ions with $E = 1.8$ keV and $j = 0.05–0.5$ mA cm^{-2}. The irradiation converted the conductivity to n-type, and the electron density in the converted layers corresponded to In concentration. In the authors' opinion, that was a direct confirmation that n in n-type layers produced by LEIT in undoped MCT is determined by the concentration of the residual donors.

5. MECHANISMS OF THE CONDUCTIVITY-TYPE CONVERSION

5.1. Vacancy-Doped MCT

The first model of the conductivity-type conversion was proposed as early as in [13]. According to this model, ion-beam etching leads, as a result of the sputtering of the surface layer, to formation of excess mercury on the crystal surface, which further diffuses into the crystal. Such mercury atoms, which occupy interstitial positions and are donors, overcompensate the acceptor defects, and this causes the conversion. In this case, the donor concentration in the surface region is described by the empirical relation $n_0 = G^2t/(D_{Hg}p_0)$, where G is the rate of the interstitial mercury generation on the surface; p_0, the acceptor concentration; t, the irradiation time; and D_{Hg}, the Hg diffusion coefficient. It is worth noting that n_0 values obtained from this relation exceeded 1×10^{19} cm^{-3}, in obvious contradiction to the experimental data obtained in the same study: the electron density at 77 K was $n = 1.4 \times 10^{15}$ cm^{-3}, and $\mu_n \approx 9.6 \times 10^4$ cm^2 V^{-1} s^{-1}.

Later models already took into account the specific characteristics of the material formed under ion-beam etching and, in particular, a low carrier density. Based on their own experimental data, the authors of [15] suggested a mechanism of MCT conductivity-type conversion under ion-beam etching that differed somewhat from the one in [13]. In the authors' opinion, the interstitial Hg atoms introduced by ion-beam etching diffuse into the crystal and recombine with Hg vacancies, i.e., with the acceptors responsible for the original conductivity type. In this case, n-type conductivity after ion-beam etching is determined by the concentration of the residual donor impurities. It was stressed that the generation rate of the interstitial Hg on the surface is the process defining the speed at which the conversion front propagates. In this case, the depth of the converted region is defined by the relation $h = kGt/(N_aA)$, where A is the sample area, G is the number of atoms incident on the sample per second, k is a coefficient, and N_a is the concentration of vacancies (acceptors) in the starting sample.

A model of the "three-stage" mechanism responsible for the change in MCT properties under ion-beam etching was offered in [17]. According to this model, extended defects (presumably, dislocation loops) are formed at the first stage under the irradiation. At the second stage, free Hg and Cd atoms migrate via these defects inward the crystal, with hopping, rather than diffusion migration mechanism, being the authors' preference. At the final stage, Hg and Cd atoms are annihilated with vacancies in the metal sublattice. To account for the fact that MCT exhibits n-type conductivity after ion-beam etching, the authors offered a hypothesis that the material properties are defined not only by residual donor impurities, but also by donor defects produced by ion-beam etching.

Thus, beginning with the very first studies of MCT conversion under LEIT, assumptions were made that annihilation of vacancies produced in the original crystal during its growth and/or annealing with the interstitial Hg atoms released from the surface during LEIT is the process responsible for conversion [15, 17, 20, 25]. These Hg atoms must migrate into the crystal by hop-

ping [17] or diffusion [15]; in the latter case, the rate of the process is determined by the rate of the generation of free Hg atoms on the surface. However, the dependences $h(t)$ and $h(N_a - N_d)$ obtained in [18] led the authors to the conclusion that precisely the diffusion processes are responsible for the speed at which conversion front propagates. The dependence obtained in [18] was

$$h^2/t \propto C_s D(N_a - N_d), \quad (2)$$

where D is the diffusion coefficient, C_s is the surface concentration of the interstitial Hg atoms, and t is the treatment time. This relation gives a qualitative description of the experimental $h(t)$ and $h(N_a - N_d)$ dependences.

However, the first attempts at numerical estimation of the diffusion coefficient from the experimental data using Eq. (2) yielded $D \geq 2 \times 10^{-6}$ cm^2 s^{-1}. Even if the uncertainty in the duration of the diffusion process under LEIT is taken into account (the lack of the "freezing" effect, which occurs at the termination of high-temperature diffusion), the value was several orders of magnitude higher than the maximum value of the coefficient of fast Hg diffusion at 225°C or even higher temperatures [20]. To solve this problem, it was proposed to regard a system of equations for the diffusion of both interstitial Hg and its vacancies [20]. The fitting of parameters in numerical solution of this system of equations made it possible to achieve coincidence between the calculated concentration profile of the p–n junction formed under LEIT and the profile obtained from the electron-microscopy data. This confirmed that the diffusion model offers the best description of the conversion front propagation in MCT under LEIT. As concerns the values of the diffusion coefficient, the authors offered a hypothesis: since the diffusion under LEIT occurs in the material oversaturated with Hg, the concentration of vacancies in the already converted layer is negligible, no recombination of interstitial Hg with vacancies occurs in this layer, and the mean free path of interstitial Hg atoms increases drastically, which leads to ultrafast diffusion. Later, the same authors showed that the observed D_{Hg} values for the diffusion of interstitial Hg under LEIT do not contradict the data on the Hg self-diffusion coefficient obtained in the experiments on MCT annealing under equilibrium conditions [43]. It was assumed that the high D_{Hg} value is due to the low activation energy of the diffusion. The energy was supposed to be <0.2 eV, and D_{Hg} varied only slightly with a decrease in temperature to 300 K.

This assumption was verified in the experiment described in a subsequent report by the same authors, where MCT samples with $N_a - N_d = 10^{16}$ and 5×10^{16} cm^{-3} were subjected to ion-beam etching by argon with $E = 750$ eV and $j = 600$ µA cm^{-2} for 20 min; the temperature of samples was not defined by their natural heating under ion-beam etching, but was controlled externally; it was 100, 130, 170, 230, and 330 K [44]. The depth of the p–n junction was determined from EBIC data.

It was established that the p–n junction depth decreases exponentially with decreasing temperature of a sample subjected to ion-beam etching. At 100 K, no p–n junction is formed at all. To determine how long the diffusion process continues after etching is terminated, an additional experiment was performed. Two identical starting MCT samples were subjected to ion-beam etching at 300 K for 20 min. Further, a 40-µm-thick surface layer was quickly etched off from one of the samples and the p–n junction depths were determined in both samples after having aged for several days. The depth appeared to be the same in both samples; i.e., the diffusion ceased nearly simultaneously with termination of the ion treatment. The authors discussed several scenarios of defect generation and recombination under ion-beam etching and chose saturated surface generation and temperature-independent surface recombination. In this case, the depth of the p–n junction $d \propto (D_I t/C_0)^{1/2}$, where C_0 is the concentration of Hg vacancies in the crystal before etching. The $d(T)$ dependence enters the Arrhenius relation for $D_1 = D_0 \exp(-E_M/k_B T)$, where D_1 is the diffusion coefficient, E_M is the migration energy of the interstitial Hg, and k_B is the Boltzmann constant. The fitting of the $d(T)$ dependence obtained with the experimental data yielded $E_M = (120 \pm 30)$ meV.

These models were developed later in [45], where a study of the long-term (up to 10^5 s) variation of the conductivity σ at 77 K in MCT samples with $x = 0.21$ served as the basis. The original samples were p-type, with $p = (1–4) \times 10^{16}$ cm^{-3}. The conversion to n-type occurred under RIE in H_2 or Ar plasma over the course of 3–20 min. According to EBIC data, the n-layer thickness reached 80 µm. After LEIT, the samples were stored in liquid nitrogen (77 K) or in air at 295 or 323 K. The van der Pauw method was used in the σ measurement. No variation of σ was observed in the samples stored for several hours at 77 K. In the case of storage in air at 300 K, the value of σ (77 K) decreased gradually, reaching an equilibrium value after several days. With an increase in storage temperature from 295 to 323 K, the relaxation of σ was five times faster. Study of the conductivity during layer-by-layer etching in the sample where σ had reached its limiting value showed that this value was uniform over the entire converted layer thickness.

To construct a model that describes the dynamics of point defects in MCT subjected to LEIT, the authors used the following set of experimental facts: (1) the thickness of the converted layer is proportional to the square root of the LEIT duration t, and it can reach ~100 µm at $t = 1000$ s; (2) the conductivity σ at 77 K is uniform over the thickness when equilibrium is attained; (3) the conversion process terminates soon after LEIT termination; (4) the conversion front propagates in a lateral, rather than only in a vertical, direc-

tion, so its shape is typical of diffusion processes; (5) the conversion process is thermally activated (the Arrhenius relation); (6) the conversion occurs not only in vacancy-doped MCT, but also in MCT doped with an acceptor impurity; (7) typical relaxation time of the electrical parameters in the converted region is longer than the LEIT time by a factor of ~1000; (8) after relaxation, the parameters of the converted region at temperatures below 70°C demonstrate a long-term stability; (9) the relaxation is an activated process with a characteristic energy higher than that in the conversion process by a factor of about 3; (10) the value of σ (77 K) is not changed by chemical etching of the surface neither during the relaxation nor after it, which means that the relaxation of the radiation-distorted surface region does not affect the relaxation in the bulk.

The authors of [45] offer the following model, which, in their opinion, satisfactorily describes all of the above-listed observations. It is generally assumed that LEIT generates interstitial Hg_I atoms on the MCT surface and that they diffuse into the crystal and are annihilated with vacancies. Further, the authors suppose that a crystal contains traps (X) which can capture Hg_I atoms. The chemical nature of the traps is not specified. The energy of the Hg_I–X bond is small, and Hg_I atoms can be captured and released many times during the diffusion process if the traps are mainly empty. If the traps are filled, Hg_I atoms are virtually free. It is assumed that X traps are electrically neutral, whereas vacancies and Hg_I atoms are singly charged acceptors and donors, respectively. Thus, a (Hg_I–X) complex must be a singly charged donor; the assumption that it is a doubly charged donor would modify only the quantitative estimations, not affecting the general trends.

Further, if a crystal contains atoms of acceptor impurity (A), they are neutralized by Hg_I atoms, with the formation of a (Hg_I–A) complex. In principle, this complex can be one of the sources of traps, i.e.,

$$Hg_I + A \longrightarrow X. \quad (3)$$

In this case, the formation of the donor complex can look as follows:

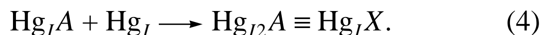

$$Hg_IA + Hg_I \longrightarrow Hg_{I2}A \equiv Hg_IX. \quad (4)$$

A system of one-dimensional equations describing the generation of Hg_1 under LEIT, their escape from surface to vacuum, diffusion to the crystal depth, and the annihilation with vacancies is as follows (this system was solved numerically by Belas *et al.* [45]):

$$\frac{\partial C_{IT}}{\partial t} = D_{Hg}\frac{\partial^2 C_I}{\partial z^2} - RC_IC_V + s\delta(z), \quad (5)$$

$$\frac{\partial C_V}{\partial t} = -RC_IC_V. \quad (6)$$

Here, $C_{IT} \equiv C_{IT}(z, t)$ is the total concentration of interstitial Hg (captured by traps and free); $C_I \equiv C_I(z, t)$, the concentration of free diffusing Hg_I; and $C_V \equiv C_V(z, t)$, the concentration of Hg vacancies, V_{Hg}. D_{Hg} is the diffusion coefficient for interstitial Hg, and $s = s_I - s_{2I}C_I(0, t)$ defines the generation and annihilation of Hg_I on the surface, where s_I and s_{2I} are temperature-independent constants. On RIE termination, $s_I = 0$. R is the coefficient of annihilation of vacancies with interstitial Hg.

The experimental data on the behavior of σ (77 K) with time in samples stored at different temperatures and on the n-layer thickness after relaxation were used for fitting in calculations. The details of the procedure can be found in [45]. The best fit of calculated to experimental data was obtained under the assumption that there exist two types of traps with concentrations of $\sim 10^{16}$, 10^{15} cm^{-3} and free energies of formation of ~500 and ~600 meV, respectively. In this situation, the diffusion coefficient for Hg_I at 300 K was $\sim 4 \times 10^{-8}$ cm^2 s^{-1}. As concerns the variation of the n-layer thickness, it was established that at the instant of LEIT termination the thickness reaches 70% of its final value, and 80% 15 min later.

In the opinion of the authors of [45], this model satisfactorily describes all ten of the experimental facts listed above, and its advantage is that both the LEIT and relaxation processes are described by the migration (diffusion) of a single type of centers, Hg_I atoms. Keeping in mind the conversion effect in acceptor-doped MCT, the authors considered as highly probable the existence of traps in the form of complexes including a Hg_I atom and an impurity acceptor atom. The last detailed derivation of this model, taking into account, among other factors, the lateral extension of the p–n junction formed in MCT under LEIT, can be found in [46].

To describe the conductivity-type conversion in MCT under RIE in a hydrogen–methane mixture, another model was proposed where the leading role was played by hydrogen atoms [47]. The experimental basis for this model were the data on the SIMS analysis of vacancy- and Au-doped MCT samples, the R_H data from a previous study by the same authors [36], and the experiments on thermal treatment of the p–n junctions obtained. MCT epilayers with $x = 0.31$, ~20 μm in thickness were studied; in vacancy-doped samples, the hole density at 80 K was 7.5×10^{15} cm^{-3}; in Au-doped samples, the acceptor concentration was 1.6×10^{16} cm^{-3}. A ZnS layer 1000 nm in thickness was deposited onto the surface of samples, and four surface areas were formed, one of which was subjected to RIE for 22 min, the second for 2 min, and the third remained under ZnS during RIE, which was removed after etching. In the fourth area, the penetration of hydrogen atoms into the ZnS layer itself was studied. The RIE process parameters used were as follows: a $H_2 + CH_4$ mixture at an RF discharge power density of ~0.2 W cm^{-2}, a total pressure of 100 mTorr, and a dc bias of 200 V on the sample. The processing time was 20 min, and the temperature of a cooled sample holder was no higher than 15°C. To raise the SIMS sensitivity in the subsequent analysis of

samples, deuterium was used instead of hydrogen in the $H_2 + CH_4$ mixture.

As expected, the analysis showed that the deepest penetration of deuterium in vacancy-doped MCT was observed in the samples subjected to RIE for 22 min, with the SIMS signal steadily decreasing away from the surface into the sample. For samples treated for 2 min, the deuterium profile had a peak at a depth of ~1200 nm and the peak position shifted more deeply inside the sample after annealing at 80°C, and still deeper at 100°C. The surface concentration of deuterium depended on the RIE time; in the sample treated for 22 min, it was nearly two times that for 2-min treatment. The deuterium penetration into MCT which remained under the ZnS film was negligible. The Au-doped MCT samples differed from vacancy-doped ones by a substantially lower deuterium concentration at large depths (>1000 nm) in the samples RIE-treated for 2 min.

To explain the data, a qualitative model was proposed according to which the plasma used in RIE, first, serves as a source of hydrogen atoms and, second, disrupts (etching off) the surface layer of the material, generating free interstitial Hg. In the authors' opinion, hydrogen itself enters the crystal in the process in three ways and the conductivity-type conversion under RIE is a complex process induced by radiation damage, by acceptor neutralization, and, possibly, also by additional doping through formation of complexes constituted by a hydrogen atom and a Hg_I atom. It was assumed in [47] that, at temperatures typical of RIE, free Hg generated at the surface could diffuse into the crystal only for a small distance. For example, at a diffusion coefficient of $D_I \approx 1 \times 10^{-5}$ cm^2 s^{-1} and an RIE time of 2 min, the converted layer would extend to a depth of <1000 nm, while the corresponding experimental values are 2500 nm. Thus, defects of another type, with a mobility higher than that of Hg_I, must exist in a crystal during RIE. It is suggested that the role of these defects is played by hydrogen, because its atom is small in size and there is an unlimited source of free atoms in the plasma. Although interstitial hydrogen by itself does not affect the electrical properties of the material, it can modify these properties up to conductivity-type conversion due to its fast diffusion and easy interaction with other lattice defects. It is supposed, in particular, that electrical properties of the surface layer in a RIE-treated crystal, with a typically higher density and lower mobility of electrons, are defined by complexes comprising hydrogen bound to radiation-induced lattice defects and/or Hg_I atoms. The bulk portion of *n*-layer is formed due to neutralization of initial acceptors (intrinsic or impurity-related) by hydrogen, so that the electrical properties are defined by the residual donor impurities, as had been assumed at the very start for MCT subjected to LEIT. The only open question was why does the depth of hydrogen penetration, determined from SIMS data, substantially exceed the conversion depth determined from the Hall data. To solve this problem, it is suggested to consider a set of equations for the diffusion of mobile hydrogen in a system of fixed acceptors, similar to one derived for Hg_I diffusion in MCT; i.e.,

$$\frac{\partial C_{H_i}}{\partial t} = D_{H_i}\nabla^2 C_{H_i} - kC_{H_i}C_{A^-}, \quad (7)$$

$$\frac{\partial C_{A^-}}{\partial t} = -kC_{H_i}C_{A^-}, \quad (8)$$

where C_{H_i} and C_{A^-} are the concentrations of interstitial hydrogen and ionized acceptors and k is a coefficient that accounts for the rate of the acceptor neutralization by hydrogen. In a 1D-approximation and under the assumption that the solubility limit for hydrogen is reached on the crystal surface, the acceptor concentration on the surface is expressed by

$$C_{A^-}(t, z = 0) = C^0_{A^-}\exp(-kC^s_{H_i}t), \quad (9)$$

where $C^0_{A^-}$ is the initial concentration of ionized acceptors and $C^s_{H_i}$ is the saturation concentration for interstitial hydrogen. This model predicts a high rate of acceptor neutralization on the surface and a rapid decrease of this rate away from the crystal surface. It is this circumstance that accounts for the smaller depth of the conversion region as compared with that of interstitial hydrogen penetration. In this situation, the shift of the peak in the hydrogen distribution profile upon thermal annealing of RIE-treated samples is attributed to partial out-diffusion of interstitial hydrogen with increasing temperature.

Thus, according to [47], the conductivity-type conversion in MCT proceeds by the two main coexisting mechanisms, with the principal role played by hydrogen from the plasma. In this context, it seems interesting to compare these results with the data from [26, 28]. In the first case, no difference was observed between the use of hydrogen or Ar plasma; in the second, the deepest conversion region was obtained with Ar plasma, rather than with that of hydrogen or methane (see Table 3). Evidently, some other mechanism of conversion must be offered for RIE in argon.

As mentioned above, in the construction of the two discussed models, the authors took into account the data on conductivity-type conversion in acceptor-impurity-doped crystals, not only vacancy-doped MCT. In this context, it was proposed to regard the reactions of LEIT-produced mobile atoms with the acceptors which defined *p*-conductivity in the starting sample, and these acceptors might be Hg vacancies in a vacancy-doped crystal or impurity atoms in an intentionally doped crystal (the latter case will be discussed in detail in the next section). On the whole, this approach yields a more general description of the conversion processes in MCT under LEIT; nevertheless, efforts have not ceased in the construction of a model for conversion in

vacancy-doped MCT in the context of intrinsic defect interactions alone.

For example, a general case of the conductivity type conversion in undoped MCT has been discussed in [48]. Earlier model [49] describing the MCT conductivity conversion from *p*- to *n*-type under annealing in a Hg vapor has been derived to obtain an analytical expression for z_J^2/t as a function of concentrations of the intrinsic crystal defects and residual donor impurities N_d (z_J is the *p–n* junction depth attained over the course of time *t*). The expression was obtained, and the fitting of the analytical curve to the experimental data on annealing of MCT single crystals under different pressures of Hg vapor allowed the authors to determine several parameters of intrinsic defects in MCT. For us, the most interesting are the estimations of the MCT LEIT process parameters obtained by the authors of [48] using the analytical expression derived by them and the experimental data on LEIT of MCT with $0.20 < x < 0.24$ from [18, 20].

The analytical expression obtained does not explicitly include the acceptor (vacancy) concentration N_a in the starting material, which affects the conversion depth under LEIT, but it includes the total concentration of the excess Te, C_{XTe}, which is equal to the sum of concentrations of Hg vacancies and Te in precipitate form. (The model in [49] assumes that the excess Te is one of the key participants in the processes in MCT and takes into consideration the propagation of the interface between the surface *n*-layer and the crystal nucleus, instead of the *p–n* junction itself.) Assuming $N_a = C_{XTe}$ and using the data from [18], the authors of [48] estimated that, for conversion induced by ion-beam etching, the value of $N_a z_J^2/t$ is by a factor of $\sim 10^8$ higher than it would be upon annealing of MCT at the temperature of 25°C typical of LEIT. It has been noted that, at so low a temperature, a complex analytical expression for z_J^2/t turns into a simple relation $N_a z_J^2/t = 2D_{Hg}C_{I0}$, where D_{Hg} is the diffusion coefficient of interstitial Hg atoms and C_{I0} is their surface concentration. Evidently, this expression is identical to those obtained earlier [18, 20] for the depth of *p–n* junctions formed in MCT under LEIT. Thus, if the diffusion coefficient D_I is assumed to be constant, the surface concentration Hg_I remains the only factor distinguishing the process of ion-beam etching from Hg diffusion in annealing in Hg vapor. The estimates [48] indicate that, under ion-beam etching, C_{I0} can be as high as $\sim 3 \times 10^{13}$ cm^{-3}, depending on the current density.

Similar estimations were made in [48] based on the experimental data [20]. It was found that in these experiments $N_a z_J^2/t$ must be, on average, 2.9×10^9 cm^{-1} s^{-1} and the effective concentration C_{I0}, $\sim 2.4 \times 10^{14}$ cm^{-3}, which is by a factor of $\sim 1.5 \times 10^8$ higher than its value in the case of annealing.

Conventional concepts of Hg chemical diffusion were used in [50] to elucidate the conversion mechanism in MCT under LEIT. Electrical properties of MCT crystals were analyzed taking into account only Hg vacancies and interstitial mercury atoms, with the diffusion transport effected by mobile Hg_I atoms and the decisive factor being the interaction of these atoms with fixed vacancies. Both types of defects were assumed to be doubly charged.

In contrast to other studies, it was assumed in [50] that the conversion is defined not by the interstitial Hg atoms formed on the surface upon etching, but by those released upon absorption of the energy of an incident ion at some depth. Three zones were distinguished in a crystal subjected to etching. The surface zone with a thickness on the order of the ion penetration depth contained a large amount of defects and was Hg-depleted due to Hg evaporation to a vacuum. The latter fact impeded further flow of interstitial Hg to the surface, because the more pronounced its deficiency in the crystal, the slower its chemical diffusion [51] (similarly to [20]). Thus, interstitial Hg diffuses away from the surface into the crystal, producing there a diffusion layer of a definite thickness, with the defect structure remaining unchanged in the inner part of the crystal (core). If the number of charged point defects does not exceed the concentration of intrinsic carriers (high temperature), the mass action law must be fulfilled:

$$[V_{Hg}][Hg_I] = K_F, \tag{10}$$

where K_F is the equilibrium constant. As a result, nearly the entire depth of the diffusion region is cleared of vacancies and the vacancy concentration at the diffusion front abruptly increases to its initial value. Then the depth of the diffusion front is given by

$$l = (2D_i t[Hg_I]_S/[V_{Hg}])^{1/2}. \tag{11}$$

All the above-said refers to chemical diffusion in thermal annealing of MCT. In the case of ion-beam etching, the density of intrinsic carriers is much lower than under annealing and a layer with a high density of charged defects is formed near the surface. In this situation, the system of equations describing the MCT annealing [51] should be supplemented with an equation that takes into account the effect of internal electric field (potential φ), and the expression for the Hg_I flow, with the drift term. Then the system of equations takes the form

$$\frac{\partial}{\partial t}[Hg_I] - D_{Hg}\frac{\partial}{\partial z}\left\{\frac{\partial}{\partial z}[Hg_I] + \frac{2e}{k_B T}[Hg_I]\frac{\partial \varphi}{\partial z}\right\} = k_F(K_F - [V_{Hg}][Hg_I]), \tag{12}$$

$$\frac{\partial}{\partial t}[V_{Hg}] = k_F(K_F - [V_{Hg}][Hg_I]), \tag{13}$$

$$\frac{\partial^2 \varphi}{\partial z^2} = \frac{e}{\varepsilon\varepsilon_0}(n - p + 2[V_{Hg}] - 2[Hg_I]). \tag{14}$$

Here, k_F is the reaction rate constant and the z axis is parallel to internal normal to the crystal surface; $z = 0$ is chosen to be at the interface between the diffusion zone and the surface defective layer. Then, assuming that the damaged layer is thin, the position of the diffusion front corresponds to $z \approx l$. Taking into account that the electric field is mainly concentrated near the $z = 0$ interface, the field is negligible in most of the diffusion region. On the whole, the authors assume that the internal field does not affect the qualitative pattern of the diffusion process; it can change only the effective surface concentration of Hg_I. Therefore, the propagation of the diffusion front occurs in accordance with Eq. (2).

Further, a series of simplifications was made in [50] taking into account the real situation in a crystal; two possible mechanisms of Hg introduction into the crystal were regarded: the diffusion of point defects and the formation of crowdions, with the dependences of the diffusion-front depth on the main parameters of a crystal obtained in both cases. The details can be found in [50]; here it should be stated that some of the estimations made by the authors led to several important conclusions. In particular, a conclusion was made that, under ion-beam etching, a greater portion of the diffusion zone is free of Hg vacancies, i.e., $[V_{Hg}] = 0$ at the diffusion front on its side facing the surface and $[Hg_I] = 0$ on the side of unconverted crystal core. This is the difference between the case of LEIT and that of thermal annealing, in which the concentration of vacancies in the diffusion zone decreases only to the value corresponding to equilibrium with the vapor phase. Therefore, in principle, the n-layer formed by ion-beam etching must have "better" quality than the one formed by thermal annealing, in the sense that the layer is virtually uncompensated and must exhibit the maximum electron mobility.

The authors of [50] offer two factors that can be responsible for the specifics of Hg diffusion under ion-beam etching. On one hand, diffusion under etching occurs at lower temperature, when the equilibrium constant K_F is small, about $\sim 10^8$ cm^{-6}. On the other hand, LEIT produces on the surface Hg_I atoms in amount greatly exceeding their concentration under equilibrium with Hg vapor. For example, estimations show that, under ion-beam etching, the Hg_I concentration at 300 K on the surface is as high as 10^{12} cm^{-3}, exceeding that under equilibrium with Hg vapor by a factor of $\sim 10^7$. By a order of magnitude, these values correlate with the estimations made in [48]. It is necessary to also note that for both mechanisms under discussion (diffusion and crowdion formation), the squared thickness of the converted layer is proportional to the irradiation dose $\Phi = jt$ and inversely proportional to the initial concentration of vacancies. This observation is in agreement with the data obtained in numerous LEIT experiments [18, 20, 22]. The authors of [50] have predicted also that with Cd content in MCT (and, correspondingly, the band gap) rising, the conversion rate must decrease, due to internal electric field. This effect was later observed in [19]. It is worth noting that the conversion mechanism developed in [42] was modified [52] by taking into account the contribution of neutral Hg divacancies.

There exists also another approach to understanding the conversion mechanism in doped MCT subjected to ion-beam etching [53]. It is based on the experimental facts, many of which contradict the above-listed. In particular, it is stated in [53] that (1) the dependence of the p–n junction depth on time does not pass through the origin of coordinates, i.e., the conversion process is much more intense in the first seconds of LEIT (by contrast to [18, 20]); (2) the size of the conversion region is virtually temperature-independent (which contradicts the data of [44]); (3) the shape of the interface in the p–n junction is nearly hemispherical (in contrast to [20]); (4) the converted layer consists of three, not two, sublayers—the radiation-damaged n^+-layer (its thickness is 0.5–1 μm), the layer with n decreasing exponentially away from the surface (2–3 μm), and the uniform n^--layer with controllable thickness; (5) the conversion depth is virtually the same in MCT doped with Ag, Na, Cu, or Au. Based on the data obtained, the authors of [53] offer the hypothesis that the effect of a low-energy ion beam can be reduced to three basic effects: (1) the destruction of the crystal lattice on the surface, (2) "implantation" into crystal of some fraction (about 0.02%) of the Hg atoms released there, and (3) plasma-stimulated diffusion. It is assumed that, in accordance with earlier observations made by the same authors [54], the LEIT mechanism of Hg-atom implantation into the crystal differs radically from the diffusion mechanism in the case of thermal treatment. The independence of the conversion rate of temperature and large conversion depths are attributed to excitation of the metal sublattice by the ion beam or to anomalous mobility of Hg atoms. In this approach, one of the conclusions is that the processes under LEIT are similar to those under ion implantation. Regretfully, a more detailed analysis of this model is hindered by the paucity of experimental data in [53].

5.2. Doped MCT

Obviously, the model of the conductivity-type conversion, derived for vacancy-doped MCT, is not expected to describe adequately the processes under LEIT of MCT doped with acceptor impurity. Post-growth annealing of these samples is performed under conditions close to crystal saturation with Hg, so that the majority of Hg vacancies are filled. In this case, the hole density in the starting material is defined by the concentration of the acceptor impurity and Hg_I atoms diffusing under LEIT cannot be annihilated effectively with the few existing vacancies.

An interesting feature in this situation is that the characteristics of Hg_I diffusion (the thickness of the converted layer and the speed of propagation of the conversion front into the sample) appeared to be almost identical for LEIT of both impurity- and vacancy-

doped MCT samples [39]. Furthermore, the parameters of LEIT-produced *n*-layers (electron density and mobility) were also very close in As-, Sb-, and vacancy-doped samples [41].

Au-doped MCT [36] appeared to be an exception to this rule. Prior to LEIT, the initial acceptor concentration in this MCT was ~2×10^{16} cm^{-3}, and after LEIT (RIE) the electron density at low temperatures (in the range of extrinsic conductivity) in the converted layer was $(1–3) \times 10^{15}$ cm^{-3}, i.e., lower by the order of magnitude. The authors attributed this fact to the effect of Au atoms being kicked out of the *n*-layer formed on the epilayer surface under LEIT more deeply into the sample, to the *p*-layer. An alternative explanation is as follows: hydrogen atoms from the $H_2 + CH_4$ plasma deactivate Au atoms with the formation of neutral $(Au^-–H^+)$ complexes. In both cases, the conversion mechanism is similar to that suggested for vacancy-doped MCT.

The idea that complexes constituted by interstitial Hg atoms and impurity atoms take part in the conductivity-type conversion was proposed also in the studies of LEIT (ion-beam etching) of MCT doped with As and Sb [39, 40]. However, the authors suggested that a donor, rather than a neutral complex, is formed; this donor complex is formed by interstitial Hg atoms, which are released at the surface under ion-beam etching and diffuse into the sample, and As or Sb atoms. The model was based on the experimental fact that the electron density in the bulk of the *n*-layer was formed in As-doped MCT under ion-beam etching coincided, within the experimental error, with As concentration in the starting sample. Thus, the impurity atoms were not neutralized; exactly the opposite—each of them made its contribution to electronic conductivity.

This idea was elaborated in [41]. The key point here was the same assumption that, under LEIT, Hg_I atoms interact with other point defects in the lattice and form, e.g., complexes with impurity atoms. Initially, prior to LEIT, Group V atoms act as acceptors (A'_X) localized in the Te sublattice. In MCT, such a center can form a stable donor complex $D^{\bullet}$ by being bound with an interstitial Hg atom by the reaction

$$Hg_I + A'_X \longrightarrow D^{\bullet}. \quad (15)$$

For this reaction, the mass action law is expressed by the relation

$$[Hg_I][A'_X] = K[D^{\bullet}]. \quad (16)$$

Here, $K = K_0\exp(-\Delta H_c/k_BT)$ is the equilibrium constant ($K_0 \approx N_0$, where N_0 is the density of sites in the metal sublattice and ΔH_c is the enthalpy of the formation of the complex). The system should be supplemented with the condition that a constant number of impurity atoms dissolve in the crystal, $[A]_{tot}$:

$$[A'_X] + [D^{\bullet}] = [A]_{tot} \quad (17)$$

(the amount of the impurity atoms in interstitial positions is negligible, and all the substituting impurity atoms are considered ionized).

Then,

$$[D^{\bullet}] = [A]_{tot}[Hg_I]/([Hg_I] + K). \quad (18)$$

It follows hence that solitary substitution centers A'_X predominate at $[Hg_I] \ll K$, while at $[Hg_I] \gg K$ the impurity atoms are predominantly included into complexes. Thus, the predominant form (a single atom or complex) of the Group V element in the sublattice is defined by the enthalpy of the formation of the complex. The calculations performed by the authors showed that at room temperature and an interstitial Hg concentration of $[Hg_I] \sim 10^{12}$ cm^{-3} (this value is reached at the generation of these atoms under LEIT), Group V atoms will be preferentially bound in complexes if $\Delta H_c > 0.6$ eV. The value of ΔH_c in As-doped MCT was estimated in [39] as (1 ± 0.1) eV. For Sb-doped MCT, ΔH_c was ~0.6–0.9 eV [40]. Thus, in both cases, ΔH_c appeared to be sufficiently high and it was necessary to take into account the formation of complexes in LEIT of MCT doped with these impurities (As, Sb). In this situation, if the complex formation is sufficiently fast, the reconstruction of the defect structure is limited by Hg_I diffusion, and the diffusion kinetics equations for LEIT of impurity-doped MCT become similar to those describing the diffusion in LEIT of vacancy-doped MCT. Under these conditions, the speed of propagation of the conversion front in impurity- and vacancy-doped samples is the same, and this was confirmed experimentally.

Thus, the proposed model of the conductivity type conversion under LEIT of As- or Sb-doped MCT assumes modification of the charge state of a center containing an impurity atom, with the formation of a complex with an Hg_I atom. The necessary condition for the formation of such a complex is an energy above 0.6 eV. Under this condition, a center having the form of a Group V atom A'_X, a singly charged acceptor, is transformed into a singly charged donor complex $(Hg_I–A'_X)$ via the formation of a new chemical bond. The formation of these complexes results in the conductivity-type conversion from *p*- to *n*-type in the layer where Hg_I diffuses. In this case, the conversion rate in LEIT of vacancy-doped MCT and that doped with As or Sb appears to be the same.

As for the electron density in the converted layer, it must be close to the hole density in the starting *p*-sample, provided that the concentration of residual impurities is lower than the doping level. Just this result was observed in the experiments with LEIT of As-doped MCT: the electron density in the converted *n*-layer was 1.6×10^{16} cm^{-3}, and the hole density in the original sample was $(1.8–2) \times 10^{16}$ cm^{-3}. For Sb-doped samples, the electron density after LEIT appears to be lower than the initial hole density in the untreated samples: 10^{16} and $(6–10) \times 10^{16}$ cm^{-3}, respectively. This fact is attributed

[41] to a lower enthalpy of formation of an (Sb_{Te}–Hg_I) pair, which is close to the critical energy of 0.6 eV. It is noteworthy that this difference would be even larger for samples doped with a Group I element, Au: (1–3) $\times 10^{15}$ and 2×10^{16} cm^{-3}, respectively [36]. Evidently, developing the concept of complex formation in the last two cases requires further study.

Nevertheless, at least for the case of LEIT of As-doped MCT, the electron density in *n*-layer is directly related to the concentration of the acceptor impurity in the starting material. This fact opens the prospect of applying LEIT of MCT for the fabrication of *p*–*n*- junctions with the prescribed carrier density in the *n*-region. It is necessary to note, however, that in this case the *p*–*n*- junction being formed is symmetrical; in contrast, for vacancy-doped MCT, the electron density in *n*-layer can also be controlled by varying the hole density in the original sample, but the densities *n* and *p* differ nearly by an order of magnitude [18, 19].

No consensus exists at present on the mechanism of conductivity-type conversion upon LEIT of MCT. It seems that, in the case of vacancy-doped MCT, the most realistic approaches are those that take into consideration only the interaction of point defects, when interstitial Hg atoms generated by LEIT on the crystal surface diffuse into the crystal and are annihilated with vacancies, thus revealing the residual donor impurities. This model qualitatively describes both the process itself (i.e., the observed dependences of the conversion region thickness on the parameters of sample and LEIT) and the properties of the material obtained. However, this approach fails to account for the conversion in doped MCT, in which the initial amount of vacancies is negligible. For this situation, models taking into consideration the formation of complexes and inter-substitution of defects have been developed. These models still require direct experimental confirmation, e.g., by studying the mechanisms of scattering in the charge transport in these crystals. An important factor, however, is the "convergence" of approaches that take into consideration the defect formation in MCT under different treatments, with low- and high-energy ions, and also in thermal treatment [55, 56]. So, we hold out in our hope that a general picture describing the formation, migration, and interaction of defects in MCT will be constructed in the future.

6. PROPERTIES OF *p*–*n* JUNCTIONS AND PHOTODETECTORS FABRICATED BY LOW-ENERGY ION TREATMENT

Despite the lack of understanding of the *p*–*n* junction formation mechanisms in MCT under LEIT, the method has been applied in the fabrication of IR photodetectors for more than a decade. Though unclassified communications are scarce, the available publications give a certain idea of the potentiality of this method. Two directions in the evolution of device structures can be expected: first, the improvement of parameters of the existing devices due to inherent advantages of the new method (e.g., reduction of the amount of undesirable intrinsic defects introduced), and second, the application of new fundamental opportunities opened up by the new method. Currently available publications illustrate the potentialities of LEIT in both directions. Furthermore, a commercial fabrication of MCT photodetectors by LEIT, with both approaches used, was reported [57]. In particular, a "traditional" approach with ion-beam etching is used in fabrication of photodiodes by the flip–chip technique (the fabrication of a planar *p*–*n* junction and formation of a contact with the read-out Si plate by In columns), and the original one, the so-called loophole technique, where the effects of ion etching and *n*-layer formation are used simultaneously, as was suggested in the patent [14].

It seems that one of the first studies on the properties of *p*–*n* junctions produced in MCT by LEIT was [58], where the loophole technique was implemented. Long-wavelength MCT photodiodes produced by ion-beam etching were studied (the cutoff wavelength $\lambda_{co} \approx 11$ µm at 77 K). The *p*–*n* junction was formed by creating an opening in the initially *p*-type material by ion-beam etching, with conductivity-type conversion to *n*-type in the vicinity of this opening. The starting MCT wafer was 5 µm thick, the opening produced by etching was 4–10 µm in diameter, and the lateral depth of the *p*–*n* junction was 3 µm from the edge of the opening. The hole density in the *p*-region of the junction was 5×10^{16} cm^{-3}, and the electron density in the forming *n*-region, 4×10^{14} cm^{-3}. Studies of the photocurrent multiplication, *I*–*V* characteristics, and noise in photodiodes of this kind have shown that the reverse *I*–*V* characteristic is defined by avalanche multiplication and by a combination of avalanche multiplication with band-to-band tunneling at a large bias.

The dark current in *p*–*n* junctions produced in MCT with $x = 0.24$ by ion-beam etching was studied in [59]. The hole density in the starting crystals was $p \approx (1.2–2) \times 10^{16}$ cm^{-3} in the temperature range 77–110 K. Argon ions with an energy of $E = 1.8$ keV and dosage of 5×10^{16} cm^{-2} were used to produce *p*–*n* junctions by ion-beam etching. The diodes were planar structures with an area of $A = 2.5 \times 10^{-5}$ cm^2, with the surface passivated with CdS.

Figure 7 shows forward *I*–*V* characteristics of a typical *p*–*n* junction produced by ion-beam etching, at temperatures of $60 \le T \le 150$ K. As seen, the slope of *I*–*V* characteristics in the logarithmic scale is temperature-independent at biases of up to ~0.8 V. After the subtraction of the drop in voltage across the series resistance of the base, the *I*–*V* characteristic itself is well described by the expression

$$I = F\exp[-\gamma(V_c - V)], \quad (19)$$

where *I* is the current across the *p*–*n* junction; *V*, the applied bias; V_c, the contact potential; and *F*, the preexponential factor. The γ parameter was temperature-

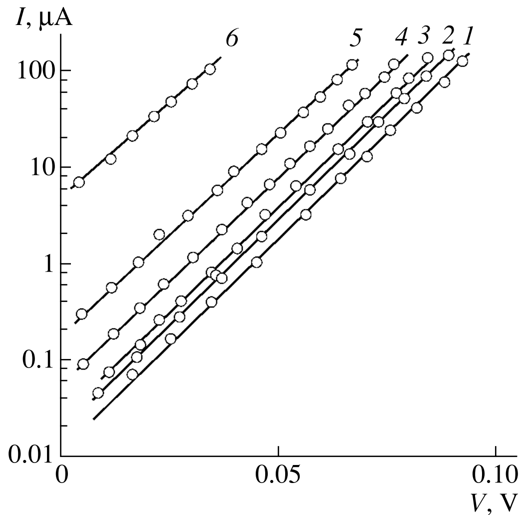

Fig. 7. Forward *I*–*V* characteristics of a *p*–*n* junction produced by ion-beam etching at temperatures of (*1*) 60, (*2*) 70, (*3*) 77, (*4*) 90, (*5*) 110, and (*6*) 150 K [59].

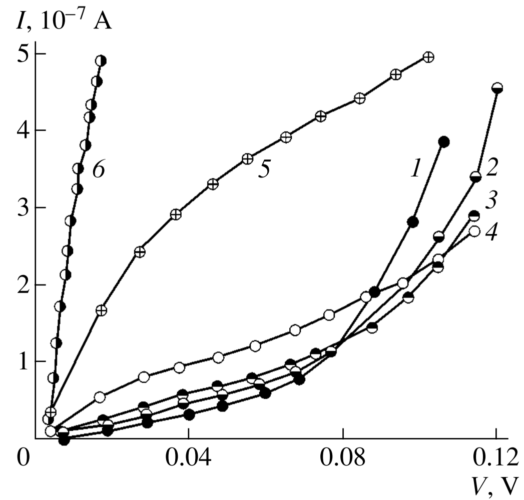

Fig. 8. Reverse *I*–*V* characteristics of the same (see Fig. 7) *p*–*n* junction [59]. For designations, see Fig. 7.

independent in the range under study, which is indicative of the tunneling mechanism of current flow across the *p*–*n* junction, with local centers involved [60]. At $T > 110$ K, the forward *I*–*V* characteristics are well described by the dependence

$$I = I_0\left[\exp\left(\frac{qV}{\beta kT}\right) - 1\right],$$

where q is the elementary charge. For $T = 150$ K, $\beta = 1.1$, which indicates the diffusion mechanism of current flow.

Figure 8 shows reverse *I*–*V* characteristics of the same *p*–*n* junction. At $T > 110$ K, the current steeply increases with increasing temperature, which means that the current is determined by thermally activated processes (diffusion or generation–recombination). In the temperature range from 60 to 90 K, at a large bias of $V \geq 0.8$ V, the reverse current decreases with increasing T, which is typical of the band-to-band tunneling mechanism. In this case, the decreasing current with increasing T is due to the positive temperature coefficient of the E_g variation. A specific feature of this mechanism is the linearity of the *I*–*V* characteristic in the coordinates $\ln[I/V(V + V_c)^{1/2}]$ versus $(V + V_c)^{-1/2}$ [61], which is indeed the case, as seen from Fig. 9. At a low bias, $0 < V < 0.08$ V, at $T = 60$ K the reverse *I*–*V* characteristic is also linear in the coordinates of Fig. 9, but the slope is smaller than for band-to-band tunneling. This is indicative of tunneling via local centers. At $T >$ 60 K, reverse *I*–*V* characteristics are not linear in the coordinates of Fig. 9, with reverse current increasing with T, and, therefore, the current in this range of temperatures and biases is defined by some other mechanisms.

The temperature dependence of differential resistance of a *p*–*n* junction R_dA was analyzed in [59]. Figure 10 shows R_dA versus inverse temperature in the range of $60 < T < 200$ K for biases of 0, –0.03, –0.05, and –0.1 V. The slope of the dependence recorded at $T > 125$ K under zero bias, (R_0A), corresponds to E_g, which is typical of the diffusion current flow across the *p*–*n* junction. At $T < 90$ K, R_dA exhibits a positive temperature coefficient under a bias of –0.1 V; this dependence is typical of band-to-band tunneling in MCT and is related to the positive temperature coefficient of E_g. The calculated curve of the R_dA temperature dependence is shown by the solid line in Fig. 10. The fitting parameter was the concentration $N_0 = N_aN_d/(N_a + N_d)$. The best fit was obtained for $N_0 = 1.6 \times 10^{16}$ cm^{-3},

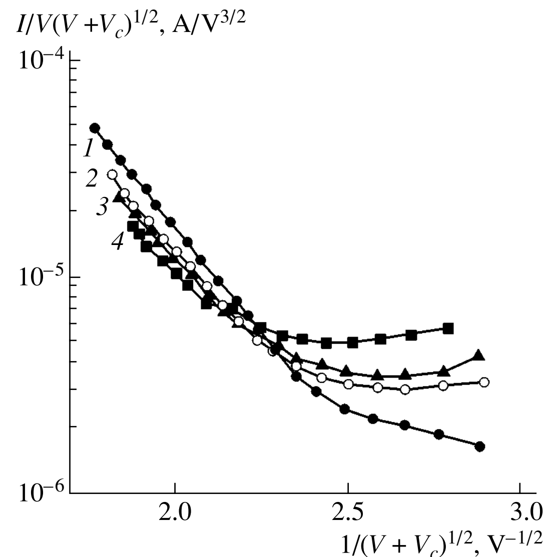

Fig. 9. Reverse *I*–*V* characteristics in the coordinates $\ln[I/V(V + V_c)^{1/2}]$ versus $(V + V_c)^{-1/2}$ at temperatures: (*1*) 60, (*2*) 70, (*3*) 77, and (*4*) 90 K [59].

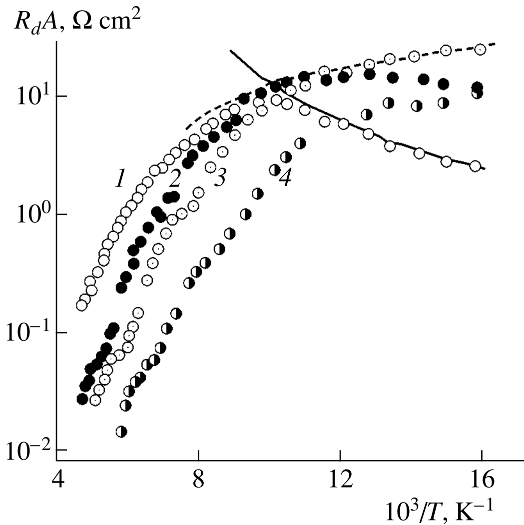

Fig. 10. Differential resistivity versus the inverse temperature at different biases: (*1*) –0.1, (*2*) –0.05, (*3*) –0.03, and (*4*) 0 V. Solid and dashed lines represent the calculated dependences [59].

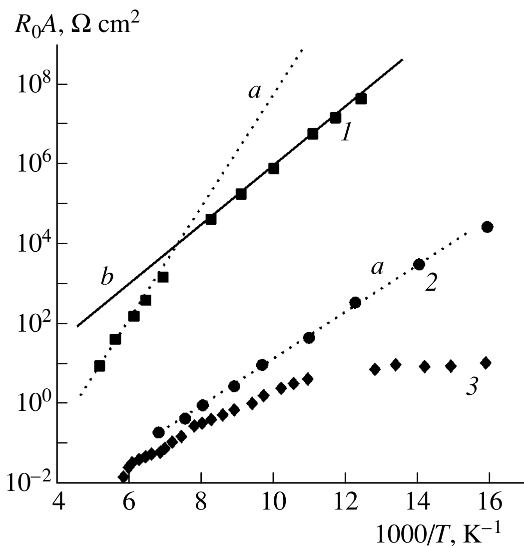

Fig. 11. R_0A versus inverse temperature in structures with *p–n* junctions produced by ion-beam etching on MCT epilayers: (*1*) photodiode, λ_{co} = 4.3 μm at 80 K [32]; (*2*) heterostructure with lateral *p–n* junctions, λ_{co} = 10.1 μm at 80 K [63]; (*3*) the structure with λ_{co} = 8.4 μm at 80 K [59]. Lines show calculated dependences for (*a*) diffusion and (*b*) generation–recombination mechanisms.

which is very close to the concentration of uncompensated acceptors in the starting *p*-material. At $T < 90$ K and $V = -0.03$ V, R_dA had a small negative temperature coefficient, typical of tunneling via local levels [62]. The calculated temperature dependence of R_dA is shown by the dashed line in Fig. 10. Again, the best fit to the experiment is obtained up to $T \approx 90$ K for $N_0 = 1.6 \times 10^{16}$ cm^{-3}.

Thus, it was established that the main mechanisms of current transport in planar *p–n* junctions produced in MCT by LEIT are thermally activated mechanisms at $T > 110$ K and band-to-band tunneling and tunneling via local centers at $60 < T < 110$ K.

The dark current in *p–n* junctions produced by LEIT in MCT epilayers with $x = 0.32$ were studied in [32]. In this case, the *p–n* junction was formed by RIE by the technique described in [29]. Vacancy-doped MCT epilayers grown by LPE on CdZnTe substrates served as the starting material. The layer thickness was 24 μm, and the hole density and mobility were $p = 5 \times 10^{15}$ cm^{-3} and $\mu_p = 430$ cm^2 V^{-1} s^{-1}. The cutoff wavelength was $\lambda_{co} = 4.3$ μm at 80 K. The device structures were fabricated by planar technology, with passivation with a ZnS layer of 3000 Å in thickness. The size of windows for the formation of photodiode elements by RIE was 250×250 μm^2.

I–V characteristics of the structures obtained were diode-type, with a cutoff voltage of 135 mV in the forward portion, and a soft breakdown in the reverse portion at high bias, which is typical of the tunneling mechanism. The current responsivity of the devices was 1.37 A W^{-1} at a wavelength of 4.3 μm. The quantum efficiency at 4 μm was 56%.

Figure 11 shows the temperature dependence of R_dA at zero bias (R_0A) (points *1*). As seen, at temperatures above $T = 135$ K, the current is governed by diffusion mechanisms; below it, by generation–recombination. At 80 K, $R_0A = 4.6 \times 10^7$ Ω cm^2.

The dependences of R_dA on reverse bias were recorded at temperatures of 80, 100, 120, 145, and 195 K. It was found that the peak in the $R_dA = f(V)$ curve shifts to higher bias with rising temperature. Based on this fact, the behavior of $R_dA = f(V)$ was modeled taking into account three mechanisms of current transport: diffusion, generation–recombination, and tunneling via local centers. The energy position of these centers was estimated as ~$0.7E_g$.

The properties of planar photodiodes of this type were studied in more detail in [64]. Studied were the parameters of photodiodes produced by RIE on three types of MCT: LPE-grown epilayers on CdZnTe substrates (in-layer $x \approx 0.32$) and on sapphire (in-layer $x \approx 0.31$), and an MBE-grown isotype *p–n* junction (x = 0.314 and 0.374 in the active and top layers, respectively). The epilayers were vacancy-doped, with the vacancy concentrations of 5×10^{15}, 2×10^{16}, and (1–2) × 10^{16} cm^{-3}, respectively. The process of photodiode fabrication was similar to that described above. Typical RIE parameters were the ratio of gas flow rates ($H_2 : CH_4 = 5 : 1$), a chamber pressure of 500 mTorr, and an rf power of <100 W.

It is worth noting that, according to the *C–V* data for MIS strictures fabricated on the ZnS layers used for passivation of the photodiode surface, the passivating properties of ZnS were improved by RIE. MIS stric-

tures were based on MCT single crystals with $x \approx 0.30$, with a 300-nm-thick ZnS layer. C–V characteristics were recorded at 1 MHz at 80 K. It appeared that the built-in charge in the insulator substantially decreased after RIE; its sample-to-sample scatter also decreased. Thus, LEIT did not disturb the passivation of the semiconductor surface, as often happens under ion implantation, but even enhanced the passivation effect. Later, the same authors showed that, from the standpoint of temperature stability, the optimal passivation of p–n junction produced in MCT by RIE is achieved by double-layer passivation with CdTe and ZnS layers [65].

Data on the temperature dependence of R_0A for a photodiode based on an epilayer with $x = 0.32$ were presented in [32]. In the authors' opinion, these data were representative and, on the whole, properly reflected the general situation with the parameters of the photodiodes obtained. For all three types of material, the best R_0A values were in the range of 5×10^6–5×10^7 Ω cm^2. The devices fabricated with MBE-grown p–p heterojunctions demonstrated maximum R_0A values on the same order as photodiodes based on homojunctions in a wider band-gap material grown by LPE. This confirmed the advantages of heterojunction devices, in which the surface leakage currents decrease in the presence of the surface wide-band-gap layer, which lessens the influence exerted on the dark currents by such processes as tunneling via surface traps and surface generation.

Temperature dependences of the low-frequency noise of the devices were also studied. Under study were diode structures with an area of 250×250 μm^2, based on homojunctions in the material grown by LPE on CdZnTe substrates. Under a bias of –0.05 V, the frequency (f) at which the flicker noise becomes comparable to the generation–recombination noise was lower than 10 Hz at 80 K and 1000 Hz at 180 K. The frequency dependence of the spectral density of excess noise was $f^{-0.93}$.

Finally, the properties of mid-wavelength IR (MWIR) and long-wavelength IR detectors with p–n junctions formed by ion-beam etching were studied in [55]. Epilayers with $x \approx 0.2$ and 0.3 were MBE-grown on CdZnTe substrates and passivated in situ with CdTe. Ion-beam etching was performed for 17 s at j = 0.54 mA cm^{-2}, which produced a p–n junction at a depth of ~3 μm, with a lateral extension of ~1.5 μm. The linear arrays of photodiodes that were formed consisted of 64 or 32 elements, and the measured parameters were $R_0A > 10^7$ Ω cm^2 for $\lambda_{co} = 4.5$ μm and R_0A = 300 Ω cm^2 for λ_{co} = 8.9–9.3 μm at T = 77 K. Three types of epilayers were studied: without composition grading, with small smooth grading, and with step grading across the layer thickness. The R_0A values in composition-graded samples were ten times those in ungraded layers.

The studies quoted above, with the exclusion of those devoted to the loophole technique, describe the application of LEIT methods for the fabrication of device structures based on currently existing technologies, in which the method is "built in" some already elaborated, e.g., for the ion implantation method, technological chain. Several publications refer to device structures originally designed for fabrication specifically by LEIT for cases when use of any other method of p–n junction formation is simply impossible or very difficult.

An example of this approach is an IR detector for a wavelength of 8–14 μm operating at elevated temperatures (200–300 K), fabricated on the basis of n^+–π–p^+ MCT heterostructures with the use of RIE [66, 67]. The idea was to create a device in which the plane of electron–hole junctions is parallel to the direction of the light beam to be detected. The point is that, in narrow-gap semiconductors at near-room temperatures, the absorption depth of IR radiation can strongly exceed the carrier diffusion length, with the result that only some fraction of the incident radiation is absorbed. This effect reduces the quantum efficiency of devices in which the plane of the p–n junction is perpendicular to the light beam, as in ordinary planar and mesa structures. This drawback can be obviated if the junction is parallel to the incident beam, with the ideal conditions created when (i) the active layer thickness is comparable to the absorption depth of the incident radiation, and (ii) the length of this region is close to, or smaller than, the carrier diffusion length. It is also known that the specific resistance of a photodiode based on narrow-gap MCT at 300 K is very small (e.g., for a detector with an area of 1×1 mm^2 operating at a wavelength of 10.6 μm at 300 K, the resistance is only ~10^{-3} Ω). The small value of R_0 results in very low voltage responsivity of the devices. An optimal way of raising the resistance is the use of an array of in-series connected N heterostructures; in this case, R_0 increases by a factor of N^2. Calculations show that for a detector with the same total area of 1×1 mm^2, consisting of 300 separate elements having an area of 3×1000 μm^2, where 3 μm is the width of the active region, it is possible to increase R_0 to 10 kΩ at 300 K. At present, no technology is capable of implementing this idea, i.e., of producing an array of heterostructures with a thick (up to 10 μm) active region and linear dimensions of each structure as small as several micrometers. However, a structure with a nearly ideal topology was produced in [67] using VPE and a combination of chemical etching with ion-beam etching.

The structures were based on As-doped p-type MCT epilayers of 5–15 μm in thickness. The layer composition was uniform across the layer to about two-thirds of the layer thickness from the surface, and then the Cd content increased gradually toward the CdZnTe substrate. The typical doping level was 10^{16} cm^{-3}. After epilayer growth, grooves with a depth of 0.7–0.9 of the total layer thickness were chemically etched. Further, p–n junctions were fabricated by ion-beam etching with Ar^+ ions, with a sample that was oriented at an

angle of 45° in respect to the ion beam, so that the conductivity-type conversion occurred on the surface between the grooves and on one of the walls of each groove. Owing to composition grading in epilayers, the structure obtained was constituted by an array of $n^+ip\underline{p}$ diodes (here $\underline{p}$ denotes the wide-band-gap region). The structures were passivated by depositing 200 nm of CdZnTe and 300 nm of ZnS.

The structures were studied by scanning electron microscopy, and it was established that carriers generated by IR radiation were effectively separated at the p–n junction. The detectivity of multiple-heterojunction devices was studied, consisting of p–n junctions arranged with a period of 15–30 μm, produced using the above-described technique. The maximum detectivity at 300 K at a wavelength of 7 μm was ~4.3×10^8 cm Hz$^{1/2}$ W^{-1}. On the whole, it was found that the sensitivity of devices produced by this method was at the same level or higher than the sensitivity of photoelectromagnetic IR detectors under the same external conditions. The devices produced by this method demonstrated, when operating with Peltier coolers, parameters comparable to the best photoconductors working in the same range of temperatures and wavelengths. However, in contrast to photoconductors, multiple heterojunction devices can operate at very low and very high frequencies. In the authors' opinion, further optimization of the geometrical and physical parameters of the devices (in particular, the doping level in the p-region) must substantially improve the operational characteristics.

Another example of the original application of the LEIT method is the development of a simplified technique for RIE fabrication of MCT photoconductors [68]. RIE in a hydrogen–methane mixture was used simultaneously (1) for the etching of a passivating layer to open windows for metallization and (2) to raise the "doping level" of n-material in the contact region of device structures. The entire process was considerably simplified as compared with the standard chemical etching procedure.

LPE-grown epilayers on CdZnTe substrates, with $x = 0.3$, $n = 9.8 \times 10^{14}$ cm^{-3}, and $\mu_n = 4 \times 10^4$ cm^2 V^{-1} s^{-1}, were studied. RIE was performed for 1 min in a $1CH_4 : 5H_2$ mixture. LBIC measurements on test structures demonstrated that, in this mode, RIE not only completely removed the passivating layer (natural anodic oxide was used), it also changed the carrier density in a surface layer of ~8 μm in thickness ($n \longrightarrow n^+$). As determined from R_H measurements, the electron density in the n^+-layer was 2×10^{15} cm^{-3} (thickness-averaged), with $\mu_n = 3.3 \times 10^4$ cm^2 V^{-1} s^{-1}.

A comparative study of the voltage responsivity of structures produced by this method and those fabricated using standard technology with chemical etching showed that the sensitivity of new structures at 3 μm at 80 K was higher by a factor of 3–4, dependending on the bias applied. The photosensitivity was measured at 1 kHz in an electric field of 10 V cm^{-1}, at $T = 80$ K and with a 60° field of vision. In this device, λ_{co} was 4.4 μm. Under these conditions, the device operated in the background-limited mode and its detectivity was 2.0×10^{11} cm Hz$^{1/2}$ W^{-1}, with a quantum efficiency of 70%. Thus, the application of RIE considerably simplified the technology of MWIR photoconductors and improved their parameters.

One more example of LEIT application has been presented in the studies where ion-beam etching was used for the fabrication of lateral p–n junctions to improve the parameters of MCT heterojunctions [63, 69]. Double-layer heterostructures were LPE-grown on CdZnTe substrates. The first MCT layer, with $x = 0.22$–0.23, was grown from a Te-enriched solution and had p-type conductivity. The second layer, 1 μm in thickness, with a wider band gap, was grown from a Hg-rich solution. The active layer was doped with In to a concentration of 1×10^{15} cm^{-3}. The top wide-band-gap layer was doped with As to 5×10^{16} cm^{-3}. After growth, the structure was annealed in saturated Hg vapor and the active layer changed its conductivity type from p to n, with $n = (5$–$10) \times 10^{14}$ cm^{-3} and $\mu_n = (4$–$8) \times 10^4$ cm^2 V^{-1} s^{-1}. The top layer remained p-type, because it was doped with an acceptor impurity. Thus, the "working" p–n junction was produced at the stages of growth and annealing. At the next stage, LEIT was used to fabricate the lateral p–n junction by ion-beam etching with argon. The etching depth was ~1000 Å, and lateral p–n and n^+–n junctions were formed at the edges of the "working" p–n junction. The p–n junction in the wide-band-gap layer provided isolation between individual diodes, and the deep lateral n^+–n structure in the active layer reduced the lifetime of minority carriers in the regions between diodes and produced an internal field that suppressed the crosstalk between individual devices.

The study of I–V characteristics and R_d dependences on bias in the range from –400 to +100 mV showed that the dark current at 80 K is governed by thermally activated mechanisms. At a bias of 0.1 V, R_0A was 10^4–10^5 Ω cm^2. Study of the temperature dependence of R_0A has shown that, at temperatures above 60 K, the p–n junction current is defined by diffusion processes (Fig. 11, points 2), and at lower temperatures, by the combination of diffusion, generation–recombination, and tunneling mechanisms. The quantum efficiency of photodiodes of 30×30 μm^2 in area, illuminated from the back, was 60–65% at 77 K. Studies of the noise spectrum under a bias of 0.05 V at 80 K showed that $1/f$ noise current in these devices was virtually frequency-independent down to 1 Hz. At this frequency, the noise current was at a level of 2×10^{-14} A Hz$^{-1/2}$. The electrical parameters of diodes did not change after low-temperature (80°C) annealing for 48 h.

It is necessary to recall that the above parameters characterized mainly the working p–n junction of the

heterostructure, and its properties were only indirectly improved by lateral *p–n* and n^+–*n* junctions produced by ion-beam etching. Nevertheless, the R_0A values obtained for diodes with cutoff wavelengths λ_{co} between 9.5 and 11.5 μm were close to the theoretical limit, which indicates promise for the method applied.

Thus, it can be concluded that, at present, the LEIT method enables fabrication of IR detectors competitive with similar devices produced by other methods. Evidently, LEIT does not rule out the appearance of reverse tunneling currents typical of devices produced by ion implantation, in which these currents were attributed to excessive doping and the extreme abruptness of *p–n* junctions. It is also evident that further studies are necessary to optimize LEIT-produced devices, especially to investigate and solve the problem of degradation of these IR detectors. Nevertheless, LEIT can considerably simplify the technology of the device structures. This conclusion follows, among others, from the recent detailed comparison of the plasma etching and ion-implantation technologies in the fabrication of MCT photodetectors [70]. Moreover, LEIT makes possible the formation of devices with novel topology, thus opening prospects for the fabrication of photodetectors with record-breaking parameters.

7. CONCLUSIONS

Analysis of studies concerned with modification of $Hg_{1-x}Cd_xTe$ properties by low-energy ions shows that the conductivity-type conversion $p \longrightarrow n$ under etching of the MCT surface with an ion beam, which was discovered more than 20 years ago, in recent years has changed from an undesirable by-effect to a promising method of *p–n* junction formation in the fabrication of IR photodetectors. Nowadays, technologies providing the conductivity-type conversion are being elaborated; they include ion-beam etching and reactive ion etching. The dependences of the conversion-region depth on the starting-material parameters (composition, vacancy, and impurity concentrations) and on the process parameters are also, on the whole, known, which facilitates the application of the technology. However, some refinement of the process parameters is necessary to obtain the prescribed size of the conversion region, taking into account the specific material used (single crystal or epilayers, the growing method, etc.). It is important that, within definite limits, the doping of the original material (with vacancies or impurities) makes it possible to control the density of carriers in the material after treatment. The method is highly promising for the technologies of IR photodetectors, especially considering the fact that its application provides reduction and simplification of technological chains and does not require any expensive equipment.

As concerns the physical processes in $Hg_{1-x}Cd_xTe$ crystal under low-energy ion treatment, the general opinion is that they are defined by diffusion mechanisms. The ultrafast rate of these processes is presumably determined by highly nonequilibrium conditions of diffusion (exceedingly high oversaturation of the crystal with mercury). It is the general opinion that interstitial mercury atoms are responsible for the diffusion transport; at the same time, the type of centers responsible, in the end, for the electrical properties of the treated material remains disputable. The proposed models of the conductivity-type conversion, which assume the formation of various defect complexes, including those in materials doped with different impurities, require experimental confirmation. Also evident is the need for further studies of the highly defective surface region formed under LEIT and of its effect on the device structure properties.

Nevertheless, it can be stated that the practice of low-energy ion treatment has formulated as a method for producing *p–n* junctions for photodiodes based on II–VI compounds containing mercury. The method opens up possibilities for designing new types of $Hg_{1-x}Cd_xTe$ device structures, which points to wide prospects for its application in the technology of IR photodetectors.

REFERENCES

1. J. Piotrowski and A. Rogalski, Sens. Actuators A **67**, 146 (1998).
2. M. A. Kinch, J. Electron. Mater. **29**, 809 (2000).
3. A. Rogalski, Infrared Phys. Technol. **43**, 187 (2002).
4. S. Krishna, A. D. Stiff-Roberts, J. D. Phillips, *et al.*, IEEE LEOS Newsl. **16** (1), 19 (2002).
5. A. Rogalski, Infrared Phys. Technol. **40**, 279 (1999).
6. N. S. Baryshev, *Properties and Applications of Narrow-Band Semiconductors* (UNIPRESS, Kazan, 2000).
7. K. Fisher and N. Rappenau, U.S. Patent No. 4128467 (1978).
8. R. B. Withers, U.S. Patent No. 4301591 (1981).
9. M. V. Blackman and M. D. Jenner, U.S. Patent No. 4321615 (1982).
10. M. S. Nikitin and K. P. Pavlov, in *Proceedings of VI All-Union Symposium on Semiconductors with Narrow Band Gap and Their Application* (Lvov, 1983), p. 136.
11. U. Solzbach and H. J. Richter, Surf. Sci. **97** (1), 191 (1980).
12. J. L. Elkind, J. Vac. Sci. Technol. B **10**, 1460 (1992).
13. J. T. M. Wotherspoon, U.S. Patent No. 4411732 (1983).
14. I. M. Baker, U.S. Patent No. 4521798 (1985).
15. M. V. Blackman, D. E. Charlton, M. D. Jenner, *et al.*, Electron. Lett. **23**, 978 (1987).
16. P. Brogowski, H. Mucha, and J. Piotrowski, Phys. Status Solidi A **114**, K37 (1989).
17. G. Bahir and E. Finkman, J. Vac. Sci. Technol. A **7**, 348 (1989).
18. V. I. Ivanov-Omskii, K. E. Mironov, and K. D. Mynbaev, Semicond. Sci. Technol. **8**, 634 (1993).
19. K. D. Mynbaev, N. L. Bazhenov, V. A. Smirnov, and V. I. Ivanov-Omskiĭ, Pis'ma Zh. Tekh. Fiz. **28** (22), 64 (2002) [Tech. Phys. Lett. **28**, 955 (2002)].
20. E. Belas, P. Hoshl, R. Grill, *et al.*, Semicond. Sci. Technol. **8**, 1695 (1993).

21. R. Haakenaasen, T. Colin, H. Steen, and L. Trosdahl-Iversen, J. Electron. Mater. **29**, 849 (2000).
22. R. Haakenaasen, T. Moen, T. Colin, *et al.*, J. Appl. Phys. **91**, 427 (2002).
23. I. I. Izhnin, A. I. Izhnin, K. R. Kurbanov, and B. B. Prytuljak, Proc. SPIE **3725**, 291 (1999).
24. S. Rolland, R. Granger, and R. Triboulet, J. Cryst. Growth **117**, 208 (1992).
25. V. I. Ivanov-Omskiĭ, K. E. Mironov, and K. D. Mynbaev, Fiz. Tekh. Poluprovodn. (Leningrad) **24**, 2222 (1990) [Sov. Phys. Semicond. **24**, 1379 (1990)].
26. E. Belas, J. Franc, A. Toth, *et al.*, Semicond. Sci. Technol. **11**, 1116 (1996).
27. V. V. Bogoboyashchiĭ, A. P. Vlasov, S. A. Dvoretskiĭ, *et al.*, in *Abstracts of 2nd Russian–Ukrainian Seminar on Nanophysics and Nanoelectronics* (Kiev, 2000), p. 63.
28. A. V. Dvurechenskiĭ, V. G. Remesnik, I. A. Ryazantsev, and N. Kh. Talipov, Fiz. Tekh. Poluprovodn. (St. Petersburg) **27**, 168 (1993) [Semiconductors **27**, 90 (1993)].
29. J. F. Siliquini, J. M. Dell, C. A. Musca, and L. Faraone, Appl. Phys. Lett. **70**, 3443 (1997).
30. V. G. Savitsky, L. G. Mansurov, I. M. Fodchuk, *et al.*, Proc. SPIE **3725**, 299 (1999).
31. J. F. Siliquini, J. M. Dell, C. A. Musca, *et al.*, J. Cryst. Growth **184/185**, 1219 (1998).
32. M. H. Rais, C. A. Musca, J. Antoszewski, *et al.*, J. Cryst. Growth **214/215**, 1106 (2000).
33. J. M. Dell, C. A. Musca, L. Faraone, *et al.*, Microelectron. J. **31**, 545 (2000).
34. P. Brogowski, J. Rutkowski, J. Piotrowski, and H. Mucha, Electron Technol. **24** (3/4), 93 (1991).
35. É. Belas, J. Franc, R. Grill, *et al.*, Neorg. Mater. **32**, 949 (1996).
36. J. Antoszewski, C. A. Musca, J. M. Dell, and L. Faraone, J. Electron. Mater. **29**, 837 (2000).
37. T. Nguen, J. Antoszewski, C. A. Musca, *et al.*, J. Electron. Mater. **31**, 652 (2002).
38. E. P. G. Smith, J. F. Siliquini, C. A. Musca, *et al.*, J. Appl. Phys. **83**, 5555 (1998).
39. V. V. Bogoboyashchiĭ, A. P. Vlasov, and I. I. Izhnin, Izv. Vyssh. Uchebn. Zaved. Fiz. **44** (1), 50 (2001).
40. N. N. Berchenko, V. V. Bogoboyashchiy, I. I. Izhnin, and A. P. Vlasov, Phys. Status Solidi B **229**, 279 (2002).
41. N. N. Berchenko, V. V. Bogoboyashchiy, I. I. Izhnin, *et al.*, Surf. Coat. Technol. **158–159**, 732 (2002).
42. I. I. Izhnin, A. I. Izhnin, K. R. Kurbanov, and B. B. Prytuljak, Proc. SPIE **3182**, 383 (1997).
43. E. Belas, P. Hoschl, R. Grill, *et al.*, J. Cryst. Growth **138**, 940 (1994).
44. E. Belas, R. Grill, J. Franc, *et al.*, J. Cryst. Growth **159**, 1117 (1996).
45. E. Belas, R. Grill, J. Franc, *et al.*, J. Cryst. Growth **224**, 52 (2001).
46. E. Belas, R. Grill, J. Franc, *et al.*, J. Electron. Mater. **31**, 738 (2002).
47. J. White, R. Pal, J. M. Dell, *et al.*, J. Electron. Mater. **30**, 762 (2001).
48. D. Shaw and P. Capper, J. Mater. Sci.: Mater. Electron. **11** (2), 169 (2000).
49. H. F. Schaake, J. H. Tregilgas, J. D. Beck, *et al.*, J. Vac. Sci. Technol. A **3**, 143 (1985).
50. V. V. Bogoboyashchiĭ and I. I. Izhnin, Izv. Vyssh. Uchebn. Zaved. Fiz. **43** (8), 16 (2000).
51. V. V. Bogoboyashchiĭ, A. I. Elizarov, V. I. Ivanov-Omskiĭ, *et al.*, Fiz. Tekh. Poluprovodn. (Leningrad) **19**, 819 (1985) [Sov. Phys. Semicond. **19**, 505 (1985)].
52. V. V. Bogoboyashchiĭ and I. I. Izhnin, in *Abstracts of XVII International Scientific and Technical Conference on Photoelectronics and Night Vision Devices* (Moscow, 2002), p. 164.
53. I. M. Baker and C. D. Maxey, J. Electron. Mater. **30**, 682 (2001).
54. M. P. Hastings, C. D. Maxey, B. E. Matthews, *et al.*, J. Cryst. Growth **138**, 917 (1994).
55. R. Haakenaasen, H. Steen, T. Lorentzen, *et al.*, J. Electron. Mater. **31**, 710 (2002).
56. N. N. Berchenko, V. V. Bogoboyashchiy, I. I. Izhnin, *et al.*, in *Abstracts of International Conference on Solid State Crystals* (Zakopane, 2002), p. 197.
57. I. M. Baker, M. P. Hastings, L. G. Hipwood, *et al.*, III–Vs Rev. **9** (2), 50 (1996).
58. C. T. Elliott, N. T. Gordon, R. S. Hall, and G. Crimes, J. Vac. Sci. Technol. A **8**, 1251 (1990).
59. N. L. Bazhenov, S. I. Gasanov, V. I. Ivanov-Omskiĭ, *et al.*, Fiz. Tekh. Poluprovodn. (Leningrad) **25**, 2196 (1991) [Sov. Phys. Semicond. **25**, 1323 (1991)].
60. R. E. DeWames, G. M. Williams, J. G. Pasko, and A. H. B. Vandervyck, J. Cryst. Growth **86**, 849 (1988).
61. S. Sze, *Physics of Semiconductor Devices*, 2nd ed. (Wiley, New York, 1981; Mir, Moscow, 1984).
62. R. E. DeWames, J. G. Pasko, E. S. Yao, *et al.*, J. Vac. Sci. Technol. A **6**, 2655 (1988).
63. G. Bahir, V. Garber, and D. Resenfeld, Appl. Phys. Lett. **78**, 1331 (2001).
64. J. M. Dell, J. Antoszewski, M. H. Rais, *et al.*, J. Electron. Mater. **29**, 841 (2000).
65. J. K. White, J. Antoszewski, R. Pal, *et al.*, J. Electron. Mater. **31**, 743 (2002).
66. C. Musca, J. Antoszewski, J. Dell, *et al.*, J. Electron. Mater. **27**, 740 (1998).
67. J. Piotrowski, Z. Nowak, J. Antoszewski, *et al.,* Semicond. Sci. Technol. **13**, 1209 (1998).
68. E. P. G. Smith, K. J. Winchester, C. A. Musca, *et al.*, Semicond. Sci. Technol. **16**, 444 (2001).
69. G. Bahir, V. Garber, and A. Dust, J. Electron. Mater. **30**, 704 (2001).
70. O. P. Agnihotri, H. C. Lee, and K. Yang, Semicond. Sci. Technol. **17**, R11 (2002).

Translated by D. Mashovets

Semiconductors, Vol. 37, No. 10, 2003, pp. 1151–1155. Translated from Fizika i Tekhnika Poluprovodnikov, Vol. 37, No. 10, 2003, pp. 1179–1183.
Original Russian Text Copyright © 2003 by Deĭbuk.

ATOMIC STRUCTURE AND NONELECTRONIC PROPERTIES OF SEMICONDUCTORS

Thermodynamic Stability of GaInSb, InAsSb, and GaInP Epitaxial Films

V. G. Deĭbuk

Chernovtsy National University, Chernovtsy, 58012 Ukraine

e-mail: vdei@chnu.cv.ua

Submitted January 22, 2003; accepted for publication January 27, 2003

Abstract—The miscibility gaps and the critical temperatures of spinodal decomposition of ternary semiconducting Ga–In–Sb, Ga–In–P, and In–As–Sb systems are calculated by taking into account the deformation energy and the effect of plastic relaxation caused by the misfit dislocations. It is shown that taking into consideration elastic energy narrows the ranges of spinodal decomposition and lowers its critical temperature. The introduction of the phenomenological parameter into Matthews–Blakeslee formula makes it possible to reach a satisfactory agreement between theoretically calculated values of critical thickness of epitaxial films and the experimental data. © *2003 MAIK "Nauka/Interperiodica".*

1. INTRODUCTION

Semiconductor devices based on the III–V compounds and their solid solutions have been finding increasing practical use in recent years. Along with well-proved heterostructures based on AlGaAs and InGaAs, such alloys as GaInSb, InAsSb, and GaInP also can be used in heterolasers, photodetectors, and in resonance tunneling devices for mid-IR and visible frequency regions [1–3]. Due to numerous experimental and theoretical studies, particular progress has been reached also in the fabrication of lasers based on self-organizing quantum wells [4].

In addition to analysis of the energy-gap width and the lattice constant as a function of the composition of a solid solution, one should take into account that the majority of solid solutions are unstable in a certain range of composition. Solid solution in the range of instability tends to lower its free energy in the process of decomposition, i.e., in the process of phase reconstruction, which disturbs the macroscopic homogeneity of the crystal and results in the formation of a mixture of phases of different composition. The decomposition that occurs without nucleation of a new phase is called spinodal decomposition. The corresponding curve appearing in the phase diagram and separating the region of solid solutions unstable even to infinitely small fluctuations of composition is called a spinodal curve [5]. Unordered semiconducting alloys have a positive enthalpy of mixing, which leads to decomposition counteracting the stabilizing affect of internal stresses. Moreover, the ternary unordered solid solutions of III–V compounds have two tendencies in phase transformations, namely, decomposition and the formation of superstructures [6].

The immiscibility and instability regions existing in many ternary and in almost all quaternary III–V solid solutions appreciably restrict the range of compositions which can be used for the fabrication of devices. As was shown in [7], the stresses and strains in III–V alloys may result in the broadening of the region of solubility. Deformation also ensures an additional degree of freedom for the alteration of optical and kinetic properties of semiconductors. The offsets in the conduction and valence bands on the interface of two semiconductors can be controlled with the aid of the corresponding deformations, which makes it possible to obtain improved devices based on heterostructures.

Strains and stresses in materials grown by epitaxial methods, such as molecular epitaxy and chemical deposition from the gaseous phase of metal-organic compounds, are mainly caused by the lattice mismatching of the epitaxial layer (epilayer) and the substrate. The elastic relaxation in thin films also affects the phase transformations and stability [8].

It should be noted that, at spinodal decomposition, a purely coherent phase matching of two phases competes with the processes accompanied by the emergence of misfit dislocations [9]. The realization of each of the possibilities depends on the kinetics of spinodal decomposition. This study is concerned with now the misfit dislocation formation in thin epitaxial films influences regions of thermodynamic instability in the context of a delta lattice parameter model [10]. The miscibility gaps are determined and the influence of biaxial deformation from the substrate and a plastic relaxation caused by the formation of misfit dislocations in these thin films are analyzed.

2. CALCULATION OF SPINODAL DECOMPOSITION TAKING INTO ACCOUNT ELASTIC ENERGY

For the thermodynamic description of pseudobinary ternary solid solutions, we consider the Gibbs free energy of mixing ΔG per mole:

$$\Delta G = \Delta H - T\Delta S, \tag{1}$$

where ΔH is the enthalpy of mixing, T is the absolute temperature, and ΔS is the entropy of mixing, which can be written in the form

$$\Delta S = -R[k\ln x + (1-x)\ln(1-x)]. \tag{2}$$

For description of enthalpy of the mixing, two models are usually used: a model of a regular solution [11], and the delta lattice-parameter model (DLP) [10]. It is know that the model of a regular solution describes well the thermodynamic properties of the liquid phase and has limitations in the case of a solid phase since the parameters of interaction in this model depend on the concentration x in the alloy. In the DLP model, the enthalpy of mixing ΔH depends only on the lattice parameter a. For solid solutions $A_{1-x}B_xC$, ΔH can be written as [12]

$$\begin{aligned}\Delta H &= E_{\text{alloy}} - xE_{\text{BC}} - (1-x)E_{\text{AC}} \\ &= K[a_{\text{alloy}}^{-2.5} - xa_{\text{BC}}^{-2.5} - (1-x)a_{\text{AC}}^{-2.5}],\end{aligned} \tag{3}$$

where K is the parameter of the model, which for nearly all III–V compounds is equal to 1.15×10^7 (cal/mol) $\text{Å}^{2.5}$ [10]. The solid solution undergoes a spinodal decomposition provided that the curve of the compositional dependence of the free energy exhibits an inflection point. The product of spinodal decomposition consists of two solid solutions of different composition. The criterion of stability of pseudobinary alloys can be written as $\partial^2 G/\partial x^2 > 0$. The region of instability is determined as a locus for which the condition $\partial^2 G/\partial x^2 = 0$ is satisfied.

For a bulk solid solution, along with the chemical part of the free energy, one should also consider an elastic component arising from the requirement for the coherent matching of phases [13] with due regard for crystal anisotropy. In [14, 15], on the basis of the model of a regular solid solution, it was shown [11] that in quaternary solid solutions of III–V semiconductors with positive enthalpy of formation, a coherent separation of phases with the formation of elastic concentration domains takes place. These domains compositionally alternate in a solid solution perpendicularly to the direction of the easiest compression. Relaxations of elastic stresses at the surface of epitaxial films were also considered and analyzed.

If a solid solution represents a thin epitaxial film and the thermodynamic process is accompanied by the formation of misfit dislocations, the mismatching of lattice constants a_{alloy} of alloy and of the substrate material of a_{sub} will give rise to biaxial strains of tension or compression, $\varepsilon_{xx} = \varepsilon_{yy}$, in the film plane. The component of the stress tensor in the perpendicular direction x for cubic crystals can be written as

$$\tau_z = C_{12}\varepsilon_{xx} + C_{12}\varepsilon_{yy} + C_{11}\varepsilon_{zz}, \tag{4}$$

where C_{11} and C_{22} are the elastic constants of the film. In view of the fact that for the "free" direction of a film (growth direction) $\tau_z = 0$, expression (4) reduces to

$$\varepsilon_{zz} = -\frac{2C_{12}}{C_{11}}\varepsilon_{xx}(x). \tag{5}$$

The energy of such strain per unit volume can be written as [16]

$$E_s = \frac{E\varepsilon^2}{1-\nu}, \tag{6}$$

where $\varepsilon = \varepsilon_{xx}$, E is the Young modulus, and ν is the Poisson ratio. Relation (6), as a special case, was derived in [1, 16]. In addition, as originally shown in [15], the energy of elastic strain in the case of an epitaxial film changes due to the relaxation of elastic stresses at the surface. Therefore, instead of expression (6), it is more correct to write

$$E_s' = \frac{C_{11}}{2(C_{11}+C_{12})}\frac{E\varepsilon^2}{1-\nu}. \tag{7}$$

The strain in a fully stressed epitaxial film is equal to

$$\varepsilon(x) = \varepsilon_m(x) = \frac{a_{\text{alloy}}(x) - a_{\text{sub}}}{a_{\text{sub}}}. \tag{8}$$

The dependence of the lattice constant on the composition $a_{\text{alloy}}(x)$ is described by the Vegard rule, which is valid for the solid solutions of III–V semiconductors to a high accuracy.

However, the situation described above is observed only if the film thickness h is smaller than a critical thickness h_c. If $h > h_c$, the processes of plastic relaxation take place with the formation of misfit dislocations—the thicker the film, the smaller its strain. In order to determine the influence of the above effects on the thermodynamic stability of solid solutions, we use the model [17] of balance of forces acting at a dislocation; as a result, we obtain

$$\varepsilon = A/h, \tag{9}$$

which means that with increasing thickness of the epitaxial film, the value of strain decreases and the film gradually relaxes. The parameter A is determined from the condition for the continuity of the function $\varepsilon(h)$ at the point $h = h_c$. Then, we use expressions (8) and (9) to obtain $A = \varepsilon_m h_c$. The majority of semiconductor structures are grown on the (001) substrate surface. This orientation will be considered below.

Theoretical expression for the critical thickness h_c can be obtained from two different approximations known as the equilibrium theories of critical thickness. The first approximation is based on the principle of

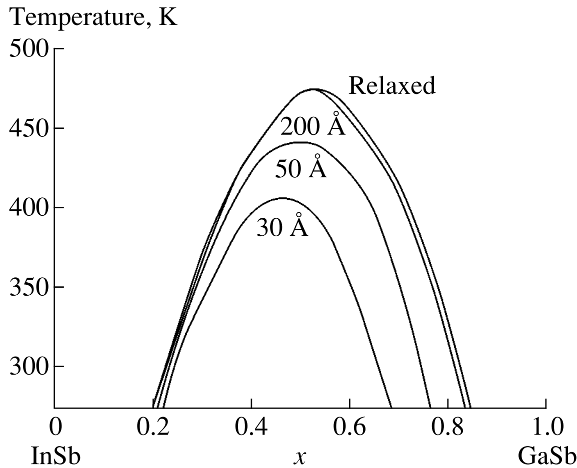

Fig. 1. Phase diagrams of spinodal decomposition of $Ga_xIn_{1-x}Sb/GaSb$ epitaxial films of various thicknesses.

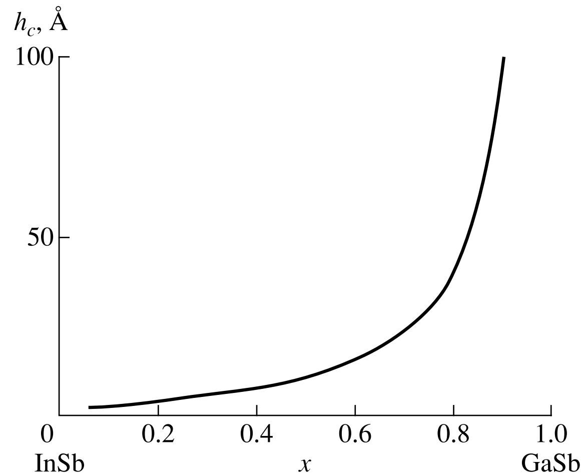

Fig. 2. Compositional dependence of the critical thickness h_c of $Ga_xIn_{1-x}Sb/GaSb$ epitaxial films.

energy minimum and was originally suggested by Frank and Van der Merve; the second one, known as the theory of force balance, by Matthews and Blakeslee (see review [18]). These two approaches are equivalent and yield the same values of critical thickness. We used the model of force balance in which the critical thickness of the epilayer is described as [17]

$$h_c = \left(\frac{b}{\varepsilon_m}\right)\frac{1}{8\pi(1+\nu)}\left[\ln\left(\alpha\frac{h_c}{b}\right)+\beta\right], \quad (10)$$

where $\alpha = 4$, $\beta = 1$ [17], and b is the magnitude of the Burgers vector. The most commonly occurring dislocations in semiconductor layers are the 60° misfit dislocations in the (001) plane; therefore, the Burgers vector can be written $(a/2)\langle 110\rangle$ as $b = a/\sqrt{2}$. In the region of the dislocation core, the stresses are too high to correctly be described in the context of the linear theory of elasticity. Therefore, we introduce a phenomenological parameter β as a measure of the deviation from nonlinearity.

Thus, the total Gibbs free energy per unit volume is the sum of the chemical energy ΔG and elastic energy E_s':

$$G = N_v\Delta G + E_s', \quad (11)$$

where N_v is the number of moles per unit volume of homogeneous solid solution prior to decomposition. Analysis of the Gibbs free energy as a function of the solid solution composition and the layer thickness allows for, together with the stability criterion, the determination of the solubility limits. Parameters for calculations are taken from [12].

3. A $Ga_xIn_{1-x}Sb/GaSb$ SYSTEM

Let us consider a $Ga_xIn_{1-x}Sb$ epilayer on a GaSb substrate in the context of the above theory. At low temperatures, unstressed alloy has a positive free energy which decreases on heating, with the formation of two minima in the compositional dependence, which indicates the possibility of spinodal decomposition. The phase diagram for this case is shown in Fig. 1 (the curve labeled “relaxed”). The curve indicates the existence of a critical temperature (T_c = 477 K at x_c = 0.53) higher than which a spinodal decomposition does not exist. The value of the critical temperature for an unstressed film is in good agreement with the theoretical calculations (T_c = 478 K) of other researchers [19]. If the epitaxial film is completely stressed, the rapid increase in elastic energy E_s' (as compared to the chemical energy represented by the first term in formula (11)) with increasing In content in the film will result in the merging of two peaks into a single peak. This circumstance is indicative of elastic stability of a film against the spinodal decomposition [7] and is typical of thin pseudomorphic films with a thickness smaller than the critical one ($h < h_c$). However, if the thickness exceeds the critical value ($h > h_c$), the film begins to relax; i.e., the elastic energy of the film (see formulas (7)–(9)) decreases with an increasing film thickness. The region of spinodal decomposition ($\partial^2G/\partial x^2 < 0$) in this case is retained but becomes somewhat narrower (Fig. 1). Asymmetric narrowing of the region of spinodal decomposition and the decrease in critical temperature can be explained by taking into consideration the compositional dependence of the critical thickness of the $Ga_xIn_{1-x}Sb$ film grown on GaSb substrate (Fig. 2). The boundary of the miscibility gap from the side having the higher Ga content is quite sensitive to variations in the film thickness. The opposite boundary with lower Ga content is almost insensitive to the film thickness, which can be attributed to a large mismatching of lattice parameters of the film and GaSb substrate, resulting in a smaller critical thickness (close to several angstroms). Therefore, films of arbitrary thickness in this

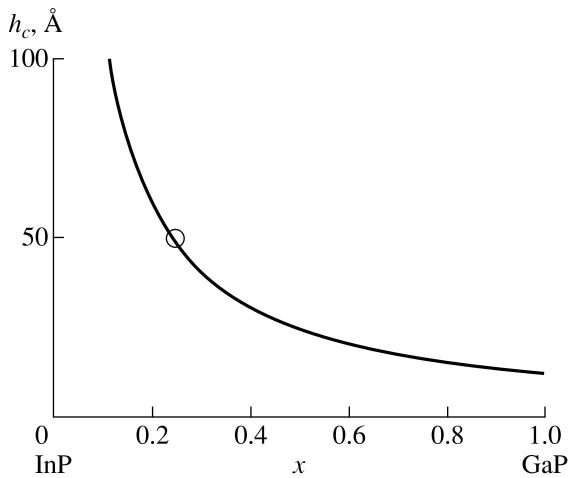

Fig. 3. Compositional dependence of the critical thickness h_c of $Ga_xIn_{1-x}P$/InP epitaxial films. The data published in [23] are indicated by the circles.

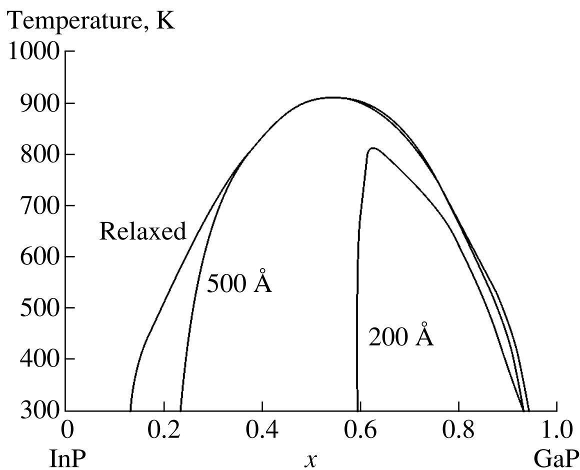

Fig. 4. Phase diagrams of spinodal decomposition of $Ga_xIn_{1-x}P$/InP epitaxial films of various thicknesses.

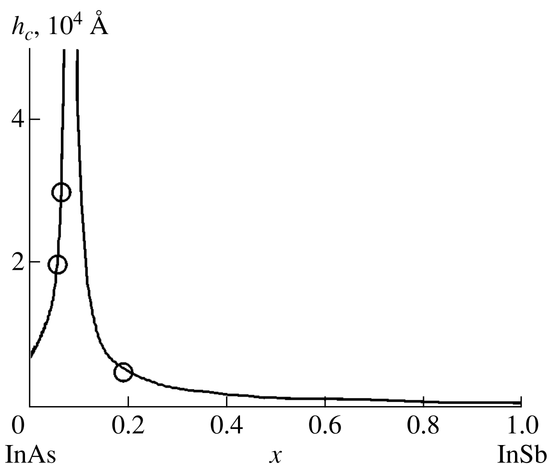

Fig. 5. Compositional dependence of the critical thickness h_c of $InAs_{1-x}Sb_x$/GaSb epitaxial films. The data published in [22] are indicated by the circles.

compositional region are completely relaxed and their residual stresses are quite small. At the same time, on the side having the high Ga content, the stresses are quite sensitive to the thickness of a layer due to a strong $h_c(x)$ dependence. The $Ga_xIn_{1-x}Sb$/GaSb films having the thickness larger than 200 Å are almost completely relaxed and approache the bulk samples in terms of their thermodynamic characteristics.

4. A $Ga_xIn_{1-x}P$/InP SYSTEM

Similar behavior can be observed in $Ga_xIn_{1-x}P$ alloys grown on InP substrates. Large mismatching of the lattice parameters at the boundary film–substrate results in larger values of the critical thickness of such films (Fig. 3) in comparison to $Ga_xIn_{1-x}Sb$/GaSb. This in turn gives rise to a large asymmetry of spinodal decomposition curves (Fig. 4). For unstressed $Ga_xIn_{1-x}P$, our calculations yield a critical temperature of $T_c = 920$ K at $x_c = 0.54$, which is in satisfactory agreement with the experimentally observed temperature of 933 K for the composition $x = 0.62$ [12], while the theoretical calculations yield $T_c = 961$ K at $x_c = 0.68$ [20]. On the side having the low Ga content, the film is very sensitive to internal stresses. This sensitivity manifests itself in a large change in the corresponding limit of solubility (Fig. 4) and critical temperature in films of various thickness. Specifically, for a film 200 Å in thickness, the miscibility gap at 300 K, according to our calculations, spans the range of $0.59 < x < 0.92$ ($T_c = 818$ K), whereas for the film 500 Å in thickness the miscibility gap covers $0.23 < x < 0.92$ ($T_c = 918$ K), and the film is almost completely relaxed; i.e., its residual stresses are close to zero.

5. AN $InAs_{1-x}Sb_x$/GaSb SYSTEM

For obtaining high-quality $InAs_{1-x}Sb_x$ films for novel optoelectronic devices operating in the mid-IR region, almost complete matching of the film–substrate lattice parameters is required in order to ensure their improved properties [21]. It was found that the most suitable substrate satisfying these requirements is GaSb, which completely matches the $InAs_{1-x}Sb_x$ film at $x \approx 0.09$. The results of our calculations of the compositional dependence of critical thickness for such films we shown in Fig. 5 and are in good agreement with experimental data [22, 23]. This provides grounds to pass to calculations of the region of spinodal decomposition of the epitaxial InAsSb/GaSb films under study (Fig. 6). For an unstressed bulk alloy, the critical temperature of spinodal decomposition $T_c = 584$ K at $x_c = 0.46$, and the miscibility gap covers the interval $0.13 < x < 0.83$ at $T = 300$ K. Films 1 μm or larger in thickness are almost completely relaxed, and residual stresses in them are close to zero. A decrease in the epitaxial film thickness narrows the miscibility gap. For example, in a film 0.15 μm in thickness, this gap corresponds to an interval of $0.47 < x < 0.82$; for smaller thickness, it disappears entirely.

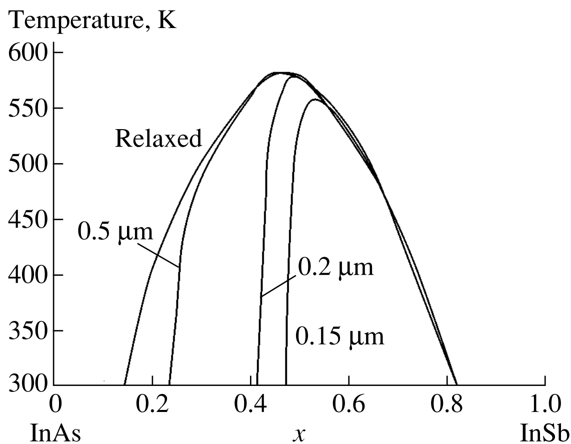

Fig. 6. Phase diagrams of spinodal decomposition of $InAs_{1-x}Sb$/GaSb epitaxial films of various thicknesses.

6. CONCLUSION

Introduction of the phenomenological parameter into the Matthews–Blakeslee formula makes it possible to attain satisfactory agreement between the theoretically calculated values of the critical thickness of epitaxial films and the known experimental data.

The miscibility gaps and critical temperatures of spinodal decomposition for ternary Ga–In–Sb, Ga–In–P, and In–As–Sb systems are calculated taking into account the deformation energy and the relaxation of elastic stresses at the surface of epitaxial films, as well as of the effect of plastic relaxation caused by misfit dislocations. It is shown that taking into consideration the elastic energy narrows the region of spinodal decomposition and decreases its critical temperature.

REFERENCES

1. S. C. Jain, M. Willander, and H. Maes, Semicond. Sci. Technol. **11**, 641 (1996).
2. A. Rogalski, Prog. Quantum Electron. **13**, 191 (1989).
3. C.-H. Lin, S. S. Pei, H. Q. Le, *et al.*, Appl. Phys. Lett. **71**, 3281 (1997).
4. M. V. Maximov, A. F. Tsatsul'nikov, B. V. Volovik, *et al.*, Physica E (Amsterdam) **7**, 326 (2000).
5. V. I. Fistul', *Decomposition of Supersaturated Solid Solutions* (Metallurgiya, Moscow, 1977).
6. V. A. Elyukhin and L. P. Sorokina, Dokl. Akad. Nauk SSSR **287**, 1384 (1986) [Sov. Phys. Dokl. **31**, 342 (1986)].
7. G. B. Stringfellow, J. Electron. Mater. **11**, 903 (1982).
8. E. D. Fitzgerald, S. B. Samavedam, Y. H. Xie, and L. M. Giovane, J. Vac. Sci. Technol. A **15**, 1048 (1997).
9. J. H. van der Merve and W. A. Jesser, J. Appl. Phys. **63**, 1509 (1988).
10. G. B. Stringfellow, J. Phys. Chem. Solids **34**, 1749 (1973).
11. M. Ilegems and M. B. Panish, J. Phys. Chem. Solids **35**, 409 (1974).
12. A. Chen and A. Sher, *Semiconductor Alloys: Physics and Material Engineering* (Plenum, New York, 1995).
13. A. G. Khachaturyan, *The Theory of Phase Transformations and the Structure of Solid Solutions* (Nauka, Moscow, 1974).
14. I. P. Ipatova, V. G. Malyshkin, A. Yu. Maslov, and V. A. Shchukin, Fiz. Tekh. Poluprovodn. (St. Petersburg) **27**, 285 (1992) [Sov. Phys. Semicond. **27**, 158 (1992)].
15. I. P. Ipatova, V. G. Malyshkin, and V. A. Shchukin, J. Appl. Phys. **74**, 7198 (1993).
16. L. D. Landau and E. M. Lifshitz, *Course of Theoretical Physics*, Vol. 7: *Theory of Elasticity*, 4th ed. (Nauka, Moscow, 1987; Pergamon, New York, 1986), Sect. 5.
17. R. Beanland, D. J. Dunstan, and P. J. Goodhew, Adv. Phys. **45**, 87 (1996).
18. S. C. Jain, *Germanium–Silicon Strained Layers and Heterostructures* (Academic, Boston, MA, 1994).
19. C. Lin and A. Z. Li, J. Cryst. Growth **203**, 511 (1999).
20. S.-H. Wei, L. G. Ferreira, and A. Zunger, Phys. Rev. B **41**, 8240 (1990).
21. A. Rakovska, V. Berger, X. Marcadet, *et al.*, Semicond. Sci. Technol. **15**, 34 (2000).
22. M. A. Marciniak, R. L. Hengehold, and Y. K. Yeo, J. Appl. Phys. **84**, 480 (1998).
23. G. M. Cohen, P. Zisman, G. Bahir, and D. Ritter, J. Vac. Sci. Technol. B **16**, 2639 (1998).

Translated by A. Zalesskiĭ

Semiconductors, Vol. 37, No. 10, 2003, pp. 1156–1159. Translated from Fizika i Tekhnika Poluprovodnikov, Vol. 37, No. 10, 2003, pp. 1184–1187.
Original Russian Text Copyright © 2003 by Abdullaev, Aliev, Kamilov.

Kinetics of Ambipolar Diffusion and Drift Currents of Nonequilibrium Carriers in Semiconductors

A. A. Abdullaev*, A. R. Aliev, and I. K. Kamilov

Institute of Physics, Dagestan Scientific Center, Russian Academy of Sciences, ul. 26 Bakinskikh Komissarov 94, Makhachkala, 367003 Russia

**e-mail: analit@dinet.ru*

Submitted December 19, 2002; accepted for publication January 10, 2003

Abstract—A radically new method is suggested for drift mobility determination in semiconductors; this method is based on the measurement of how much time it takes to attain a peak value of the diffusion-drift current of nonequilibrium charge carriers excited by short pulses of light from a high-absorption region through the one of the contacts. The estimations show that the method is applicable if the drift flow exceeds the diffusion flow. This condition is satisfied at voltages exceeding those corresponding to the highest rate of $t_{max}(U)$ decay. Mobility μ can be calculated by the formula $\mu = d^2(2Ut_{max})^{-1}$, where d is the distance between contacts, U is the applied voltage, and t_{max} is the time the peak value of the photocurrent is attained. © *2003 MAIK "Nauka/Interperiodica".*

For studying the kinetics of the ambipolar diffusion and drift currents of nonequilibrium carriers in semiconductors, we chose the illumination configuration at which the short pulses of light from a high-absorption region pass through one of the ohmic contacts. Figure 1a shows a cell for such an illumination. Sample *1* with ohmic contact *2* is soldered to a sapphire plate *3* with deposited indium layer *4*. The plate is attached to a cold finger *5* of an optical cryostat. The pressure contact is ensured by diaphragm *6* through a quartz glass *7*. The finest copper mesh *8* coated on both sides with indium was pressed between the sample and a quartz glass. This mesh served as a transparent contact. The light was excited by an LGI-21 laser (wavelength λ = 0.337 μm) with a pulse duration of 10^{-8} s. The details of photocurrent detection were reported in [1]. Stroboscopic integration allowed the shape of pulses to be recorded.

In Fig. 1b, we show the time-dependent variations in photocurrent Δi in undoped p-$CdCr_2Se_4$ at room temperature (300 K) after excitation by a laser pulse. The photocurrent passes through a maximum and remains nonzero within a time interval of hundreds of μs, while the duration of excitation is a thousand times shorter.

Diffusion and drift of a packet Δn of nonequilibrium carriers excited at the illuminated sample surface—in this case, of the minority carriers (electrons)—is described by the continuity equation

$$\frac{\partial n}{\partial t} - \mu E_x \frac{\partial n}{\partial x} - D\frac{\partial^2 n}{\partial x^2} = G - \frac{\Delta n}{\tau}, \quad (1)$$

where n is the total concentration, μ is the mobility, D is the diffusion coefficient, G is the generation rate, τ is the carrier lifetime, and E_x is the component of electric field along the x axis normal to the surface. The distribution law of nonequilibrium carriers in relation to the coordinate x and the time t after cessation of excitation, i.e., at $G = 0$, is given as a solution of Eq. (1) in [2] and has the form

$$\Delta n(x, t) = \frac{\Delta n_0 \exp(-t/\tau)}{2\sqrt{\pi D t}} \exp\left[-\frac{(x-\mu E_x t)^2}{4Dt}\right], \quad (2)$$

where Δn_0 is the initial concentration of nonequilibrium carriers per unit cross-section area at the moment generation is terminated, i.e., at $t = 0$ and $x = 0$.

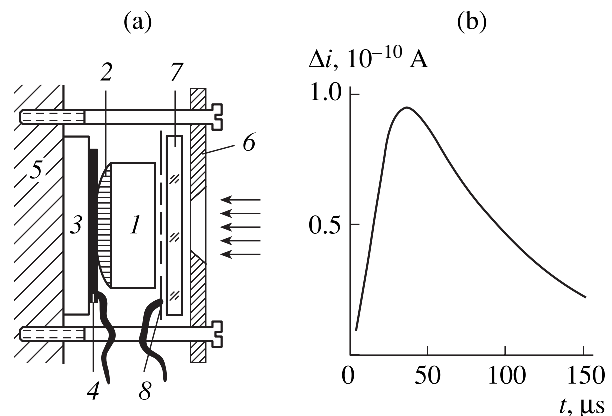

Fig. 1. (a) The cell for measurements: (*1*) sample, (*2*) ohmic contact, (*3*) sapphire plate, (*4*) indium layer, (*5*) cold carrier of the optical cryostat, (*6*) diaphragm, (*7*) quartz glass, and (*8*) copper grid. (b) The photocurrent pulse in $CdCr_2Se_4$ corresponding to the laser pulse with the duration of 10 ns at 300 K (an LGI-21 laser was used).

The current passing through the sample is determined in this case by the expression

$$i(t) = US\left\{\int_0^d \frac{dx}{e\mu n(x,t)}\right\}^{-1},$$

where d is the distance between contacts, U is the voltage applied along the x axis, and S is the cross-section area. Under our experimental conditions, $\Delta n(x, t) \gg n_0(x, t)$; therefore, we can write the expression for photocurrent

$$\Delta i(t) = US\left\{\int_0^d \frac{dx}{e\mu\Delta n(x,t)}\right\}^{-1}. \quad (3)$$

After substitution of formula, (2) into formula (3) and introduction of new notation,

$$X = \frac{x}{\mu|E_x|\tau}, \quad T = \frac{t}{\tau}, \quad L = \frac{d}{\mu|E_x|\tau},$$
$$B = \frac{\mu^2 E_x^2 \tau^2}{4D\tau} = \left(\frac{l_E}{2l_D}\right)^2, \quad (4)$$

where $l_E = \mu|E_x|\tau$ and $l_D = D\tau$ are the drift and diffusion lengths, respectively, the integrand will contain only dimensionless quantities:

$$\Delta i(t) = \Delta i_0$$
$$\times\left\{\int_0^L \sqrt{T}\exp T\exp\left[\frac{B[X-(E_x/|E_x|)T]^2}{T}\right]dX\right\}^{-1},$$

$$\Delta i_0 = \frac{edS\Delta n_0}{2\tau\sqrt{\pi D\tau}}.$$

Since the time of attaining the peak values of photocurrent within the pulse is determined by the integral, we shall seek the dependence of relative photocurrent $\Delta i/\Delta i_0$ on dimensionless time T:

$$I(T) \equiv \frac{\Delta i(t)}{\Delta i_0}$$
$$= \left\{\sqrt{T}\exp T\int_0^L \exp\left[\frac{B[X-(E_x/|E_x|)T]^2}{T}\right]dX\right\}^{-1}. \quad (5)$$

The integral in expression (5) cannot be evaluated analytically; its derivative contains the same integral. Therefore, in order to find the form of the function $I(T)$, we used a computer in calculating the integral for various discrete values of L and B.

As can be seen from formulas (4), parameters L and B characterize the drift length and the ratio of the drift and diffusion lengths, respectively. By varying the parameter B, we can control the degree to which diffusion predominates over drift, and vice versa.

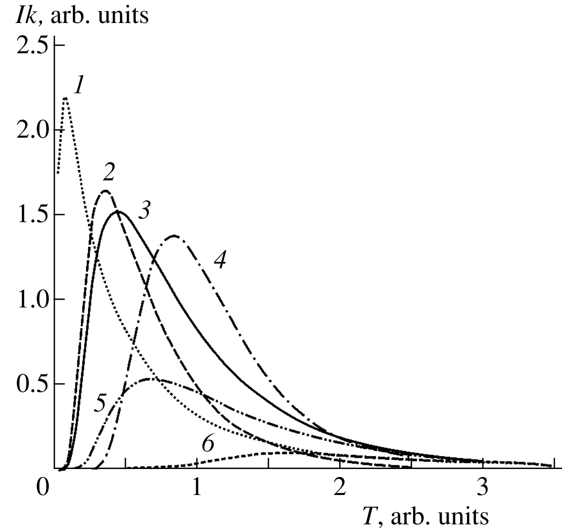

Fig. 2. Dependence of relative photocurrent I on the dimensionless time T at various values L and B and various relations between l_E and l_D: (1) $L = 1$ ($l_E = d$), $B = 1/9$ ($l_E = 2l_D/3$), $k = 1$; (2) $L = 1$ ($l_E = d$), $B = 1$ ($l_E = 2l_D$), $k = 2$; (3) $L = 2$ ($l_E = d/2$), $B = 1/4$ ($l_E = l_D$), $k = 5$; (4) $L = 2$ ($l_E = d/2$), $B = 1$ ($l_E = 2l_D$), $k = 10$; (5) $L = 10$ ($l_E = d/10$), $B = 1/64$ ($l_E = l_D/4$), $k = 20$; and (6) $L = 10$ ($l_E = d/10$), $B = 1/16$ ($l_E = l_D/2$), $k = 20$.

Figure 2 shows several $I(T)$ curves calculated by formula (5) at various values of L and B. The heights of the peaks differ from each other by several orders of magnitude. Therefore, for illustrative purposes the values of $I(T)$ in Fig. 2 were multiplied by the normalizing factor k. The shapes of the $I(T)$ curves are similar to those observed experimentally (Fig. 1b). A nanosecond excitation pulse may be considered to be merged with the ordinate axis because of its negligibly small duration. The increase in current intensity corresponds to the penetration of nonequilibrium carriers into the sample bulk due to diffusion and drift (according to formula (2)), resulting in layer-by-layer time-dependent resistance reduction. The descending part of the curves is caused by the decrease in the number of carriers due to recombination. From Fig 2, it is seen that the larger the values l_D and l_E (at smaller values of L and B), the smaller the times T_{max} for attaining peak values of photocurrent. They correspond to larger values of peak photocurrent.

The dependence of time T_{max} and the half-width of the curve $I(T)$ on the polarity of applied field $E \equiv E_x$ is noteworthy (Fig. 3). The change in polarity manifests itself in the change from "–" to "+" in the square brackets in formula (5). From the pairs of curves *1*, *2* and *3*, *4* it can be seen that, as long as diffusion predominates over drift ($l_E < l_D$), the time of attaining the peak does not depend on the polarity of the applied field. In this case, the peak value of a photocurrent decreases with increasing B. For $l_E = l_D$ (curves *5*, *6*), the change in polarity of E results in a small shift in the time of a maximum and a sharp increase of a half-width. For $l_E = l_D$

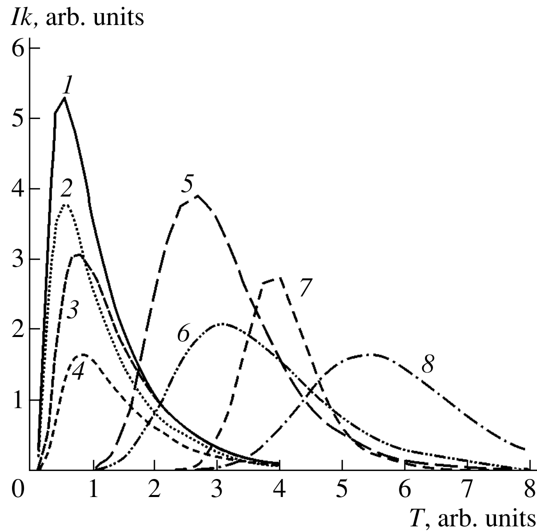

Fig. 3. Dependence of relative photocurrent I on the dimensionless time T at $L = 8$ ($l_E = d/8$) for (*1*, *3*, *5*, and *7*) forward and (*2*, *4*, *6*, and *8*) reverse directions of electric field E and various values of B = (*1*, *2*) 1/64 ($l_E = l_D/4$), $k = 1$; (*3*, *4*) 1/36 ($l_E = l_D/3$), $k = 1$; (*5*) 1/4 ($l_E = l_D$), $k = 5$; (*6*) 1/4 ($l_E = l_D$), $k = 10^4$; (*7*) 1 ($l_E = 2l_D$), $k = 200$; and (*8*) 1 ($l_E = 2l_D$), $k = 5 \times 10^{14}$.

(curves *7*, *8*), the times of attainment of peaks and the half-width of $I(T)$ curves markedly differ from each other with the change in the sign of E.

For a detailed study of the dependence of the time of attainment of peaks T_{max} on the relation between L and B, we calculated the dependences $T_{max}(L)$ at various values of B (Fig. 4) and $T_{max}(B)$ at various values of L (Fig. 5). The curves $T_{max}(L)$ at $l_E < l_D$ are almost linear with a slope that increases with increasing B. At $l_E \geq 2l_D$ (i.e., at $B \geq 1$), all $T_{max}(L)$ curves merge into a single straight line with the slope equal to 1/2. Thus, under the condition of the suppression of diffusion flow by the drift flow, we can unambiguously relate T_{max} and L ($T_{max} = L/2$) and, according to formula (4), determine the mobility of carriers as

$$\mu = \frac{d^2}{2Ut_{max}}, \tag{6}$$

where t_{max} is the real time of attaining the peak value of photocurrent. It should be mentioned that the values of U and t_{max} should satisfy the condition $l_E \geq 2l_D$.

The dependences $T_{max}(B)$ at various values of L (Fig. 5) represent curves with saturation. At $B > 1$, T_{max} is independent of B and its steady-state values are also equal to halved L for the corresponding curve.

In order to calculate using formula (6) the mobility of carriers in an actual experiment, it is necessary to choose a criterion $l_E \geq 2l_D$. Since L and B can be changed by the variation of E, we calculated the $T_{max}(E)$

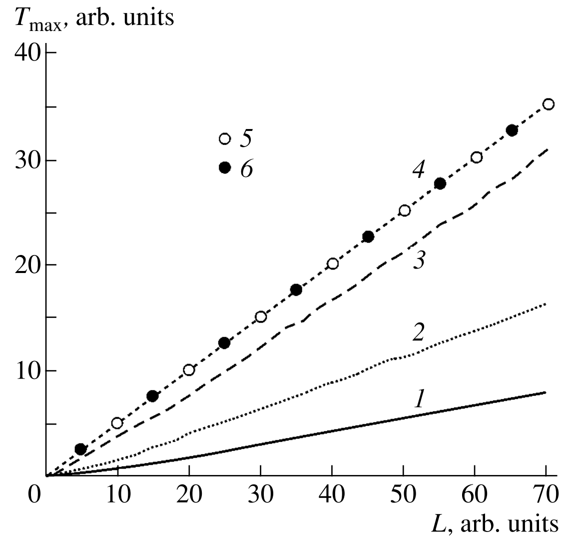

Fig. 4. Dependences of the dimensional time of attainment of the peak value of photocurrent T_{max} on L at B = (*1*) 1/64 ($l_E = l_D/4$); (*2*) 1/16 ($l_E = l_D/2$); (*3*) 1/4 ($l_E = l_D$); (*4*) 1 ($l_E = 2l_D$); (*5*) 4 ($l_E = 4l_D$); and (*6*) 9 ($l_E = 6l_D$).

dependence at the values d, μ, and τ close to their actual values, assuming the validity of the Einstein relation

$$D = \mu k_B \Theta / e,$$

where Θ is the temperature, k_B is the Boltzmann constant, and e is the elementary charge. Assuming $L = a/E$, where $a = d/\mu\tau$ and $B = bE^2$, ($b = \mu^2\tau/4D = e\mu\tau/4k\Theta$), we obtain $a = 2 \times 10^3$ and $b = 3.62 \times 10^{-4}$ for $\mu = 1$ cm^2/(V s), $\tau = 5 \times 10^{-5}$ s, $\Theta = 400$ K, and $d = 0.1$ cm. Note, that the condition $B \geq 1$ corresponds to the field intensity $E \geq 50$ V/cm ($B = bE^2 \approx 1$).

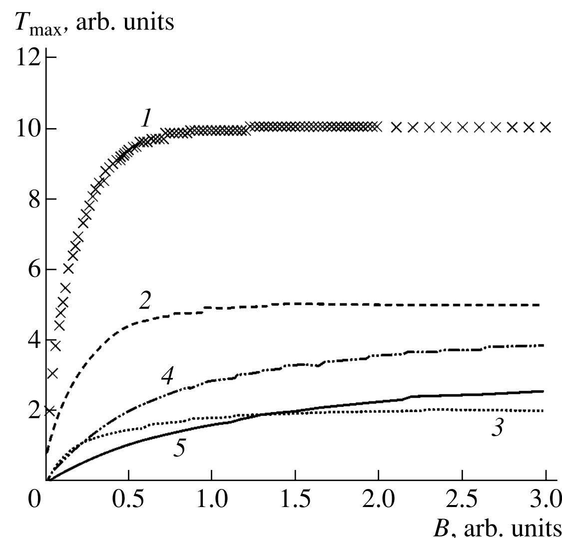

Fig. 5. Dependences of dimensionless time T_{max} of attainment of the peak values of photocurrent on B at L = (*1*) 20, (*2*) 10, (*3*) 4, (*4*) 1 ($T_{max} \times 8$), and (*5*) 0.5 ($T_{max} \times 12$).

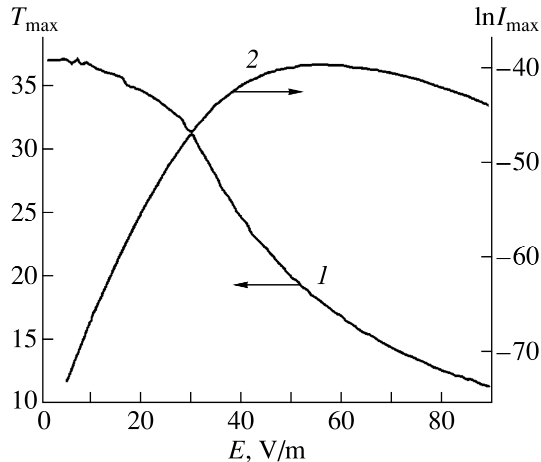

Fig. 6. Dimensionless time of the attainment of (*1*) the peak values of the dimensionless photocurrent T_{max} and (*2*) the peak values the current I_{max} in relation to function of the electric-field strength E.

For the obtained values of a and b, the arrays of $B(E)$ and $L(E)$ were formed and the dependence $T_{max}(E)$ was calculated with the aid of formula (5) (Fig. 6, curve *1*). It can be seen that the condition $B = 1$ in Fig. 6 corresponds to the portion of the curve with the highest rate of decrease in $T_{max}(E)$. Thus, for determining drift mobility in a semiconductor, it is sufficient to obtain the $t_{max}(U)$ dependence, to choose a pair of values t_{max} and U from the region of the highest falloff rate of this dependence, and to calculate the sought-for value by the formula (6). This method allows for the determination of the mobility in high-resistivity samples, magnetic materials, in vitreous semiconductors with hopping conductivity, in which Hall effect measurements meet difficulties.

Figure 6 (curve *2*) shows the variation in the peak value of photocurrent with a strength of the applied field E. At a voltage higher than $E = 50$ V/cm, i.e., at $l_E \geq 2l_D$, there exists an interval with negative differential resistance, which likely corresponds to the transition from ambipolar diffusion conductivity to drift conductivity with the mobility determined by the minority carriers whose charge sign at a given polarity of the external field reduces the length of pulling. The observed maximum in this curve at $l_E = l_D$ allows the lifetime of charge carriers to be independently determined.

ACKNOWLEDGMENTS

For our studies, we used the equipment of the Analytical Center of Collective Usage of Dagestan National Center of Russian Academy of Sciences. This study was supported by the Russian Foundation for Basic Research (project no. 00-05-72031) and by the Federal Special Program "Integration" (project no. 4.15-Ch0009 (2002)).

REFERENCES

1. A. A. Abdullaev and A. Z. Gadzhiev, Fiz. Tekh. Poluprovodn. (Leningrad) **25**, 30 (1991) [Sov. Phys. Semicond. **25**, 16 (1991)].
2. K. Seeger, *Semiconductor Physics* (Springer, Berlin, 1974; Mir, Moscow, 1977), p. 161.

Translated by A. Zalesskiĭ

Semiconductors, Vol. 37, No. 10, 2003, pp. 1160–1164. Translated from Fizika i Tekhnika Poluprovodnikov, Vol. 37, No. 10, 2003, pp. 1188–1192.
Original Russian Text Copyright © 2003 by Venger, Matyash, Serdega.

A Study of Linear Dichroism Induced by Uniaxial Strain in Silicon Crystals

E. F. Venger, I. E. Matyash, and B. K. Serdega

Institute of Semiconductor Physics, National Academy of Sciences of Ukraine, Kiev, 03028 Ukraine

e-mail: serdega@isp.kiev.ua

Submitted January 8, 2003; accepted for publication January 21, 2003

Abstract—Spectral characteristics of linear dichroism in uniaxially-strained silicon crystals in the region of edge absorption were studied using the polarization-modulation technique. The fine structure of the spectra due to participation of acoustic and optical phonons in interband transitions caused by absorption of linearly polarized radiation was observed. The spectral characteristics of induced absorption-coefficient anisotropy, revealing the phonon-related features, were determined from the combination of transmission and dichroism spectra. A phenomenological description of polarization-modulation measurements is considered; it is shown that the spectral dependence of the dichroism is given by the derivative of the transmission function with respect to the absorption coefficient. *© 2003 MAIK "Nauka/Interperiodica".*

1. Crystals of silicon have cubic symmetry; thus, they may become anisotropic and, consequently, exhibit linear dichroism only due to some directional effect. One of such effects, lowering the symmetry of the crystal, is uniaxial strain.

It is worth noting that, in real crystals, the presence of some nonuniform potential gradient, which is related either to the temperature or to the concentration of doping impurities, results leads in almost every case in internal elastic strain, whose parameters are governed by the direction and the magnitude of the potential gradient [1]. Linear-dichroism spectroscopy, which consists in recording the spectral dependence of the difference between the absorption coefficients of linearly polarized light with electric-field vector oriented parallel and perpendicular to the strain axis, may serve as a technique for measuring and investigating the anisotropy of dielectric properties induced by such a strain in real crystals.

As far as Si crystals are concerned, no studies of this kind have been reported. Meanwhile, evidence of dichroism was observed in a study of electroreflectance in Si [2], which revealed the difference between the spectral characteristics obtained for the two orthogonal polarizations of light. However, in [2] (as well as in [3]), only the spectral region of direct transitions was considered, which, in silicon, is far from the fundamental-absorption edge. Due to the features of the energy-band structure, of Si, the absorption in this material is related to indirect band-to-band transitions in a wide spectral range; thus, one can expect that phonon-related features will appear in the dichroism spectra. Indeed, the parameters of light passing through a sample should contain information about the mechanisms of interaction of light with the sample material; the adequacy of the analysis of these parameters controls the detectivity of a given measurement technique with respect to any particular property of the material.

In an attempt to study induced dichroism in silicon, we see that the latter statement is of special importance in this case. Due to the large values of the deformation-potential constant, it is difficult to observe and measure the effect using conventional techniques. At the same time, polarization modulation, one of the methods of differential spectroscopy, has a number of advantages characteristic of modulation techniques; meanwhile, it has been poorly studied up to now. Thus, there is not only methodological interest in testing this technique, which has already been successfully applied to investigate polarization-related phenomena (photoelastic and thermophotoelastic effects [4]).

A Reason for optimism is that, as shown in [5, 6] the electroabsorption spectra of silicon, reveal oscillations and nonmonotonic behavior due to the participation of phonons in indirect band-to-band optical transitions at small values of the absorption coefficient. In addition, of dichroism manifests itself in photoelectric effects in uniaxially strained cubic crystals (see, for example, studies on how excitonic emission depends on phonons in the region of indirect transitions in Si [7] and intrinsic photoconductivity in narrow-gap semiconductors [8]).

2. It is of key importance in this study that the charge-carrier scattering in the chosen material is mainly due to phonons. Thus, we used samples cut from a lightly doped *p*-Si ingot with a resistivity of 200 Ω cm, shaped as rectangular plate with a size of the illuminated side of 10×5 mm^2 and a thicknesses of 3, 2, 1, and 0.5 mm. The crystallographic axes were oriented in such a way that the direction of the uniaxial compression force applied to the samples coincided

with one of the main directions, [100], [110], or [111]. The treatment of the sample surfaces ensured an equal optical path length for all rays and reduced the light scattering to a minimum. The design of the device used to apply a compressive force to the samples had one difference from the conventional design for this kind of studies: it was equipped with a silicon force sensor (based on the transverse piezovesistive effect) to measure the mechanical stress.

We used an MDR-12 grating monochromator with a KGM-150 halogen lamp at its input as a wavelength-tunable light source. It produced a constant photon flux of 10^{15} cm^{-2} s^{-1} in the wavelength range of interest. An important feature of the optical layout of the experimental setup (see Fig. 1a) is the use of a polarization modulator—a dynamic phase plate utilizing the photoelastic effect [9]. This plate is made of fused silica, which is an isotropic material; anisotropy of the dielectric properties was induced by alternating tensile–compressive strain. The strain appears because of excitation of a normal oscillation mode of the plate by a standing acoustic wave from a crystal-quartz resonator to which an ac voltage is applied. At certain values of the voltage amplitude, two times over each period of oscillations, the fused silica plate acts as a quarter-wave plate and the circular polarization of the incoming light is then converted into linear polarization of the outgoing light; the electric-field vector changes its orientation periodically by 90° with a frequency of 50 kHz (see Fig. 1b). Thus, with the total intensity of light incident on the sample being constant, the signal at the detector (a Ge photodiode) is proportional to the difference between the transmission coefficients of light polarized along the optical axes of the sample. This signal was amplified by a selective nanovoltmeter and recorded by an analog plotter.

It is important that the modulator can be rotated about the optical axis. Since the polarization of the light passed through the modulator is related to its azimuthal orientation, the specified polarization state with respect to the sample axes can be set by the rotation of the modulator. This makes it possible to identify the nature of the effect under study by checking the parallel orientation of the electric-field vector of the light wave relative to the axes of the sample. Thus, one can verify the absence of spurious components in the recorded signal; these may originate, e.g., from off-normal incidence of light on the sample or imperfections in the optical elements.

Thus, we recorded the differences in the transmission spectra for the linearly polarized radiation with the electric-field vectors of light waves parallel to different optical axes of the sample. The dependences of these differential spectra on the sample thickness along the direction of light propagation and the magnitude of the sample deformation were examined. All the measurements were carried out at room temperature.

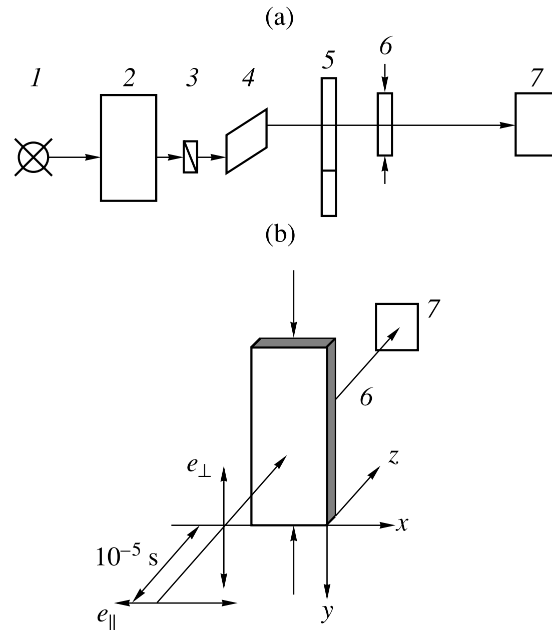

Fig. 1. (a) Layout of the optical setup and (b) schematic representation of the experiment: (*1*) light source (halogen lamp), (*2*) monochromator, (*3*) polarizer, (*4*) Fresnel's rhomb, (*5*) photoelastic polarization modulator, (*6*) sample in the compression unit, and (*7*) photodetector.

3. Let us recall that application of uniaxial strain to a Si crystal along the [$11\bar{1}$] direction raises the degeneracy of the valence band at the center of the Brillouin zone; in the case of the [110] and [100] directions, the conduction-band degeneracy is raised. The splitting of the levels under compression is accompanied by a variation in the band gap [10] and, thus, by an increase in the absorption coefficient for unpolarized light [11].

For polarized light, the situation is more complicated. Since the energy states in the valence band are mixed with each other (in particular, the V_+ and V_- bands appear in reverse order along the directions perpendicular to the strain axis), the selection rules for interband transitions induced by polarized radiation change [12]. For example, transitions from the V_+ band are allowed for both polarization states of the excitation light wave. At the same time, transitions from the V_- band are allowed only in the case of polarization perpendicular to the strain axis. It is this difference that causes linear dichroism, i.e., the difference in the absorption coefficients in uniaxially strained direct-gap cubic crystals.

In silicon, there is more complexity due to the multivalley energy structure of the conduction band, which implies indirect transitions and results in orientational dependence of the transition probabilities under uniaxial strain. It is these two factors that manifest themselves in a considerable discrepancy between the differ-

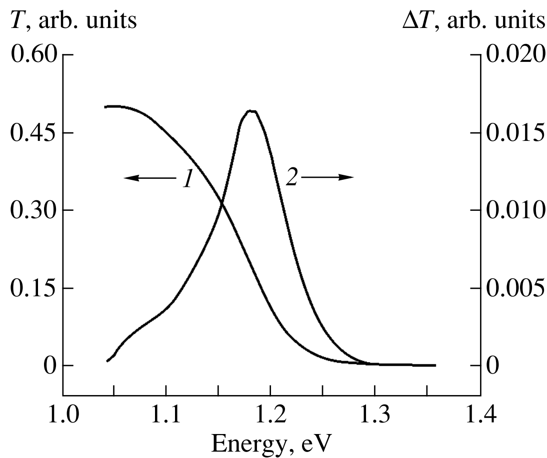

Fig. 2. Spectra of (*1*) transmission and (*2*) strain-induced differential transmission. The sample thickness is 0.38 mm; the stress of 3 kbar is applied along the [110] direction.

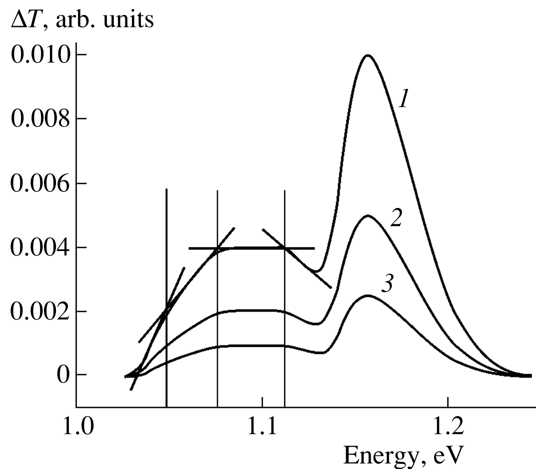

Fig. 3. Differential transmission spectra for polarization-modulated light at the applied uniaxial stress equal to (*1*) 4, (*2*) 2, and (*3*) 1 kbar. The sample thickness is 0.5 mm; the [100] orientation.

ential transmission spectra of Si samples oriented along different crystallographic axes (see Figs. 2, 3). However, what the dichroism spectra have in common, despite all these circumstances, is fine structure: in the case of [110] orientation, we see a dichroic band of complex and nonmonotonic shape (Fig. 2); in the case of the [100] orientation, we even see two bands (Fig. 3). In addition, one can note that, to a first approximation, curve *2* in Fig. 2 represents a derivative of the transmission spectrum (curve *1* in Fig. 2), which could be obtained by λ modulation. Indeed, one might expect that, due to uniaxial strain, a single transmission curve characterizing the isotropic sample splits in two, each corresponding to a certain polarization (parallel or perpendicular to the compression axis). Then, the difference between the ordinates of these two curves—which is the quantity measured by the polarization-modulation technique—will be largest in the region of the steepest slope of curve *1*. However, this is not quite correct, as follows from Fig. 3, which shows a set of dichroism spectra for the sample of another orientation. There is a definite distinction between the differential spectra of the two samples; meanwhile, their transmission spectra nearly coincide. We note here that, as expected, the dichroism is very weak in the range of mechanical stresses under consideration: the transmission spectra for the two orthogonal polarizations nearly merge into a single curve. The idea of the relationship between the magnitudes of the transmission T and its change ΔT is consistent with the numbers on the left and the right vertical axes in Fig. 2.

It can be clearly seen that the spectral characteristics of dichroism in Figs. 2 and 3 contain rather long linear segments separated by inflections. Extrapolating adjacent linear segments until intersection with one an other, we find certain relationships regarding their size and position. The length of the projection of the first linear segment on the energy axis coincides within 1 meV with the value of the exciton binding energy reported in [13]. The next segment has a different slope, but its projection equals twice the exciton binding energy. Note that a similar interpretation is given for the electroabsorption spectra of silicon samples in the same energy range presented in [6]. Finally, the length of the third linear segment, located between 1.075 and 1.109 eV, twice excellently matches the energy of the transverse acoustic (TA) phonon given in [14]. In Fig. 3, we illustrate this kind of analysis only for one of the curves. However, such analysis was carried out for other curves as well and indicated that the energy positions of the points of intersection between the linear segments are independent of the stress applied to the samples. Moreover, the energy positions are also independent of the sample thickness. In this case, the transmission curve shifts in energy and this causes a change in the relationship between the extrema of the differential characteristics (for the [100] orientation) or in their absolute values (for the [110] and [111] orientations); however, the positions of the extrema themselves and the phonon-related features remain unchanged.

4. Obviously, the shape of the measured differential transmission spectral curves is related to the peculiarities of the energy spectrum of crystalline silicon. Among these, the most important is the multivalley structure of the conduction band, which, first of all, results in the spatial dependence of the spectral characteristics of the dichroism. To verity this, let us analyze the measurement procedure qualitatively.

Let us recall that the signal measured is proportional to $\Delta T = T(\alpha_\perp) - T(\alpha_\parallel)$, i.e., to the difference between the values of the function T for the arguments $\alpha_\perp$ and $\alpha_\parallel$. If the dichroism parameter $\Delta\alpha < \alpha_\perp, \alpha_\parallel$ (which is true for

the case under consideration), one can easily derive the expression

$$\Delta T = T(\alpha_{\perp} + \Delta\alpha) - T(\alpha_{\perp}) = (dT/d\alpha)\Delta\alpha,$$

thus, the measured quantity is the derivative of the transmission function with respect to the absorption coefficient, multiplied by the value of the dichroism parameter. The derivative of the transmission function can be represented as a product of two partial derivatives: $dT/d\alpha = (\partial T/\partial\lambda)(\partial\lambda/\partial\alpha)$; this makes explicit the distinction between the results obtained by polarization modulation and λ modulation in optical and photoelectric studies. We conclude that we need to know the derivative of the transmission and the inverse of the derivative of the absorption coefficient—i.e., to perform two additional measurements—to obtain the value of the dichroism parameter, which represents the reaction of the cubic crystal to an external effect. However, we may used another approach, in which only one additional measurement is actually required; specifically, we record the transmission spectrum. From the combination of the differential and the integral characteristics of transmission (Fig. 2), we can determine the difference in the absorption coefficients $\Delta\alpha = \alpha_{\perp} - \alpha_{\parallel}$ for light polarized along two orthogonal optical axes of the sample. Indeed, from the well-known relation between the transmission T and the absorption coefficient α, we derive (under the condition $\Delta T \leq T$, which is true in our case) the expression $\Delta\alpha = B\ln(1 + \Delta T/T)$, which describes the spectral characteristic of the dichroism (here, the coefficient B is controlled by the sample thickness and the reflection losses).

A set of these characteristics corresponding to the three main crystallographic directions is shown in Fig. 4. One can clearly see that the spectra of induced dichroism in Si crystals are orientation-dependent. It should be mentioned that the same is true for the spectral curves of the change in the absorption coefficient for unpolarized light [11]. However, unlike that case, here we observe that the change in the absorption coefficient for polarized light is a nonmonotonic function of energy for all three orientations. Interpretation of this energy dependence is straightforward if one takes into account the known data on properties of Si crystals. Thus, a distinct kink in the spectral characteristics at $h\nu \approx 1.14$ eV is related to the fact that, with an increase in the photon energy, interband transitions with phonon absorption are replaced by those with phonon emission; this leads to an increase in the transition probability when the photon energy exceeds the band gap. Note that a similar kink at the same energy in the spectrum of the absorption coefficient for an isotropic sample can be seen only if the spectral curve is plotted on a semi-quadratic scale (see Fig. 4 in [10]). As for the drop in the value of the dichroism parameter at energies above 1.26 eV, it can be explained taking into account the fact that the known spectral characteristic of the absorption coefficient of Si [15] starts to deviate from the quadratic law toward a lower slope in this energy range. In this case, the vertical spacing between the two curves corresponding to the two polarizations should decrease, which is observed in experiment. Hence, the features in the spectral dependence of the absorption coefficient related to changes in the mechanism of interband transitions manifest themselves more clearly in the spectra of linear dichroism.

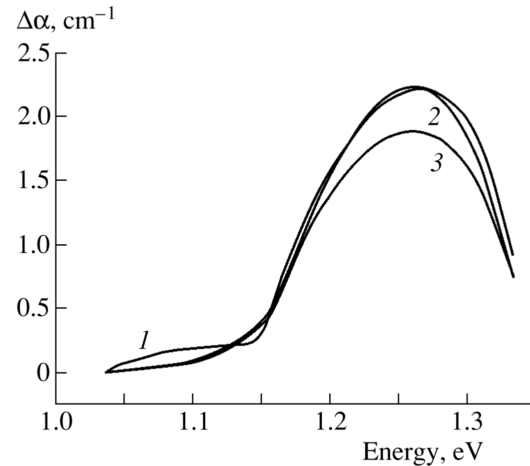

Fig. 4. Dichroism spectra of samples under stress of the same magnitude applied along the (*1*) [100], (*2*) [110], and (*3*) [111] directions.

Taking into account the difference in the selection rules for interband transitions for orthogonal polarization of light, it is possible to explain the origin of linear segments related to TA phonons (Fig. 3). It should be remembered that the difference between the two transmission functions is recorded; let us expand each of them into a series. Keeping in mind the above-mentioned modification of the valence band under uniaxial strain, it is not unreasonable to suppose that the coefficients with linear terms will differ, while those with higher terms will coincide. Indeed, it is the mixing of the valence-band states involved in the absorption of light with the polarization normal to the compression-force direction that makes this suggestion appropriate.

5. Thus, as expected, we found in this study that phonon-related features are present in the spectra of linear dichroism originating from band-to-band absorption of light in uniaxially strained silicon crystals; similar to the case of electroabsorption, it is acoustic phonons that are observed. High detectivity of the employed polarization modulation spectroscopy with respect to the value of anisotropy is demonstrated. Next, it is shown that the spectral characteristic of the dichroism is the derivative of the transmission function with respect to the absorption coefficient. In this context, it seems feasible that polarization modulation can be used to study the energy spectrum not only in the vicinity of the absorption edge, but in the entire energy range of the band gap and over the entire quasimomentum space. To accomplish this, the condition of sample semitransparency should be varied by varying the sam-

ple thickness, which will make possible measurements in the region of high absorption coefficients. Since the polarization modulation spectroscopy is quite sensitive to nonmonotonic behavior and other features in the spectral dependence of the absorption coefficient (which is demonstrated in this study), it seems likely that this technique will prove useful in finding and investigating such features in the energy band spectrum as Van Hove singularities.

Finally, it is worth mentioning that the effect of induced linear dichroism can be used for characterization of internal stresses in crystals. The experiment indicates that, under the physical conditions and with the standard equipment used in this study, the lowest reliably detectable level of stress is about 1 kg/cm^2; this value is obtained for the peak of the spectral dependence of the differential transmission.

REFERENCES

1. V. T. Grinchenko, E. V. Nikitenko, and B. K. Serdega, Dokl. Nats. Akad. Nauk Ukr., No. 1, 83 (1998).
2. G. W. Gobel and E. O. Kane, Phys. Rev. Lett. **15** (4), 142 (1965).
3. E. H. Pollak and M. Kardona, Phys. Rev. **172**, 816 (1968).
4. B. K. Serdega, Ye. F. Venger, and Ye. V. Nikitenko, Semicond. Phys. Quantum Electron. Opt. **2** (1), 153 (1999).
5. A. Frova and P. Handler, Phys. Rev. Lett. **14** (6), 178 (1965).
6. A. Frova, P. Handler, F. A. Germano, and D. E. Aspnes, Phys. Rev. **145**, 575 (1966).
7. L. D. Laude, F. H. Pollak, and M. Kardona, Phys. Rev. **3**, 2623 (1971).
8. F. T. Vas'ko, S. G. Gasan-zade, M. V. Strikha, and G. A. Shepeel'skii, Fiz. Tekh. Poluprovodn. (St. Petersburg) **29**, 708 (1995) [Semiconductors **29**, 368 (1995)].
9. S. N. Jasperson and S. E. Sahnatterly, Rev. Sci. Instrum. **40**, 761 (1969).
10. G. G. Macfarlane, T. P. McLean, J. E. Quarington, and V. Roberts, Phys. Rev. **111**, 1245 (1958).
11. L. A. Delimova, Fiz. Tekh. Poluprovodn. (Leningrad) **20**, 2188 (1986) [Sov. Phys. Semicond. **20**, 1369 (1986)].
12. F. T. Vas'ko and M. V. Strikha, Fiz. Tekh. Poluprovodn. (Leningrad) **24**, 1227 (1990) [Sov. Phys. Semicond. **24**, 773 (1990)].
13. K. L. Shaklee and R. E. Nahory, Phys. Rev. Lett. **24** (17), 942 (1970).
14. F. A. Jonson, Proc. Phys. Soc. **73**, 181 (1959).
15. D. E. Aspnes and A. A. Stunda, Phys. Rev. B **27**, 985 (1983).

Translated by M. Skorikov

Semiconductors, Vol. 37, No. 10, 2003, pp. 1165–1168. Translated from Fizika i Tekhnika Poluprovodnikov, Vol. 37, No. 10, 2003, pp. 1193–1196.
Original Russian Text Copyright © 2003 by Yastrebov, Ivanov-Omskiĭ, Richter.

ELECTRONIC AND OPTICAL PROPERTIES OF SEMICONDUCTORS

Photoluminescence from Amorphous Carbon Grown by Laser Ablation of Graphite

S. G. Yastrebov*, V. I. Ivanov-Omskiĭ*, and A. Richter**

**Ioffe Physicotechnical Institute, Russian Academy of Sciences, St. Petersburg, 194021 Russia*
e-mail: Yastrebov@mail.ioffe.ru
***University of Applied Physics, Wildau, 15745 Berlin, FRG*
Submitted February 11, 2003; accepted for publication February 17, 2003

Abstract—Photoexcitation and photoluminescence (1–7 eV) spectra of amorphous carbon films grown by laser ablation of a graphite target have been measured. The experimental data obtained are analyzed using the sum rule, and the energy dependence of the effective electron density of states is determined. Characteristic threshold energies in the effective density of states are revealed at ~1.4 and ~4 eV, and the conclusion is made that the energy distribution of the density of states is nonuniform, which is attributed to different contributions from the σ and π states of electrons. The temperature of the electron system excited by light is estimated to exceed the lattice temperature by a factor of ~40. This circumstance is attributed to heating of electrons by light.
© 2003 MAIK "Nauka/Interperiodica".

1. INTRODUCTION

Optical diagnostics of amorphous carbon is widely used to characterize its physical properties [1, 2]. Amorphous carbon obtained in various technological processes, which possesses widely diverse properties, is actually a set of different materials. A particular position in this group of materials is occupied by carbon grown by laser ablation of graphite [3–5]. The attractiveness of this technique is that it enables relatively simple control over the preparation conditions of the material, which makes it possible to widely vary the properties of these films. The product obtained as a result of its application, coatings for compact discs, must exhibit good optical transparency in the visible spectral range. It seems natural in this case that optical methods for monitoring the quality of such films should be developed, and it is desirable that these methods should be nondestructive. Photoluminescence (PL) undoubtedly belongs to methods of this kind, even though its virtually structureless spectrum, characteristic of an amorphous material, imposes specific requirements on the procedures for experimental data processing. By this is meant extraction from an experiment of parameters that can quantitatively characterize the specific features of a material produced under the technology in question.

This communication presents the results obtained in studying PL and photoexcitation spectra of amorphous carbon grown by laser ablation. Analysis of the experimental data obtained is used to extract information about the effective density of electron states and allotropic composition of carbon in the layers grown. Both photoexcitation and PL spectra are analyzed. It is shown that PL spectra are rather informative and can be used to determine the density of states related to π electrons, whereas the photoexcitation spectrum is determined by the density of states related to σ electrons.

2. EXPERIMENT

Amorphous carbon layers were deposited onto silicon substrates by laser ablation of a target made of highly oriented pyrolytic graphite. The deposition was conducted in a vacuum chamber at a pressure of 10^{-3} Pa, with the substrate intentionally unheated. A Lambda Physic excimer laser, in which a mixture of argon and fluorine gases served as the working medium, was used for target ablation. The ablation process was characterized by the following parameters: pulse repetition frequency and energy, 10 Hz and 500 mJ, respectively; ablation rate, 6 nm per pulse; flux, 260 MW/cm^2. Ellipsometric measurements demonstrated that the film thickness was 50 nm. The method of film detachment in a liquid medium was applied to determine the film density as 2.85 g/cm^3. According to [6], where a semiempirical relationship between the density of a material and the content of the sp^3 phase in it was presented, the films studied contain this phase in the amount of 72%.

A Hitachi F4010 spectrophotometer was used to measure the photoexcitation (Fig. 1) and PL spectra (Fig. 2). Luminescence in the Stokes region at 0.75–6 eV under excitation with photons with energies of 4.96 and 5.6 eV was observed. The luminescence photoexcitation spectrum was measured at energies of 3.1, 3.26, and 3.54 eV.

Figure 1 shows luminescence photoexcitation spectra for a typical sample. It can be seen that the luminescence intensity grows with increasing excitation

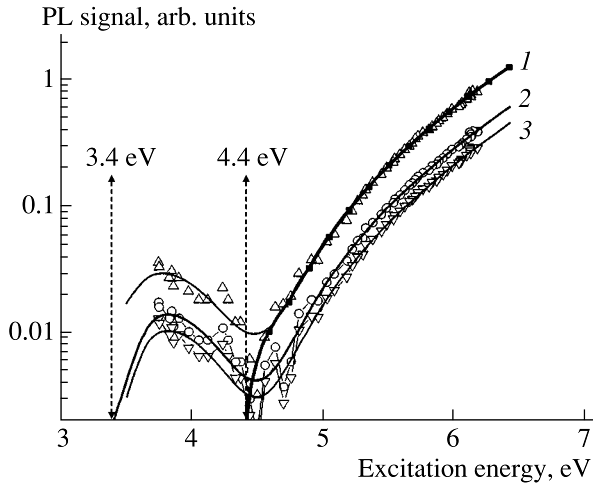

Fig. 1. Photoexcitation spectra of samples measured at (*1*) 3.5, (*2*) 4.4, and (*3*) 3.1 eV. Solid curves obtained as a result of filtering.

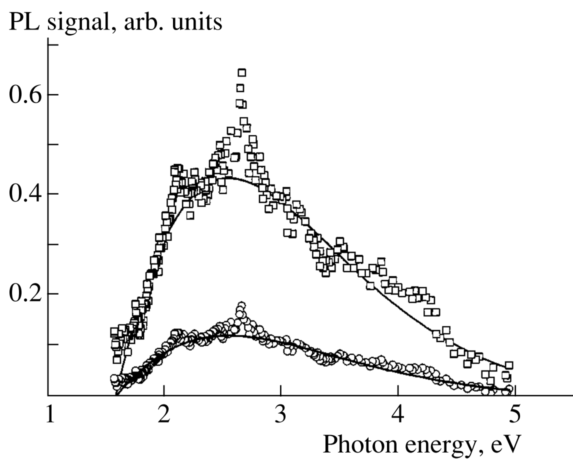

Fig. 2. PL spectra of amorphous diamond-like carbon: squares, excitation energy 5.63 eV; circles, 4.96 eV.

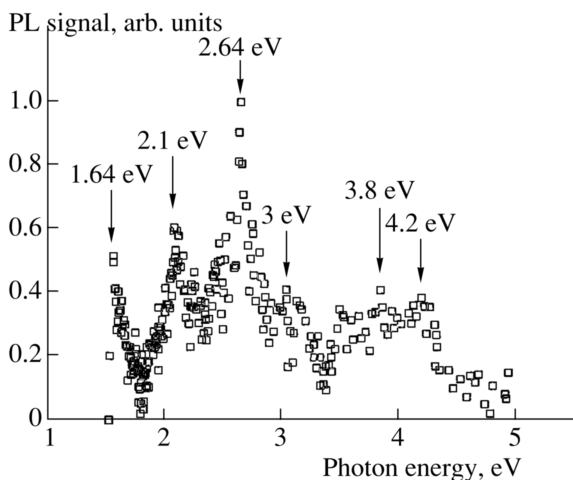

Fig. 3. PL spectrum after trend subtraction.

energy, beginning at ~3.4 eV, and reaches the maximum value at 6 eV. Comparison of this result with the PL spectrum in Fig. 2 shows that there exists a pronounced Stokes shift, which is so highly characteristic of disordered substances. Two characteristic cutoff energies are revealed. Extrapolation of the photoexcitation spectrum reveals a cutoff energy of ~4.4 eV, which can be attributed to the fundamental absorption edge related to σ–σ* transitions (Fig. 1). The low-frequency cutoff of the photoexcitation spectra at ~3.4 eV, which is masked in the spectrum by the PL band related to π–π* transitions, points to the contribution of structural defects to absorption by σ electrons.

Figure 2 shows PL spectra measured under excitation by photons with energies of 4.96 and 5.63 eV. It can be readily seen that the spectra have a pronounced structure, with its main elements independent of the excitation wavelength. In order to further reveal the structure of the spectrum, the original experimental data were subjected to smoothing by filtering. This yielded the trend curve shown in the figure by solid lines. It is noteworthy that, after scaling, the absolute values of both the trends nearly coincide. Then, the trend values were subtracted from the experimental data. The differences were normalized to the maximum value for both excitation energies. The results obtained are shown in Fig. 3. It can be seen that, in both cases, the curves coincide. The rather well-pronounced peaks at 1.6 eV can be attributed to the contribution from GR1 vacancies [7] in nanoclusters of highly tetrahedral carbon (nanodiamonds), which are present in the structure of a film grown by laser ablation. The peaks at 2.1 eV (complexes incorporating nitrogen impurities), 2.64 eV (interstitial or interstitial-vacancy complex TR12), 3 eV (N3 center comprising three nitrogen atoms and a vacancy), 3.8 eV (*A* center), and 4.2 eV are similarly attributable to the presence of nanoclusters of highly tetrahedral carbon (nanodiamonds) in the films. The appearance of structural defects characteristic of diamond is the first indication of a high concentration of sp^3 carbon in the films studied.

3. ANALYSIS OF EXPERIMENTAL RESULTS

3.1. PL and Photoexcitation Spectra

The emission intensity can be written using the results of [8]:

$$I_{pl}(\varepsilon) \propto \frac{(\varepsilon)^2}{\exp\left(\frac{\varepsilon}{kT}\right) - 1} D(\varepsilon), \quad (1)$$

$$D(\varepsilon) = (\varepsilon)^2 \kappa''(\varepsilon), \quad (2)$$

where κ'' and $\varepsilon = \hbar\omega$ are, respectively, the imaginary part of the dielectric constant of the material and energy.

In this case, the expression for the photoexcitation intensity has the form

$$I_{pe} \propto \varepsilon D(\varepsilon). \quad (3)$$

Let us determine the temperature of the electron system, which appears in expression (1). For this purpose, we assume that the function $D(\varepsilon)$ depends on energy more weakly than the function $1/(\exp(\varepsilon/kT) - 1)$. It can be seen that to solve this problem, it is necessary to extract from (3) the function $1/(\exp(\varepsilon/kT) - 1)$. This can be done in the following steps.

(i) Experimental values of the photoexcitation intensity, $I_{pl\exp}(\varepsilon)$, are normalized to the squared value of the corresponding energy, $(\varepsilon)^2$. This gives a function that is, in turn, normalized to its area. Then we obtain another function, designated as $U(\varepsilon)$.

(ii) The function $(1/U(\varepsilon)) + 1$ is plotted in the logarithmic scale (Fig. 4).

(iii) The temperature is determined from the slope of the plot in the high-frequency range (solid line in Fig. 4).

The high temperature in expression (1), $kT = 1.2$ eV, can be attributed to the influence exerted by carrier heating, which manifests itself because thermalization of carriers passing from the neighboring regions of space, occupied by a graphitelike phase, is hindered by heterogeneities in the nanostructure of the material.

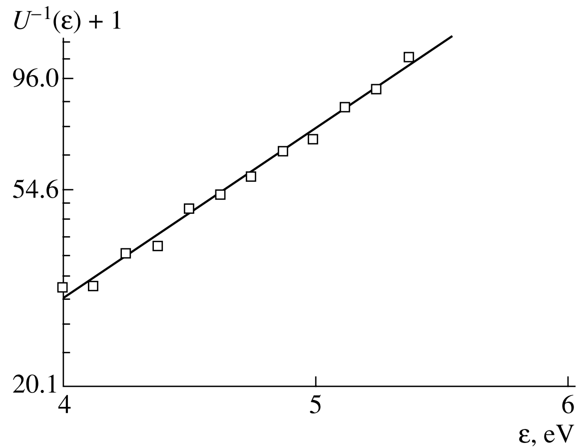

Fig. 4. Function of energy, $U^{-1}(\hbar\omega) + 1$, found from experiment. The slope of the straight line gives $kT = 1.2$ eV.

3.2. Effective Density of States

Multiplying the function $U(\varepsilon)$ derived on executing step 2 of the procedure described in the preceding paragraph by $(\exp(\varepsilon/kT) - 1)$, we obtain the function $D(\varepsilon)$, from which the dispersion of the imaginary part of the dielectric function $\kappa''(\varepsilon)$ can readily be found using expression (2). This dependence is shown in Fig. 5 (curve *1*). The same figure (curve *2*) shows the dependence of the imaginary part of the dielectric function on the photon energy, which is obtained directly from photoexcitation spectra with the use of expression (3). The low- and high-frequency cutoffs at ~1.5 and 4.4 eV are related to fundamental absorption edges formed by transitions of, respectively, π and σ electrons.

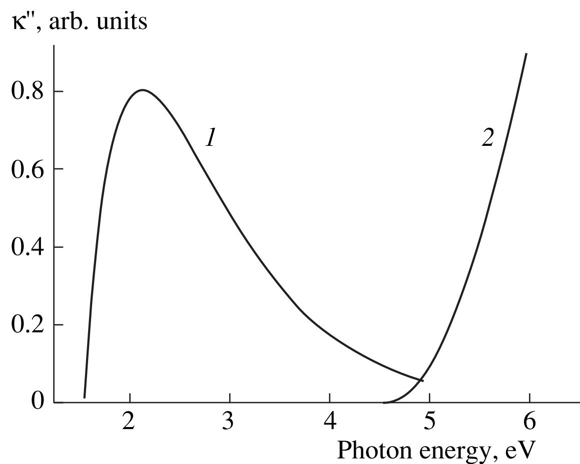

Fig. 5. Dispersion of the imaginary part of the dielectric function, found from data on (*1*) PL and (*2*) photoexcitation.

Let us use the resulting values of the imaginary part of the dielectric constant κ'' to calculate the number N of electrons in unit volume from the sum rule [9]:

$$g = \frac{4\pi N e^2}{m} = \frac{2}{\pi}\int_0^{\hbar\omega} \varepsilon\kappa''(\varepsilon)d\varepsilon. \quad (4)$$

Here ε, m, and e are, respectively, the electron energy, the effective mass, and the elementary charge. The result obtained in calculating the total electron density by formula (4) is shown in Fig. 6. It can be seen that two inflections appear in the frequency dependence of the density of excited electrons, which apparently corresponds to features in the density of electron states in the amorphous carbon films studied. Differentiating the data in Fig. 6 (curve *1*) numerically with respect to

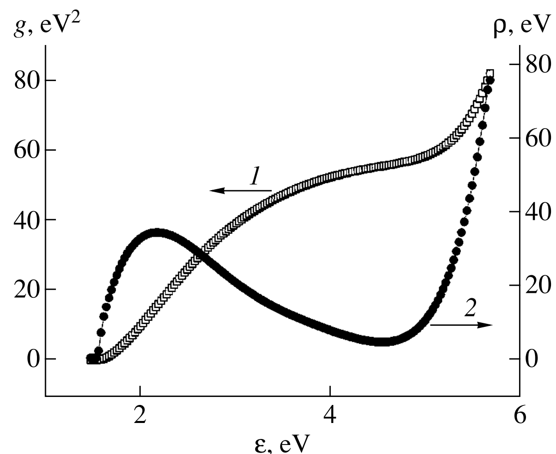

Fig. 6. Total electron density according to formula (4) and data of Fig. 4 (curve *1*). Effective density of states (curve *2*).

energy, we obtain the effective density of states $\rho(\omega)$, also shown in Fig. 6 (curve *2*). It is noteworthy that, since Fig. 5 shows the dispersion in arbitrary units, the data in Fig. 5 were additionally normalized to the number of electrons actually present in the π band, using the relation between the density of the material, P (g/cm^3), and the energy $E_{\sigma+\pi}$ of the $(\sigma + \pi)$ plasmon [6]: $P \approx 3.63 \times 10^{-3}(E_{\sigma+\pi})^2$. We obtain $E_{\sigma+\pi} = 28$ eV. As mentioned above, a sample contains 28% sp^2 atoms and 72% of atoms of the sp^3 phase. We assume that each atom donates four electrons: 4 σ electrons in the case of the sp^3 phase and three σ and one π electrons in the case of the sp^2 phase.

Then,

$$E^2_{\pi+\sigma(sp^2)} = 0.28E^2_{\sigma+\pi},$$

$$E^2_{\pi(sp^2)} = (1/4)E^2_{\pi+\sigma(sp^2)}.$$

Here, $E_{\pi+\sigma(sp^2)}$ is the energy of the $(\pi + \sigma(sp^2))$ plasmon. The square of this energy is proportional to the number of electrons contained in the sp^2 phase. $E^2_{\pi(sp^2)}$ is the energy of the $\pi(sp^2)$ plasmon, and its square is proportional to the total number of π electrons contained in the sample. The value $E^2_{\pi(sp^2)} = 54.88$ eV^2 was used in plotting the data in Fig. 6.

Figure 6 (curve *2*) can be used to evaluate the characteristic threshold energies in the effective density of states to be ~1.4 and ~4 eV. These energies can be attributed to difference in contributions from the π and σ electron states to the effective density of states.

4. CONCLUSIONS

Laser ablation of a graphite target has been applied to obtain samples of amorphous diamond-like carbon containing 72% sp^2 phase. Photoexcitation and PL spectra have been studied and used to find the dispersion of the imaginary part of the dielectric function. The energy dependence of the effective electron density of states has been determined with the use of the sum rule. Characteristic threshold energies have been revealed in the effective density of states at ~1.4 and ~4 eV and a conclusion was made on the nonuniform energy distribution of the density of states, which is attributed to the difference in contributions from σ and π electron states. The temperature of the electron system excited by radiation was found to exceed the lattice temperature by a factor of ~40. This circumstance is attributed to electron heating by light.

ACKNOWLEDGMENTS

We thank the Russian Foundation for Basic Research for the financial support (project no. 03-02-16289-a).

The study was supported by the DAAD/ZIP Program (Deutscher Akademischer Austauschdienst/zukunft investitions program) and "International Quality Networks" in the framework of the research direction "Technology of New Materials" (grant no. 214/IQN).

REFERENCES

1. J. Robertson and E. P. O'Reilly, Phys. Rev. B **35**, 2946 (1987).
2. J. Robertson, Phys. Rev. B **53**, 16302 (1996).
3. A. Richter, J. Non-Cryst. Solids **88**, 131 (1986).
4. A. Richter, Opt. Lasers Technol. **24**, 215 (1992).
5. B. Schultrich, Adv. Eng. Mater. **2**, 419 (2000).
6. A. C. Ferrari, A. Libassi, B. K. Tanner, *et al.*, Phys. Rev. B **62**, 11089 (2000).
7. V. S. Vavilov, A. A. Gippius, and E. A. Konorova, *Electronic and Optical Properties of Diamond* (Nauka, Moscow, 1985).
8. A. Einstein, Phys. Z. **18**, 121 (1917).
9. L. D. Landau and E. M. Lifshitz, *Course of Theoretical Physics*, Vol. 8: *Electrodynamics of Continuous Media,* 2nd ed. (Nauka, Moscow, 1982; Pergamon Press, Oxford, 1984).

Translated by M. Tagirdzhanov

Semiconductors, Vol. 37, No. 10, 2003, pp. 1169–1176. Translated from Fizika i Tekhnika Poluprovodnikov, Vol. 37, No. 10, 2003, pp. 1197–1204.
Original Russian Text Copyright © 2003 by Stetsun.

Photodeposition of Silver at the Interface of a Heterojunction Based on a Solid Electrolyte: The Case of CdSe–As_2S_3:Ag_x (x = 0.9–2.4) Heterojunctions

A. I. Stetsun

Institute of Semiconductor Physics, National Academy of Sciences of Ukraine, Kiev, 03028 Ukraine

Submitted December 14, 2002; accepted for publication December 14, 2002

Abstract—The phenomenon of photodeposition of silver has been detected in CdSe–As_2S_3:Ag_x (x = 0.9–2.4) heterojunctions. The mass transfer of silver ions to the interface is caused by an electric field arising due to separation of electron–hole pairs in the space-charge regions of the heterojunction upon photovoltage generation. The migration of ions is also stimulated by their entrainment by the electron flow. Recombination of electrons with ions at the interface causes photodeposition of clusters of a chemical element responsible for ionic conduction in the solid electrolyte. A new method is suggested for preparing materials for optical data storage. The method is based on the phenomenon of photostimulated transport of ions and photodeposition of a metal at the interfaces of heterojunctions based on solid electrolytes. © *2003 MAIK "Nauka/Interperiodica".*

1. INTRODUCTION

The statement of the problem for this study is based on the results of investigated of photodoping [1, 2]. This phenomenon consists of photostimulated diffusion of a metal into a semiconductor in structures containing a metal–semiconductor junction. Such photosensitive metal–semiconductor structures for various applications [3–5] can be produced by sequential deposition of metal (Ag, Cu, and others) layers and layers of a chalcogenide glass onto a substrate. When photosensitive semiconductor–metal structures are exposed to light in the spectral range close to the region of interband transitions in the semiconductor, rapid diffusion of the metal into the semiconductor is observed. Due to this, an intermediate layer of a semiconductor photodoped with metal is formed.

Systematization of the basic experimental features characteristic of this phenomenon allows us to conclude that the migration of metal ions is caused by the interaction between the ions and photoexcited electron carriers [6–8]. It was ascertained that a heterojunction (HJ) between the metal-doped and undoped regions of the semiconductor is naturally formed during the photodiffusion [1, 9–11]. Illumination causes photovoltage generation and changes the electric field in the space-charge region of the HJ, which was observed experimentally [12]. Separation of photogenerated electron–hole pairs in the HJ electric field induces an additional electric field, which causes penetration of metal ions from the doped region into the undoped region of the semiconductor. A similar mechanism accounts for the copper photodiffusion in GaAs [13].

At a certain ratio of the semiconductor- and metal-film thicknesses, the metal film is totally dissolved in the semiconductor film. Thus, the semiconductor and metal layers form a single layer of a semiconductor photodoped with metal.

According to the model considered above, illumination of the heterojunction between undoped and photodoped chalcogenide glasses may stimulate ion migration from one HJ region to another. One region of such an HJ, i.e., the photodoped layer, is a solid electrolyte with mixed conduction [1, 14].

This paper is devoted to studying the possibility of artificial formation of an HJ between a solid electrolyte with mixed ionic–electronic (hole) conduction and another material: a semiconductor, insulator, or metal characterized by either electronic or hole conduction. In this case, illumination of the HJ should cause photostimulated mass transfer of ions within only one region, i.e., within the solid-electrolyte layer. Such an HJ is also studied here.

The natural process characteristic of photodoping may be artificially directed only into the solid-electrolyte layer in HJs formed of a solid electrolyte, characterized by mixed conduction, and a semiconductor (insulator, metal). The creation of such artificial HJs allows the use of solid electrolytes with mixed conduction for optical data storage. The studies of photodoping indicate that a necessary condition of photostimulated mass transfer of ions is photovoltage generation upon illumination of an HJ.

To solve this problem, we studied the influence of illumination on HJs between II–VI semiconductors and vitreous As_2S_3 photodoped with silver. As is well known, II–VI semiconductors are used to form HJs exhibiting photovoltaic effect [15].

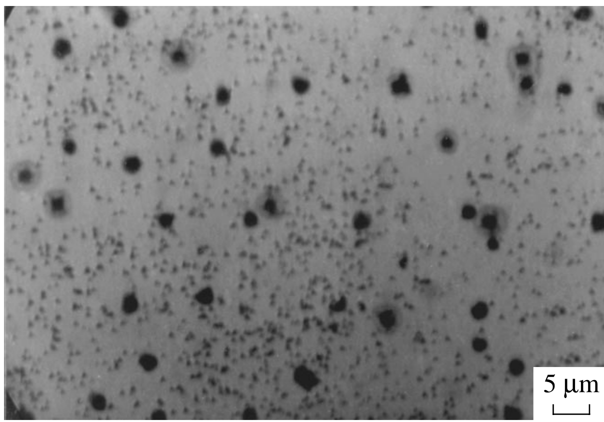

Fig. 1. Micrograph of the exposed CdSe–As_2S_3:$Ag_{2.4}$ heterojunction as viewed from the CdSe layer. The thicknesses of the CdSe and As_2S_3:$Ag_{2.4}$ layers are 200 and 450 nm, respectively. Clusters from 2 to 3.5 μm and from 0.2 to 0.5 μm in size are distinct.

Photodoping makes it possible to produce As_2S_3 layers with various contents of silver, as well as to modify their properties. Thus, a combination of the two semiconductors noted can be used to form an HJ characterized by photovoltage, where photostimulated transport of ions at a distance equal to the solid-electrolyte thickness and photodeposition of a chemical element may occur. The interface between materials with different bond lengths contains defects, i.e., dangling bonds. These defects serve as trapping and recombination centers. Recombination processes between electrons and ions at the interface may cause photodeposition of a chemical element responsible for ionic conduction in the solid electrolyte. Thus, the photostimulated transport of ions in the HJ based on a solid electrolyte may cause photodeposition.

The phenomenon of photostimulated transport of ions and photodeposition of silver was detected for the CdSe–As_2S_3:Ag_x (x = 0.9–2.4) HJ. The study of these HJs illustrates (as an example) the basic experimental features of photodeposition in HJs based on solid electrolytes with mixed conduction. This paper is the first report on the phenomenon of photodeposition of a chemical element providing ionic conduction in a solid electrolyte that an HJ is based on.

2. EXPERIMENTAL

The HJs were formed by thermal evaporation in a vacuum chamber with a residual pressure of no higher than 10^{-3} Pa during the process. The thickness of each layer in the HJ formed of CdSe and As_2S_3 photodoped with Ag was 50–500 nm.[1] Initially, the photodoped layer was formed on a quartz substrate. To this end, silver and As_2S_3 layers were deposited onto the quartz substrate. A reverse order of layer deposition was also used. Such structures incorporating two layers were exposed to light up to total and uniform dissolution of the metal film in the chalcogenide film. The photodoping uniformity was monitored by multiangle ellipsometry [16]. Then a CdSe layer was deposited onto the photodoped layer. HJs formed in such a way were used in the studies.

[1] Hereafter, for brevity, CdSe–As_2S_3:Ag.

To detect photostimulated changes, the CdSe–As_2S_3:Ag HJ was exposed to the light of a 500-W KG-220-500 halogen lamp. The illuminance was 8×10^4–1×10^6 lx. After a certain exposure time, the HJ was studied using a Biolam optical microscope. The depth profile of silver in the two-layer CdSe–As_2S_3:Ag structure was studied using a JAMP-10S Auger microanalyzer.

The reflectance and transmittance spectra of exposed and unexposed HJs were measured using a KSVU-23 spectrophotometer in the spectral range of 200–1200 nm. The measurement accuracy was within ±0.5%.

A V7-45 digital voltmeter with an internal resistance of 10^{16} Ω was used to measure the photovoltage at the HJs. The measurement accuracy was ±0.5%. A contact with the CdSe layer was formed by deposition of an indium or silver layer. The Ag layer also provided contact with the photodoped layer.

3. RESULTS

We studied the photostimulated processes in the CdSe–As_2S_3:Ag HJs containing 2, 5, 10, 15, 20, 25, and 32 at. % of Ag in the photodoped layer. Metal photodeposition was observed for Ag contents of 15, 20, 25, and 32 at. % in the photodoped layer. At an Ag content of 15 and 20 at. %, the repeatability of the metal photodeposition was about 80%. When the Ag content was as high as 25 or 32 at. %, the repeatability was almost 100%.

Exposure of the CdSe–As_2S_3:$Ag_{2.4}$ HJ to integrated light of the halogen lamp at an illuminance of 8×10^4 lx for two hours leads to the formation of two types of disk-shaped silver clusters. The transverse size of smaller clusters was 0.2–0.5 μm. The diametrical size of larger clusters was 2–3.5 μm. The results of the Auger studies show that clusters nucleate at the interface and grow into the photodoped layer. The micrograph in Fig. 1 shows the two-layer CdSe–As_2S_3:$Ag_{2.4}$ structure exposed to light as viewed from the CdSe layer. After exposure of the CdSe–As_2S_3:$Ag_{2.4}$ heterostructure for two hours, photodeposition becomes saturated; therefore, the height of larger clusters is equal to the photodoped-layer thickness.

When bulky As_2S_3 glass containing more than 30 at. % Ag impurity is exposed to intense light with a wavelength shorter than the interband absorption edge

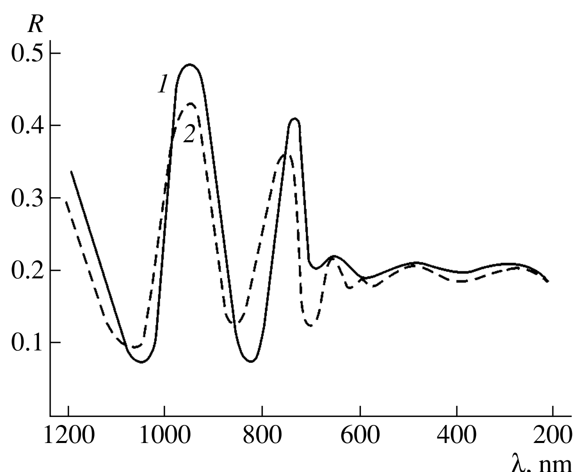

Fig. 2. Reflectance spectrum of the CdSe–As_2S_3:$Ag_{2.4}$ heterojunction (*1*) before and (2) after exposure. The thicknesses of the CdSe and As_2S_3:$Ag_{2.4}$ layers are 200 and 450 nm, respectively.

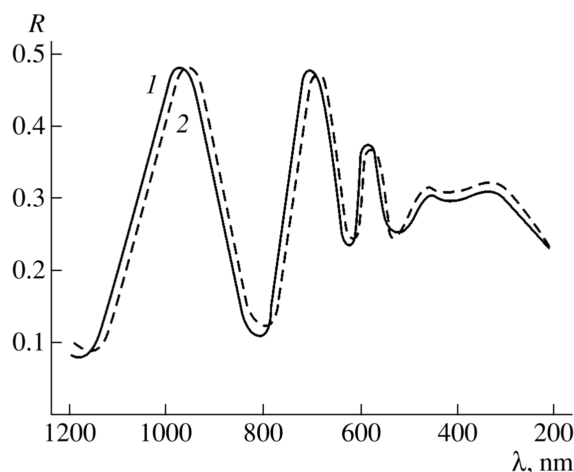

Fig. 3. Reflectance spectrum of the As_2S_3:$Ag_{2.4}$ layer 450 nm thick (*1*) before and (*2*) after exposure.

of the glass, the phenomenon of photosurface deposition of metal is observed [17]. Silver forms disk-shaped clusters on the glass surface.

A similar phenomenon of photoinduced chemical modification was observed for As–S layers photodoped with silver [18].

It was ascertained [12] that the mechanism of photosurface silver deposition is caused by the interaction of ions with electron–hole pairs, which are separated due to the Dember effect. The Dember field characteristic of the photodoped layer is 10^3 V cm^{-1} [12]. Under such a field, silver ions move to the surface and recombine with electrons there.

The electric field induced upon illumination of the HJs may exceed the Dember field by a few orders of magnitude. Therefore, the rate of Ag photodeposition in the CdSe–As_2S_3:Ag_x ($x = 0.9$–2.4) HJs should exceed the rate of photosurface metal deposition. Hence, the HJ photosensitivity should exceed the photosensitivity of a single photodoped layer.

For quantitative comparison of the photosensitivity of the As_2S_3:$Ag_{2.4}$ layer and the CdSe–As_2S_3:$Ag_{2.4}$ HJ, we used the photosensitivity definition, known from the studies of photochemical transformations in metal–semiconductor structures (see [1]). The photosensitivity S is defined as

$$S = \frac{A}{Et}. \quad (1)$$

Here, E is the illuminance, t is the exposure time, and A is the relative change in the reflectance,

$$A = \frac{\Delta R}{R}. \quad (2)$$

Figure 2 shows the reflectance spectra of the unexposed and exposed (2 h, 8×10^4 lx) CdSe–As_2S_3:$Ag_{2.4}$ HJ. We can see that the exposure decreases the amplitude of interference oscillations and change their spectral position.

The photodoped As_2S_3:$Ag_{2.4}$ layer was exposed for 6.5 h at an illuminance of 8×10^5 lx. The exposure of the photodoped layer exceeds the exposure of the HJ by a factor of 32.5. However, the relative changes in the

Table 1. Photosensitivities S_h and S_l of the CdSe–As_2S_3 : $Ag_{2.4}$ heterojunction and the As_2S_3 : $Ag_{2.4}$ layer, respectively

λ, nm	S_h, 10^{-9} lx^{-1} s^{-1}	S_l, 10^{-11} lx^{-1} s^{-1}
1200	0.42	0.62
1140	0.41	0.73
1100	0.18	0.80
1060	1.66	0.96
1020	0.81	0.49
980	0.04	0.11
940	0.14	0.02
900	0.42	0.09
860	0.66	0.66
820	2.11	0.92
780	0.31	1.58
740	0.44	0.49
700	0.03	0.03
660	0.05	0.14
620	0.22	1.99
580	0.04	0.66
540	0.05	0.46
500	0.07	0.44

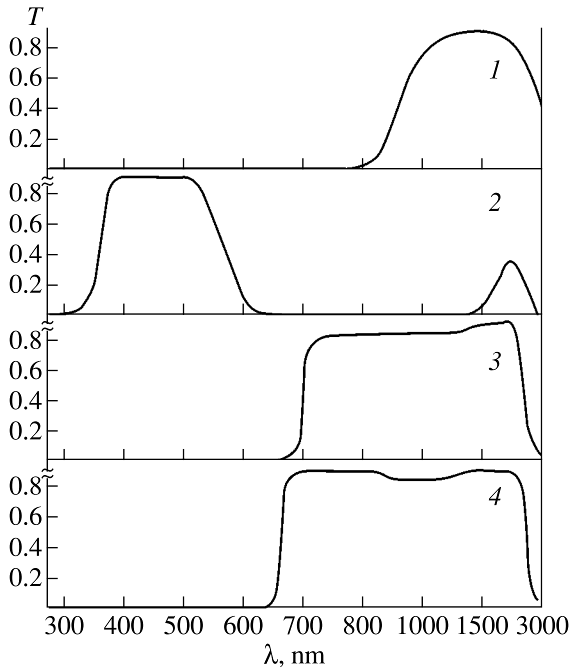

Fig. 4. Transmittance spectra of optical filters.

reflectance spectrum of the photodoped layer (Fig. 3) are much less pronounced than in the HJ spectrum.

Table 1 lists the photosensitivities S_l and S_h of the photodoped layer and the HJ, respectively, in the spectral range of 500–1200 nm. The HJ photosensitivity exceeds the photodoped-layer photosensitivity by a factor of ~130 in this spectral range. This indicates that the photostimulated transport of ions and the photodeposition of silver in the two-layer structure are caused by processes occurring specifically upon illumination of the HJ between the CdSe and As_2S_3:Ag_x layers.

The photosensitivity of the CdSe–As_2S_3:Ag_x (x = 0.9–2.4) HJs depends on the thicknesses of the CdSe and As_2S_3:Ag_x (x = 0.9–2.4) layers. At layer thicknesses of 200–500 nm, the photosensitivity correlates with the data of Table 1. However, the relative changes in the reflectance of the two-layer structure do not significantly exceed the measurement error at a CdSe-layer thickness of 50 nm. This fact indicates that the photodeposition efficiency depends on the width of the space-charge region in the CdSe layer.

Both the dark voltage and photovoltage are detected in the CdSe–As_2S_3:Ag_x (x = 0.9–2.4) HJs. The sign of the dark voltage corresponds to a positive potential at the CdSe layer. Under illumination, a photovoltage with a negative potential at the CdSe layer is detected. At a thickness of 400–500 nm of the CdSe layer and a thickness of 450–500 nm of the As_2S_3 layer photodoped with Ag to 30–32 at. %, the dark voltage is 110 mV. At an illuminance of 8×10^4 lx, the photovoltage is 95 mV.

The characteristic Dember photovoltage for the photodoped layer is 10 mV [12]. The photovoltages measured in the two-layer structure significantly exceed this value, which indicates that the photovoltage generation in the two-layer structure is caused specifically by the processes in the HJ.

The HJ photovoltage can be written as

$$V = \int\left(\frac{\Delta\sigma_n + \Delta\sigma_p}{\sigma}\right)\xi_0 dx - \int\left(\frac{\Delta\sigma_n}{\sigma}\right)\left(\frac{d\chi}{dx}\right)dx - \int\left(\frac{\Delta\sigma_p}{\sigma}\right)\left(\frac{d\chi}{dx} + \frac{dE_g}{dx}\right)dx \qquad (3)$$
$$+ kT\int\left[\left(\frac{\Delta\sigma_p}{\sigma}\right)\frac{d}{dx}(\ln N_v) - \left(\frac{\Delta\sigma_n}{\sigma}\right)\frac{d}{dx}(\ln N_c)\right]dx,$$

where σ is the conductivity under illumination, $\Delta\sigma$ is the photoconductivity, χ is the electron affinity, N_c is the density of electron states in the conduction band, N_v is the density of states in the valence band, ξ_0 is the electric field strength in the HJ, and E_g is the band gap [19].

In the case of an HJ based on a solid electrolyte with mixed conduction, both electron–hole and ion carriers contribute to the photovoltage. However, under illumination of such heterojunctions, ion carriers will be distributed over the thickness of the solid electrolyte layer in such a way as to compensate for the electric field of electron–hole carriers. Therefore, the contribution from ion carriers to the photovoltage will decrease the contribution from electron–hole carriers.

To determine the spectral range of light causing Ag photodeposition, the CdSe–As_2S_3:$Ag_{2.4}$ heterostructure was exposed to the light of a halogen lamp through various light filters from the photodoped-layer side. The As_2S_3:$Ag_{2.4}$-layer thickness was 300 nm, and the CdSe-layer thickness was 500 nm. The transmittance spectra of the light filters are shown in Fig. 4.

It was found that exposure of the HJ to infrared light with a photon energy lower than the As_2S_3:$Ag_{2.4}$ band gap (curve *1*) does not result in photodeposition. Exposure to light with an photon energy significantly exceeding the band gap of the photodoped layer does not cause photodeposition either (curve *2*). At a thickness of the As_2S_3:$Ag_{2.4}$ film of 300 nm, light separated by a light filter with a high-energy band does not reach the interface. There is also no photodeposition observed when the heterostructure is exposed to light with a photon energy as high as the absorption edge of As_2S_3:$Ag_{2.4}$ (curve *3*). However, if the filter transmission band is wider (670 nm) photodeposition is observed (curve *4*). Thus, it was ascertained that photodeposition occurs if the interface is exposed to light with a photon energy that exceed the As_2S_3:$Ag_{2.4}$ band gap by ~0.25 eV. Such a feature of the HJ photosensitivity points to the fact that the HJ energy-band diagram contains a peak near the interface as viewed from the photodoped layer.

4. DISCUSSION

The experimental results considered above show that the photostimulated transport of ions and photodeposition are caused by the effect of the electric field induced under illumination of the CdSe–As_2S_3:Ag_x (x = 0.9–2.4) HJ on Ag ions. In order to construct the energy-band diagram of the HJ, we should take into account the interaction between particles of three types, namely, electrons, holes, and ions.

Arsenic sulfide photodoped with silver to contents higher than 20 at. % is a solid electrolyte with mixed conduction. The transport number varies from 0.23 to 0.83 for an Ag content ranging from 1.67 to 2.4. The ionic conductivity is 8.2×10^{-6} Ω^{-1} cm^{-1} for As_2S_3:$Ag_{1.67}$ and 3.1×10^{-4} Ω^{-1} cm^{-1} for As_2S_3:$Ag_{2.4}$. The content of mobile silver ions in the As_2S_3:$Ag_{2.4}$ layer is 8.8×10^{21} cm^{-1}. The content of mobile ions may be as high as 40–50% of the total content of ions introduced into As_2S_3 [14]. Holes are major electron carriers in the photodoped As_2S_3 layer [7, 20]. Estimation of the hole density on the basis of the corresponding values of the hole conductivity [14] and mobility μ [21] by the formula

$$\sigma = qn\mu \tag{4}$$

yields a value of 3.94×10^{19} cm^{-3} for the As_2S_3:$Ag_{2.4}$ layer.

A thermally deposited CdSe layer has an n-type conductivity no less than 10^{-7} Ω^{-1} cm^{-1}. The electron density in such a layer can be in the range of 10^{17}–10^{18} cm^{-3}, depending on the deposition conditions [22, 23].

The results of photoelectric studies carried out by us agree with the data of [24], according to which the work function of CdSe is lower by 0.3 eV than that of As_2S_3.

Therefore, when CdSe is deposited onto As_2S_3:$Ag_{2.4}$, electrons from the CdSe layer diffuse into the photodoped layer and recombine with holes there. Holes from the photodoped layer diffuse into the CdSe layer and also recombine with electrons. Thus, positive and negative space-charge regions arise in CdSe and As_2S_3:$Ag_{2.4}$, respectively.

The formation of such space-charge regions causes two competing processes of Ag^+ ion migration. First, due to the electric field between the positive space-charge region in CdSe and the negative space-charge region in As_2S_3:$Ag_{2.4}$, Ag^+ ions located in the As_2S_3:$Ag_{2.4}$ space-charge region move beyond this region.

Second, ion migration is caused by the interaction of silver ions located deep in the photodoped layer with the fields of the HJ space-charge regions. When the number of charges in the CdSe depletion region is equal to the number of charges in the space-charge region of the photodoped layer, such an interaction may be

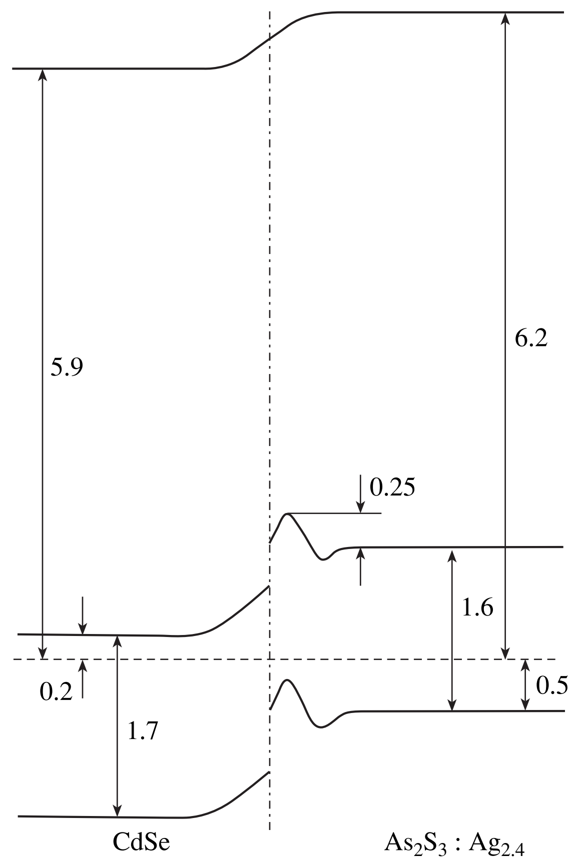

Fig. 5. Energy-band diagram of the CdSe–As_2S_3:$Ag_{2.4}$ heterojunction.

approximated in the multipole representation by the electric field of the dipole moment of these charges,

$$\mathbf{E} = \frac{3\sum_i q_i \mathbf{r}_i \mathbf{r} \mathbf{r}}{4\pi\varepsilon\varepsilon_0 r^5} - \frac{\sum_i q_i \mathbf{r}_i}{4\pi\varepsilon\varepsilon_0 r^3}, \tag{5}$$

where $\mathbf{r}_i$ is the radius vector of the ith charge, $\mathbf{r}$ is the radius vector of an ion located deep in the solid-electrolyte layer, ε is the solid-electrolyte permittivity, and ε_0 is the permittivity of free space.

The interaction with the dipole field causes ion migration from the bulk of the photodoped layer to its depletion region. As a result of the migration processes, a layer with high ion density arises behind the negative space-charge region in As_2S_3:$Ag_{2.4}$. The arrangement of the charged regions in the heterostructure corresponds to the energy-band diagram shown in Fig. 5. A similar energy-band diagram was suggested for a graded HJ [25].

The HJ formation corresponds to such an arrangement of ions, when the sum of forces acting on each ion from all other charges located in the heterostructure is zero.

Illumination of the HJ causes separation of electron–hole pairs according to the energy-band diagram.

Table 2. Distance d between the centers of photodeposited clusters and the number of atoms in a cluster N at various ion concentrations C in a solid-electrolyte layer 50 nm thick

C, cm^{-3}	d, Å	N
10^{22}	4.6	108
10^{21}	10.0	50
10^{20}	21.5	23
10^{19}	46.4	11
10^{18}	100.0	5
8×10^{15}	500.0	1

Electrons are collected in the quasi-neutral region of the CdSe layer. The transport of photoexcited electrons from the photodoped layer to the CdSe layer occurs due to injection above the barrier in the conduction band, injection after partial thermalization, and tunneling through the barrier. These processes are mechanisms characteristic of overcoming the potential barrier by photoexcited electrons [26]. Holes are collected in the quasi-neutral region of the photodoped layer. Thus, separated photoexcited carriers induce an electric field, which stimulates ion motion to the interface. This electric field is responsible for the photovoltage generation. The photovoltage sign corresponds to a negative potential at the CdSe layer, which agrees with the experimental results. The transport of ions to the interface is also stimulated by the electron-flow entrainment (the "electron wind" effect) [27].

The silver photodeposition is a result of the interaction between ions and electrons at the interface between the CdSe and photodoped layers. As is well known, dangling bonds are present at the interface of materials forming an HJ [28]. These bonds may be electrically active or neutral. The surface states corresponding to these bonds serve as electron and hole recombination centers in an HJ formed of materials with n-type (p-type) conduction. The experimental results of this study show that the surface states also serve as electron and ion recombination centers in the HJ based on a solid electrolyte. Since silver clusters begin to grow at the interface, photodeposition occurs when electrons recombine with silver ions at the interface between the CdSe and photodoped layers.

The neutral dangling bond at the interface acquires a negative charge when this bond captures an electron moving toward CdSe:

$$C^0 + e^- \xrightarrow{h\nu} C^-. \quad (6)$$

According to the direction of the band bending (Fig. 5), the HJ electric field in the space-charge region of the solid electrolyte prevents motion of positive ions to the interface between the layers. However, the electric field induced by photoexcited carriers is oppositely directed and stimulates motion of positive ions to the interface. In the case of high illuminance, such a field may flatten the HJ bands. Moreover, the electron flow entrains ions into the space-charge region of the solid electrolyte. Due to these reasons, ions enter the space-charge region of the solid electrolyte. The sum of the electric field induced by photoexcited carriers and the field between the negatively charged dangling bond and the Ag^+ ion exceeds the HJ field in the regions where electrons are trapped at the interface. Therefore, the following reaction occurs

$$C^- + Ag^+ \xrightarrow{h\nu} C_0 + Ag. \quad (7)$$

Due to multiple repetition of this reaction, silver clusters are nucleated at the interface.

The size of clusters formed due to the photodeposition of ions from the solid electrolyte of a certain thickness depends on the ion concentration. The dependence of the cluster size on the properties of materials forming the HJ can be determined by analyzing the cluster photodeposition in a model HJ between a material with n-type conduction and a solid electrolyte with mixed conduction. Let us assume that the thickness of the solid-electrolyte layer is 50 nm and the solid electrolyte has a crystal structure. Table 2 lists the calculated numbers of atoms in a photodeposited cluster and distances between cluster centers for thee case when all ions are deposited from the solid electrolyte, at a ion concentration in the solid electrolyte ranging from 8×10^{15} to 10^{22} cm^{-3}. Taking into account that the atomic radii of chemical elements providing ionic conduction in solid electrolytes are 1.16–2.57 Å [29, 30], it becomes obvious that the cluster size exceeds or is comparable to the distance between cluster centers at high ion concentrations (10^{22}–10^{20} cm^{-3}). In this case, the solid electrolyte in the narrow region near the interface will be supersaturated. As the critical content of the photodeposited element is attained, the clusters of this element agglomerate in larger grains, such that the grain size and shape are governed by the condition of minimum free energy (see [31])

$$\Delta F = \frac{g}{3}\Delta f R^3 + \frac{\mu}{2}\Gamma R^2, \quad (8)$$

where g and μ are the coefficients related to the grain shape, Δf is the difference between the specific free energies of two phases, Γ is the surface-tension coefficient, and R is the grain size. In the case of high ion concentrations, the criterion of minimum free energy controls the grain size and shape independently of the structural features of crystalline or amorphous solid electrolyte. This tendency is observed for Ag deposition in two-layer CdSe–As_2S_3:Ag_x (x = 0.9–2.4) structures.

In the case of low ion concentrations (10^{19}–8×10^{15} cm^{-3}), the distance between the centers of clusters significantly exceeds their sizes and clusters do not

agglomerate. This circumstance makes it possible to use photodeposition in heterostructures based on solid electrolytes as a method for cluster formation. Clusters may include different numbers of atoms, depending on the ion concentration and the layer thickness. After illumination of the HJ, the upper film can be etched. The solid-electrolyte film will contain clusters of certain sizes.

The results of calculations show that a smallest microformation photodeposited in the heterostructure based on a solid electrolyte consists of a single atom. Such single-atom photoformations are spaced at a distance of ~50 nm when the ion concentration in the solid-electrolyte layer is 8×10^{15} cm^{-3} (Table 2). In the general case, the minimum distance between clusters is limited by the distance of the interatomic interaction for the ion component and the supersaturation concentration of the solid electrolyte. These parameters control the resolution of the heterostructure based on a solid electrolyte, as applied to optical data storage.

The studies of the photostimulated processes occurring in the HJ based on a solid electrolyte make it possible to suggest a new method of forming a medium for optical data storage. Such a medium represents a two-layer or multilayer structure including a solid-electrolyte layer with mixed conduction and a semiconductor (insulator, metal) layer with *n*-type or *p*-type conduction. Materials with certain properties should be chosen as to provide photovoltage generation under illumination of the heterostructure, which would cause redistribution of the metal over the solid-electrolyte layer and photodeposition of the chemical element responsible for ionic conduction in the solid electrolyte. The resolution of this medium is comparable to the interatomic-interaction distance.[2]

One of the possible applications of the photodeposition of a chemical element responsible for ionic conduction in a solid electrolyte is photography. The construction principle for media based on solid electrolytes covers many combinations of insulators, semiconductors, and metals with solid electrolytes. It is possible to form HJs with various energy-band diagrams. Many solid electrolytes are characterized by ionic conductivity higher than that of As_2S_3:Ag_x ($x = 0.9$–2.4) by a few orders of magnitude [29]. Correspondingly, the exposure required for optical data storage may be much lower in comparison with the CdSe–As_2S_3:Ag_x ($x = 0.9$–2.4) HJs.[3]

[2] The resolution limit in the optical data storage is half the light wavelength; for the visible range, this value is ≥200 nm. The generalization to the interatomic-interaction level is not quite correct, since it calls for studies in the corresponding (i.e., X-ray) spectral range [32] (editor's comment).

[3] In fact, concerning photosensitivity, classic photography remains uncompetitive due to the chemical enhancement (development), which may be as high as 10^9 [33] (editor's comment).

ACKNOWLEDGMENTS

I thank A.A. Kudryavtsev and V.V. Kislyuk for their helpful participation discussions.

REFERENCES

1. I. Z. Indutnyi, M. T. Kostyshin, V. I. Min'ko, E. V. Mikhailovskaya, and P. F. Romanenko, *Photostimulated Interactions in Metal–Semiconductor Structures* (Naukova Dumka, Kiev, 1992), p. 134.
2. A. V. Kolobov and S. R. Elliott, Adv. Phys. **40**, 625 (1991).
3. Y. Utsugi, A. Yoshikawa, and T. Kitayama, Microelectron. Eng. **2**, 281 (1984).
4. I. Z. Indutnyi, A. V. Stronski, S. A. Kostioukevich, *et al.*, Opt. Eng. **34**, 1030 (1995).
5. W. M. Moreau, *Microlitography* (Plenum, New York, 1988), p. 269.
6. K. Tanaka and H. Sanjoh, J. Appl. Phys. **74**, 1106 (1993).
7. K. Tanaka, J. Non-Cryst. Solids **137–138**, 1021 (1991).
8. G. A. Kluge, Phys. Status Solidi **101**, 105 (1987).
9. S. T. Lakshmikumar, J. Non-Cryst. Solids **88**, 196 (1986).
10. V. A. Dan'ko, I. Z. Indutnyi, A. A. Kudryavtsev, *et al.*, Ukr. Fiz. Zh. **36**, 937 (1991).
11. I. Z. Indutnyi, V. A. Dan'ko, A. A. Kudryavtsev, *et al.*, J. Non-Cryst. Solids **185**, 176 (1995).
12. V. A. Dan'ko, I. Z. Indutnyi, O. P. Kosyarum, *et al.*, Preprint No. 8-89 (Inst. of Semiconductor Physics, National Academy of Sciences of Ukraine, 1989).
13. B. I. Boltaks, S. M. Gorodetskiĭ, and T. D. Dzhafarov, Fiz. Tverd. Tela (Leningrad) **13**, 3420 (1971) [Sov. Phys. Solid State **13**, 2877 (1971)].
14. V. A. Dan'ko, I. Z. Indutnyĭ, and V. I. Min'ko, Fiz. Khim. Stekla **18**, 128 (1992).
15. A. G. Milnes and D. L. Feucht, *Heterojunctions and Metal–Semiconductor Junctions* (Academic, New York, 1972; Mir, Moscow, 1975).
16. M. V. Sopinskiĭ, Optoélektronika **1**, 95 (1997).
17. S. Maruno and T. Kawaguchi, J. Appl. Phys. **46**, 5312 (1975).
18. K. Tanaka, N. Yoshida, and Y. Yamaoka, Phys. Mag. Lett. **68**, 81 (1993).
19. *Current Topics in Photovoltaics,* Ed. by T. G. Coutts and J. D. Meakin (Academic, London, 1972; Mir, Moscow, 1988), p. 25.
20. I. Z. Indutnyĭ, Zh. Nauchn. Prikl. Fotogr. **39**, 65 (1994).
21. A. M. Andriesh, M. S. Iovu, D. I. Tsiulyanu, and S. D. Shutov, *Arsenic Sulfide and Its Alloys* (Shtiintsa, Kishinev, 1981).
22. K. L. Chopra and S. R. Das, *Thin-Film Solar Cells* (Plenum, New York, 1983; Mir, Moscow, 1986).
23. N. D. Dhere, N. R. Parikh, and A. Ferreira, Thin Solid Films **36**, 133 (1976).
24. V. S. Fomenko, *Emission Properties of Materials: Handbook* (Naukova Dumka, Kiev, 1981), p. 184.

25. W. G. Oldham and A. G. Milnes, Solid-State Electron. **6**, 121 (1963).

26. B. Augusta and R. L. Anderson, J. Appl. Phys. **36**, 206 (1965).

27. V. B. Fiks, *Ionic Conductivity in Metals and Semiconductors* (Nauka, Moscow, 1969), p. 108.

28. A. L. Fahrenbruch and R. H. Bube, *Fundamentals of Solar Cells. Photovoltaic Solar Energy Conversion* (Academic, New York, 1983; Énergoatommash, Moscow, 1987), p. 65.

29. V. N. Chebotin and M. V. Perfil'ev, *Electrochemistry of Solid Electrolytes* (Khimiya, Moscow, 1978).

30. S. S. Batsanov, *Electronegativity of Elements and Chemical Bond* (Nauka, Novosibirsk, 1962).

31. A. G. Khachaturyan, *Theory of Phase Transitions and Structure of Solid Solutions* (Nauka, Moscow, 1974).

32. R. J. Kollier, C. B. Burckhart, and L. H. Lin, *Optical Holography* (Academic, New York, 1971; Mir, Moscow, 1973).

33. *Theory of Photographic Process*, 4th ed., Ed. by T. H. James (Macmillan, New York, 1977; Khimiya, Leningrad, 1980).

Translated by A. Kazantsev

Semiconductors, Vol. 37, No. 10, 2003, pp. 1177–1184. Translated from Fizika i Tekhnika Poluprovodnikov, Vol. 37, No. 10, 2003, pp. 1205–1213.
Original Russian Text Copyright © 2003 by Torkhov.

SEMICONDUCTORS STRUCTURES, INTERFACES, AND SURFACES

Formation of a Native-Oxide Structure on the Surface of *n*-GaAs under Natural Oxidation in Air

N. A. Torkhov

Kuznetsov Physicotechnical Institute, pl. Revolyutsii 1, Tomsk, 634050 Russia

e-mail: tna@ic.tsu.ru

Submitted February 3, 2003; accepted for publication February 6, 2003

Abstract—Using scanning tunneling microscopy, the native-oxide film on epitaxial *n*-GaAs(100) was found to be formed by tightly joining nanoclusters involving oxides of Ga and As as well as an excess As layer on the interface between Ga_2O_3 and *n*-GaAs. The fractal structure of surface of the clusters is formed by three levels of similar grainlike elements, whose sizes satisfy the ratio 9 : 3 : 1. In the three-dimensional case, approximately six finer grains can be arranged on a coarser grain. Two possible cases of forming the fractal structure of clusters were considered. If the As_2O_3 and As fluxes to the surface are identical (the first case), the formation of cluster structure is governed by the As diffusion over the cluster surface. If the As flux exceeds that of As_2O_3, the cluster-structure formation is governed by the Ga diffusion over the cluster surface (the second case). The cluster growth under normal conditions and, therefore, the increase in the oxide-film thickness cease when the clusters are tightly joined because it hampers reactants through the oxide film and the chemical reactions to proceed.
© 2003 MAIK "Nauka/Interperiodica".

1. INTRODUCTION

During technological operations in the manufacturing of semiconductor devices, it is often impossible to avoid contact between atmospheric oxygen and a semiconductor surface, which inevitably leads to surface oxidation [1–5]. In this case, not only are the electrochemical properties of the surface modified, but its structure and morphology as well. In turn, this fact must be taken into account in developing technological operations at the nanoscale and submicroscale levels.

Up to now, there have seen few studies devoted to investigating the structure of *n*-GaAs native-oxide films and their effect on surface morphology. It is believed only that the native-oxide film is amorphous [1–19]. A dominant body of investigations performed in this field was aimed at studying the chemical composition of these films [12–19]. For example, Thurmond *et al.* [12] use the results of calculations of the Ga–As–O phase diagram and the experimental data to show that the thermodynamic equilibrium with GaAs is possible only for Ga_2O_3 and elemental As under normal conditions. The As_2O_3–Ga_2O_3 system on the GaAs surface is considered thermodynamically unstable. Already at room temperature, the system slowly tends to the state of thermodynamic equilibrium in agreement with the phase diagram via the endothermic substitution reaction. Thus, as was reported in [12], there exists a thin native-oxide layer on the GaAs surface in air under normal conditions; this layer is composed predominantly of Ga_2O_3 with inclusions of As_2O_3 and a free-As monolayer. Later on, it was shown [20, 21] that the intrinsic-oxide film on GaAs(100) involved predominantly Ga_2O_3 and an excess As layer on the interface between GaAs(100) and Ga_2O_3.

With the use of scanning tunneling microscopy (SIM) in this study, we investigated the structure of the native-oxide surface for epitaxial *n*-GaAs and its growth mechanism in air under normal conditions. The intrinsic-oxide film of epitaxial *n*-GaAs was shown to be formed by nanoclusters with a fractal structure and composed of Ga_2O_3 with an excess As layer on the interface between GaAs(100) and Ga_2O_3.

2. EXPERIMENTAL

For investigating the structure of the native-oxide surface, we used the *n*-GaAs(100) epitaxial layers. The state of the *n*-GaAs-layer surface was investigated by STM using an SMM-2000TA scanning microscope [ZAO "KPD" (Moscow Institute of Electronic Engineering)]. For obtaining high-quality STM images of the surface, we formed an ohmic contact by the electrochemical deposition of GeNi + Au on the n^+-layer side of the substrate with subsequent annealing in a hydrogen atmosphere at a temperature of 450°C. We then soldered a gold or copper wire to the deposited alloy to ensure the electric contact between the sample and the electric circuit of the microscope. As was shown previously [2, 3], a similar procedure makes it possible to obtain a reasonably good image of surfaces at the atomic-scale level not only for native oxides of doped epitaxial *n*-GaAs layers, but also for thin (~10 nm) insulating SiO_2 films [3]. The three-dimensional (3D) STM measurements of the surface profile were carried out using a platinum tip (Pt 99.99) under normal condi-

tions in the dc mode. The voltage between the tip and the semiconductor surface was chosen to be equal to 1.5 V. For quantitative investigations of the profile of surfaces using the software package supplied with the scanning multimicroscope, we plotted the cross sections (profiles) of the surfaces under study. The image was also analyzed using the software, making it possible to trace the profile image of the surface along a contour with a preset accuracy L. As a result of tracing, we obtained a contour image of the surface profile. Simultaneously, the computer program calculated the number of such objects (contours) detected as a result of tracing. From the analysis of the STM images obtained, we determined the fractal (Hausdorff) dimension D of the surface under investigation by triangulation [22–24] using the expression

$$D = \frac{\ln n}{\ln \eta}, \quad (1)$$

where η is the change in the scale of sizes and n is the change in the number of scales fit into the object under measurement.

The structure of a thin surface region of samples was studied by reflection high-energy electron diffraction (RHEED) at an electron energy of 75 keV using an EMR-102 commercial electron diffractometer. For investigating the structure of the n-GaAs surface region free of the native oxide, the intrinsic-oxide film was removed from the surface in the ammonium hydroxide etchant $NH_4OH : H_2O = 1 : 5$ (AM etchant [2]) immediately before loading the sample into the electron-diffractometer vacuum chamber. From this point, the AM-etched surface is called the free surface, while an oxidized surface is called the starting our face. From the ellipsometry data, the thickness of the intrinsic-oxide film amounted to ~3.5 nm for the starting surface, whereas the thickness of the surface layer with the permittivity ε differing from the bulk permittivity was 0.6–1 nm for the free surface after the AM-etchant treatment, which nearly coincided with the modified-layer thickness on the GaAs(100) surface [2]. The thickness of the layer within which the electron-beam diffraction took place was determined from the central-spot position in the electron-diffraction pattern and amounted to ~3 nm. With the aim of obtaining an image with a higher contrast, the negatives of electron-diffraction patterns were processed using the CorelDrow9 graphic editor with the 3D "profile" effect.

3. RESULTS AND DISCUSSION

To analyze the profile of the intrinsic-oxide surface for epitaxial n-GaAs, we used the 3D image of its area obtained by the scanning tunneling microscope. As the results of investigations at the nanoscale level showed, the profile of the intrinsic-oxide surface for epitaxial n-GaAs is very nonuniform. As can be seen from Fig. 1a, the surface is not smooth but has a grain structure characteristic of the native oxide of epitaxial n-GaAs [2]. Analysis of STM images showed that the intrinsic-oxide film has a quasiperiodic "grainlike" profile with a characteristic horizontal size of l_{xy} and a vertical size of l_z, which depend on the value of measurement scale L. The grains turned out to be arranged on the surface as assembled in isolated, tightly joining aggregates (clusters) with a characteristic horizontal size l_{xy} of about 9 nm instead of being random. The surface image after the complete oxidation involving the oxide clusters (~9 nm) are not displayed in its entirety in order to show the surface structure of a cluster at different levels in more detail and on the same scale.

As an example, Fig. 1a shows the contour image of the surface area for one such cluster instead of its entire surface. A detailed investigation of the surface for a large number of clusters showed that their surfaces can involve six, on average, similar finer objects with l_{xy} ~ 3 nm (Fig. 1b). In turn, these objects also involve six similar, still finer objects with $l_{xy} \approx 1$ nm each (Fig. 1c). A further decrease in L showed that the objects with $l_{xy} \approx 1$ nm can also involve six finer objects each with a characteristic size of 0.5 nm or less (Fig. 1d). Further, a finer structure is not observed. The investigations show that these objects already do not meet similarity conditions with respect to previous similar objects.

Thus, each following three fold decrease in L results in the division of each similar figure into still six other finer ones. For the sake of convenience in the visual observation, the figures into which the larger figure (object) is divided are colored in an individual shade of gray (Figs. 1b–1d).

The quantitative investigations of the surface profile also corroborated the results. From the transverse profiles (Figs. 2a–2c), it can be seen that the length of the envelope curve substantially depends on the magnitude of L in the one-dimensional case. In addition, the number of scales fit in along the curve are determined by the relationship KL^{-D}, which points to the existence of similarity elements; here, K is a constant, and D is the dimension of the space [22]. The analysis of the surface image shows that the similarity elements are hills or "grains" in the 3D case. As can be seen from Figs. 1b, 1c, and 2, fine grains are arranged on coarser grains. In turn, the latter are arranged on still coarser grains. We performed a statistical analysis of the grain sizes in the film under investigation using the tracing program; we found that the grains can be conventionally divided into three sets according to their sizes. The grains from one set are called a level. For the first level, we assume that $L_{xy} = 9$ nm and $L_z = 3$ nm. It follows that the horizontal size of the first-level grains amounts on average to $l_{xy} \approx$ 9 nm in the transverse diameter and $l_z \approx 3.5$ nm along the vertical. The peak-to-peak value [9] is also identical on average and amounts to ~9 nm. The investigations performed with different scales show that the surface morphology and the grain shape remain virtually invariable for the second level [$L_{xy} = 3$ nm and $L_z =$ 1.2 nm (Fig. 1b)] and for the third level [$L_{xy} = 1$ nm and

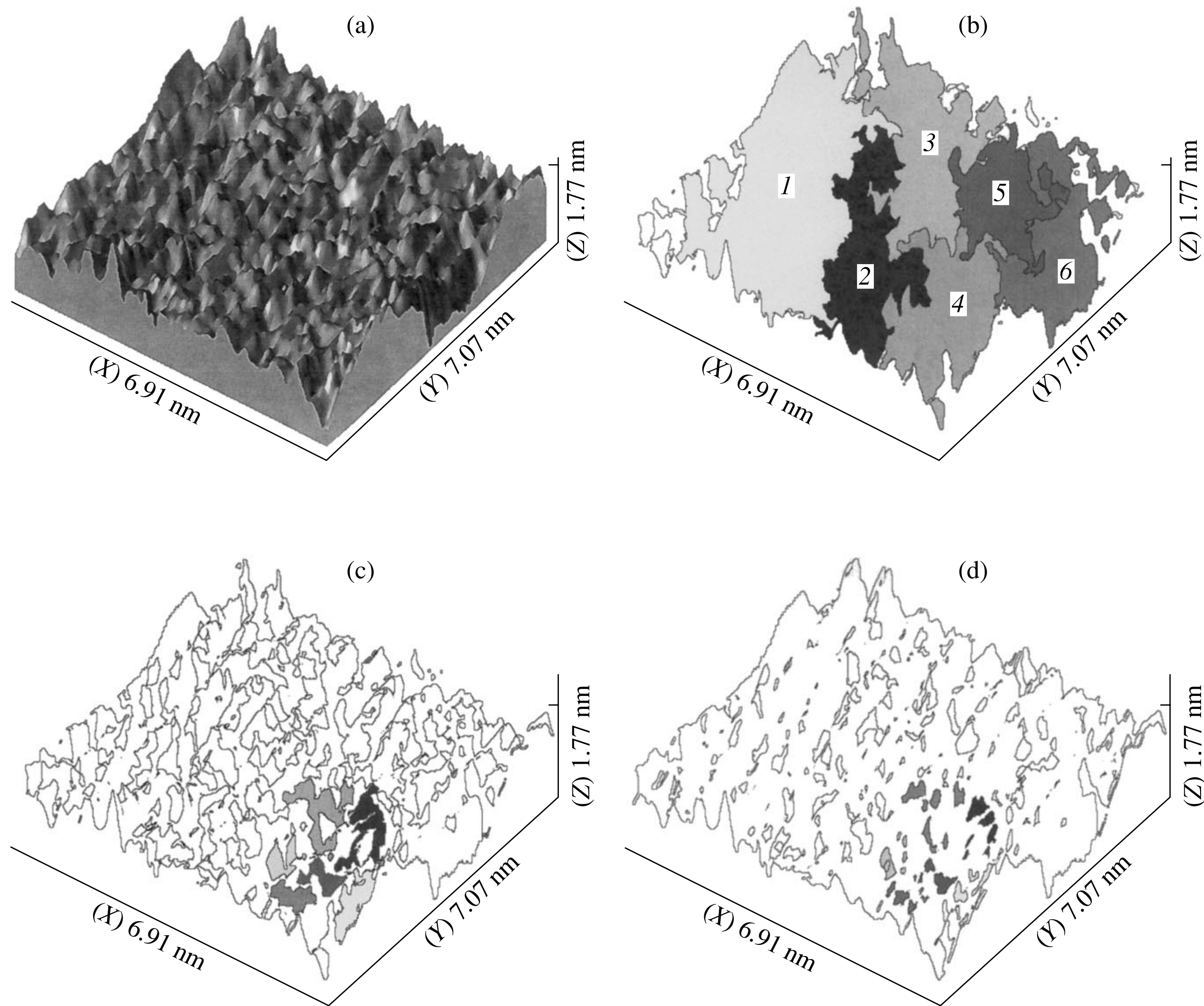

Fig. 1. STM image of an intrinsic-oxide surface area for n-GaAs starting sample: (a) obtained with a magnification of 2^{21}; (b–d) contour images for the measurement scale L_{xy} = (b) 3, (c) 1, and (d) 0.1 nm.

L_z = 0.4 nm (Fig. 1c)]. These are the only grain sizes and peak-to-peak value that vary. According to the results obtained, the grain sizes amount to l_{xy} = 3 nm and $l_z \approx$ 1–1.3 nm for the second level, and the peak-to-peak value is ~3 nm. For the third (last) level, $l_{xy} \approx$ 1 nm, $l_z \approx$ 0.4–0.5 nm, and the peak-to-peak value is ~1 nm.

Thus, the linear sizes of grains from the first, second, and third levels are proportional at a ratio of 9 : 3 : 1. As a result, it can be seen that the intrinsic-oxide surface of epitaxial n-GaAs obtained by oxididation in air under normal conditions is formed by three levels of similar grainlike elements. The presence of similar elements (grains) on the surface of n-GaAs oxide in the investigated region of scales (1 nm $\le L_{xy} \le$ 9 nm and 0.4 nm $\le L_z \le$ 3 nm) makes it possible to state that the surface is self-affine. As a result of simple calculations using expression (1), the value of the Hausdorff dimension D occurs to be equal to ~2.34 for the self-affine intrinsic-oxide surface. The interpretation of the fractional dimension relies on the assumption that, although the surface under investigation is close to the ZD one (D = 2), it also has certain 3D properties; i.e., in a way, the surface is characterized not only by area, but also by volume. The narrow range of the scales under investigation in which the surface can have the bulk properties points to the fact that the properties of the intrinsic-oxide surface at the nanoscale level can significantly differ from those of the same surface at the submicroscale level; it is most likely necessary to this take into account when planning and performing technological operations. For $L \gg$ 9 nm, figures similar to grains on the surface of the intrinsic-oxide film in a starting sample are not observed, and the surface itself appears smooth (Fig. 3a). The measurement of the dimension of the intrinsic-oxide surface at the submicroscale level (for $L \gg$ 9 nm) yielded a value D = 2.

For investigating how a thickness of the intrinsic-oxide film affects the structure of its surface, we

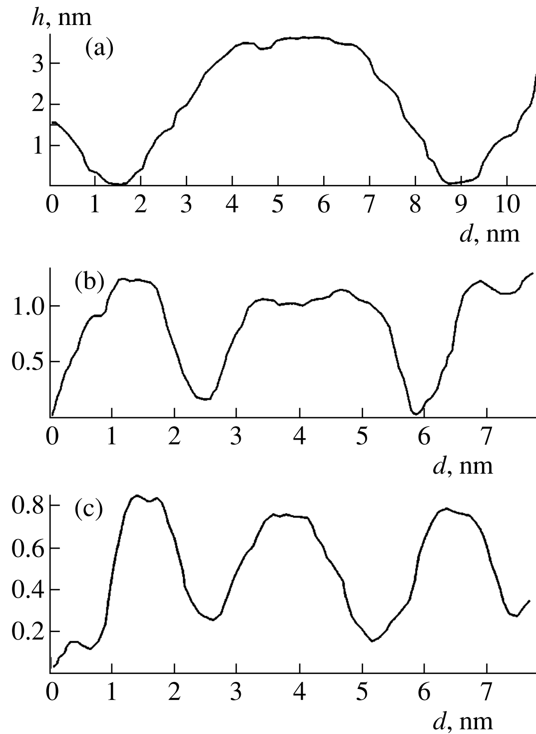

Fig. 2. Cross sections of the oxidized-surface profile for a starting sample; the measurement scale L_{xy} = (a) 9, (b) 3, and (c) 1 nm.

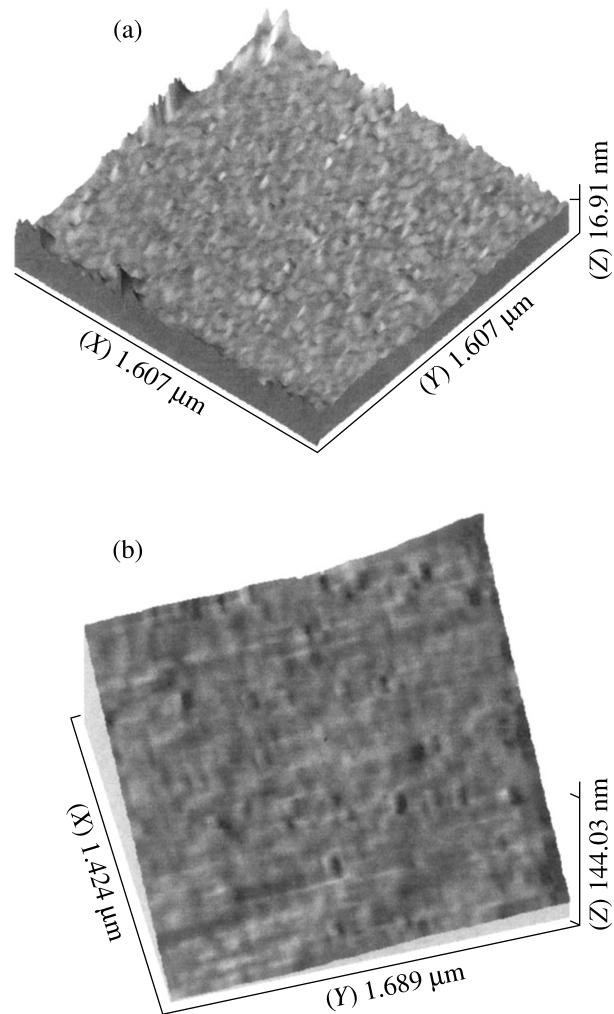

Fig. 3. STM images of the contact-layer surface for the *n*-GaAs starting sample; the magnification in 2^{13} and $L \gg 9$ nm: (a) with native oxide, and (b) without native oxide.

obtained the intrinsic-oxide films with a thickness of ~30 nm (Fig. 4a) and ~90 nm (Fig. 4b) by thermal oxidation in air. Surfaces thus obtained are also covered by grainlike formations with characteristic sizes dependent on the value of measurement scale *L*. For example, the horizontal size l_{xy} amounts to ~27 nm for L_{xy} = 27 nm, the vertical size $l_z \approx 32$ nm for $L_z = 30$ nm, $l_{xy} \approx$ 90 nm for $L_{xy} = 90$ nm, and $l_z \approx 97$ nm for $L_z = 90$ nm. The measurement of the dimension *D* of an intrinsic-oxide surface 90 nm thick also yielded a value $D \approx 2.34$.

Thus, the intrinsic-oxide film grows on heating with the conservation of its structure. The scale range in which the surface is self-affine is now wider and amounts to 1 nm $\le L_{xy} \le$ 90 nm and 0.4 nm $\le L_z \le$ 97 nm. From this fact, it follows that unusual (bulk) properties of the surface can manifest themselves already at the submicroscale level. In addition, it should be noted that the largest horizontal size of similar figures (natural irregularities on the oxidized *n*-GaAs surface) are directly related to the thickness of the intrinsic-oxide film. Note that the similar effect was also observed for SiO_2 films deposited plasmochemicalally on the surface of epitaxial *n*-GaAs. As was reported recently [3], the size of irregularities increases with the thickness of the SiO_2-film, and the fractal structure of the surface is retained [4].

The structure investigations of a starting surface performed RHEED also showed that there was no periodic structure (long-range order) in the surface layer ~3 nm thick. This fact is corroborated by the absence of reflections from atomic planes and by the presence of a diffusive “halo” in the electron-diffraction pattern near the central spot (Fig. 5a).

4. MECHANISM OF INTRINSIC-OXIDE FORMATION

For investigating the mechanism of the intrinsic-oxide formation, we studied the natural oxidation of *n*-GaAs surfaces in air under normal conditions. The investigation of a large number of samples enables us to state that the surface morphology is modified regularly and identically with time under the natural oxidation in air. For investigating the oxidation, we used a starting sample from the surface of which the intrinsic-oxide layer was removed in the AM etchant immediately before the STM measurements. It can be seen (Fig. 3b) that the free surface has a different morphology as com-

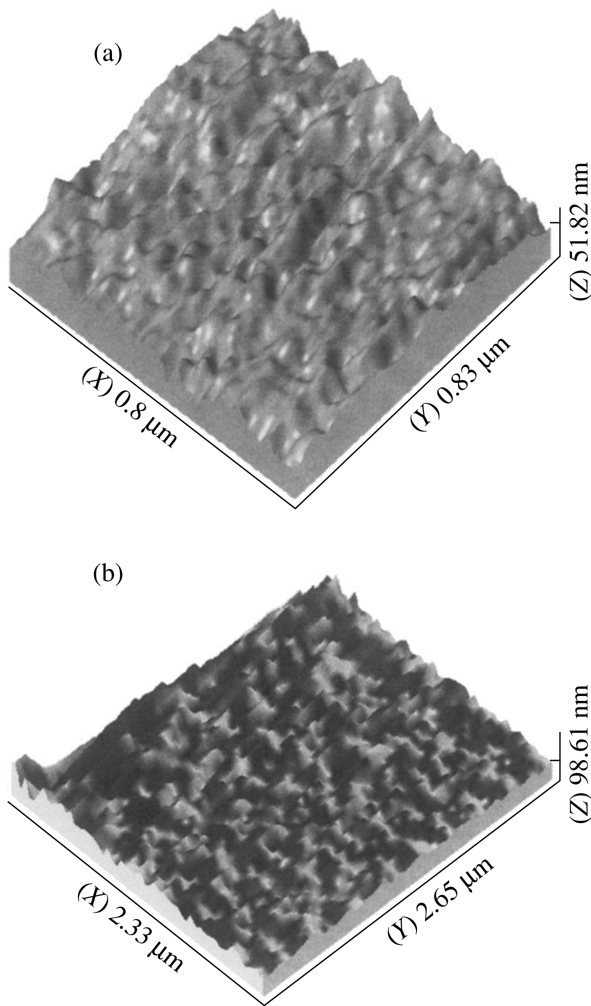

Fig. 4. STM image of the surface of films of *n*-GaAs native oxide with thickness of (a) ~30 nm (a magnification of 2^{15}) and (b) ~90 nm (a magnification of 2^{13}). The films are obtained on heating in air under normal conditions for various intervals of time.

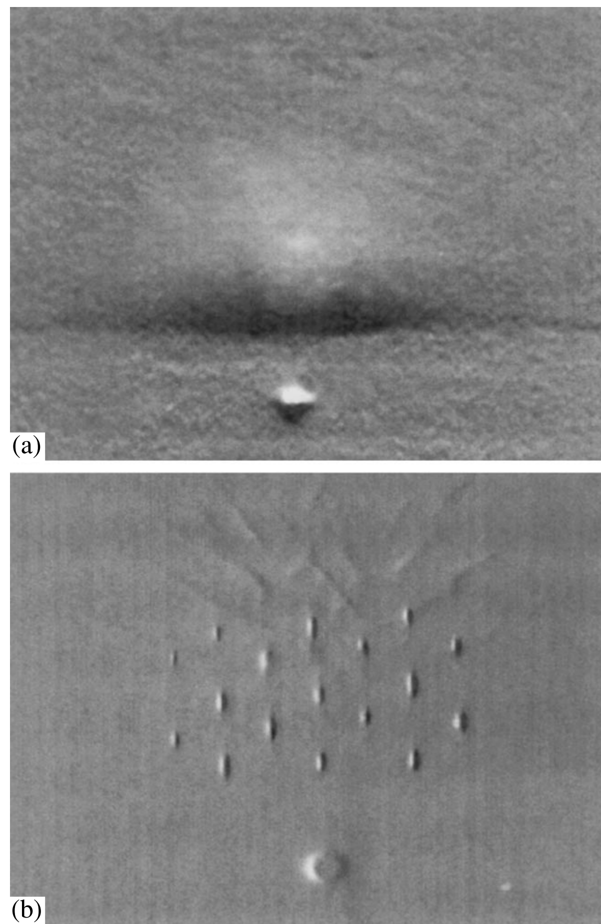

Fig. 5. Electron diffraction patterns of the surface region: (a) starting sample, and (b) sample from the surface of which the native oxide was removed.

pared to the oxidized one. The characteristic irregularities (grains) disappeared, and the surface itself became smooth. It was reported recently [2] that the surface of epitaxial *n*-GaAs obtained by treatment in the AM etchant can manifest a periodic structure. The structural investigations of a free surface (Fig. 6a) performed by RHEED also pointed to a high quality of the crystalline structure of the ~3-nm-thick surface layer. This is corroborated by the presence of a diffraction peak from atomic planes near the central spot (Fig. 5b). The lack of a "halo" near the central spot points to an almost complete absence of the amorphous intrinsic-oxide layer on the *n*-GaAs surface. The measurement of the free-surface dimension showed that the quantity D is equal to 2 irrespective of linear sizes of the measurement scale. This circumstance indicates that the free surface has identical properties at the nanoscale and microscale levels in contrast to the oxidized one. As a result, we may conclude that the surface structure observed for the *n*-GaAs native oxide is inherent precisely to the intrinsic-oxide film instead of the *n*-GaAs surface; i.e., the intrinsic-oxide film does not replicate the surface of epitaxial *n*-GaAs.

When a free surface is in contact with air under normal conditions (Figs. 3b, 6a), natural oxidation sets in. This inference is corroborated by surface image obtained after several minutes of the surface being treated in the AM etchant (Fig. 6b). Growth islands (clusters ~9 nm in diameter) appear on the surface. As atoms are known to have a higher mobility on the surface of crystalline GaAs(100) and can even congregate in isolated droplets of microscopic size at high temperatures (~400°C). In this context, it is possible to assume that the size of the As clusters observed under normal conditions is also governed by specific features of the As-atom diffusion over the *n*-GaAs surface. Since the As diffusion in the *n*-GaAs surface has an activation energy, there is a specific diffusion length Δl for every temperature. The value of Δl increases with temperature, which leads to enlargement of the As clusters.

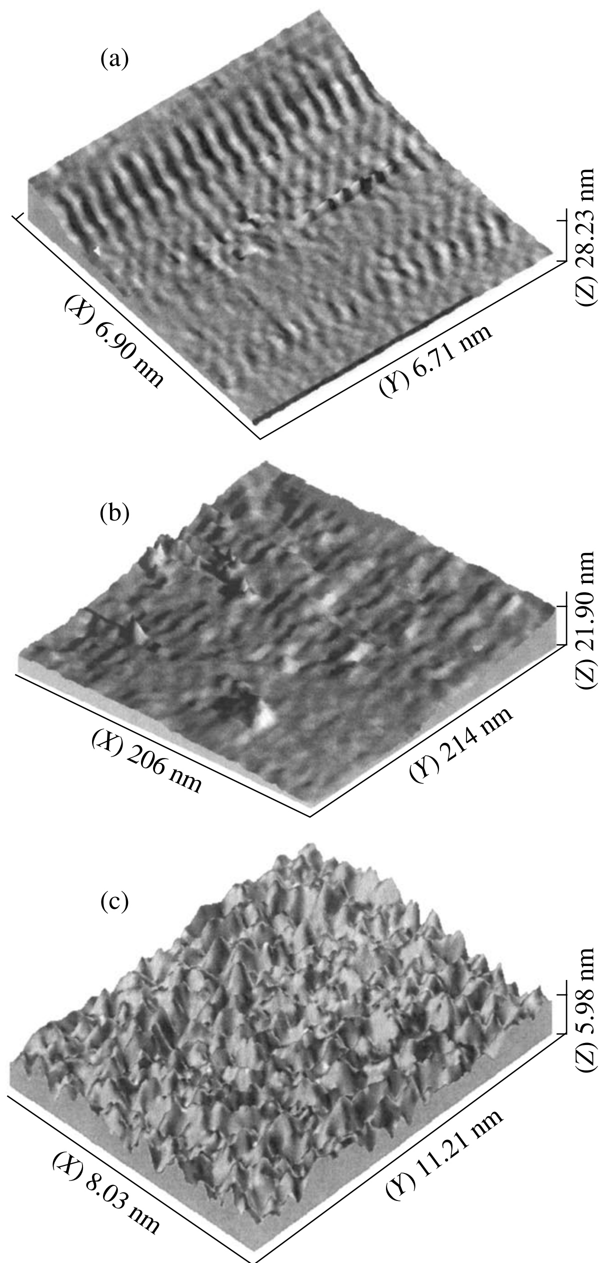

Fig. 6. STM image of epitaxial-*n*-GaAs surface free of native oxide: (a) with a magnification of 2^{22}; (b) with a magnification of 2^{15} after 3 min of exposure to air; and (c) STM image of epitaxial-*n*-GaAs surface obtained with a magnification of 2^{22} after 20 min of exposure to air.

Since the number of As atoms on the *n*-GaAs(100) is restricted, the increase in the cluster sizes is accompanied by a decrease in their number and vice versa. A decrease in temperature leads to a decrease in the value of Δl, which results in an increase in the number of clusters and in a decrease in their sizes. In this case, the As clusters are now arranged in the immediate vicinity of one another. Thus, it is the As atoms assembled in clusters (whose sizes, as follows from above, depend on the activation character of the As diffusion over the surface) that begin oxidize. According to the data obtained, if we perform the oxidation at a higher temperature, a large number of atoms are assembled in clusters by the moment of the onset of oxidation, which leads to an increase in the intrinsic-oxide film thickness (Fig. 4). If the temperature decreases, the As-atom diffusivity over the surface becomes lower and, a smaller number of atoms assemble in clusters by the onset of oxidation. Since, the As clusters cease to grow after oxidation, the intrinsic-oxide film also becomes thinner at a lower temperature. As the surface is oxidized via the formation of individual clusters rather than uniformly, we may assume that the As is oxidized more efficiently in the presence of the native oxide than on the free surface. For this reason, the As free atoms have time to reach a nucleus and to take part in the formation of its structure.

The remaining Ga atoms under the developing nuclei form an excess layer. Because the total amount of matter at the interface between the air and *n*-GaAs is not changed, we may assume that the number of Ga atoms in the excess layer virtually coincides with that of As atoms in nuclei.

The nucleation character of the intrinsic-oxide-film growth and also the largest size of grains (~9 nm) may indicate that the intrinsic-oxide film is formed from isolated grains (Fig. 6b). According to the results obtained, each grain represents a cluster, which has a fractal structure. The clusters grow according to a certain law instead of in a random way. For example, it can be seen from Fig. 1d that, on the surface of similar figures (grains) of the third level, the objects are arranged with a characteristic size of l_{xy} on the order of 0.5 nm, which can be identified with individual atoms or molecules and which can be the nucleation centers for new-level grains under favorable conditions. As can be seen from Fig. 1d, the number of such objects is also equal to six. It is most likely that the surface energy is lowest in the case when six finer objects are arranged on the surface of a similar element that determines the character of its growth. It is also not inconceivable that a rigorously determined number of nucleation centers for similarity elements on an isolated area can depend on the surface configuration and on the features of atomic diffusion over the surface.

After 20-min exposure of the free surface to air under normal conditions, the surface again acquires the grainlike structure (Fig. 6c). The measurements of the spatial dimension corroborated the presence of the fractal structure on the newly oxidized surface in the used range of measurement scales. In spite of the short interval of time that had elapsed since the moment the sample was treated in an ammonium hygroxide etchant (20 min), the surface morphology is identical to that for the surface of a starting sample. It follows from this fact that the structure of the intrinsic-oxide surface for

n-GaAs is almost completely formed during the first 10 min of exposure to air.

In the case of thermal oxidation of the free surface in air, the intrinsic-oxide film grows with retained fractal structure. An increase in the As diffusivity on the surface with temperature causes a primary nucleus to be formed on the *n*-GaAs surface with the participation of a larger number of As atoms. This fact results in increasing thickness of the intrinsic-oxide film.

On the basis of the experimental data obtained and also on the results of previous studies [12, 20, 21], we may conclude that the nanostructure of clusters is formed in the course of the chemical reaction of oxidation

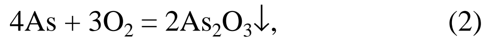

$$4As + 3O_2 = 2As_2O_3\downarrow, \quad (2)$$

the substitution reaction [12]

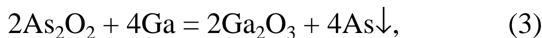

$$2As_2O_2 + 4Ga = 2Ga_2O_3 + 4As\downarrow, \quad (3)$$

and also, as follows from above, the diffusion of As and Ga atoms. Let us consider the flows of matter arising as a result of reactions (2) and (3), and also due to the diffusion through an area of the cluster surface; we denote the fluxes of As_2O_3, Ga_2O_3, As, and Ga as Q_1, Q_2, Q_3, and Q_4, respectively. In this case, the oxidized As and Ga atoms are assumed to have zero mobility.

Since the As oxidation proceeds at a higher rate than the substitution reaction, $Q_1 > Q_2$ in the general case, and the As-diffusion rate exceeds the Ga-diffusion rate, $Q_3 > Q_4$. It is also known that the substitution reaction proceeds after the oxidation reaction.

We consider two cases.

Since the source for the flux Q_1 is As from the Q_3 flux, $Q_3 = 2Q_1$ according to the stoichiometric coefficients in the first case we consider. This means that all the As atoms assembled in a cluster have time to be oxidized. The chemical potential is lower on the arsenic-oxide surface; as a result, As is oxidized more efficiently at the intrinsic-oxide nuclei, which favors their growth. The similarity elements of the first, second, and third levels are formed as the oxidation proceeds. In this case, the formation of the cluster structure correlates with the shape of the oxidation-reaction front, which depends on the As diffusion fluxes over the surface of the similarity element of the previous level. As was indicated above, a specific number of nucleation centers on the similarity-element surface can depend both on energy properties of the surface and on the features of the As diffusion as well as on the configuration of the surface itself. Then, according to [12, 20], Ga atoms from the excess layer diffuse to the above-lying layer as a result of the formed concentration gradient, participate there in the substitution reaction with arsenic oxide, and complete the formation of the similarity elements of the first, second, and third levels. It is most probable that the Ga diffusion is more efficient over the surface of grains than through their bulk; therefore, the substitution of As in clusters can proceed in the reverse sequence beginning from the third level of similar elements and, thus, follow the oxide structure. As a result of this, a Ga-enriched layer is replaced by the As-enriched layer and arsenic oxide is replaced by gallium oxide. In this case, the amorphous layer of excess As below the clusters is formed under the effect of the substitution reaction.

The second case corresponds to $Q_3 > 2Q_1$. Here, As atoms are not oxidized at once when approaching a cluster and can move for a time over its surface filling the space between the oxidized atoms. As a result, the original arsenic-oxide nucleus occurs to be more dense than in the first case. The formation of the cluster structure sets in under the effect of substitution of As atoms for Ga ones (3), which depends on the Ga-atom diffusion from the excess layer. In this case, a specific number of nucleation centers on the similarity-element surface can also depend both on energy properties of the film surface itself and on Ga-diffusion features and the configuration of the surface. The As atoms released as a result of reaction (3) can be again oxidized and, thus, form the similarity elements of the next level. Since As atoms are released only at the sites where Ga arrived instead of in a uniform way over the entire surface, the cluster-structure formation follows the shape of the Ga-diffusion front.

As a result, it can be seen that the mechanism of the cluster-structure formation is governed by the ratio between the fluxes Q_1 and Q_2 of matter.

The chemical composition of intrinsic-oxide structure formed in such a way can be represented as follows. The densest layer composed of Ga_2O_3 is formed predominantly from the similarity elements of the first, second, and third levels. Below this layer, the As-enriched layer is arranged on the interface between GaAs and Ga_2O_3. Thus, it can be seen that the oxide-film chemical composition obtained according to the model proposed is consistent with existing concepts [20, 21].

5. CONCLUSIONS

Using STM, the intrinsic-oxide film formed on epitaxial *n*-GaAs(100) and obtained by the natural oxidation in air under normal conditions is shown to be formed by tightly joining nanoclusters composed of the Ga and As oxides and the As excess layer at the interface between Ga_2O_3 and *n*-GaAs. It is possible to recognize three levels of self-similar elements on the surface of the cluster. According to the data obtained, the linear sizes of grains of the first, second, and third level meet the ratio 9 : 3 : 1, respectively. Thus, a grain can involve approximately six finer grains in the 3D case. The cluster-structure formation was shown to depend on As_2O_3 and As fluxes through the cluster-surface area. In this case, characteristic elements of every level are formed with the participation of two types of chemical reactions (oxidation and substitution). Two possible cases of the formation of a self-affine structure of clusters were considered. In the first case, when the

As_2O_3 and As fluxes are identical, the cluster-structure formation is governed by the As diffusion over the cluster surface. In the second case, when the As flux exceeds the As_2O_3 flux, the cluster-structure formation is governed by Ga diffusion over the cluster surface. The cluster growth under normal conditions and, consequently, an increase in the oxide-film thickness ceases when the clusters are tightly joined because this hampers the diffusion of reactants through the oxide film and the process of chemical reactions.

REFERENCES

1. M. P. Sinha and S. Mahapatra, Microelectron. J. **18** (2), 48 (1987).
2. N. A. Torkhov and V. G. Bozhkov, Poverkhnost **8**, 100 (2001).
3. A. V. Panin and N. A. Torkhov, Fiz. Tekh. Poluprovodn. (St. Petersburg) **34**, 698 (2000) [Semiconductors **34**, 671 (2000)].
4. A. V. Panin, A. P. Shugurov, and A. N. Puchkareva, Fiz. Mezomekh. **3** (3), 53 (2000).
5. L. M. Weegels, T. Saitoh, and H. Kanbe, Appl. Phys. Lett. **66**, 2870 (1995).
6. M. Somogyi, Cryst. Res. Technol. **17**, 1129 (1982).
7. P. Alnot, F. Wyczisk, and A. Friederich, Surf. Sci. **162**, 708 (1985).
8. R. P. H. Chang and S. Darack, Appl. Phys. Lett. **38**, 898 (1981).
9. A. Kishimoto, I. Suemune, K. Hamaoka, *et al.*, Jpn. J. Appl. Phys. **29**, 2273 (1990).
10. T. Kimura and C. Yamada, Jpn. J. Appl. Phys. **34**, 1498 (1995).
11. N. Watanabe, T. Nittono, H. Ito, *et al.*, J. Appl. Phys. **73**, 8146 (1993).
12. C. D. Thurmond, G. P. Schwartz, G. W. Kammlott, and B. Schwartz, Solid State Sci. Technol. **127**, 1366 (1980).
13. M. Alonso and F. Soria, Surf. Sci. **182**, 530 (1987).
14. F. Bartels and W. Mönch, Solid State Commun. **57**, 571 (1986).
15. B. R. Singh, O. P. Daga, M. K. Sharma, and W. S. Kholke, Int. J. Electron. **52**, 3 (1982).
16. I. Ya. Mittova, S. S. Lavrushina, V. R. Pshestanchik, and O. Yu. Novikova, Neorg. Mater. **12**, 1448 (1997).
17. K. Watanabe, M. Hashiba, Y. Hirohata, *et al.*, Thin Solid Films **56**, 63 (1979).
18. V. A. Kagadei, D. I. Proskurovskiĭ, and L. M. Romas’, Mikroélektronika **27** (3), 200 (1998).
19. N. A. Torkhov, in *Proceedings of III International Conference on Radiation–Thermal Effects and Processes in Inorganic Materials* (Tomsk, 2002), p. 301.
20. V. L. Berkovits, A. B. Gordeeva, and V. A. Kosobukin, Fiz. Tverd. Tela (St. Petersburg) **43**, 985 (2001) [Phys. Solid State **43**, 1018 (2001)].
21. I. Gerard, C. Debiemme-Chouvy, J. Vigneron, *et al.*, Surf. Sci. **433–435**, 131 (1999).
22. J. Feder, *Fractals* (Plenum, New York, 1988; Mir, Moscow, 1991).
23. M. Strome Mattsson, G. A. Niklasson, and C. G. Granqvist, Phys. Rev. B **54**, 17884 (1996).
24. P. A. Artyunov and A. L. Tolstikhina, Mikroélektronika **26**, 426 (1997).

Translated by V. Bukhanov

Semiconductors, Vol. 37, No. 10, 2003, pp. 1185–1189. Translated from Fizika i Tekhnika Poluprovodnikov, Vol. 37, No. 10, 2003, pp. 1214–1219.
Original Russian Text Copyright © 2003 by Moiseev, Mikhaĭlova, Yakovlev, Oswald, Hulicius, Pangrac, Šimeček.

SEMICONDUCTORS STRUCTURES, INTERFACES, AND SURFACES

Electroluminescence in a Semimetal Channel at a Single Type II Broken-Gap Heterointerface

K. D. Moiseev*, M. P. Mikhaĭlova*, Yu. P. Yakovlev*, I. Oswald, E. Hulicius**, J. Pangrac**, and T. Šimeček****

**Ioffe Physicotechnical Institute, Russian Academy of Sciences, Politekhnicheskaya ul. 26, St. Petersburg, 194021 Russia*
e-mail: mkd@iropt2.ioffe.rssi.ru

***Institute of Physics, Academy of Sciences of the Czech Republic, 16253 Prague 6, Czech Republic*

Submitted March 13, 2003; accepted for publication March 18, 2003

Abstract—The radiative recombination at the broken-gap *p*-GaInAsSb/*p*-InAs type-II interface is investigated in the temperature range of 4–100 K. It is shown that the electroluminescence band $h\nu_A = 0.37$ eV can be attributed to a large extent to the recombination of electrons from the semimetal channel at the interface with the participation of a deep acceptor level at the interface. At the same time, the band $h\nu_B = 0.40$ eV corresponds to radiative transitions in the InAs bulk to a shallow acceptor level. The participation of the interface states in the recombination across the GaInAsSb/InAs type-II interface becomes appreciable due to the overlapping of wave functions of holes, which are localized at the interface on the solid-solution side, with the wave functions of deep acceptor states. *© 2003 MAIK "Nauka/Interperiodica".*

1. INTRODUCTION

In recent years, increased interest in semiconductor lasers operating in the mid-IR-wavelength range of 3–5 μm has arisen due to the fact that this spectral range is important for application in systems of gas analysis and ecological monitoring as well as solving the problems in high-resolution laser spectroscopy [1, 2]. GaInAsSb quaternary solid solutions, which form type-II heterojunctions with InAs, are promising materials for the development of efficient optoelectronic devices that emit in this spectral range. The specific features of the energy-band diagram of the broken-gap GaInAsSb/InAs type-II heterojunctions make it possible to control the emission wavelength of a device based on this heterostructure. This is achieved by varying the energy gap and overlapping of the energy bands at the heterointerface. In the broken-gap GaInAsSb/InAs type-II heterojunction, the spatially separated electrons and holes are localized in the self-consistent quantum wells (QWs) on both sides of the interface. This phenomenon is caused by the electron flow from the valence band of the solid solution into the conduction band of InAs [3]. A semimetal channel is formed in such a system at the heterointerface due to the internal electric field, which arises due to the interfacial charges [4].

Recently, we observed and investigated the interface electroluminescence (EL) in the single isotype *p*-$Ga_{0.84}In_{0.16}As_{0.22}Sb_{0.78}$/*p*-InAs type-II heterojunction with a broken gap [5, 6]. The EL spectra at $T = 77$ K included two emission bands with photon energies of 0.311 and 0.378 eV at the reverse external bias applied to the sample. By reverse bias is meant that when the positive potential is applied to the wide-gap GaInAsSb layer while the negative potential is applied to the narrow-gap *p*-InAs. The third high-energy band, with the highest photon energy of 0.633 eV, emerged only at a strong injection level [5]. Upon application of the forward bias to the structure, the EL spectra contained only two emission bands, namely, at 0.384 and 0.408 eV. The dynamics of variations in the spectrum shape with the temperature in the range of 4–100 K for the case of reverse bias was studied by Bazhenov *et al.* [6]. With a more careful consideration, it turned out that, at low temperatures $T < 15$ K, the emission band at 0.384 eV consisted of two peaks, namely, $h\nu_A = 0.372$ eV and $h\nu_B = 0.400$ eV. It was also shown that for the *p*–*p* heterostructure considered, the EL is caused by the indirect (tunneling) radiative electron–hole recombination across the GaInAsSb/InAs interface. These electrons and holes are localized in the self-consistent QWs on both sides of the interface.

It should be noted that the structures considered were obtained on the basis of heavily doped layers of the GaInAsSb quaternary solid solution with a hole density of $p > 10^{18}$ cm^{-3}. It was shown that the transport properties of the isotype *p*-type heterostructure depend strongly on the degree of doping of the solid solution with the acceptor impurity [7]. Starting from a certain amount of Zn introduced into the solution-melt, the *n*-type conduction abruptly changes to *p*-type; i.e., depletion of the electron channel at the interface sets in. This can be explained by the fact that the Fermi level in the valence band of the degenerate solid solution is located lower in energy than the top of the conduction band of InAs. In this case, the transition from interface semimetal conduction to bulk semiconductor conduction

1063-7826/03/3710-1185$24.00 © 2003 MAIK "Nauka/Interperiodica"

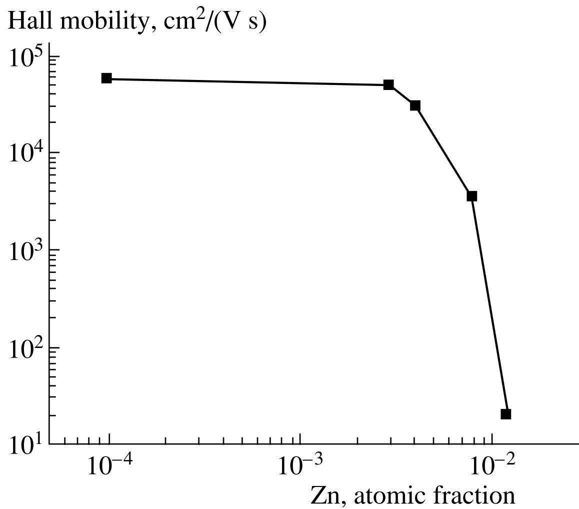

Fig. 1. Hall mobility at T = 77 K for the p-$Ga_{0.84}In_{0.16}As_{0.22}Sb_{0.78}$:Zn/$p$-InAs heterostructure at T = 77 K as a function of the amount of the Zn acceptor impurity introduced into the solution.

occurs in the broken-gap p-GaInAsSb/p-InAs heterojunction. Until this transition occurs, the major part of the conduction of the heterostructure under investigation will be governed by the semimetal (electron–hole) channel at the heterointerface.

In the case of the GaInAsSb heavily doped layer, the main drop in the external bias and, consequently, the main band bending at the heterointerface occur on the narrow-gap InAs side. The electron QW is populated by the carriers injected. At the same time, the effective potential barrier for electrons on the solid solution side decreases. This circumstance manifests itself experimentally in the form of the short-wave length (0.633 eV) band due to the recombination of the Auger electrons from the channel with the holes in the solid-solution bulk.

The aim of this study was to gain insight into electroluminescence at low temperatures in a single isotype broken-gap p-GaInAsSb/p-InAs heterostructure with lightly doped solid-solution layers in the presence of a semimetallic channel with high electron mobility at the heterointerface.

2. EXPERIMENTAL

Isolated isotype p-$Ga_{0.84}In_{0.16}As_{0.22}Sb_{0.78}$/$p$-InAs heterostructures were fabricated by liquid-phase epitaxy by growing the GaInAsSb quaternary solid solution layer on the InAs(100) substrate. The heterostructures were lattice-matched and free of strains due to the fulfillment of thermodynamic conditions of the growth from the solution–melt which was in equilibrium with the substrate. The high quality of heterostructures was confirmed by preliminary investigations using X-ray structural analysis and transmission electron microscopy [8]. The energy-band diagram of such a heterostructure comprises the broken-gap type-II heterojunction with the band offset at the heterointerface of about 60 meV [5]. The technology for preparing the samples under investigation and the measurement technique of their magnetotransport properties were described previously [9, 10].

In this study, we used p-InAs:Zn substrates (E_g = 0.417 eV at T = 4 K [11]) with a carrier density of $p = 5 \times 10^{16}$ cm^{-3} at T = 300 K. These substrates were weakly conductive at a temperature below 80 K. The layers of the GaInAsSb wide-gap solid solution (E_g = 0.644 eV at T = 7 K [12]) were of p-type conductivity, and the hole density did not exceed $p \approx 8 \times 10^{16}$ cm^{-3} at T = 77 K. The Hall electron mobility in such structures was high, specifically, $(3.5–5) \times 10^4$ $cm^2/(V s)$.

The p-$Ga_{0.84}In_{0.16}As_{0.22}Sb_{0.78}$/$p$-InAs isolated heterostructures for the EL measurements comprised the mesa diodes, which were prepared by the conventional technique of postgrowth treatment using the procedure of photolithography-mask deposition and selective chemical etching. The profiles of the round mesa structure with a diameter on the layer side of 400 μm and a height of 2 μm were obtained using a CrO_3 + HCl water solution. The diameter of the point contact to the mesa center was no larger than 50 μm. The metal contact to the upper mesa part was prepared by deposition of a thin Au layer (200 nm), which was fused in at T = 350°C in the flow of purified hydrogen. Square chips of 800 × 800 μm in size were cleaved from the epitaxial structure.

The EL measurements were carried out applying the forward and reverse biases in the quasi-steady mode, as well as in the pulse mode with a pulse width no larger than 1 ms in the temperature range of 4–100 K. The output emission was analyzed using an SDL-1 double-grating monochromator and recorded with a PbS cooled photoresistor using a standard mode of synchronous detection.

3. RESULTS AND DISCUSSION

As mentioned above, on doping of the GaInAsSb solid solution with the acceptor Zn impurity, the semimetal channel at the single heterointerface exists only in a limited range of concentrations [7]. Figure 1 shows the dependence of the Hall mobility on the amount of atomic Zn introduced into the solution–melt. It is clearly seen that, up to ~0.01 at. %, the mobility remains constant and rather high. The electron channel width, which was estimated at the Fermi level, was about 30–40 nm. This is a rather wide QW, which, however, contains several electron subbands arranged close to each other. The two-dimensional nature of this phenomenon was recently confirmed by the observation of the Hall effect in the p-GaInAsSb/p-InAs structures based on undoped quaternary solid solutions [13].

The addition of a small amount of Sn or Ge instead of Zn to the solution–melt does not substantially affect the character of the semimetal channel at the heterointerface. This circumstance is caused by the specific features of the atomic structure of Sn and Ge (Group IV), which manifest themselves on doping of solid solutions in the GaSb–InAs system (Groups III and V) by these elements [12]. A high value and the electron character of the Hall mobility is retained for all structures investigated in this study (see table). We may assume that a strongly charged plane, which is positioned perpendicularly to the direction of the current through the sample while measuring the EL spectra, exists in these heterostructures. This assumption explains the fact that the most efficient emission is achieved on applying long pulses, right up to the continuous mode.

Figure 2 shows the EL spectra for two polarities of the bias voltage applied at temperatures of 10 and 50 K. The spectra contain only two emission bands with photon energies of $h\nu_A = 0.372$ eV and $h\nu_B = 0.400$ eV. The shape of the peaks is similar, and their spectral positions are close to each other both for the forward and for the reverse biases. However, several substantial distinctions exist between the peaks.

It should be noted that at low temperatures ($T < 50$ K), redistribution of the intensity of the EL peaks was observed, depending on the polarity of the bias applied. For the forward bias, when the negative potential is applied to the wide-gap layer of the solid solution, and the positive potential is applied to InAs, the intensity of the high-energy emission band $h\nu_B$ is higher than that of the low-energy band $h\nu_A$ by a factor of 20 at $T = 10$ K and by a factor of 12 at $T = 50$ K. For the reverse bias, the intensity of the $h\nu_B$ band decreases, whereas the intensity of the $h\nu_A$ band, in contrast to this, increases. The ratio of these intensities decreases to $I(h\nu_B)/I(h\nu_A) = 8$ ($T = 10$ K) and 6 ($T = 50$ K) compared with the spectrum for the forward bias.

In addition, the asymmetry of the $h\nu_B$ peak depends on the polarity of the voltage applied. For the forward bias, an abrupt falloff of intensity was observed on the low-energy side, whereas the energy distribution on the high photon-energy side falls off more gradually and can be described by the exponential law. For the reverse bias, on the contrary, an abrupt high-energy edge and highly extended "tail" of the EL intensity distribution on the low photon-energy side right up to the $h\nu_A$ band were observed.

The difference in the shape of the $h\nu_B$ peaks can be associated with various mechanisms of radiative transitions depending on the polarity of the bias applied. For the forward bias, the slightly extended high-energy edge of the EL spectrum can be caused by the contribution of electrons from the conduction band of InAs, which follow the Maxwell distribution law ($\propto \exp(-\varepsilon/kT)$). The opposite pattern is observed for the reverse bias. As it was mentioned above, the self-consistent QW is fairly wide at the Fermi level, which admits the possibile

Hall mobility in a weak magnetic field ($B < 2$ T) at $T = 77$ K

Sample	Impurity (at. %)	μ_H, cm^2/(V s)
MK-531/2	Zn (0.015)	48800
MK-531/3	Sn (0.046)	42400
MK-531/4	Ge (0.0025)	35000
MK-535/3	Sn (0.1)	11700

existence of several electronic levels, which are close to each other. Consequently, the low-energy edge of the $h\nu_B$ band can consist of several close (in energy) radiative electron transitions from the levels in the semimetal channel at the heterointerface, which are positioned below the Fermi level in the QW. An increase in the temperature from 10 to 50 K leads to broadening of the $h\nu_B$ peak and a shift of the emission band peak to higher photon energies. It should be also noted that the intensity of the $h\nu_B$ peak depends more strongly on the temperature for the reverse bias than for the forward bias. The difference in the spectral position of the $h\nu_B$ peak for the forward and reverse biases at $T = 10$ K can correspond to the activation energy of the donor in InAs (E_D = 2meV). This is in good agreement with the published data [11]. In contrast to the $h\nu_B$ peak, the spectral position of the $h\nu_A$ peak is independent of temperature

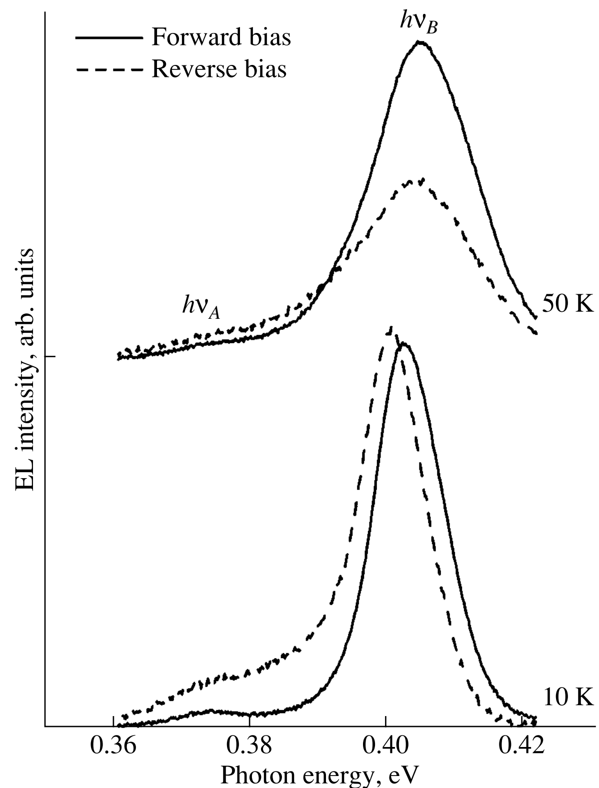

Fig. 2. Electroluminescence spectra for two directions of the current through the sample $i = 1$ A at temperatures of 10 and 50 K. The sample MK-531/3.

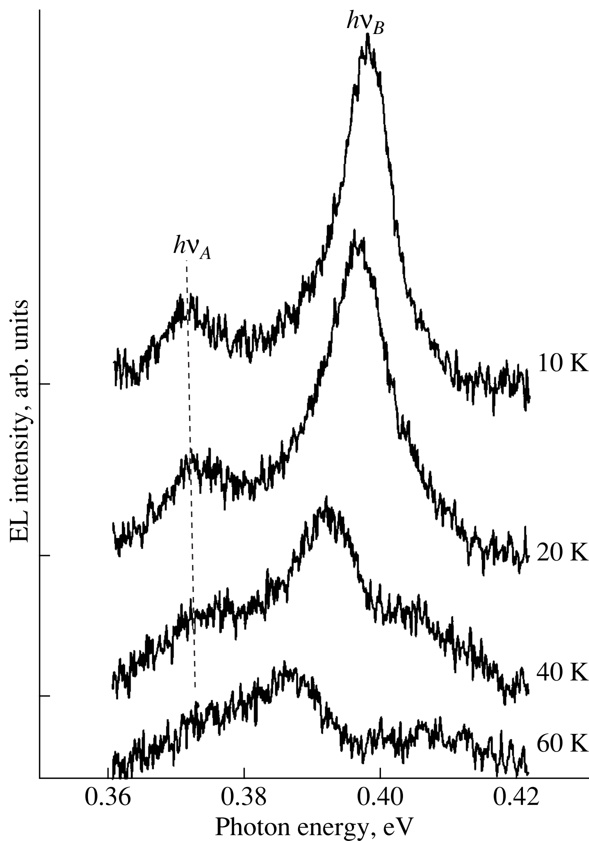

Fig. 3. Electroluminescence spectra at $T = 10–60$ K and the forward bias for the current $i = 25$ Å in a constant mode. Sample MK-531/3.

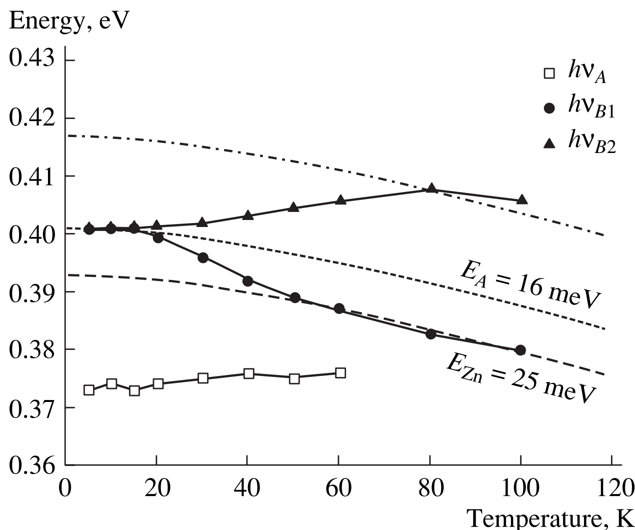

Fig. 4. Temperature dependences of the position of the electroluminescence peaks for the *p*-GaInAsSb/*p*-InAs heterostructure at $i = 25$ mA. The calculated curves for the band-gap width of InAs (dash-and-dot line), for transitions with the participation of the electron–hole pair (dotted line), and for transitions to the Zn impurity level in InAs (dashed line) are presented. Sample MK-531/3.

in the range of 10–50 K both for the forward and for the reverse external biases.

Typical EL spectra in the temperature range of 10–60 K are shown in Fig. 3. With increasing temperature, the intensity of the $h\nu_A$ band initially increases slowly, attains a maximum at $T = 30$ K, and then decreases. At 60 K, the $h\nu_A$ band manifests itself only as a long-wavelength shoulder of the $h\nu_B$ band. With increasing temperature, the peak broadens and its maximum shifts to higher photon energies. Starting from $T > 40$ K, the $h\nu_B$ band splits into two clearly pronounced emission bands $h\nu_{B1}$ and $h\nu_{B2}$. The approximation of the bands with the Gaussian distribution of intensities permits us to estimate the spectral position of the peaks of these bands as $h\nu_{B1} = 0.383$ eV and $h\nu_{B2} = 0.410$ eV at $T = 80$ K. It is clearly seen that one of the bands ($h\nu_{B1}$) can be attributed to the band-to-acceptor transitions. The second band ($h\nu_{B2}$) can be attributed to the band-to-band transitions (Fig. 4). At low temperatures (up to 30 K), the $h\nu_B$ band corresponds to radiative transitions from the conduction band to a native acceptor level with an ionization energy of $E_A = 16$ meV. With increasing temperature ($T > 30$ K), the ionization of shallow levels in the conduction band occurs and the contribution of band-to-band transitions increases. The dash-and-dot line in Fig. 4 shows the temperature dependence of the band gap for InAs:

$$E_g[\text{eV}] = 0.417 - 2.5 \times 10^{-4} T^2/(T + 90).$$

At higher temperatures ($T > 60$ K), the transitions with the participation of the holes at the Zn impurity level in InAs ($E_{Zn} = 25$ meV) are distinct; these transitions were observed previously at $T = 77$ K [5].

We assume that, most likely, the radiative recombination occurs at the *p*-GaInAsSb/*p*-InAs interface. However, the $h\nu_A$ and $h\nu_B$ peaks are of different nature. It is possible to assume that both peaks correspond to the transitions to the acceptor levels in InAs. However, the $h\nu_A$ band can be attributed to a larger extent to the recombination of electrons from the semimetal channel at the heterointerface with the participation of the deep surface level at the interface. In contrast, the $h\nu_B$ band corresponds to radiative transitions to a shallow acceptor level in the InAs bulk. The nature of the deep acceptor level ($E_{DA} = 45$ meV) is not completely understood at present [14, 15]. It is possible that this level is related to the interface states at the InAs surface. In this case, its participation in the recombination across the GaInAsSb/InAs type-II interface becomes significant due to overlap of the wave functions of holes, which are localized on the solid solution side of the interface, with the wave functions of the states at the deep acceptor.

It was noted that the electron QW on the InAs side has a complicated profile and can consist of two parts [6]. At the interface, a high gradient of the electric field and a rather abrupt bending of the conduction band occur. In this case, the well is virtually rectangular,

whereas, when away from the heterointerface, its shape is described well by the Poisson distribution.

Our model involves the energy-band diagram of the single broken-gap *p*-GaInAsSb/*p*-InAs type-II junction, which is based on lightly doped layers of the quaternary solid solution. In the context of this model, the absence of the bias dependence of the spectral position of the EL bands can be explained by the fact that the electron QW occurs at the *p*–*p* interface. The shape of this QW is practically independent of the polarity of the external bias. This circumstance is caused by the existence of the internal electric field in the sample, which forms the semimetal channel at the broken-gap *p*-GaInAsSb/*p*-InAs interface and keeps the spatially separated electrons and holes on different sides of the interface. This internal field considerably exceeds the external field, which is applied to the sample in the course of the experiment. On application of the external bias, the QW at the heterointerface acts as the electron source, which leads to the emergence of the $h\nu_B$ band. We assume that the $h\nu_A$ band is caused by tunneling of holes across the heterointerface to deep acceptor states in the InAs band gap and their subsequent recombination with the electrons localized in the QW on the InAs side. The existence of a wide, strongly charged interfacial layer ($d \approx 40$ nm) leads to trapping of the carriers at the interface. However, the existence of the QWs for the carriers provides strong overlapping of spatially separated holes and electrons and is favorable for increasing the interfacial radiative recombination. It is rather difficult to overcome the internal field for this structure because of sample heating due to the Joule heat, which manifests itself at high injection levels. The tunnel character of the current flowing across the heterointerface was also noted previously [6].

4. CONCLUSION

Thus, the semimetal channel with a high mobility of charge carriers exists at the broken-gap *p*-GaInAsSb/*p*-InAs type-II heterojunction. This gives rise to radiative transitions in the semiconductor between the states, which are located on the side of localization of electrons. It should also be noted that the semimetal conduction of the channel shunts one of the heterojunction sides, which adversely affects the radiative recombination. The intensity of the EL associated with the transitions between the states localized at the interface is more temperature-dependent than the EL associated with the electron transitions in the bulk. The conduction type at the heterointerface changes from that of a semimetal to that of a semiconductor. With retention of the carriers localized in the self-consistent QWs, this provides an abrupt increase in the interfacial EL and opens the way to the development of IR emitters operating at temperatures close to 293 K.

ACKNOWLEDGMENTS

This study was supported by the Russian Foundation for Basic Research (project no. 02-02-17633) and the European Union (grant no. IST-2001-35178 GLADIS).

REFERENCES

1. A. I. Nadezhdinski and A. M. Prokhorov, Proc. SPIE **1724**, 2 (1992).
2. A. N. Imenkov, N. M. Kolchanova, P. Kubat, *et al.*, Fiz. Tekh. Poluprovodn. (St. Petersburg) **35**, 375 (2001) [Semiconductors **35**, 360 (2001)].
3. M. P. Mikhaĭlova and A. N. Titkov, Semicond. Sci. Technol. **9**, 1279 (1994).
4. T. I. Voronina, T. S. Lagunova, M. P. Mikhaĭlova, *et al.*, Fiz. Tekh. Poluprovodn. (St. Petersburg) **30**, 985 (1996) [Semiconductors **30**, 523 (1996)].
5. M. P. Mikhaĭlova, K. D. Moiseev, G. G. Zegrya, and Yu. P. Yakovlev, Solid-State Electron. **40**, 673 (1996).
6. N. L. Bazhenov, G. G. Zegrya, V. I. Ivanov-Omskiĭ, *et al.*, Fiz. Tekh. Poluprovodn. (St. Petersburg) **31**, 1216 (1997) [Semiconductors **31**, 1046 (1997)].
7. T. I. Voronina, T. S. Lagunova, M. P. Mikhaĭlova, *et al.*, Fiz. Tekh. Poluprovodn. (St. Petersburg) **32**, 215 (1998) [Semiconductors **32**, 195 (1998)].
8. K. D. Moiseev, A. A. Sitnikova, N. N. Faleev, and Yu. P. Yakovlev, Fiz. Tekh. Poluprovodn. (St. Petersburg) **34**, 1438 (2000) [Semiconductors **34**, 1381 (2000)].
9. T. I. Voronina, T. S. Lagunova, M. P. Mikhaĭlova, *et al.*, Superlattices Microstruct. **24**, 105 (1998).
10. N. L. Bazhenov, G. G. Zegrya, M. P. Mikhaĭlova, *et al.*, Fiz. Tekh. Poluprovodn. (St. Petersburg) **31**, 658 (1997) [Semiconductors **31**, 560 (1997)].
11. *Handbook Series on Semiconductor Parameters*, Ed. by M. Levinshtein, S. Rumyantsev, and M. Shur (World Sci., Singapore, 1996), Vol. 1.
12. K. D. Moiseev, M. P. Mikhaĭlova, Yu. P. Yakovlev, *et al.*, J. Appl. Phys. **90**, 2813 (2001).
13. K. D. Moiseev, V. A. Berezovets, M. P. Mikhaĭlova, *et al.*, Surf. Sci. **482–485**, 1083 (2001).
14. Y. Lacroix, C. A. Tran, S. P. Watkins, and M. L. W. Thewalt, J. Appl. Phys. **80**, 6416 (1996).
15. G. Bastard, E. E. Mendez, L. L. Chang, and L. Esaki, J. Vac. Sci. Technol. **21**, 531 (1982).

Translated by N. Korovin

Semiconductors, Vol. 37, No. 10, 2003, pp. 1190–1194. Translated from Fizika i Tekhnika Poluprovodnikov, Vol. 37, No. 10, 2003, pp. 1220–1224.
Original Russian Text Copyright © 2003 by Volodin, Efremov, Nikiforov, Orekhov, Pchelyakov, Ul'yanov.

LOW-DIMENSIONAL SYSTEMS

Resonance Raman Scattering in Ge Nanoislands Grown on a Si(111) Substrate Coated with an Ultrathin SiO_2 Layer

V. A. Volodin*, M. D. Efremov*, A. I. Nikiforov*, D. A. Orekhov, O. P. Pchelyakov*, and V. V. Ul'yanov***

**Institute of Semiconductor Physics, Siberian Division, Russian Academy of Sciences, pr. Akademika Lavrent'eva 13, Novosibirsk, 630090 Russia*

e-mail: volodin@isp.nsc.ru

***Novosibirsk State University, ul. Pirogova 2, Novosibirsk, 630090 Russia*

Submitted November 18, 2002; accepted for publication January 31, 2003

Abstract—Germanium nanoislands formed on a Si (111) surface coated with an ultrathin oxide layer were investigated by Raman spectroscopy. For analysis of the experimental data, the spectra of real islands containing some hundreds of Ge atoms were calculated numerically. The effects of the resonance enhancement of the intensity of Raman scattering in the Ge-nanoisland–SiO_2–Si system and the influence of the lateral sizes of nanoislands on the frequencies of phonons localized in them are discussed. © *2003 MAIK "Nauka/Interperiodica".*

The interest in the clusters of narrow-gap semiconductors in a wide-gap semiconductor matrix is caused by the possibility of forming (using the self-organization phenomenon) arrays of quantum dots with a quasi-atomic electronic spectrum [1]. New electronic and, primarily, optoelectronic properties of these objects stimulate investigations in this field. The possibility of using nanostructures based on the most widely spread microelectronics materials, Ge and Si, for fabrication of new optoelectronic devices is now studied. In this context, the formation of Ge islands in Si according to the Stranski–Krastanov mechanism (see [1] and references therein) and other relatively new approaches, such as formation of Ge clusters in submonolayer coatings [2], the control of island nucleation by introduction of various impurities [1], and the growth of Ge layers on ultrathin silicon oxide [3–5], have been widely investigated. Raman spectroscopy, being a rapid and nondestructive method, serves as an informative technique for studying semiconductor nanoobjects. Similar to the electron spectrum, the phonon spectrum is governed both by the nanoobject structure and by the properties of the surrounding material [6].

Four experimental samples were fabricated on the basis of a Si (111) substrate by molecular-beam epitaxy. At first, a buffer Si layer 40 nm thick was grown at 700°C. In the growth chamber, a SiO_2 layer of specified thickness (0.3 nm) was then grown at 420°C. Finally, Ge layers of an average thickness of 2, 4, 6, and 8 bilayers (samples 1, 2, 3, 4, respectively) were grown at the same temperature. One Ge bilayer contains 1.56×10^{15} atoms/cm^2, and its thickness is 3.27 Å. The Ge islands formed were coated with a Si layer 4 nm thick grown at 420°C. The Si surface was oxidized, and Ge was deposited on the oxidized surface again. For all the samples studied, this cycle was repeated five times; then, each sample was coated with a Si protective layer. The samples formed were investigated by Raman spectroscopy. The spectra were recorded at room temperature using an automated system based on a DFS-52 spectrometer (LOMO, St. Petersburg) with the use of the Ar-laser line at 514.5 nm (2.41 eV). The quasi-backscattering geometry was used; both the incident and scattered light were polarized in the (111) crystallographic plane. For analysis of the Raman data on the structural properties of Ge nanoislands, the eigenfrequencies and eigenvectors of oscillations in the Ge–Si heterostructures were calculated numerically in terms of the Born–von Karman approximation. On the basis of the results obtained, the Raman spectra were calculated within the Vol'kenshtein model for additive bond polarizability [7]. The calculations were carried out both for planar heterostructures (the one-dimensional (1D) model) and for Ge nanoislands surrounded by Si (the three-dimensional (2D) model).

Figure 1 shows the Raman spectra of samples 1–4 in the regions of oscillation frequencies for both Ge–Ge (~300 cm^{-1}) and Ge–Si (~400 cm^{-1}) bonds. For comparison, the spectrum of a Si (111) substrate recorded under the same conditions is also shown. In this spectrum, the features in the vicinity of 300 cm^{-1} can be seen, which are related to the two-phonon scattering by transverse acoustic (TA) phonons in Si. The difficulties in analyzing the Raman spectra of Ge quantum dots in

Si, caused by the presence of the peak from the substrate, were noted in [3, 8]. It was concluded in [8] that the use of photons with an energy of 2.4 eV is most preferable for observing the Raman peaks from Ge against the background of two-phonon scattering from a Si substrate. It can be seen from the experimental spectra that the Raman signal, even for sample 1 (with the smallest content of Ge), significantly exceeds the substrate signal. Nevertheless, in order to analyze the intensities and positions of the experimental peaks, we subtracted the substrate signal from the peak signals. The most intense peak in the spectra corresponds to the Raman scattering in the first-order localized mode; the low-energy wing is related to the scattering in higher order modes. It can be seen from Fig. 1 that the position of the Raman peak due to the Ge–Ge bonds is almost independent of the average thickness of Ge in the samples and amounts to 301.5–302 cm^{-1} for samples 1–3 and 301 cm^{-1} for sample 4. For all the samples, the peaks due to the Raman scattering by the oscillations of Ge–Si bonds hardly manifest themselves at all. The intensity of the Raman peaks from Ge–Ge bonds considerably and disproportionately increases with the increasing average thickness of Ge.

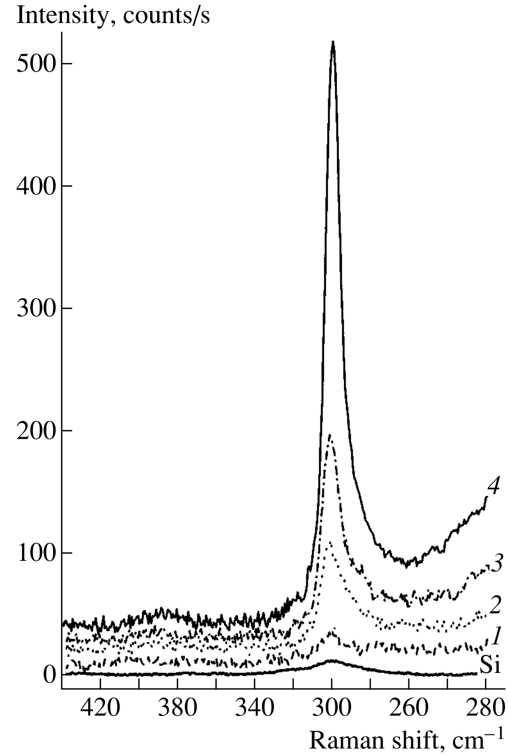

Fig. 1. Raman spectra of the samples with Ge nanoislands (*1–4*) and of the Si substrate (bold solid line). The numbers of curves correspond to the numbers of samples containing (*1*) two, (*2*) four, (*3*) six, and (*4*) eight Ge bilayers.

The Raman peak intensity normalized to the Ge amount is shown in Fig. 2 as a function of the average thickness of Ge. It can be seen that the normalized intensity changes by more than an order of magnitude in the sample with eight Ge bilayers in comparison with the sample containing two Ge bilayers. Such an increase may be caused only by the resonance Raman effects. Indeed, in the photoluminescence (PL) spectra of Ge nanoislands grown on thin SiO_2 layers, a peak at 2.4 eV is observed, which, apparently, is due to the presence of electronic states in the ultrathin GeO_2 layer between Ge and Si [3]. The Raman cross section is calculated by summation over all possible intermediate (virtual) states. The creation or absorption of a phonon by a virtual electron–hole pair occurs due to the electron–phonon interaction between an electron and a hole [9]. The differential scattering cross section is determined from the expression

$$\frac{d^2\sigma}{d\Omega d\omega} = \left(\frac{\omega_2}{c}\right)^4 \frac{\omega_2}{\omega_1} V^2$$
$$\times \sum_{i,f} P(E_i)\delta\left(\frac{E_i - E_f}{\hbar} - \omega\right) \left|\hat{e}^2_\mu \langle f|\delta\chi_{\mu\nu}|\hat{e}^1_\nu\rangle\right|^2,$$

where ω_1 and ω_2 are the frequencies of incident and scattered light, respectively; $\omega = \omega_1 - \omega_2$ is the frequency of scattering excitation; V is the scattering volume; E_i and E_f are the initial and final energies of a crystal, respectively; $P(E_i)$ is the probability of existence of a crystal in the corresponding initial state with respect to the phonon occupation numbers; and $\mathbf{e}^1$ and $\mathbf{e}^2$ are the unit polarization vectors for incident and scattered photons. The probability of the $|\langle f|\delta\chi_{\mu\nu}|i\rangle$ transition is determined by summation over all possible virtual states. The contribution of the resonance (the first term)

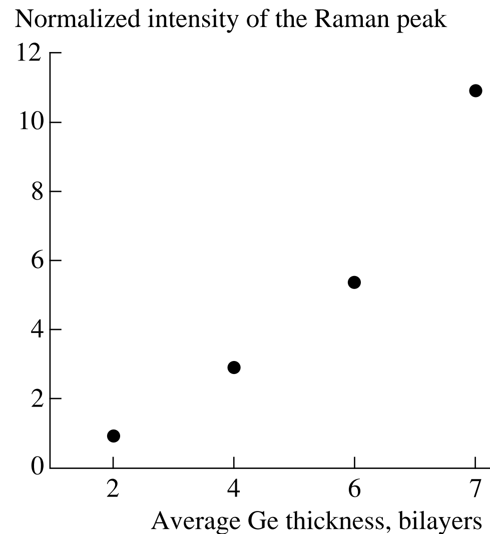

Fig. 2. Intensity of the Raman peak from oscillations of the Ge–Ge bonds, normalized to the amount of Ge, as a function of the average thickness of Ge.

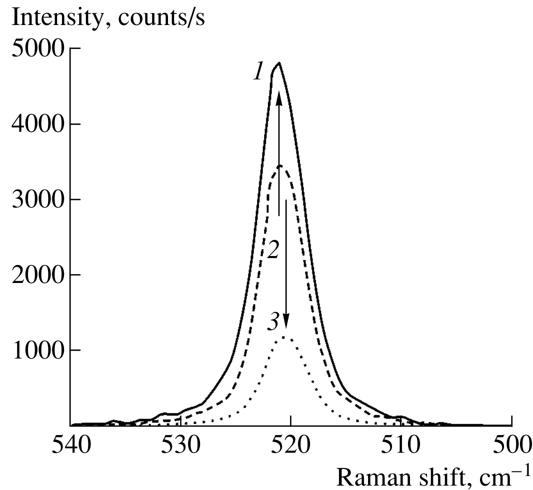

Fig. 3. Raman spectra of samples (*2*) 1 and (*3*) 4 with Ge nanoislands and of (*1*) the Si substrate in the frequency region corresponding to oscillations of the Si–Si bonds. The number of Ge bilayers is (*2*) two and (*3*) eight.

and nonresonant (the second term) components can be written as [9]

$$\left(\frac{e^2}{m^2\omega_2^2 V}\right)\left\{\sum_b \frac{\langle f|p_\mu(k_2)|b\rangle\langle b|p_\nu(-k_1)|i\rangle}{E_b - E_i - \hbar\omega_1} + \frac{\langle f|p_\nu(-k_1)|b\rangle\langle b|p_\mu(k_2)|i\rangle}{E_b - E_i + \hbar\omega_2}\right\},$$

where E_b is the energy of the intermediate (virtual) state of the crystal and k_1 and k_2 are the wave vectors of the absorbed and emitted photons, respectively. Expanding the matrix elements (up to the first order) that appear in the numerator of the resonance term in the shift of ions within the perturbation theory, we obtain the following expression for the probability of resonance scattering ([10]):

$$I_{\mathrm{res}} \propto \left\{\sum_{b,i} M_{b0} \times M_{i0}\left[\frac{\langle n_0 + 1|R_\zeta|n_0\rangle\langle b|H_{ev}|i\rangle}{(E_b - E_i - \hbar\omega_1)(E_b - E_i - \hbar\omega_2)}\right]\right\},$$

where H_{ev} is the Hamiltonian of the electron–phonon interaction, n_0 is the phonon occupation number, R_ζ are the generalized shifts of atoms (the phonon wave function), and M_{b0} and M_{i0} are the matrix elements of the dipole transitions in the crystal. If the energy of an absorbed (ω_1) or emitted (ω_2) photon coincides with the energy of a real electronic transition, an "input" or "output" resonance arises, respectively.

It is worth noting that a PL signal in the green spectral region was observed for similar structures in [11]. The spectral shape depended heavily on the excitation wavelength. For the structures we investigated, a PL peak was also observed at 2.4 eV upon excitation by a nitrogen laser (3.68 eV). Among the direct transitions in bulk Ge, the $L_1 - L_3'$ transition between light and heavy holes at point L of the Brillouin zone has an energy closest to this spectral region (2.1 eV) ([12, p. 38]). The energy of this transition may increase due to the quantum-confinement effect. The emission bands in the green spectral region were attributed in [11] to the transitions between the localized hole states in Ge quantum dots and the electronic states in a thin SiO_2 layer. The assumption that an actual, and, most probably, direct transition exists in the vicinity of 2.4 eV is also confirmed indirectly by the data of Fig. 3, which shows the intensity of the Raman signal from optical phonons in Si for samples 4 and 1 and for the Si substrate. We can see some decrease in the signal from sample 1 (with two Ge bilayers) and a fivefold decrease in the signal from sample 4 (with eight Ge bilayers). This phenomenon may be caused by strong absorption of both incident photons with an energy of 2.41 eV and photons with an energy of 2.34 eV, which are inelastically scattered by longitudinal optical (LO) and transverse optical (TO) phonons (in sample 4). Apparently, in the latter case, the light fails to reach the substrate and is almost completely absorbed in the heterostructure, whose thickness is only 32 nm. Since transitions in single-crystal Si are indirect, the absorption length of light having an energy of photons of 2.4 eV in single-crystal Si is about 700 nm [12]. Thus, the strong absorption in sample 4 may be related to the existence of direct transitions in the green spectral region. We should note that the absorption length in bulk Ge at the same wavelength is 17 nm [12] and the integrated thickness of Ge in sample 4 is as large as 12 nm. Therefore, quantitative analysis of the contribution of the centers arising at the Ge–SiO_2 interface to the integrated light absorption [3] is hindered. It can also be seen from Fig. 3 that the Raman peak from Si in the spectrum of sample 4 is shifted to lower frequencies, which is caused by the presence of tensile stresses. The average stresses in Si layers calculated using the values of the shift are about 1 kbar; the local stresses may be considerably higher.

As noted above, for analysis of the structure of Ge nanoislands from the experimental Raman spectra, we performed a numerical simulation of the spectra. The rigidity constants for the bonds in Ge were determined in terms of the Born–von Karman model by fitting the phonon dispersion calculated for the bulk material to the data obtained from the experiments with slow-neutron scattering [13]. Since the phonon dispersions for Ge and Si are very similar, the method of mass substitution was used to simulate the Ge–Si heterostructures. Some aspects of calculations were reported in [14, 15]. The ratio of the derivatives of the bond polarizability for Ge and Si was determined from the ratios of the Raman peak intensities for bulk Ge and Si, normalized to the scattering volume. The calculated spectra are shown in Fig. 4. For the planar heterostructure with two Ge bilayers, the calculated frequency of the fundamental localized mode of optical oscillations is equal to

289 cm^{-1}, whereas a peak at 302 cm^{-1} is observed experimentally. It is well known that compressive stresses may lead to an increase in the frequency of oscillations of the Ge–Ge bonds. For the localized LO phonons, the frequency shift may be as large as 17 cm^{-1} at a mismatch in the lattice constants of 4.2% in the system under consideration [16, 17]. According to estimates, the corresponding shift for the TO phonons is equal to 12 cm^{-1}. However, if the peak observed experimentally was due to the scattering by TO phonons in strained Ge two bilayers thick, the peaks due to the scattering by the oscillations of the Si–Ge bonds would also be present in the spectrum. In this case, half the Ge atoms are bound with Si, and, as calculations showed, the intensities of the Ge–Ge and Ge–Si peaks should be equal. The Raman peaks due to the oscillations of the Ge–Si bonds are not observed experimentally. Therefore, the fraction of the boundary Ge atoms is small; i.e., Ge nanoislands with an abrupt interface (without a transition layer of a solid solution) are formed and the mutual dissolution of Si and Ge in these structures is negligible. It should also be noted that, in the case of resonance Raman scattering, the symmetry selection rules may change, which may also affect the ratio of intensities of the Raman peaks due to the oscillations of the Ge–Ge and Ge–Si bonds. According to the data obtained by scanning electron microscopy [3], these islands are up to 2.5 nm in height and 5–7 nm in diameter [3–5, 11]. For islands of such thickness, the frequency shift for phonons localized in Ge is small and their frequency is close to that of phonons in the bulk material. Hence, we may suggest that the average stresses in the islands relax considerably and the local stresses manifest themselves in a high-frequency shoulder (310–315 cm^{-1}) on the experimental peaks (Fig. 1).

In order to determine the effect of limitation of the lateral sizes of islands, we calculated the phonon and Raman spectra of Ge islands surrounded by Si in terms of the 3D model. The presence of an ultrathin (about 3 Å) oxide layer at one of the island boundaries was disregarded. The calculations were carried out for triangular islands to take into account the symmetry of the (111) plane. Figure 4 shows the spectrum calculated for an island two bilayers high with a lateral size of 3.2 nm (in this case, the elementary cell includes 1200 Ge and Si atoms). It can be seen that the localization in the lateral direction for such a size leads to a shift of the fundamental localized mode to lower frequencies by 1.6 cm^{-1}. At larger lateral sizes of islands, this effect will be even less significant. We may suggest that the lateral sizes of real Ge nanoislands are, at least, larger than 3 nm, which is consistent with published data [3–5].

Thus, on the basis of the analysis of the Raman spectra, we may suggest that, even when a Ge coating is as thin as two bilayers, Ge nanoislands are formed on an oxidized Si (111) surface without a wetting layer. The average elastic stresses in the islands are considerably relaxed. The resonance enhancement of the Raman scattering intensity in the Ge-nanoisland–oxide–Si system is revealed and is apparently related to the presence of electronic states with an energy of the direct optical transition of about 2.4 eV in this system. In our opinion, this transition occurs between the localized hole states in Ge islands and electronic states at the interface between Ge and silicon oxide.

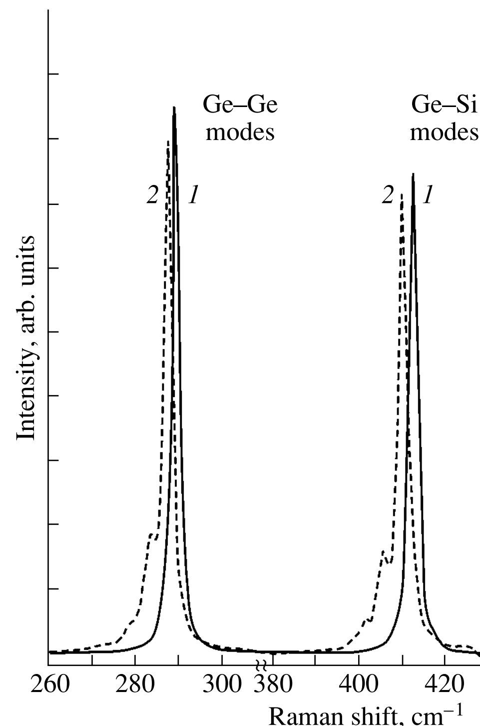

Fig. 4. Raman spectra calculated for (*1*) a plane layer and (*2*) a Ge nanoisland consisting of two bilayers.

ACKNOWLEDGMENTS

This study was supported by the Russian Foundation for Basic Research (project no. 00-02-18012) and by the Comission for Training of Young Scientists of the Russian Academy of Sciences (grant no. 60 of the 6th Competition of Young Scientists)

We thank V.A. Sachkov for his interest in the study and helpful comments. Volodin acknowledges the support of the Scientific Council of the Institute of Semiconductor Physics, Siberian Division, Russian Academy of Sciences, (award of the Grant for Young Scientists).

REFERENCES

1. O. P. Pchelyakov, Yu. B. Bolkhovityanov, A. V. Dvurechenskiĭ, *et al.*, Fiz. Tekh. Poluprovodn. (St. Petersburg) **34**, 1281 (2000) [Semiconductors **34**, 1229 (2000)].
2. N. D. Zakharov, G. E. Cirlin, P. Werner, *et al.*, in *Proceedings of 9th International Symposium on Nanostructures: Physics and Technology* (St. Petersburg, 2001), p. 21.

3. A. V. Kolobov, A. A. Shklyaev, H. Oyanagy, *et al.*, Appl. Phys. Lett. **78**, 2563 (2001).
4. A. A. Shklyaev, M. Shibata, and M. Ichikawa, Phys. Rev. B **62**, 1540 (2000).
5. A. A. Shklyaev, M. Shibata, and M. Ichikawa, J. Appl. Phys. **88**, 1397 (2000).
6. *Light Scattering in Solids*, No. 5: *Superlattices and Other Microstructures*, Ed. by M. Cardona and G. Güntherodt (Springer, Berlin, 1989).
7. M. Vol'kenshteĭn, Dokl. Akad. Nauk SSSR **32**, 185 (1941).
8. A. V. Kolobov, J. Appl. Phys. **87**, 2926 (2000).
9. *Light Scattering in Solids*, Ed. by M. Cardona (Springer, Berlin, 1975; Mir, Moscow, 1979), No. 1.
10. *Light Scattering in Solids*, No. 2: *Basic Concepts and Instrumentation*, Ed. by M. Cardona and G. Güntherodt (Springer, Berlin, 1975; Mir, Moscow, 1982).
11. A. A. Shklyaev and M. Ichikawa, Surf. Sci. **514** (1–3), 19 (2002).
12. V. I. Gavrilenko, A. M. Grekhov, D. V. Korbutyak, and V. G. Litovchenko, *Optical Properties of Semiconductors* (Naukova Dumka, Kiev, 1987).
13. G. Nelin and G. Nilsson, Phys. Rev. B **5**, 3151 (1972).
14. M. D. Efremov, V. A. Volodin, V. A. Sachkov, *et al.*, Pis'ma Zh. Éksp. Teor. Fiz. **70**, 73 (1999) [JETP Lett. **70**, 75 (1999)].
15. V. A. Sachkov, V. V. Bolotov, V. A. Volodin, and M. D. Efremov, Preprint No. 2000-01, ISME SO RAN (Inst. of Sensor Microelectronics, Siberian Division, Russian Academy of Sciences, Novosibirsk, 2000).
16. F. Cerdeira, C. J. Buchenauer, F. H. Pollak, and M. Cardona, Phys. Rev. B **5**, 580 (1972).
17. A. G. Milekhin, A. I. Nikiforov, O. P. Pchelyakov, *et al.*, Pis'ma Zh. Éksp. Teor. Fiz. **73**, 521 (2001) [JETP Lett. **73**, 461 (2001)].

Translated by Yu. Sin'kov

Semiconductors, Vol. 37, No. 10, 2003, pp. 1195–1200. Translated from Fizika i Tekhnika Poluprovodnikov, Vol. 37, No. 10, 2003, pp. 1225–1230.
Original Russian Text Copyright © 2003 by Kovalev, Chaplik.

LOW-DIMENSIONAL SYSTEMS

Electronic Absorption of Surface Acoustic Waves by Quantum Rings in a Magnetic Field

V. M. Kovalev and A. V. Chaplik

Institute of Semiconductor Physics, Siberian Division, Russian Academy of Sciences, ul. Akademika Lavrent'eva 13, Novosibirsk, 630090 Russia

e-mail: chaplik@isp.nsc.ru

Submitted January 29, 2003; accepted for publication January 31, 2003

Abstract—Absorption of a surface acoustic wave by a quantum-ring array occupied by one or two electrons is considered. Dependences of the absorption coefficient on the magnetic flux through the quantum ring and the acoustic-wave frequency with allowance made for the Coulomb interaction between electrons are calculated. It is shown that the absorption coefficient is an oscillatory function of the magnetic flux with a period equal to the magnetic-flux quantum. © *2003 MAIK "Nauka/Interperiodica"*.

1. INTRODUCTION

There are a great number of publications concerned with the electronic properties of quantum rings in recent issues of scientific journals. Current advances in technology make it possible not only to design semiconductor systems with the size of the quantum rings on the order of the effective Bohr radius but also to control the occupation of these systems by charge carriers using the gate voltage. In this case, one can detect the appearance of each consecutive electron in the ring: Warburton *et al.* [1] observed the recombination emission from quantum rings, in which the number of electrons was sequentially varied from one to five. Such structures are of interest for a field that has recently emerged in semiconductor physics; this field is referred to as single-electronics and is concerned with artificial atoms with a small number of electrons. Such artificial atoms are objects in which it is convenient to study the electron–electron interaction because the system's kinetic energy, which competes with this interaction, is governed by dimensional quantization and, consequently, can be varied controllably in experiment.

Optical properties of a two-electron Wigner molecule were studied theoretically by Wendler *et al.* [2]. Interaction with an electromagnetic field was described in the dipole approximation since the sizes of mesoscopic rings were smaller than the resonance wavelength by several orders of magnitude. However, a spatial inhomogeneity of a perturbing field can be important for the interaction of electrons with acoustic waves. In this context, it should be recalled that considerable progress has been achieved recently in gaining insight into hybrid systems in which a two-dimensional electron gas is subjected to a surface acoustic wave (SAW) [3].

In this study, we consider the absorption of a SAW by electrons localized in a quantum ring and subjected to a magnetic field. There is a radical difference between the situations where quantum rings contain one or two electrons. In the single-electron case, there is a nonzero nondiagonal matrix element of the dipole moment; as a result, electronic transitions are possible even in the limit of a homogeneous field. In the two-electron and multielectron cases, electrons form a ring Wigner molecule when subjected to a strong Coulomb interaction; the dipole moment of this molecule is exactly equal to zero owing to symmetry. In this situation, absorption is due to transitions of higher multipolarity.

Taking into consideration Pauli's exclusion principle gives rise to correlations between the center-of-mass angular momentum and the resultant spin of a system of two electrons, which, naturally, manifests itself in the magnetic-field dependence of the SAW absorption coefficient. Finally, taking into consideration the relative motion of particles (oscillations of a Wigner molecule) complicates the absorption pattern even more; however, it is self-evident that the periodicity in the magnetic flux is retained.

For definiteness, we will consider the following structure. There is a substrate (GaAs) on the surface of which quantum rings (InAs) are formed. A SAW propagates over the surface; a constant homogeneous magnetic field is applied orthogonally to the surface. For simplicity, we will consider a model of a one-dimensional (1D) ring and disregard both the Zeeman energy and the spin–orbit interaction. These effects bring about a small splitting of single-particle energy levels, whereas we are interested in clarifying the role of Coulomb interaction and in radical differences between the SAW absorption by independent particles and by a strongly correlated system (a Wigner molecule).

2. NONINTERACTING ELECTRONS

In this section, we consider briefly the situation where only a single electron is present in a quantum

ring. Let the substrate occupy the half-space $z < 0$, and let a homogeneous magnetic field $\mathbf{B} = (0, 0, B)$ be applied perpendicularly to the surface. The magnetic flux penetrating through the quantum ring is defined as $\Phi = B\pi a^2$. The SAW propagates in the (x, y) plane and has a wave vector of $\mathbf{q} = (\omega/s, 0)$. Here, ω and s are the SAW frequency and velocity, respectively. We can then represent the perturbation, which acts on an electron, as

$$V(x) = V_0\exp(iqx - i\omega t) + \text{complex-conjugate term}, \tag{1}$$

where $V_0 = e\varphi_{\mathrm{SAW}}$ for piezoelectric interaction; here, φ_{SAW} is the amplitude of the SAW electric-field potential. Henceforth, we will drop multipliers of the form $\exp(i\omega t)$.

The Schrödinger equation has the following form in the model of a 1D quantum ring:

$$-\frac{\hbar^2}{2m^*a^2}\left(\frac{d}{d\varphi} - i\frac{\Phi}{\Phi_0}\right)^2\Psi_j(\varphi) = \varepsilon_j\Psi_j(\varphi). \tag{2}$$

The wave functions and the spectrum are given by

$$\Psi_j(\varphi) = (2\pi)^{-1/2}\exp(ij\varphi),$$
$$\varepsilon_j = \frac{\hbar^2}{2m^*a^2}\left(j + \frac{\Phi}{\Phi_0}\right)^2, \quad j = 0, \pm1, \pm2, \ldots, \tag{3}$$

where $\Phi_0 = hc/e$ is the magetic-flux quantum.

In order to calculate the SAW absorption coefficient, we use the expression

$$\Gamma = \frac{2\pi\omega}{I_0}\sum_{j, j'}|V_{j'j}|^2\delta(\varepsilon_{j'} - \varepsilon_j - \hbar\omega). \tag{4}$$

Here, I_0 is the SAW intensity and $V_{j'j}$ is the matrix element of perturbation (1) over states (3). In expression (4), the magnetic flux appears only in combination $j + \Phi/\Phi_0$ in terms of the energy levels ε_j. It follows immediately that Γ depends periodically on Φ with a period of Φ_0. The results of calculating the absorption coefficient using formula (4) are discussed in Section 4.

3. A TWO-ELECTRON WIGNER MOLECULE

The Hamiltonian of a system consisting of two interacting electrons in a quantum ring is given by

$$H = \sum_{\alpha=1}^{2}\frac{1}{2m^*}\left(p_\alpha + \frac{e}{c}A_\alpha\right)^2 + V(x_1, x_2) + U(|x_1 - x_2|), \tag{5}$$

where

$$V(x_1, x_2) = V_0[\exp(iqx_1) + \exp(iqx_2)] + \text{complex-conjugate term}, \tag{6}$$

is the potential of electron interaction with a SAW, $U(|\mathbf{x}_1 - \mathbf{x}_2|)$ is the potential of Coulomb interaction between electrons, $p_\alpha = -i\hbar\nabla_\alpha$ is the momentum operator of the αth electron, and $A_\alpha = Ba/2$ is the angular component of the vector potential at the ring. On separating the variables in a polar coordinate system, we obtain the equations

$$-\frac{\hbar^2}{4m^*a^2}\left(\frac{d}{d\varphi_c} - 2i\frac{\Phi}{\Phi_0}\right)^2F(\varphi_c) = E_1F(\varphi_c),$$
$$-\frac{\hbar^2}{m^*a^2}\frac{d^2}{d\theta^2}G(\theta) + U(\theta)G(\theta) = E_2G(\theta) \tag{7}$$

for the center-of-mass motion and relative motion of electrons, respectively. In Eqs. (7),

$$U(\theta) = \frac{e^2}{4\pi\varepsilon_0\varepsilon_s a\sqrt{2(1-\cos\theta)}},$$
$$E = E_1 + E_2 \tag{8}$$

is the interaction energy and the total energy of the system, $\varphi_c = (\varphi_1 + \varphi_2)/2$ is the center-of-mass coordinate, and $\theta = \varphi_2 - \varphi_1$ is the coordinate of relative motion of electrons.

The wave function of the system is expressed as

$$\psi(\varphi_c, \theta) = (2\pi)^{-1/2}\exp(iJ\varphi_c)G(\theta), \tag{9}$$

where $G(\theta)$ is the solution to the second equation in (7) with a periodic potential and, as such, should have the Bloch form; i.e.,

$$G(\theta) = e^{ip\theta}u(\theta),$$
$$u(\theta + 2\pi) = u(\theta).$$

In order to solve the second equation in (7), we consider the limiting case where the Coulomb interaction potential is much larger than the kinetic energy of the electrons; i.e., we require that the following condition be satisfied:

$$\frac{e^2}{4\pi\varepsilon_0\varepsilon_s a} \gg \frac{\hbar^2}{m^*a^2}.$$

It is easy to understand that the validity of this condition makes it possible to use the tight-binding approximation

$$G(\theta) = \frac{1}{N}\sum_{m=-N/2}^{m=+N/2}e^{ip\theta_m}\chi(\theta - \theta_m), \quad N \longrightarrow +\infty, \tag{10}$$

where

$$\theta_m = \pi(2m + 1),$$
$$-1/2 < p \le 1/2.$$

In the same approximation, we can represent the potential $U(\theta)$ as

$$U(\theta) = \frac{e^2}{4\pi\varepsilon_0\varepsilon_s a\sqrt{2(1-\cos\theta)}} \approx \frac{e^2}{8\pi\varepsilon_0\varepsilon_s a} + \sum_{m=-\infty}^{+\infty} \frac{m^*\Omega^2 a^2}{2}(\theta-\theta_m)^2\Theta(\pi-|\theta-\theta_m|), \quad (11)$$

where

$$\Omega^2 = \frac{e^2}{8\pi\varepsilon_0\varepsilon_s m^* a^3}$$

and $\Theta(x)$ is the unit-step function. As a result, the Schrödinger equation for relative motion becomes oscillatory and we obtain

$$E_2 = \hbar\Omega(n+1/2)+\Delta(p), \quad n = 0, 1, 2, \ldots,$$
$$\chi_n(\theta-\theta_m) = C_n \exp\left[-\frac{1}{2}\left(\frac{\theta-\theta_m}{x_0}\right)^2\right] H_n\left(\frac{\theta-\theta_m}{x_0}\right), \quad (12)$$

where $x_0 = [\hbar/(m^*\Omega a^2)]^{1/2}$ is the oscillation length; $H_n(x)$ is the Hermitian polynomial; $C_n = 1/(2^n n!\pi^{1/2}x_0)^{1/2}$ is the normalizing constant; and $\Delta(p)$ is a small (in the tight-binding approximation) addition to the relative-motion energy and accounts for tunneling of electrons through the potential barrier toward each other.

Substituting expression (9) into the first of Eqs. (7), we obtain the energy of the center-of-mass motion as

$$E_1 = \hbar\omega_0\left(J+2\frac{\Phi}{\Phi_0}\right)^2, \quad \omega_0 = \frac{\hbar}{2m^*a^2}. \quad (13)$$

The parameters J and p should be determined independently of the conditions for periodicity of the total wave function with respect to φ_1 and φ_2. These conditions are written as

$$J\pi + 2\pi p = 2\pi N_1, \quad J\pi - 2\pi p = 2\pi N_2, \quad (14)$$

where N_1 and N_2 are integers. As a result, we find that J is an integer and p is either an integer or a half-integer; i.e., within the first "Brillouin zone," we have either $p = 0$ if J is even-valued and $p = 1/2$ if the total-momentum number is odd-valued.

In order to determine the ground state and the wave function of the system, we have to take into account the Pauli exclusion principle, which gives rise to a correlation between the quantum numbers of orbital motion and the total spin S of the system; i.e.,

$$J = 2l+1, \quad l = 0, \pm1, \pm2, \ldots \quad \text{at} \quad S = 1, \quad p = 1/2,$$
$$J = 2l, \quad l = 0, \pm1, \pm2, \ldots \quad \text{at} \quad S = 0, \quad p = 0. \quad (15)$$

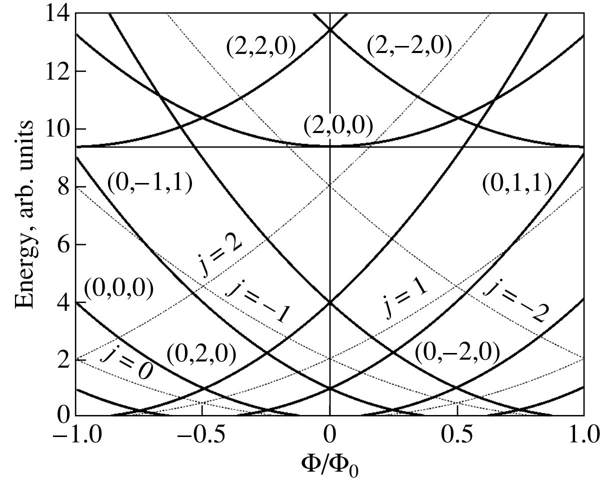

Fig. 1. Energy levels of a free electron (dashed lines) and two interacting electrons (solid lines) in relation to the magnetic flux.

Thus, if external perturbation applied to the system is independent of electron spins ($\Delta S = 0$), only the transitions with changes of J by an even number are possible: $\Delta J = 2l$, where $l = 0, \pm1, \pm2, \ldots$.

Since we do not restrict our consideration only to the dipole approximation, we express the external perturbation (6) in terms of expansion in the Bessel functions $J_n(x)$ when calculating the SAW absorption; i.e.,

$$V(\varphi_1, \varphi_2) = V_0\sum_k i^k J_k(qa)(e^{ik\varphi_1}+e^{ik\varphi_2}) + \text{complex-conjugate term}, \quad (16)$$

where subscripts 1 and 2 correspond to the first and second electrons, respectively. Passing to the center-of-mass system, we obtain

$$V(\varphi_c, \theta) = 2V_0\sum_k i^k J_k(qa)e^{ik\varphi_c}\cos\left(\frac{k\theta}{2}\right). \quad (17)$$

In order to calculate the SAW absorption coefficient in the case of two electrons in a quantum ring, it is not sufficient just to replace the matrix element $V_{j'j}$ in expression (4) with the perturbation matrix element (17). The point is that the total spin S of the system's ground state changes periodically as the magnetic flux through the quantum ring varies. Figure 1 shows the dependence of energy levels of a Wigner molecule in a quantum ring on the magnetic flux; it can be seen from Fig. 1 that the

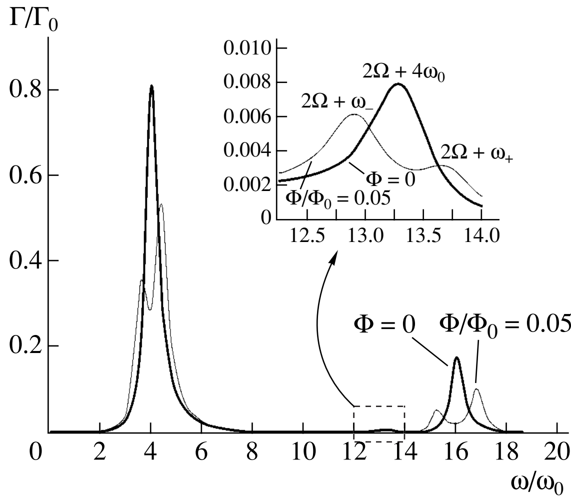

Fig. 2. Dependences of the absorption coefficient on the frequency of a SAW for two values of the magnetic flux and for the system's total spin $S = 0$. Thick solid lines correspond to absorption at $\Phi = 0$ and thin solid lines correspond to absorption at $\Phi = 0.05\Phi_0$. Dependences of the absorptance by vibrational degrees of freedom of a Wigner molecule on the SAW frequency are shown in the inset.

role of the ground state with the total spin $S = 0$ is replaced by the state with $S = 1$. This phenomenon (the so-called singlet–triplet oscillations) was predicted by Wagner *et al.* [4] for the first time. Taking into account these oscillations, we can express the SAW absorption as

$$\frac{\Gamma}{\Gamma_0} = g_{\text{singlet}}\sum_{\eta'\eta}\frac{A_{\eta'\eta}A^*_{\eta'\eta}}{1+(\omega_{\eta'\eta}-\omega)^2\tau^2} + g_{\text{triplet}}\sum_{\eta'\eta}\frac{A_{\eta'\eta}A^*_{\eta'\eta}}{1+(\omega_{\eta'\eta}-\omega)^2\tau^2}. \tag{18}$$

The following designations are used in (18):

$$A_{\eta'\eta} = \frac{V_{\eta'\eta}}{2V_0};\quad V_{\eta'\eta} = \langle\eta'|V(\varphi_c,\theta)|\eta\rangle,$$

$$\omega_{\eta'\eta} = \frac{E_{\eta'}-E_\eta}{\hbar},$$

$$\Gamma_0 = 64\pi N_R\frac{e^2}{(\varepsilon+1)}\frac{\tau}{\hbar}K^2_{\text{eff}},$$

η is the totality of quantum numbers, i.e., the total angular momentum quantum number J and the oscillation quantum number n; τ is the relaxation time; K_{eff} is the electromechanical-coupling coefficient; N_R is the surface density of quantum rings; ε is the relative permittivity of the substrate; and $g_{\text{singlet}} = 1$ and $g_{\text{triplet}} = 3$ are the weighting factors of the singlet and triplet states, respectively. It is noteworthy that the summation in expression (18) is performed over even values of J in the first sum and over odd values of J in the second sum according to the rules of (15). Referring to hybride structures of the type described by Rotter *et al.* [3], we assume that $N_R = 10^6$ cm^{-2}, $\varepsilon = 50$, $\tau \approx 5 \times 10^{-11}$ s, and $K_{\text{eff}} = 0.237$; as a result, we obtain $\Gamma_0 \approx 2.4 \times 10^3$ cm^{-1}.

When deriving expression (18), we took into account that the initial state $|\eta\rangle = |n, J\rangle$ is always occupied, whereas the final state $|\eta'\rangle = |n', J'\rangle$ is always unoccupied. Taking into account (9), (10), and (12), we obtain the following expression for the matrix element $V_{\eta'\eta}$ (see Appendix):

$$\langle n', J'|V|0, J\rangle = \frac{V_0}{\sqrt{2^{n'}n'!}}\sum_k(-i)^kJ_k(qa)\left(\frac{ikx_0}{2}\right)^{n'} \times \exp\left(-\frac{k^2x_0^2}{16}\right)\delta_{J',J+k}\delta_{S'S}[1+(-1)^{n'}]. \tag{19}$$

Here, $x_0 = \sqrt{\hbar/(m^*\Omega a^2)}$. Since the transitions involving J are possible only for an even value of ΔJ ($\Delta J = 2l$), it follows from (19) that $k = 2l$. It is worth noting that, in the model under consideration, the matrix element (19) is independent of the magnetic flux, which threads through the quantum ring; consequently, we may posit that the heights of the absorption peaks are not sensitive to variations in the magnetic field, at least in the approximation of a 1D quantum ring. The results of numerical calculation of the absorption coefficient on the basis of formulas (4) and (18) are shown in Figs. 3a and 3b and are discussed below. When performing calculations, we assumed that $a = 800$ Å and $m^* = 0.04m_0$.

4. DISCUSSION

The energy spectrum of a system consisting of two electrons is shown in Fig. 1 in relation to the magnetic flux; the states of a Wigner molecule are described using the quantum numbers n, J, and S. Here, $n = 0, 1, 2, \ldots$ is the oscillation quantum number; $J = 0, \pm2, \pm4, \ldots$ is the azimuthal quantum number (the total angular moment of the system); and $S = 0$ (or 1) is the total spin. The values of the energy are given in units of the rotational quantum $\hbar\omega_0$. The angular electron momentum j is indicated for the states of free electron. The energy levels of the type $(1, J, S)$ are not shown in Fig. 1; the reason is that [as can be seen from expression (19)] these levels are not involved in absorption owing to the selection rules $n' = 0, 2, 4, \ldots$.

The frequency dependence of the coefficient of SAW absorption $\Gamma(\omega)$ by a Wigner molecule in a quantum ring at $S = 0$ and two values of magnetic flux is illustrated in Fig. 2. It can be seen that, aside from the high-intensity peaks corresponding to the transitions $(0, 0, 0) \longrightarrow (0, \pm2, 0)$, there are additional peaks (phonon replicas) related to absorption of SAWs by the vibrational degree of freedom of a Wigner molecule (see the inset in Fig. 2). The first (low-frequency) group of peaks corresponds to a single transition for $\Phi = 0$ (the resonance frequency is $4\omega_0$) and two transitions at $\Phi = 0.05\Phi_0$ since the degeneracy with respect to

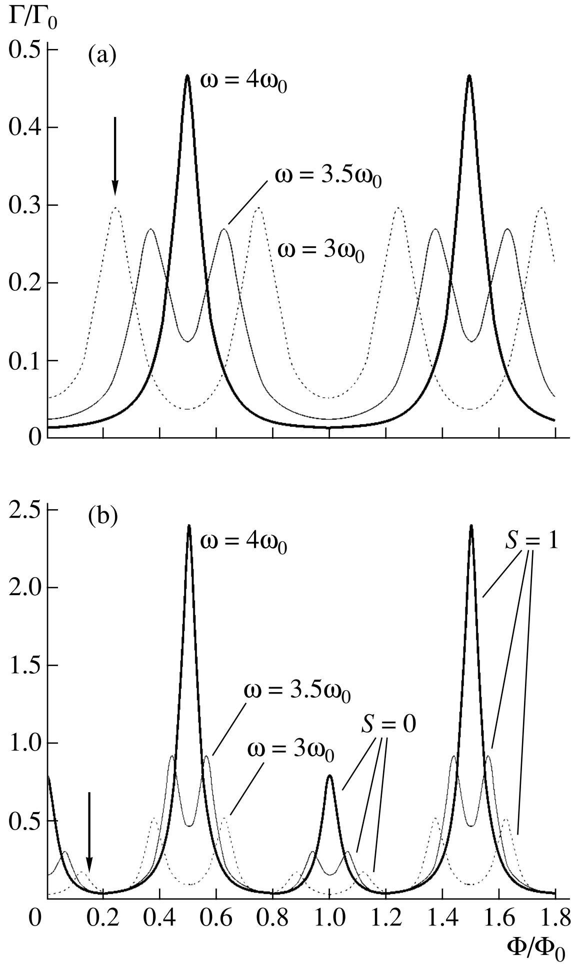

Fig. 3. Dependences of the absorption coefficient on the magnetic flux at frequencies $\omega = 4\omega_0$, $\omega = 3.5\omega_0$, and $\omega = 3\omega_0$: (a) for a single electron and (b) for two interacting electrons.

momentum is removed in this case; as a result, two peaks at the frequencies designated as ω_+ and ω_- in Fig. 2 are observed in the absorption spectrum. The phonon replicas are shifted by the frequency of allowed vibrational transition 2Ω and also include three peaks at $\omega = 2\Omega + \omega_-$, $\omega = 2\Omega + 4\omega_0$, and $\omega = 2\Omega + \omega_+$. A group of high-frequency peaks in the vicinity of $\omega = 16\omega_0$ corresponds to transitions $(0, 0, 0) \longrightarrow (0, \pm 4, 0)$.

It is noteworthy that the parameter $\omega a/s$ is much larger than unity ($4\omega_0 a/s = 2.22$) for all peaks shown in Fig. 2; this means that the dipole approximation is certainly inapplicable.

The most interesting (and simplest for experimental observation) is the dependence of the SAW absorption spectra on the magnetic flux through a quantum ring. These spectra are shown in Figs. 3a and 3b for the cases of a single electron and two strongly interacting electrons in a quantum ring. It can be seen that, when the second electron appears in the quantum ring (i.e., at a certain voltage), positions of the peaks change jumpwise (see the thick arrows in Figs. 3a and 3b) since the effective rotational quanta in formulas (3) and (13) differ from each other by a factor of 2. The height of the peaks is determined by the quantity $J_k(\omega a/s)$. If the parameter $\omega a/s$ is not small compared to unity (as in our calculations), the peak heights vary rapidly as the values of ω or a vary; a reverse ratio (with respect to that shown in Fig. 3) between the heights of absorption peaks for one electron or two interacting electrons can also be observed.

5. CONCLUSIONS

Thus, we have shown that electronic absorption of SAW in a structure with a quantum ring depends periodically on the magnetic flux. Taking into consideration the Coulomb interaction between electrons radically changes the pattern of dependences of the SAW absorption on magnetic flux with respect to both the positions and heights of the absorption peaks.

APPENDIX

Let us consider the calculation of matrix element (19). The total electron wave function has the form given by (9). The matrix element $V_{\eta'\eta}$ is expressed as

$$V_{\eta'\eta} = \int_0^{2\pi} d\varphi_c \int_{-\infty}^{\infty} d\theta \psi^*(\varphi_c, \theta) V(\varphi_c, \theta) \psi(\varphi_c, \theta) \langle S|S' \rangle.$$

Integration with respect to φ_c is elementary; as a result, we obtain the following expression for the matrix element:

$$V_{\eta'\eta} = 2V_0 \sum_{m, m', k} i^k J_k(qa) \exp(ip\theta_m - ip'\theta_{m'}) \times \delta_{SS'} \delta_{J', J+k} I_n^{n'}(m, m', k).$$

Here, we used the designation

$$I_n^{n'}(m, m', k) = C_{n'} C_n \times \int_{-\infty}^{\infty} \chi_{n'}^*(\theta - \theta_{m'}) \chi_n(\theta - \theta_m) \cos\left(\frac{k\theta}{2}\right) d\theta.$$

Calculation of this integral in the general form is cumbersome, albeit possible. Since we consider the electron transitions from the ground state $n = 0$ (low temperatures), the integral under analysis can be represented as

$$I_0^{n'}(m, m', k) = \delta_{m'm} C_0 C_{n'} i^k \left[\exp\left(ik\frac{\theta_m}{2}\right) + (-1)^{n'} \exp\left(-ik\frac{\theta_m}{2}\right)\right] \sqrt{\pi} x_0 \left(\frac{ikx_0}{2}\right)^{n'} \exp\left(-\frac{x_0^2 k^2}{16}\right).$$

In this expression, we disregard the overlap of the states with different values of m since these values are

exponentially small, which accounts for the presence of the Kronecker delta for m.

We now consider in detail the calculation of the sum over m in the matrix element. This sum is given by

$$\sum_m \exp[i(p-p')\theta_m]$$

$$\times\left[\exp\left(ik\frac{\theta_m}{2}\right)+(-1)^{n'}\exp\left(-ik\frac{\theta_m}{2}\right)\right],$$

where θ_m was defined in expression (10). We then use (10) to obtain

$$\exp\left(\pm ik\frac{\theta_m}{2}\right) = \exp\left(\pm ik\pi m \pm ik\frac{\pi}{2}\right)$$

$$= (\pm i)^k \exp(\pm ikm\pi) = (\pm i)^k \cos(km\pi) = (\pm i)^k.$$

When deriving this equality, we made use of the fact that k is an even integer in accordance with the selection rules. Further, since the absorption occurs without a spin flip, we have $p - p' = 0$. The sum over m is then equal to

$$\sum_n \exp[i(p-p')\theta_m]$$

$$\times\left[\exp\left(ik\frac{\theta_m}{2}\right)+(-1)^{n'}\exp\left(-ik\frac{\theta_m}{2}\right)\right] = i^k[1+(-1)^{n'}].$$

Taking into account the explicit expression for C_n, we obtain expression (19) in the main text.

ACKNOWLEDGMENTS

This study was supported by the Russian Foundation for Basic Research (project nos. 01-02-16377 and 02-02-06174) and a program of the Ministry of Industry and Science of the Russian Federation.

REFERENCES

1. R. J. Warburton, C. Schaflen, D. Haft, *et al.*, Nature **405**, 926 (2000).

2. L. Wendler, V. M. Fomin, A. V. Chaplik, and A. O. Govorov, Phys. Rev. B **54**, 4794 (1996).

3. M. Rotter, A. V. Kalameitsev, A. O. Govorov, *et al.*, Phys. Rev. Lett. **82**, 2171 (1999); A. O. Govorov, A. V. Kalameitsev, V. M. Kovalev, *et al.*, Phys. Rev. Lett. **87**, 226803 (2001).

4. M. Wagner, U. Merkt, and A. V. Chaplik, Phys. Rev. B **45**, 1951 (1992).

Translated by A. Spitsyn

Semiconductors, Vol. 37, No. 10, 2003, pp. 1201–1204. Translated from Fizika i Tekhnika Poluprovodnikov, Vol. 37, No. 10, 2003, pp. 1231–1234.
Original Russian Text Copyright © 2003 by Abramov, Ignatenko, Novik.

Characteristics of Multiple-Island Single-Electron Chains in Relation to Various Factors

I. I. Abramov*, S. A. Ignatenko, and E. G. Novik

Belarussian State University of Informatics and Radioelectronics, Minsk, 220027 Belarus

**e-mail: nanodev@bsuir.edu.by*

Submitted February 6, 2003; accepted for publication February 10, 2003

Abstract—The characteristics of multiple-island single-electron chains are analyzed theoretically in relation to the design parameters, the materials, the background charge, and the environmental temperature with the aid of a model developed on the basis of the solution of the Poisson equation and the Monte Carlo method. It is shown that the main parameter which determines the temperature stability of the phenomenon of the Coulomb blockade is the potential-barrier height for tunneling junctions. The investigations of three systems of materials (Co–Al–O, Au–Al_2O_3, and Cr–Cr_2O_3) take shown that the multiple-island single-electron chains based on Co–Al–O are most preferable at the operating temperature. The chains based on Cr–Cr_2O_3 are less preferable.
© 2003 MAIK "Nauka/Interperiodica".

1. INTRODUCTION

The multiple-island single-electron chains of tunneling junctions are promising for the development of a variety of device structures for nanoelectronics [1–4]. Their main advantages in comparison to single-island single-electron transistors with identical dimensions of islands and tunneling junctions are a higher threshold voltage of Coulomb blockade and, as a consequence, a higher operation temperature. The characteristics are less sensitive to the parasitic effect of cotunneling and to the inevitable spread of the main sizes (of islands, tunneling junctions, etc).

As a rule, in the models of multiple-island single-electron chains, the parameters fitting the theory to the experiment, are the capacitances and resistances of tunneling junctions. Due to this circumstance, the relation to the physics of processes in these device structures is lost to a great extent. The models of two-island and multiple-island single-electron chains on the basis of the solution of the Poisson equation, as well as on the basis of either the solution of the master equation or the use of the Monte Carlo method, were suggested previously [5, 6]. These models are free of the above disadvantage to some extent.

The purpose of this study is the theoretical analysis of the characteristics of the multiple-island single-electron chains, depending on the design parameters, the materials, the background charge, and the environmental temperature using the model that we suggested previously [6]. This model is based on the solution of the Poisson equation and the use of the Monte Carlo method.

2. THE EFFECTS OF THE STRUCTURE PARAMETERS, MATERIALS, AND BACKGROUND CHARGE

Let us first analyze the effect of the design parameters on the drain current–voltage (*I–V*) characteristics of the five-island single-electron structure based on the AuPd nanoparticles (see [7]).

Figure 1 shows the effect of varying the widths of tunneling junctions on the *I–V* characteristic of the device structure. For definiteness, the main specific fea-

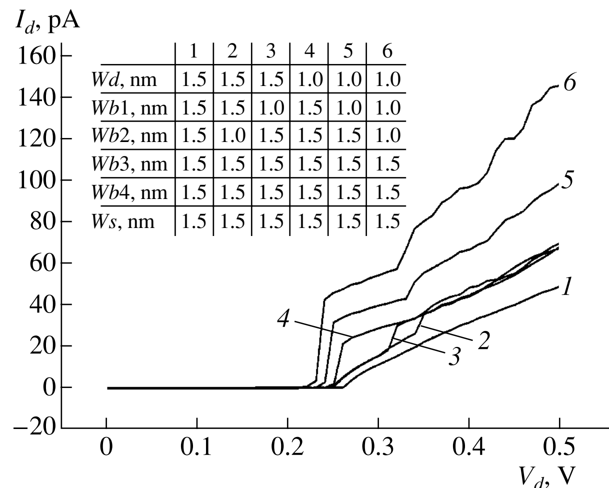

	1	2	3	4	5	6
Wd, nm	1.5	1.5	1.5	1.0	1.0	1.0
*Wb*1, nm	1.5	1.5	1.0	1.5	1.0	1.0
*Wb*2, nm	1.5	1.0	1.5	1.5	1.5	1.0
*Wb*3, nm	1.5	1.5	1.5	1.5	1.5	1.5
*Wb*4, nm	1.5	1.5	1.5	1.5	1.5	1.5
Ws, nm	1.5	1.5	1.5	1.5	1.5	1.5

Fig. 1. Effect that the widths of tunneling junctions have on the current–voltage characteristics of a five-island chain. Corresponding widths are listed in the table in the inset. W_d is the width of the junction of drain–island *1*, W_{b1} is the width of the junction of island *1*–island *2*, etc., W_s is the width of the junction of island *5*–source. The curve numbers correspond to the column numbers in the table.

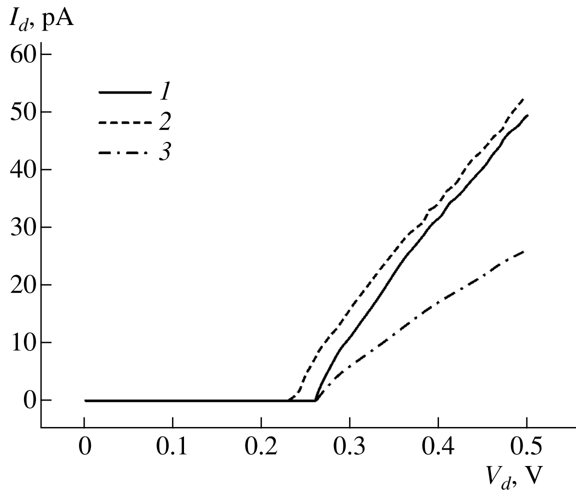

Fig. 2. Effect that the parameters of the material (ε_d and ϕ) have on the current–voltage characteristics of a five-island chain: (*1*) $\varepsilon_d = 10$ and $\phi = 1.5$ eV; (*2*) $\varepsilon_d = 11$ and $\phi = 1.5$ eV; and (*3*) $\varepsilon_d = 10$ and $\phi = 1.6$ eV.

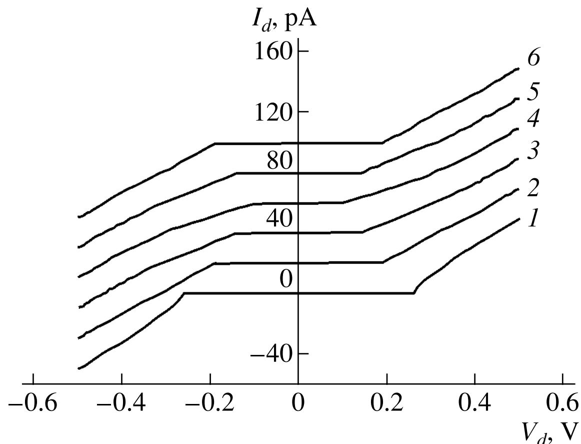

Fig. 3. Effect of the background charge on the current–voltage characteristics of a five-island chain. Curve *1* corresponds to the case of all background charges equal to zero, and curves *2–6* correspond to the number of background charges $N_{0i} = 0.5$ only at a single island with a number less by unity. In this case, all other islands are uncharged. Curves (*2–6*) are given for the shift with a step of 20 pA.

tures are established with a decrease in the width(s) from 1.5 to 1.0 nm. Since a large number of combinations is possible, only the most characteristic results are shown in Fig. 1.

Let us note the following characteristic features.

(i) With nonequivalent widths, the Coulomb staircase emerges in the *I–V* characteristics along with the Coulomb blockade. This fact is attributed to the emergence of stable combinations of excess carriers at the islands; a certain stable combination corresponds to each step.

(ii) With a decrease in the width of the tunneling junction and an increase in the number of such junctions, the tunneling current increases. This circumstance is explained by an increase in probability of tunneling of electrons across the corresponding potential barrier (barriers).

(iii) With an increase in the number of small-width junctions, the region of the Coulomb blockade is narrowed (curves *4–6*). However, the location of the narrowest junction does not affect the blockade region (curves *2–4*). These characteristic features are attributed to the corresponding redistribution of voltages, which drop across the tunneling junctions of the system.

Figure 2 shows the effect of the relative dielectric constants of insulator ε_d and of the height of the potential barriers of tunneling junctions ϕ on the *I–V* characteristic. Curve *1* is obtained for $\varepsilon_d = 10$ and $\phi = 1.5$ eV, curve *2* is obtained for $\varepsilon_d = 11$ and $\phi = 1.5$ eV, and curve *3* is obtained for $\varepsilon_d = 10$ and $\phi = 1.6$ eV. It can be seen that the *I–V* characteristics are especially sensitive to variations in the potential-barrier height. This is explained by the substantial decrease in the probability of electron tunneling through the potential barriers with the larger height. The decrease in the region of the Coulomb blockade with an increase in ε_d is explained by the redistribution of voltages in the structure. These specific features of the effect that the parameters of the materials have on the drain *I–V* characteristics of the five-island chain agree well with those established for the two-island chains [5].

Figure 3 shows the family of *I–V* characteristics of the five-island single-electron chain for various background charges at the islands. It can be seen that the background charge affects the region of the Coulomb blockade. For curve *1* (with zero background charges), this region is the widest (~0.26 V), whereas for the number of the background charges $N_{0.3} = 0.5$ at the center island, this region is the narrowest (~0.1 V). This characteristic feature is consistent with the known data on single-electron structures [1] and is explained by variation in the electrostatic energy of the system; as a result, the conditions for the emergence of the Coulomb blockade are modified.

3. THRESHOLD VOLTAGE AND ULTIMATE OPERATION TEMPERATURE

The ultimate operation temperature is the temperature at which the threshold voltage of the Coulomb blockade V_{th} has a nonzero value.

As the objects for the investigation we chose the single-island, two-island, and five-island chains for three promising materials, namely, $Au–Al_2O_3$, Co–Al–O, and $Cr–Cr_2O_3$. To calculate the *I–V* characteristics of the single-island and two-island chains, the model [5], based on the master equation, was used. For the five-island chain, the model based on the Monte Carlo method was used [6].

To obtain the most reliable estimates of T_{op}, the calculations of the *I–V* characteristics were first compared

with the experimental results. To do this, we used the data for the two-island chain based on the Au–Al_2O_3 system [8], the data for the two-island chain based on the Co–Al–O system [9], and the data for the single-island transistor based on the Cr–Cr_2O_3 system [10].

The most important parameters of the materials for the subsequent analysis are the potential-barrier height ϕ and the relative dielectric constant of insulator ε_d. The geometric sizes of the islands and widths of tunneling junctions correspond to those used for the real chains mentioned above [8–10]. The parameters making it possible to fit the model to the experiment were used individually for each of the systems. The following parameters of the materials were used in calculations: $\phi = 1.65$ eV and $\varepsilon_d = 9$ (for Au–Al_2O_3); $\phi = 2.0$ eV and $\varepsilon_d = 9$ (for Co–Al–O); and $\phi = 0.17$ eV and $\varepsilon_d = 12$ (for Cr–Cr_2O_3). Thus, the most important distinction between the systems is the height of the potential barrier of the tunneling junction.

Figure 4 shows the results of calculating V_{th} for various chains for the systems under investigation. Based on these results, the following conclusions can be made: (i) the threshold voltage increases with an increase in the number of islands, and (ii) V_{th} decreases with increasing temperature. These conclusions are in complete agreement with the known experimental [11] and theoretical [12] data. The first conclusion is based on the fact that, with an increase in the number of islands, it is necessary to apply a higher voltage in order to overcome the blockade region of additional tunneling junctions in the system. In turn, increasing the temperature leads to a rise in thermal fluctuations and, consequently, the Coulomb blockade occurs in the narrower range of voltages (conclusion 2). The consequence of the first and the second conclusions is that the multiple-island chains are stabler in temperature (see Fig. 4). Therefore, it is reasonable to use these chains in developing highly integrated systems.

Let us estimate T_{op} for the chains under consideration. For the first system (Au–Al_2O_3, Fig. 4a), V_{th} is low even at $T = 200$ K. It should be noted that this temperature agrees well with the data [12] for a similar system (Au–SiO_2, $T_{op} = 185$ K). Note that for the system under investigation, V_{th} nevertheless has a nonzero value even at $T = 300$ K. However, this value is very small even for the five-island chain (Fig. 4a). The second system (Co–Al–O, Fig. 4b) is the stablest in temperature. For example, $V_{th} = 0.21$ V at $T = 300$ K for the five-island chain. Consequently, this device structure can operate even at room temperature, which is consistent with experimental data [9] for the two-island chain. The third system (Cr–Cr_2O_3, see Fig. 4c, inset) is less stable in temperature among the systems under investigation. The estimated T_{op} quantity is about 10 K, although V_{th} is very low even at $T = 1$ K (Fig. 4c, inset). Note that these data are given for island dimensions of 20×20 nm^2. As for the results of Figs. 4a and 4b, they are given for much lower values. Therefore, Fig. 4c also

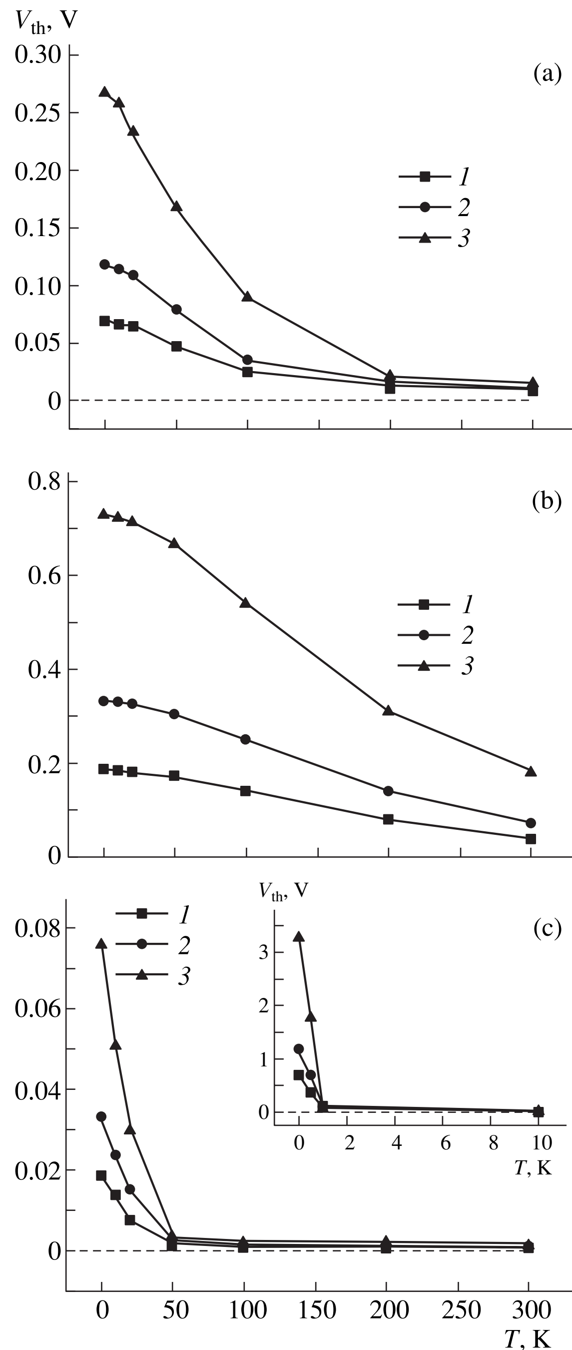

Fig. 4. Temperature dependence of V_{th} for the single-electron chains with (*1*) one, (*2*) two, and (*3*) five islands for the three systems: (a) Au–Al_2O_3, (b) Co–Al–O, and (c) Cr–Cr_2O_3.

shows the prediction results for the Cr–Cr_2O_3 system for comparison with the island dimensions given in Fig. 4a and 4b, specifically, 4×4 nm^2. It can be seen that, with decreasing island sizes, V_{th} increases, whereas T_{op} increases, which is consistent with the available data [1]. As follows from Fig. 4c, V_{th} is low for the Cr–Cr_2O_3 system even at $T = 50$ K in this case.

The aforementioned results permit us to arrange the systems investigated in the following order: (i) Co–Al–O, (ii) Au–Al_2O_3, and (iii) Cr–Cr_2O_3. The Co–Al–O system is the stablest in temperature, and the Cr–Cr_2O_3 system is the least stable. Notably, the highest temperature stability is inherent in the system with the largest barrier height ϕ. This can be attributed to a lower sensitivity to the effect of thermal fluctuations for systems with higher potential barriers of tunneling junctions. However, the thermal fluctuations are the main factor that destroys the region of the Coulomb blockade with increasing temperature.

It follows from our results that V_{th} depends on ϕ even at $T \longrightarrow 0$ K (see Fig. 4). However, it has been commonly assumed that V_{th} should depend only on the capacitances of the junctions in this case [1, 12]. The cause of this disagreement is associated, on the one hand, with the complexity of extrapolation of the parameters fitting the theory to the experiment to this temperature range. On the other hand, it is associated with the fact that consistency with the experiment is attained for various geometrical sizes of the chains and background charges due to the insufficiency of experimental data. However, it is necessary to point out here that, for an actual system, the current always flows for $V \neq 0$ even in the region of the Coulomb blockade, although the current is very weak in this case. Therefore, the energy of the system in the region of the Coulomb blockade, strictly speaking, will be determined not only by the capacitive characteristics of the system, but also by flowing currents. The latter depend to a great extent on the height of the potential barriers of the junctions and on temperature.

4. CONCLUSIONS

The analysis carried out using the suggested models allowed us to explain how the operation of the multiple-island single-electron chains depends on their design parameters and materials as well as on the background charges at the islands. It was shown that the main parameter, which determines the efficiency of the Coulomb blockade for the single-electron chains, is the height of the potential barriers of the tunneling junctions. The ultimate operation temperatures were determined for three systems of materials, namely, Co–Al–O, Au–Al_2O_3, and Cr–Cr_2O_3. It was found that the multiple-island single-electron chains based on the Co–Al–O structures are the most suitable from the standpoint of operation temperature, whereas the chains based on the Cr–Cr_2O_3 are least suitable.

ACKNOWLEDGMENTS

This study was partly supported by the Belarussian research programs “Electronics,” “Nanoelectronics,” and the Ministry of Education of the Republic of Belarus.

REFERENCES

1. *Single Charge Tunneling: Coulomb Blocade Phenomena in Nanostructures*, Ed. by H. Grabert and M. H. Devoret (Plenum, New York, 1992), NATO ASI Ser., Ser. B, Vol. 294.
2. I. I. Abramov and E. G. Novik, Fiz. Tekh. Poluprovodn. (St. Petersburg) **33**, 1388 (1999) [Semiconductors **33**, 1254 (1999)].
3. I. I. Abramov and E. G. Novik, *Numerical Simulation of Metal Single-Electron Transistors* (Bestprint, Minsk, 2000).
4. *Technology Roadmap for Nanoelectronics*, Ed. by R. Compano (European Commission, IST Program, Future and Emerging Technologies, Brussels, 2000).
5. I. I. Abramov, S. A. Ignatenko, and E. G. Novik, Fiz. Tekh. Poluprovodn. (St. Petersburg) **36**, 1272 (2002) [Semiconductors **36**, 1192 (2002)].
6. I. I. Abramov, S. A. Ignatenko, and E. G. Novik, Fiz. Tekh. Poluprovodn. (St. Petersburg) **37**, 583 (2003) [Semiconductors **37**, 564 (2003)].
7. H. Ahmed, J. Vac. Sci. Technol. B **15**, 2101 (1997).
8. E. Bar-Sadeh, Y. Goldstein, M. Wolovelsky, *et al.*, J. Vac. Sci. Technol. B **13**, 1084 (1995).
9. H. Imamura, J. Chiba, S. Mitani, *et al.*, Phys. Rev. B **61**, 46 (2000).
10. L. S. Kuzmin, Yu. A. Pashkin, A. N. Tavkhelidze, *et al.*, Appl. Phys. Lett. **68**, 2902 (1996).
11. A. Bezryadin, R. M. Westervelt, and M. Tinkham, Appl. Phys. Lett. **74**, 2699 (1999).
12. A. S. Cordan, Y. Leroy, A. Goltzene, *et al.*, J. Appl. Phys. **87**, 345 (2000).

Translated by N. Korovin

Semiconductors, Vol. 37, No. 10, 2003, pp. 1205–1210. Translated from Fizika i Tekhnika Poluprovodnikov, Vol. 37, No. 10, 2003, pp. 1235–1240.
Original Russian Text Copyright © 2003 by Sergeev, Suris.

LOW-DIMENSIONAL SYSTEMS

The X^+ Trion in a System with Spatial Separation of the Charge Carriers

R. A. Sergeev* and R. A. Suris

Ioffe Physicotechnical Institute, Russian Academy of Sciences, ul. Politekhnicheskaya 26, St. Petersburg, 194021 Russia

**e-mail: rinat@theory.ioffe.rssi.ru*

Submitted April 10, 2003; accepted for publication April 15, 2003

Abstract—A system composed of two heavy holes located in a two-dimensional (2D) quantum well (QW) and bound via mediation of an electron in a neighboring 2D QW is considered. Using a simple qualitative trial wave function, the ground-state energy of this kind of X^+ trion is determined in the infinite-hole-mass approximation as a function of the QW spacing. Coordinate dependence of the effective potential binding the holes to each other is calculated for different values of QW spacing. In the adiabatic approximation, a set of dependences describing the X^+ trion binding energy as a function of the electron mass to the hole mass ratio is obtained. Several estimates for the trion binding energy in GaAs- and ZnSe-based double-QW heterostructures are given.
© 2003 MAIK "Nauka/Interperiodica".

1. INTRODUCTION

The existence of three-particle electron–hole complexes (trions) in semiconductors was predicted for the first time by Lampert in 1958 [1]. However, it was as far back as the 1920s when this kind of quantum-mechanical system, consisting of two identical particles and a third oppositely charged particle with another mass, came to the attention of scientists; for example, the H^- ion was first considered by Bethe as early as 1929 [2].

Over the span of many years, experimental investigation of trions in bulk semiconductors was impossible, mainly due to the very low value of the trion binding energy (on the order of tenths of a millielectronvolt). The "new life" for trions began with the development of heterostructures, opening the way for "molecule engineering" based on the use of low-dimensional structures (quantum wells (QWs), quantum wires, and quantum dots), where new artificial objects may be formed and the characteristics of "conventional" ones can be controlled.

One of the most typical effects originating from lowered dimensionality is an increase in binding energies of two- and multiple-particle complexes in comparison to the three-dimensional (3D) case. When the number of the degrees of freedom is reduced, the energy related to particle localization within a complex decreases. Meanwhile, the importance of the potential that binds the particles together increases under conditions of spatial confinement, since the mutually attracting particles spend more time in the vicinity of each other. A two-dimensional (2D) exciton, which has a fourfold higher binding energy than its 3D counterpart, serves as an example.

Reduction of the dimensionality has a still greater effect on the exchange energy; this leads to a significant increase in the binding energy of complex multiparticle systems (trions and biexcitons), where the contribution of exchange interaction is dominant. Indeed, theoretical studies carried out in the 1980s revealed that the trion binding energy in QW heterostructures can be almost an order of magnitude higher than the corresponding value in the bulk [3–5]. The relatively high value of the binding energy, combined with the possibility of controlling the conditions in the QW (carrier and exciton densities, electric and magnetic fields) selectively and over a wide range, enabled the first experimental observation and identification of X^- trions (two electrons + hole) in such heterostructures. These data were reported in 1992 for CdTe [6].

Since then, observation of both X^- and X^+ (two holes + electron) trions in various heterostructures at low temperatures was reported many times. The possibility of carrying out experimental studies of trions stimulated theoretical research as well. For instance, only in recent years has there been a large number of publications devoted to the calculations of the binding energy and the ground-state wave function of trions in a single QW [7–13].

Heterostructures with spatial separation of the charge carriers are of special interest. Obviously, separation of electrons and holes leads to a decrease in the binding energy of the complex, since this separation effectively reduces the electron–hole interaction in comparison to electron–electron and hole–hole interaction. However, due to a decrease in the overlap of electron and hole wave functions, the recombination probability decreases and, thus, the trion lifetime should increase. Another attractive feature is the appearance of one more length scale in the system, the spacing between the electron and the hole spatial regions. This

brings about the additional possibility of controlling the trion parameters.

The simplest heterostructure where spatial separation of the charge carriers can occur is the double QW under a strong electric field applied along the growth axis [14–20]. In this paper, we consider a simple qualitative model of the X^+ trion in such a heterostructure. We examine the dependence of the binding energy and the structure of such a trion on the QW spacing and the ratio of the electron and the hole effective masses; this may be of key importance for understanding the behavior of more complicated systems with spatial separation of the charge carriers, e.g., the interaction of two spatially indirect excitons with the formation of a biexciton.

Furthermore, the results yielded in analysis of the model for the X^+ trion are of interest by themselves. When the spacing d between the QWs is large, there are two competing independent terms that contribute to the binding energy of the exciton–hole system: repulsion caused by the relative decrease of electron–hole interaction in comparison to hole–hole interaction, and attraction caused by a decrease in the localization energy of electron upon its collectivization among the two holes. With increasing distance between the holes, the first term decreases following the power-law dependence and the second term decreases exponentially. It is evident that, for some sufficiently large spacing between the QWs, the effective attraction between the holes due to electron collectivization becomes insufficient to overcome the uncompensated part of the hole–hole Coulomb repulsion and the trion dissociates with the formation of an exciton and a free hole. Thus, one may assume that there is a certain critical spacing between the QWs d_{cr}, so that bound states of the X^+ trion do not exist for $d > d_{cr}$. Calculations indicate [20] that, in full agreement with intuitive expectations, the trion binding energy falls off rapidly as the spacing between the QWs increases: already for $d \approx 1$ (here, the 3D Bohr radius is taken as the unit length), the binding energy decreases by more than an order of magnitude as compared with an ideal 2D QW. At the same time, it unexpectedly seems that the trion still remains bound up to very large values of d (although the binding energy is extremely small) and dissociates only for $d \approx 34$.

The purpose of this paper is to examine the evolution of this kind of trion as the spacing between the wells changes. We use a simple model of two ideal 2D QWs and assume that the hole mass is infinite, and then, in an adiabatic approximation, we extend the results of the calculation of the binding energy to the case of a finite hole mass.

The results of the variational calculations for the spatially indirect exciton and trion are given in Sections 2 and 3, respectively. In Section 4, evolution of the coordinate dependence of the effective potential binding holes in the trion is analyzed and the case of finite hole mass is considered using the adiabatic approximation. Estimates for the binding energy of a spatially indirect trion in different materials are given in Section 5. Conclusions are formulated in the final section.

2. THE WAVE FUNCTION OF A SPATIALLY INDIRECT EXCITON

We analyze a simplified model taking into consideration a heterostructure with spatially separated electrons and holes consisting of two ideal 2D QWs, one for electrons and the other for holes. The trion energy is determined using the simplest trial wave function with a minimum set of variational parameters. Such choice not only results in the reduction of cumbersome calculations, it makes the wave function more comprehensible and each of the parameters physically meaningful. In order to determine the binding energy of the trion by variational calculation, we need to find its total energy and subtract it from the exciton energy. However, even for an ideal 2D QW, the exciton binding energy exceeds the trion binding energy by almost an order of magnitude. Consequently, the result will be obviously incorrect unless error in the calculation of the exciton energy is compensated in the calculation of the trion energy. Thus, the trial wave function for the trion should be based on the trial wave function for the exciton and transform into the latter as the distance between the holes grows infinitely. Keeping in mind that we decided to use a small number of variational parameters, we conclude that first we need to find a trial function that, with a minimum set of parameters, yields a reasonable value for the binding energy and the wave function of the exciton for any spacing between the QWs.

The Schrodinger equation for the relative motion of an electron and a hole composing an exciton in a system of two 2D QWs, where both the electron and the hole can move only in the plane of the corresponding well, is written as

$$\frac{1}{\rho}\frac{\partial}{\partial\rho}\rho\frac{\partial}{\partial\rho}\Psi_{ex}(\rho) + \left(-E_{ex} + \frac{2}{\sqrt{\rho^2 + d^2}}\right)\Psi_{ex}(\rho) = 0. \quad (1)$$

Here, ρ is the in-plane component of the vector drawn from the hole to the electron position, d is the spacing between the QWs, and E_{ex} is the exciton binding energy. The 3D exciton binding energy $\mu e^4/2\varepsilon^2\hbar^2$ is taken as the energy unit, and the Bohr radius $\hbar^2\varepsilon/\mu e^2$ is taken as the length unit (μ is the electron–hole reduced mass and ε is the permittivity). One can easily see that Eq. (1) transforms into the Schrodinger equation for the 2D exciton as $d \longrightarrow 0$, and, consequently, the wave function $\Psi_{ex}(\rho)$ should assume exponential form:

$$\Psi_{ex}(\rho) = \exp(-2\rho) \quad (2)$$

(the normalization factor is disregarded). The exciton binding energy in the chosen units becomes $E_{ex} = 4$. In the opposite limiting case, when the interwell spacing d is much greater than the characteristic in-plane size of the wave function (note that, in turn, it depends on d),

the potential in Eq. (1) can be approximated by the oscillator potential:

$$V(\rho) = -\frac{2}{\sqrt{\rho^2 + d^2}} \approx -\frac{2}{d} + \frac{\rho^2}{d^3}. \quad (3)$$

Then, the exciton wave function assumes Gaussian shape,

$$\Psi_{ex}(\rho) = \exp\left(-\frac{\rho^2}{2d^{3/2}}\right), \quad (4)$$

and the exciton binding energy becomes

$$E_{ex} = \frac{2}{d} - \frac{2}{d^{3/2}}. \quad (5)$$

Apparently, the characteristic scale of the function (4) is given by $\rho \sim d^{3/4}$. This means that the approximation (3) can be valid only under the condition

$$d^{3/2} \ll d^2. \quad (6)$$

It is reasonable to choose the exciton wave function in such a way that, in the limiting cases $d \longrightarrow 0$ and $d \longrightarrow \infty$, it is given by expressions (2) and (4), respectively. The wave function that satisfies this condition and has a minimum set of parameters is written as

$$\Psi_{ex}(\rho) = \exp(-\beta_{ex}\sqrt{\rho^2 + d^2}). \quad (7)$$

Here, β_{ex} is the only variational parameter, which determines the length scale of the exciton wave function.

It can be seen easily that the function (7) yields reasonable results for the exciton binding energy and the shape of the wave function for all values of d. For $d \longrightarrow 0$, it transforms into (2), with the parameter β_{ex} approaching 2. In the other limiting case, $d \longrightarrow \infty$, it assumes Gaussian form (4) for $\rho \ll d$, with the parameter β_{ex} given asymptotically by

$$\beta_{ex} = 1/\sqrt{d}. \quad (8)$$

Thus, function (7) becomes an exact exciton wave function and yields an exact value of the energy in both limiting cases.

The dependence of the exciton binding energy on the spacing between the QWs calculated using function (7) is plotted in Fig. 1. For comparison, approximation (5) is shown as well. As expected, the exciton binding energy decreases rapidly starting from the exact value $E_{ex} = 4$, which corresponds to the 2D exciton; for $d > 10$, where the condition (6) is valid, the dependence obtained nearly coincides with the curve corresponding to Eq. (5), derived in the parabolic-potential approximation.

It is worth noting that, even for very large d, the falloff of the exact wave function of the exciton at $\rho > d$ is described exponentially rather than by Gaussian function (4). The exponent is determined solely by the exciton binding energy:

$$\Psi_{ex}(\rho) \propto \exp(-\sqrt{E_{ex}}\rho) \approx \exp\left(-\sqrt{\frac{2}{d}}\rho\right). \quad (9)$$

Function (7) also depends exponentially on the in-plane spacing between the electron and the hole. However, it yields an incorrect value for the exponent in the case of large spacing between the QWs:

$$\Psi_{ex}(\rho) \propto \exp(-\beta_{ex}\rho) \approx \left(-\frac{1}{\sqrt{d}}\rho\right). \quad (10)$$

However, when d is large, the shape of the tail of the wave function is not so important. Indeed, substituting β_{ex} from (8) into (7), we can easily estimate that, even for $d = 10$, the probability of finding the electron in the region $\rho < d$ is 90% and the probability of finding the electron at $\rho > 2d$ is less than 0.1%.

For smaller values of d, when the parameters of the tail of the wave function significantly affect the exciton binding energy, the accuracy of the wave function (7) increases as well. In the limiting case $d \longrightarrow 0$, the form of the exact wave function is exponential (2), and function (7) assumes precisely the same shape.

Comparing the values of the exciton binding energy obtained using wave function (7) with the exact ones determined by direct numerical solution of the Schrodinger equation (1), we see that the relative error for the binding energy is largest for $d \approx 0.1$, where it amounts to just 0.5%; it decreases rapidly both for $d \longrightarrow 0$ and $d \longrightarrow \infty$. Note, however, that the error in the trion binding energy determined on the basis of function (7) may be more significant: due to the incorrect shape of the tail of the wave function, the calculated overlap integral for the electron wave functions centered in the potential wells created by each of the holes may be inaccurate.

3. THE GROUND STATE OF THE X^+ TRION WITH INFINITELY HEAVY HOLES

The X^+ trion in the system under study can be treated as the bound state of two holes residing in a 2D QW that are held together due to their attraction to an electron in the neighboring 2D QW. In this section, we assume that the hole mass is infinite, which means that adiabatic approximation can be used and the electron and the hole wave functions can be separated. The trial wave function for the electron will be chosen as a sum of two exciton-type functions (7) related to the first and the second hole, with the function centroids being shifted toward each other due to the polarization effect:

$$\Psi_{tr}(\boldsymbol{\rho}) = \exp\left(-\beta_{tr}\sqrt{\left(\boldsymbol{\rho} + \frac{1-c}{2}\mathbf{R}\right)^2 + d^2}\right) + \exp\left(-\beta_{tr}\sqrt{\left(\boldsymbol{\rho} - \frac{1-c}{2}\mathbf{R}\right)^2 + d^2}\right). \quad (11)$$

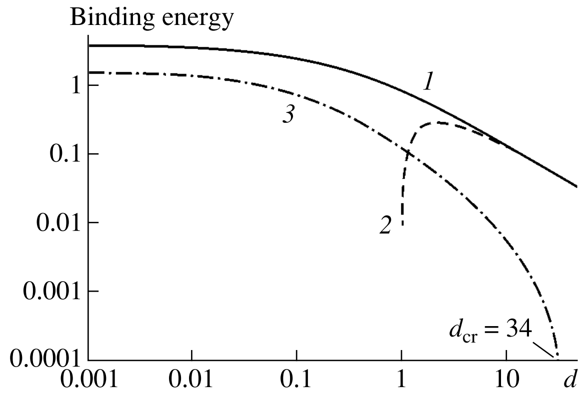

Fig. 1. Dependence of the binding energies of the exciton (curve *1*) and the trion (curve *3*) on the QW spacing d; the 3D exciton binding energy is taken as the energy unit and the Bohr radius, as the length unit. Curve *2* corresponds to the approximation (5) for the exciton binding energy.

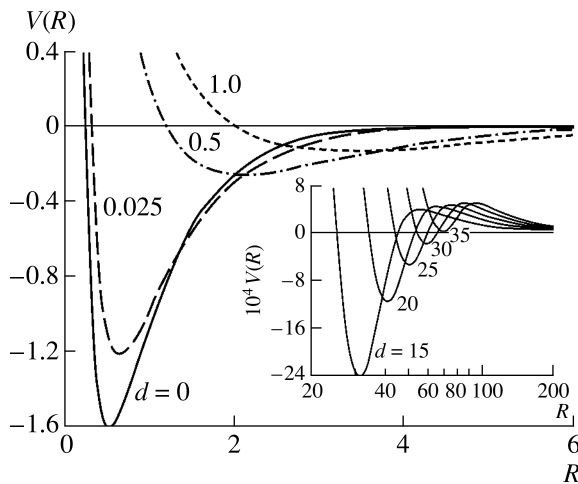

Fig. 2. Coordinate dependence of the effective potential, responsible for binding holes in the trion, for different values of QW spacing d; the potential curves obtained for large values of d are shown in the inset. The 3D exciton binding energy is taken as the energy unit and the Bohr radius, as the length unit.

Here, $\boldsymbol{\rho}$ is the in-plane component of the electron radius vector with respect to the center of mass of the holes, $\mathbf{R}$ is the 2D vector drawn from one hole to the other, d is the spacing between the QWs, β_{tr} is the parameter of the same physical meaning as β_{ex} in the exciton wave function (7), and c is the parameter accounting for polarization. If $c = 0$, each exciton-like term in (11) peaks strictly opposite the corresponding hole; if $c = 1$, the electron wave function is centered midway between the holes.

It turns out that we need just two variational parameters to build the electron wave function for any spacing R between infinitely heavy holes. The parameter β_{tr} accounts for the degree of localization of the electron wave function in the vicinity of each of the holes; the parameter c, apart from accounting for the polarization, controls the overlap between the two exciton-like terms of wave function (11).

The dependence of the binding energy of the spatially indirect trion E_{tr}, obtained using trial function (11), on the QW spacing is shown in Fig. 1. One can see that the trion binding energy falls off rapidly with increasing d, since the electron–hole Coulomb attraction decreases in comparison to the hole–hole Coulomb repulsion. Even for $d = 1$, the trion binding energy is just 8% of its value in the limiting case of a single 2D QW. For $d \approx 34$, the trion binding energy becomes negative, which means that, for $d > 34$, the trion dissociates into an exciton and a free hole. However, the effective potential, binding holes within the trion, has a minimum at relatively small values of R (the energy in this minimum is higher than the exciton energy). This means that there is a metastable state, separated by a potential barrier from the ground state ($R \longrightarrow \infty$).

Since exciton function (7) is not accurate, the use of trion function (11) to determine the trion binding energy results in a noticeable error for small values of the interwell spacing ($d \ll 1$). However, for $d = 0$, function (11) yields a reasonable result of $E_{tr}/E_{ex} = 0.40$ (the exact value is $E_{tr}/E_{ex} = 0.41$ [8]). Variations in the structure of the trion wave function with the spacing between the QWs is investigated in more detail elsewhere [20].

4. THE BINDING ENERGY OF THE X^+ TRION IN THE ADIABATIC APPROXIMATION

Using trial functions (7) and (11), we can calculate the effective potential responsible for the binding of holes in the trion:

$$V_d(R) \approx E_{tr}(R, d) - E_{ex}(d). \tag{12}$$

Here, $E_{tr}(R, d)$ is the total energy of the trion calculated using function (11) and minimized over c and β_{tr} for fixed spacing R between the holes, and $E_{ex}(d)$ is the total energy of the exciton calculated using function (7) and minimized over β_{ex}.

The coordinate dependence of potential (12) for different values of the spacing d between the QWs is shown in Fig. 2. For each potential curve, the absolute value of the minimum corresponds to the binding energy of the trion with infinitely heavy holes in the system with a given interwell spacing. The limiting case $R \longrightarrow \infty$ and $V(R) \longrightarrow 0$ corresponds to the situation where a trion dissociates into an exciton and a free hole. The depth of the potential minimum decreases rapidly as the QW spacing increases. Moreover, for $d > 1.87$ the potential (12) becomes repulsive at sufficiently large R [20]. This means that, if the distance between the holes is sufficiently large, the exciton and the hole must overcome a certain potential barrier to bind into a trion. However, the barrier is very low. As can be seen

in the inset to Fig. 2, the barrier height increases only slightly with increasing QW spacing, but. Even for the largest spacing sufficient for the existence of the bound state of the trion ($d \approx 34$), the barrier height does not exceed 0.0005 for a GaAs-based heterostructure; this corresponds to a temperature of just 26 mK.

Using the expression for the potential (12), we can extend the calculation of the trion binding energy to the case of a finite hole mass. In the adiabatic approximation, the relative motion of holes is described by the Schrodinger equation

$$\frac{m_e}{m_e + m_h}\Delta_R\varphi(R) - [\varepsilon_{\rm tr} + V_d(R)]\varphi(R) = 0. \quad (13)$$

Equation (13) can be solved numerically. The dependences of the binding energy of the ground state of the trion $\varepsilon_{\rm tr} = E_{\rm ex} - E_{\rm tr}$ on the ratio between the electron and hole masses m_e/m_h for different values of the QW spacing d are plotted in Fig. 3. We find that the binding energy $\varepsilon_{\rm tr}$ decreases rapidly with increasing mass ratio $\sigma = m_e/m_h$. For small values of σ, the decrease in energy is proportional to the square root of the mass ratio [20]; this results from the zero-point oscillations of holes bound together by the potential $V_d(R)$:

$$\varepsilon_{\rm tr}(\sigma) \approx \varepsilon_{\rm tr}(0) - \sqrt{\frac{m_e}{m_e + m_h}\frac{\varepsilon_{\rm tr}(0)}{R^2}}. \quad (14)$$

5. ESTIMATES FOR THE BINDING ENERGY OF X^+ TRIONS IN DIFFERENT MATERIALS

Finally, it is useful to present several simple estimates for the trion binding energy in various double-QW heterostructures. To perform these estimations, we need only know the in-plane Bohr radius $a_{\rm B}$, the bulk Bohr energy $E_{\rm B}$, and the ratio of the electron mass to the hole mass for the material of which the QWs are made. For example, typical values for a GaAs QW are as follows [10]:

$$a_{\rm B} = \frac{m_e + m_h}{m_e m_h}\frac{\hbar^2\varepsilon}{e^2} \approx 120 \text{ Å},$$
$$E_{\rm B} = \frac{m_e m_h}{m_e + m_h}\frac{e^4}{2\varepsilon^2\hbar^2} \approx 4.84 \text{ meV}, \quad \frac{m_e}{m_h} \approx 0.196. \quad (15)$$

Using the curves shown in Fig. 3, we can estimate the binding energy of the spatially indirect trion for any value of reduced QW spacing. For an interwell spacing of 50 Å, we find that, for GaAs QWs,

$$d \approx 0.42, \quad \varepsilon_{\rm tr} \approx 0.09\text{Ry} \approx 0.43 \text{ meV}. \quad (16)$$

For ZnSe, $a_{\rm B} \approx 40$ Å, $E_{\rm B} \approx 20$ meV, and $m_e/m_h \approx 0.26$ (according to [21], the data correspond to ~50-Å-wide QWs). Assuming again that the QW spacing is 50 Å, we obtain

$$d \approx 1.25, \quad \varepsilon_{\rm tr} \approx 0.024\text{Ry} \approx 0.48 \text{ meV}. \quad (17)$$

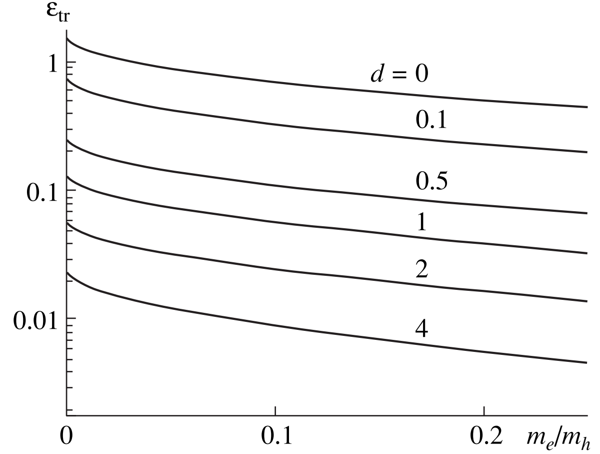

Fig. 3. Dependence of the trion binding energy on the ratio of electron and hole masses for different values of the QW spacing d. The 3D exciton binding energy is taken as the energy unit and the Bohr radius, as the length unit.

These estimates are not very accurate: the error originating from the simplified character of wave function (11) is combined with the inaccuracy of the physical model used, which, for instance, does not take into account that the QWs have finite width. The results (16), (17) are also very sensitive to the choice of the ratio of in-plane electron and hole masses, which may vary with the QW width. In addition, for large values of this ratio, the adiabatic approximation becomes less and less accurate: in an ideal 2D QW ($d = 0$) for $m_e/m_h = 0.25$ this approximation yields a value of the trion binding energy $\varepsilon_{\rm tr} =$ 0.42Ry, while the exact value is $\varepsilon_{\rm tr} = 0.65$Ry [8].

Still, it is noteworthy that we obtain nearly equal values for the trion binding energy in a GaAs- and a ZnSe-based heterostructure, while the exciton binding energy in ZnSe exceeds that in GaAs by more than a factor of 4. This fact is attributed to the difference in the Bohr radii for these semiconductors: in ZnSe, it is three times smaller than in GaAs. Consequently, the same spacing between the QWs 50 Å corresponds to larger reduced spacing d in the case of ZnSe than in the case of GaAs. In addition, the value of the mass ratio taken for ZnSe was larger than that for GaAs. The influence of these two factors appears to be sufficiently strong to compensate even the large difference in the exciton binding energy.

6. CONCLUSION

We obtained a series of dependences for the binding energy of a spatially indirect trion in a double-QW system with spatial separation of the charge carriers on the electron- to the hole-mass ratio for different values of the spacing between the QWs. We showed that the binding energy decreases with an increase in the interwell spacing and the mass ratio. We traced the evolu-

tion of the shape of the effective potential, responsible for the binding of holes in the trion, with the interwell spacing.

ACKNOWLEDGMENTS

The study was supported by the Russian Foundation for Basic Research (project no. 02-02-17610), the Federal Program in Support of Leading Scientific Schools of the Ministry of Industry, Science, and Technology of Russia (project no. 97-1035), and the program "Low-Dimensional Quantum Structures" of the Presidium of the Russian Academy of Sciences.

REFERENCES

1. M. A. Lampert, Phys. Rev. Lett. **1**, 450 (1958).
2. H. A. Bethe, Z. Phys. **57**, 815 (1929).
3. B. Stebe and C. Comte, Phys. Rev. B **15**, 3967 (1977).
4. R. Schilling and D. C. Mattis, Phys. Rev. Lett. **49**, 808 (1982).
5. B. Stebe and A. Ainane, Superlattices Microstruct. **5**, 545 (1989).
6. K. Kheng, R. T. Cox, Y. M. d'Aubigne, *et al.*, Phys. Rev. Lett. **71**, 1752 (1993).
7. B. Stebe, G. Munschy, L. Stauffer, *et al.*, Phys. Rev. B **56**, 12454 (1997).
8. J. Usukura, Y. Suzuki, and K. Varga, Phys. Rev. B **59**, 5652 (1999).
9. W. Y. Ruan, K. S. Chan, H. P. Ho, *et al.*, Phys. Rev. B **60**, 5714 (1999).
10. B. Stebe, A. Moradi, and F. Dujardin, Phys. Rev. B **61**, 7231 (2000).
11. A. Esser, E. Runge, and R. Zimmermann, Phys. Rev. B **62**, 8232 (2000).
12. C. Riva, F. M. Peeters, and K. Varga, Phys. Status Solidi A **178**, 513 (2000).
13. R. A. Sergeev and R. A. Suris, Fiz. Tverd. Tela (St. Petersburg) **43**, 714 (2001) [Phys. Solid State **43**, 746 (2001)].
14. M. M. Dignam and J. E. Sipe, Phys. Rev. B **43**, 4084 (1991).
15. F. M. Peeters and J. E. Golub, Phys. Rev. B **43**, 5159 (1991).
16. E. Binder, T. Kuhn, and G. Mahler, Phys. Rev. B **50**, 18319 (1994).
17. P. Bigenwald and B. Gil, Phys. Rev. B **51**, 9780 (1995).
18. A. J. Shields, J. L. Osborne, D. M. Whittaker, *et al.*, Phys. Rev. B **55**, 1318 (1997).
19. V. B. Timofeev, A. V. Larionov, M. G. Alessi, *et al.*, Phys. Rev. B **60**, 8897 (1999).
20. R. A. Sergeev and R. A. Suris, in *Proceedings of NATO Advanced Research Workshop, St. Petersburg, 2002* (NATO Sci. Ser. II, 2003).
21. G. V. Astakhov, D. R. Yakovlev, V. P. Kochereshko, *et al.*, Phys. Rev. B **65**, 165335 (2002).

Translated by M. Skorikov

Semiconductors, Vol. 37, No. 10, 2003, pp. 1211–1213. Translated from Fizika i Tekhnika Poluprovodnikov, Vol. 37, No. 10, 2003, pp. 1241–1243.
Original Russian Text Copyright © 2003 by Yastrebov, Garriga, Alonso, Ivanov-Omskiĭ.

Spectral Ellipsometry of Amorphous Hydrogenated Carbon Grown by Magnetron Sputtering of Graphite

S. G. Yastrebov*, M. Garriga, M. I. Alonso**, and V. I. Ivanov-Omskiĭ***

**Ioffe Physicotechnical Institute, Russian Academy of Sciences, Politekhnicheskaya ul. 26, St. Petersburg, 194021 Russia*

***Institut de Ciencia de Materials de Barcelona, CSIC 08193 Bellaterra, Spain*

Submitted February 3, 2003; accepted for publication February 4, 2003

Abstract—Polarization angles for films of amorphous hydrogenated carbon produced by magnetron sputtering of graphite in argon–hydrogen plasma have been measured using spectral ellipsometry (in the range of photon energies 1–5 eV). The dispersion of the imaginary and real parts of the permittivity has been reconstructed. It is shown that the data obtained are consistent with the Kramers–Kronig formalism in the frequency range under study. The sum rule allowed us to conclude that the density of states is nonuniformly distributed over energies and to reveal the characteristic threshold energies in the spectrum of the effective density of states (2 and 3.8 eV). The possibility of describing the energy spectrum of electrons using Gaussian curves is shown. The features of the energy distribution of states are attributed to the contribution of the σ and π states. *© 2003 MAIK "Nauka/Interperiodica".*

1. INTRODUCTION

The study of the optical properties of amorphous carbon is important from the viewpoint of application, i.e., for diagnostics of the processes of applying protective coatings [1] and for optimization of diamond synthesis [2, 3]. Moreover, the results are used for solving problems of light scattering in astrophysics [4]. As is known, the data on optical constants of amorphous carbon can be obtained by processing the transmission and reflection spectra [5]; however, this problem statement is not quite correct, in that it is required to find three unknowns; the refractive index, extinction coefficient, and film thickness, from two measurands, i.e., the transmittance and reflectance. The problem can be solved more accurately using ellipsometric methods. In this study, the optical constants of films of amorphous hydrogenated carbon *a*-C:H grown by magnetron sputtering of graphite [6] were reconstructed using ellipsometric data and their features were analyzed. The analysis was carried out under the assumption that both π and σ electronic states contribute to the permittivity

2. EXPERIMENTAL

The technology of *a*-C:H films was considered in detail in [6, 7]. The density of amorphous carbon films was determined by Rutherford backscattering spectrometry to be 1.79 g cm^{-3} [6]. The polarization angles Ψ and Δ were measured using an ellipsometer with a rotating polarizer. As a light source, a 75-W xenon lamp was used. The optical signal was measured using a multichannel photomultiplier positioned at the exit slit of a prism–grating monochromator with a focal length of 750 mm. The setup described allows studies in the spectral range of 1.4–5.1 eV with a resolution of ~1 meV. The permittivity of an amorphous quartz substrate was measured at an angle of light incidence onto a sample of 65°. The spectral dependence of the ellipsometric angles Ψ and Δ was measured in the indicated range of photon energies with a step of 20 meV at angles of incidence of 60°, 65° and 70°.

3. RESULTS AND DISCUSSION

Figure 1 shows the spectra of the functions of ellipsometric angles of the samples under study. The common feature of the samples investigated is similar refractive indices of the substrate (amorphous quartz, 1.468) and the film (~1.6) [8]. In this case, the reflec-

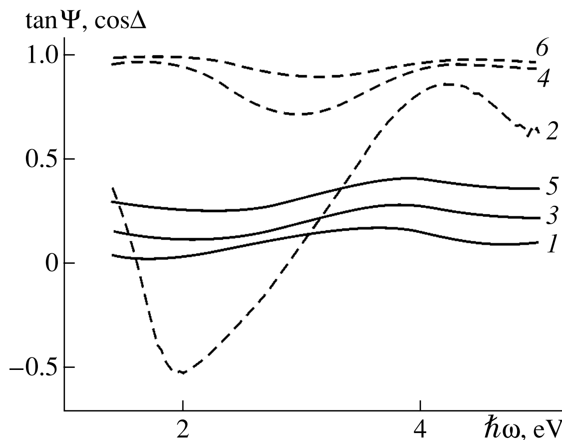

Fig. 1. Spectral dependences of the functions of ellipsometric angles: (*1*, *3*, *5*) tanΨ and (*2*, *4*, *6*) cosΔ. The angle of light incidence is (*1*, *2*) 60°, (*3*, *4*) 65°, and (*5*, *6*) 70°.

1063-7826/03/3710-1211$24.00 © 2003 MAIK "Nauka/Interperiodica"

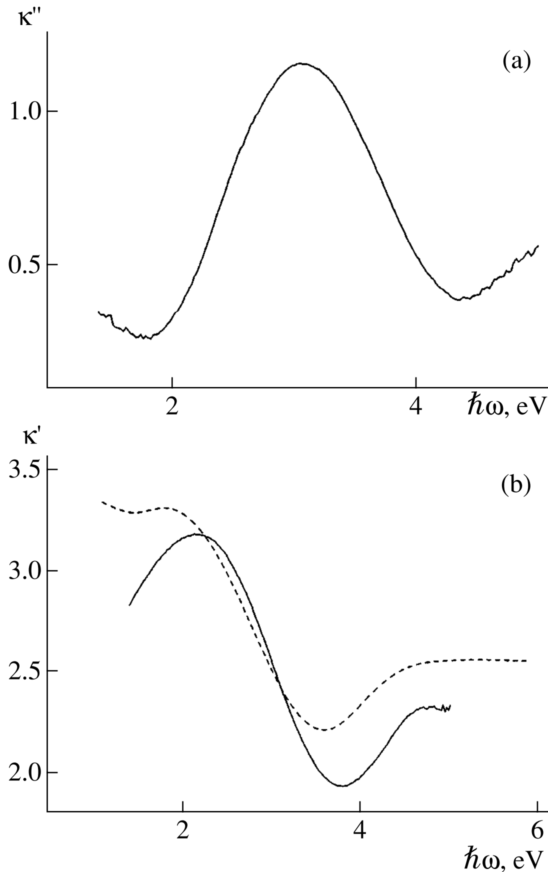

Fig. 2. Permittivity spectrum: (a) imaginary and (b) real parts. The dashed line (b) is the result of applying the Kramers–Kronig transformation to κ'' (a).

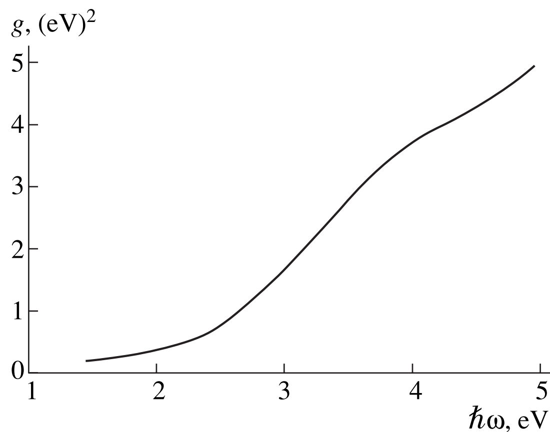

Fig. 3. Spectrum of the total electron density according to formula (1) and to the data of Fig. 2.

tance of the substrate–film interface is lower than 0.5% and can be disregarded. Figure 2 shows the dispersion of the imaginary (κ') and real (κ'') parts of the permittivity, determined by the conventional method [9] under the assumption of zero reflectance. The spectra constructed from the ellipsometric measurements at various angles of incidence differ insignificantly; therefore, the averaged κ' and κ'' curves are shown. Moreover, Fig. 2b shows the real part of the permittivity, calculated for a limited frequency range by applying the Kramers–Kronig transformation to the imaginary part of the permittivity. In the calculation, it was assumed that the imaginary part vanishes both at the zero frequency $\omega = 0$ and at ω_p, where ω_p is the bulk-plasmon frequency. According to [10], $\hbar\omega_p = 22$ eV for amorphous carbon with a density of 1.79 g cm^{-3}. The discrepancy between the calculation and experiment is caused by the roughness of the approximation used. However, even within this approximation, it is evident that the experimental data are consistent with the Kramers-Kronig formalism in the frequency range under study.

We will use the obtained values of the imaginary part κ'' of the permittivity to determine the number of electrons N per unit volume from the sum rule (see [11])

$$g \equiv \frac{4\pi\hbar^2 Ne^2}{m} = \frac{2}{\pi}\int_0^{\hbar\omega} \varepsilon\kappa''(\varepsilon)d\varepsilon, \qquad (1)$$

where ε, m, and e are the electron energy, the effective electron mass, and the elementary charge, respectively. The total electron density calculated using formula (1) is shown in Fig. 3. We can see two inflections in the energy dependence $g \propto N$ (the density of excited electrons); this circumstance, is obviously related to the features in the spectrum of the density of electron states in the amorphous carbon films under study. Differentiating the curve in Fig. 3 with respect to energy, we obtain the spectrum of a quantity, which we refer to as the effective density of states ρ(ω). The spectrum ρ(ω) is shown in Fig. 4, as well as its approximation by two Gaussian curves, which provides the best fit of the experimental data. The possibility of describing the energy spectrum of the effective density of states by Gaussian curves is consistent with the model concepts of [12].

The low-frequency edge of the spectrum of the density of states for amorphous semiconductors is generally described by the Tauc model. This implies presupposes a quadratic dependence of the energy on quasimomentum. In the case under consideration, the fundamental absorption edge corresponding to the low-frequency threshold of the density of states can be determined directly by linear extrapolation. As shown in Fig. 4, the edge energy is 2 eV. Let us compare this result to the experimental value of the energy of the fundamental absorption edge in amorphous carbon grown by magnetron sputtering of graphite [7]. The linear extrapolation of the spectrum of the density of states in Fig. 4 also reveals the second (high-frequency) threshold, with an energy of ~3.8 eV. This threshold may be related to the contribution of electrons in the σ states. The possibility of observing the contribution of the σ states to the energy spectrum of amorphous

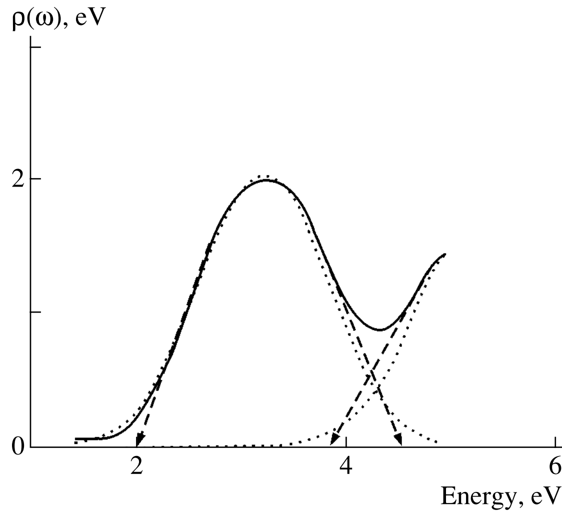

Fig. 4. Spectrum of the effective density of states. The solid line represents the experimental data. The dashed line is the result of approximation of the experimental spectrum by Gaussian profiles; the sum of two Gaussian curves coincides with the experimental data. Arrows indicate the characteristic threshold energies.

hydrogenated carbon is an advantage of the ellipsometric method in comparison with the method commonly used for measuring direct optical absorption. Thus, the results of ellipsometric measurements suggest a nonuniform energy distribution of the effective density of states in *a*-C:H. The electron states with optical-transition energies in the range of 0–3.8 eV observed in the spectra of *a*-C:H, which, are, most likely, caused by the π electrons, form a band ~2.7 eV wide, as shown in Fig. 4. The behavior of the effective density of states in the high-energy region may be caused by the influence of the σ band.

4. CONCLUSION

The spectral ellipsometry of amorphous carbon layers grown by magnetron sputtering of graphite makes it possible to reconstruct the dispersion of the imaginary and real parts of the permittivity. It was shown that the data obtained are consistent with the Kramers–Kronig formalism in the photon-energy range of 1–5 eV. The use of the sum rule allows us to conclude that the energy distribution of the density of states is nonuniform and to reveal the characteristic threshold energies in the spectrum of the effective density of states, ~2 and ~3.8 eV. It was shown that the effective density of energy states is described by the sum of two normal distributions. The nonuniformity of the energy distribution of the electron states may be related to the contributions of the σ and π states.

ACKNOWLEDGMENTS

This study was supported in part by the Russian Foundation for Basic Research (project no. 03-02-16289a) and by the Project DGI MAT2001-1873 (Spain).

REFERENCES

1. J. Angus and C. C. Hayman, Science **24**, 913 (1988).
2. Q. Wang, R. Schliesing, H. Zacharias, and V. Buck, Appl. Surf. Sci. **138–139**, 429 (1999).
3. Q. Wang and V. Buck, Appl. Surf. Sci. **180**, 255 (2001).
4. B. T. Draine and H. M. Lee, Astrophys. J. **285**, 89 (1984).
5. V. I. Ivanov-Omskii, I. N. Krivorotov, and S. G. Yastrebov, Zh. Tekh. Fiz. **65** (9), 121 (1995) [Tech. Phys. **40**, 930 (1995)].
6. T. K. Zvonareva, V. M. Lebedev, T. A. Polyanskaya, *et al.*, Fiz. Tekh. Poluprovodn. (St. Petersburg) **34**, 1135 (2000) [Semiconductors **34**, 1094 (2000)].
7. V. I. Ivanov-Omskiĭ, A. V. Tolmachev, and S. G. Yastrebov, Fiz. Tekh. Poluprovodn. (St. Petersburg) **35**, 227 (2001) [Semiconductors **35**, 220 (2001)].
8. T. K. Zvonareva and L. V. Sharonova, Fiz. Tekh. Poluprovodn. (St. Petersburg) **33**, 742 (1999) [Semiconductors **33**, 684 (1999)].
9. R. M. A. Azzam and N. M. Bashara, *Ellipsometry and Polarized Light* (Elsevier, Amsterdam, 1977).
10. A. C. Ferrari, A. Libassi, B. K. Tanner, *et al.*, Phys. Rev. B **62**, 11089 (2000).
11. L. D. Landau and E. M. Lifshitz, *Course of Theoretical Physics*, Vol. 8: *Electrodynamics of Continuous Media*, 2nd ed. (Nauka, Moscow, 1982; Pergamon Press, Oxford, 1984).
12. V. I. Ivanov-Omskiĭ, A. Tagliaferro, G. Fanchini, and S. G. Yastrebov, Fiz. Tekh. Poluprovodn. (St. Petersburg) **36**, 117 (2002) [Semiconductors **36**, 110 (2002)].

Translated by A. Kazantsev

Semiconductors, Vol. 37, No. 10, 2003, pp. 1214–1216. Translated from Fizika i Tekhnika Poluprovodnikov, Vol. 37, No. 10, 2003, pp. 1244–1247.
Original Russian Text Copyright © 2003 by Averkiev, Kazakova, Piryatinskiĭ, Smirnova.

AMORPHOUS, VITREOUS, AND POROUS SEMICONDUCTORS

Transient Photocurrent and Photoluminescence in Porous Silicon

N. S. Averkiev, L. P. Kazakova, Yu. P. Piryatinskiĭ, and N. N. Smirnova

Ioffe Physicotechnical Institute, Russian Academy of Sciences, St. Petersburg, 194021 Russia

e-mail: kazakova@mail.ioffe.ru

Submitted March 25, 2003; accepted for publication March 25, 2003

Abstract—Transient photocurrent in porous silicon samples subjected to prolonged storage in air has been studied using the time-of-flight technique at temperatures in the range 300–350 K and electric field strengths of 10^4–10^5 V/cm. Photoluminescence has been studied in the same samples at T = 300 K using time-resolved spectroscopy. A conclusion is made on the basis of comparison of the data obtained that localized states play important part in both the processes at characteristic times of these processes falling within the microsecond range. © *2003 MAIK "Nauka/Interperiodica".*

Porous silicon (PS), which possesses a number of unique properties, has been drawing keen attention for several years in view of the possibility of its use in optoelectronics. On the one hand, many of the physical properties of this material are determined by quantum confinement [1–3], and, on the other, it has disordered structure because of the scatter in both the size of nanocrystallites and distances between them [2–5]. Up to now, there has been no complete understanding of the luminescent and transport properties of PS.

In this study, the photoluminescence (PL) and transient current were measured on the same PS samples in order to elucidate the role of localized states.

PS layers were prepared electrochemically from p-type silicon with a resistivity of $\rho \approx 2\ \Omega$ cm in an electrolyte containing (1 : 1) hydrofluoric acid and isopropyl alcohol at current density of 8 mA/cm^2. The PS layer thickness $L = 3.5$ μm. The samples were subjected to prolonged storage in air (>1 month). Since the PS surface rapidly oxidizes after layer fabrication [6], all the measurements were done for oxidized PS. The samples had a "sandwich" structure. In studying the transient current, crystalline silicon was used as an electrode. A semitransparent aluminum film deposited onto PS by vacuum evaporation served as the other electrode. The sample resistance was 10^9–$10^{10}\ \Omega$ at upper electrode area of 3×10^{-2} cm^2.

The transient photocurrent was studied by measuring the transit time in the strong injection mode [7, 8] at temperatures of T = 300–350 K and electric field strengths of $F = 10^4$–10^5 V/cm.

The PL was studied by time-resolved spectroscopy. The recording time delay (t_d) with respect to the excitation pulse peak was varied in the microsecond range (0–45 μs).

Steady-state and time-resolved PL spectra were recorded with an MDR-12 monochromator with a photoelectric attachment and computer interface. The PL was excited with light of nitrogen laser (wavelength, 337.1 nm; pulse duration, 10 ns; pulse repetition frequency, 100 Hz; peak power 5 kW). Time-resolved PL spectra were recorded with a stroboscopic system with a "time window" of 0.1 ns.

Figure 1 shows a stationary PL spectrum (curve *1*) and time-resolved spectra (curves *2–11*), obtained experimentally at T = 300 K. The stationary spectrum has the form of a band peaked at $\lambda \approx 670$ nm. It can be seen that, with the delay time t_d increasing from 0 to 45 μs, the peak of the time-resolved PL spectra shifts to longer wavelengths (650–700 nm).

Analysis of the data obtained shows that the experimentally observed decay of the PL intensity with time t can be described by a set of exponentials [$\exp(-t/\tau)$], where τ is the characteristic time of PL decay. The value of τ increases in every subsequent time interval in which the approximation is performed. In Fig. 2, values of τ, which correspond to PL intensity decay by a factor e,

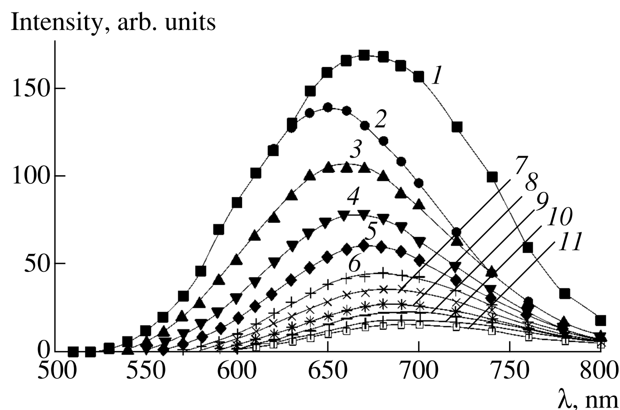

Fig. 1. (*1*) Steady-state and (*2–11*) time-resolved PL spectra at T = 300 K in a porous silicon layer of thickness L = 3.5 μm at different delays of the instant of recording with respect to the laser pulse peak, t_d: (*2*) 0, (*3*) 5, (*4*) 10, (*5*) 15, (*6*) 20, (*7*) 25, (*8*) 30, (*9*) 35, (*10*) 40, and (*11*) 45 μs.

1063-7826/03/3710-1214$24.00 © 2003 MAIK "Nauka/Interperiodica"

are shown in relation to the emission wavelength. It can be seen that, with λ increasing from 560 to 780 nm, the value of τ grows from 6 to 22 μs.

The results are in good agreement with the data reported in [1–4, 9, 10]. It was demonstrated in these studies that time-resolved PL spectra observed experimentally in oxidized PS when t_d falls within the microsecond range can be accounted for not only by quantum confinement in a system of nanocrystals of different sizes [1–3, 9], but also by the influence of localized states in the energy gap of PS [2–4, 10]. This standpoint is confirmed by the results obtained by us in studying the transient photocurrent in the same PS layers on which the PL was measured.

The transient photocurrent observed in the drift of electrons and holes has the form of a continuous structureless decay of the current with time, $I(t)$. The time of carrier transit across the sample was determined from $I(t)$ curves plotted on the log–log scale (Fig. 3). In this figure, the transit time is shown by arrows. It should be noted that, in this experiment, the value of t_T was, similarly to the characteristic time τ of PL decay, within the microsecond range. It was also established that the photocurrent increases with voltage by a nearly quadratic law and is independent of the intensity of the incident light. Such a behavior of the photocurrent corresponds to the flow in a sample of space-charge-limited current (SCLC) under dispersive transport conditions [11]. In this measurement mode, the carrier drift mobility μ can be found in two ways: from the transit time and from the photocurrent value [8, 11]. In the former case, μ is calculated using the formula

$$\mu = \frac{0.8L^2}{t_T U}, \quad (1)$$

where U is the voltage applied to the sample and L is the PS layer thickness. The thus obtained drift mobility of electrons (μ_e) and holes (μ_h) is, respectively, ~2×10^{-3} and 3×10^{-3} cm²/(V s) at $T = 300$ K and $F = 1 \times 10^4$ V/cm. In the latter case, the mobility is found from the expression for the initial current density under SCLC conditions

$$j_0[\mathrm{A/cm^2}] = I_0/S = \mu\varepsilon U^2/2.25 \times 10^{13} L^3, \quad (2)$$

where ε is the dielectric constant. Previously, a value $\varepsilon \approx 5$ has been obtained for porous silicon [12]. When this value is substituted into formula (2), the electron ($\mu_e \approx 1.4 \times 10^{-3}$ cm²/(V s)) and hole ($\mu_h \approx 5 \times 10^{-3}$ cm²/(V s)) mobilities are found to be close to the values calculated from the transit time by formula (1).

This study demonstrated that the carrier drift mobility is weakly dependent on electric field strength ($\mu \propto F^{0.2}$) and grows exponentially with temperature, following the law $\mu = A\exp(-E_a/kT)$, with approximately the same activation energy for μ_e and μ_h: $E_a = (0.35 \pm 0/05)$ eV. The preexponential factor $A \approx 10^4$ cm²/(V s).

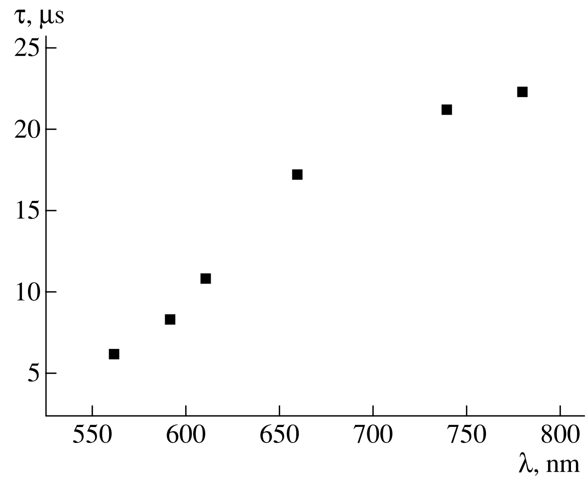

Fig. 2. Characteristic time of PL decay in porous silicon vs. emission wavelength. $T = 300$ K. $L = 3.5$ μm.

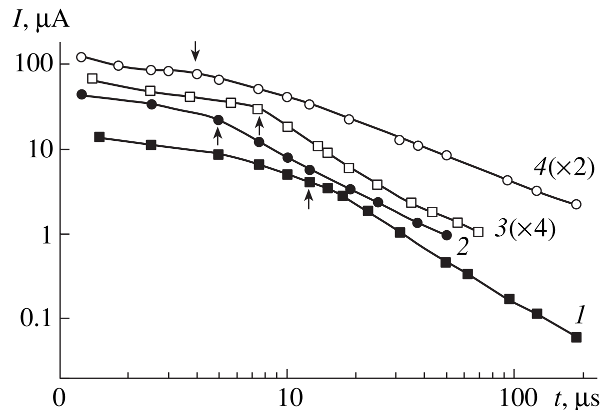

Fig. 3. (*1*, *2*) Electron and (*3*, *4*) hole current vs. time in a porous silicon layer of thickness $L = 3.5$ μm at different voltages U applied to the sample: (*1*, *3*) 5 and (*2*, *4*) 10 V. $T = 300$ K. (*1*, *2*) The values of current are given with the opposite sign. The values of current for curves *3* and *4* are multiplied by 4 and 2, respectively.

The low values of the drift mobility and the type of activation of its temperature dependence, as well as the rather large preexponential factor, indicate that the transport is controlled by capture into localized states. Such a transport is commonly observed in semiconductors with disordered structure [13]. It should be noted, in addition, that the experimentally established behavior of the transient photocurrent curves and drift mobility is characteristic of the dispersive transport occurring in the presence of localized stated distributed over energy in the band gap, $n(E)$ [13, 14].

In [15], a similar behavior of $I(t)$ and μ, observed in PS layers prepared from n-type silicon, was attributed to an exponential distribution $n(E)$ at allowed band edges: $n(E) \propto \exp(-E/E_0)$, where $E_0 = 0.03$ eV. Thus, the data obtained show the existence of “tails” of the density of localized states in the band gap of PS.

The concepts of carrier capture by localized states and gradual motion of the carrier packet deeper into the energy gap over the "tails" of the allowed bands make it possible to account for the specific features of not only the transient photocurrent, but also the PL of oxidized PS. Indeed, as a result of the motion of the packet of carriers captured by localized states deeper into the energy gap, the energy of photons emitted in PL will gradually decrease and, consequently, the time-resolved spectra will shift to longer wavelengths, with the characteristic time of PL decay correspondingly increasing. A similar model of radiative recombination, which assumes carrier capture by localized states distributed over energy, has been applied previously for explaining analogous data on PL for amorphous silicon [16] and was suggested for PS in [2–4, 10].

Thus, it may be concluded that contributions to the experimentally observed time-resolved PL spectra of PS in the microsecond range of t_d are made both by radiative transitions between localized states in the tails of the allowed bands and by band-to-band transitions, with the energy gap between the bands resulting from quantum confinement in nanocrystallites of relatively large size. The localized states may appear for a number of reasons, including structural disorder [2, 13] and the existence of Si=O bonds on the surface of PS [3–6].

The comparison of the experimental data obtained in studying the transient photocurrent and PL in oxidized PS made in this communication suggests that localized states play an important part in both these processes when their characteristic times fall within the microsecond range.

Analysis of the data obtained demonstrates that the behavior of the basic characteristics of the transient photocurrent and time-resolved PL in oxidized porous silicon is similar to that observed in amorphous materials. This fact makes it possible when interpreting the experimental data to use the concepts developed for semiconductors with disordered structure.

We are grateful to A.B. Pevtsov and A.V. Chernyshov for helpful discussions.

The study was carried out in the framework of the program of the Ministry of Industry, Science, and Technology.

REFERENCES

1. A. G. Cullis, L. T. Canham, and P. D. J. Calcott, J. Appl. Phys. **82**, 909 (1997).
2. M. S. Bresler and I. N. Yassievich, Fiz. Tekh. Poluprovodn. (St. Petersburg) **27**, 871 (1993) [Semiconductors **27**, 475 (1993)].
3. O. Bisi, S. Ossicini, and L. Pavesi, Surf. Sci. Rep. **38**, 1 (2000).
4. S. Komuro, T. Kato, and T. Morikawa, J. Appl. Phys. **80**, 1749 (1996).
5. N. S. Averkiev, L. P. Kazakova, E. A. Lebedev, and N. N. Smirnova, Fiz. Tekh. Poluprovodn. (St. Petersburg) **35**, 609 (2001) [Semiconductors **35**, 588 (2001)].
6. M. V. Wolkin, J. Jorne, P. M. Fauchet, *et al.*, Phys. Rev. Lett. **82**, 197 (1999).
7. W. E. Spear, J. Non-Cryst. Solids **1**, 197 (1969).
8. M. A. Lampert and P. Mark, *Current Injection in Solids* (Academic, New York, 1970; Mir, Moscow, 1973).
9. Y. H. Xie, W. L. Wilson, F. M. Ross, *et al.*, J. Appl. Phys. **71**, 2403 (1992).
10. L. R. Tessler, F. Alvarez, and O. Teschke, Appl. Phys. Lett. **62**, 2381 (1993).
11. M. Silver, E. Snow, D. Wesson, and K. Okamoto, J. Non-Cryst. Solids **66**, 237 (1984).
12. L. P. Kazakova, A. A. Lebedev, and É. A. Lebedev, Fiz. Tekh. Poluprovodn. (St. Petersburg) **31**, 609 (1997) [Semiconductors **31**, 517 (1997)].
13. N. F. Mott and E. A. Davis, *Electronic Processes in Non-Crystalline Materials*, 2nd ed. (Clarendon Press, Oxford, 1979; Mir, Moscow, 1982).
14. A. I. Rudenko and V. I. Arkhipov, Philos. Mag. B **45**, 189 (1982).
15. N. S. Averkiev, L. P. Kazakova, and N. N. Smirnova, Fiz. Tekh. Poluprovodn. (St. Petersburg) **36**, 355 (2002) [Semiconductors **36**, 336 (2002)].
16. C. Tsang and R. A. Street, Phys. Rev. B **19**, 3027 (1979).

Translated by M. Tagirdzhanov

Semiconductors, Vol. 37, No. 10, 2003, pp. 1217–1221. Translated from Fizika i Tekhnika Poluprovodnikov, Vol. 37, No. 10, 2003, pp. 1248–1252.
Original Russian Text Copyright © 2003 by Mokerov, Pozela, Fedorov.

PHYSICS OF SEMICONDUCTOR DEVICES

Electron Transport in Unipolar Heterostructure Transistors with Quantum Dots in Strong Electric Fields

V. G. Mokerov*, Yu. K. Pozela, and Yu. V. Fedorov***

*Institute of Ultra High Frequency Semiconductor Electronics, Russian Academy of Sciences, Moscow, 117105 Russia
e-mail: mok@mail.cplire.ru
**Semiconductor Physics Institute, 26000, Vilnius, Lithuania
e-mail: pozela@uj.pfi.lt

Submitted November 25, 2002; accepted for publication December 23, 2002

Abstract—A model for the explaining specific features of the electron transport in strong electric fields in the quantum-dot unipolar heterostructure transistor (AlGaAs/GaAs/InAs/GaAs/InAs) is presented. It is shown that the two-step shape of the output current–voltage characteristic $I_D(V_D)$ and the anomalous dependence of the drain current I_D on the gate voltage V_G are caused by the ionization of quantum dots in the strong electric field at the drain gate edge. The ionization of quantum dots sets in at the drain voltage V_D that exceeds the V_{D1} value, at which the $I_D(V_D)$ dependence is saturated (the first step of the *I–V* characteristic). With the subsequent increase in V_D, i.e., for $V_D > V_{D1}$, the $I_D(V_D)$ dependence has a second abrupt rise due to the ionization of quantum dots, and then, for $V_D = V_{D2} > V_{D1}$, the current I_D is saturated for the second time (the second step in the current–voltage characteristic). It is suggested to use this phenomenon for the determining the population of quantum dots with electrons. The model presented also describes the twice-repeated variation in the sign of transconductance $g_m = dI_D/dV_G$ as a function of V_G. *© 2003 MAIK "Nauka/Interperiodica".*

1. INTRODUCTION

It was originally shown [1–3] that the dependences of the drain current I_D on the drain voltage V_D and the gate voltage V_G for a heterostructure unipolar transistor with quantum dots (QD transistor) differ radically from the characteristics of the conventional transistor. First, the $I_D(V_D)$ dependence has not only one but two steps with the saturation of the current and, second, the negative bias V_G does not block but unblocks the electron channel of the transistor. In this report, we suggest a calculation model that explains the unusual characteristics of QD transistors reported previously [1–3].

2. THE STRUCTURE OF A QD TRANSISTOR

The QD transistor, which was investigated by Mokerov *et al.* [1–3], is based on AlGaAs/GaAs/InAs/GaAs/InAs heterostructures with modulation doping. In these structures, InAs QDs with zero-dimensional electrons are incorporated into the GaAs quantum well (QW) with a two-dimensional (2D) electron gas. According to [4–10], the QDs in the InAs/GaAs system are lens-shaped. According to [1–3], their diameter $D_T = 40$ nm, and their height $h = 5$ nm.

Let us present the transistor channel, which includes the conducting part, namely, the QW, and the multitude of nonconducting QDs with the electrons, which are trapped by QDs and, correspondingly, do not contribute to conduction. Thus, the electrons introduced into the channel are distributed between the QDs and the QW, and this distribution governs the channel conductivity.

3. THE POPULATION OF QUANTUM DOTS IN THE TRANSISTOR CHANNEL

For a conventional QW, i.e., without QDs, n_{s0} carriers emerge under equilibrium conditions due to modulation doping. On introduction of QDs of density N_T into this QW, a fraction of carriers n_d are trapped at the E_D level in QDs. This reduces the number of free carriers n_{w0} in the QW by the n_d quantity. Due to this circumstance,

$$n_{s0} = n_{w0} + n_d. \quad (1)$$

The concentration of 2D carriers in the QW of the E_w subband is

$$n_{w0} = \int_{E_w}^{\infty} D f_F(E - E_F) dF = DkT \ln\left(1 + \exp\frac{E_F - E_w}{kT}\right) \quad (2)$$

or, for $E_F - E_w > kT$,

$$n_{w0} = D(E_F - E_w), \quad (3)$$

where $f_F(E - E_F)$ is the Fermi–Dirac distribution function and $D = m/\pi\hbar^2$ is the density of 2D electron states

1063-7826/03/3710-1217$24.00 © 2003 MAIK "Nauka/Interperiodica"

in a QW. For GaAs, $D = 2.8 \times 10^{13}$ cm^{-2} eV^{-1}. The carrier density in the QW at the E_D level equals

$$n_d = \int_{E_D}^{\infty} \delta(E-E_D) N_D f_F(E-E_F) dE = \frac{N_D}{1+\exp[(E_D-E_F)/kT]}, \qquad (4)$$

where $\delta(E-E_D)$ is the delta function, $N_D \approx N_T M$, and M is the population of the QD with electrons, which is estimated as one to three electrons. It follows from expressions (1), (3), and (4) that, by varying in any way the total carrier concentration n_{s0} in the QD, we change the position of the Fermi level and thereby the number of carriers trapped at the QDs. These carriers do not contribute to the conduction.

In such QDs, the electron-trapping energy determined by the QD height h, i.e., by the QD narrow part, constitutes a band composed of closely spaced levels, which arise due to quantization in the broad part, i.e., by the extension of the QD along the layer plane D_T. The spread of QD heights h leads to the additional broadening of the electron-trapping level in the QD array under investigation. Usually (see, for example, [8]), this broadening amounts to ~50 meV; it is Gaussian-shaped. The energy of the fundamental optical transition E_0 for the QDs is ~1 eV. The level depth for electrons and holes in the QDs is 0.27 and ~0.07 eV, respectively [6]. The observed QD density is (3–10) × 10^{10} cm^{-2}. It should be noted that in our case the InAs QD is located in the 2D GaAs QW rather than in the three-dimensional GaAs matrix as in reports cited above. Thus, the channel of the transistor investigated by us can be presented as consisting of two parts. One of them, namely, the conducting part, is presented by the high electron-mobility transistor (HEMT) QW, and the second, i.e., the nonconducting part, is presented by the QDs.

For simplicity, we will make allowance for the only 2D subband E_W in the QW and one level E_D in the QDs. It seems difficult to make an allowance for their larger number. We assume that the level of modulation doping for the structure under consideration is such that under thermal equilibrium, the E_D level in the QDs is occupied, i.e., $E_F > E_D$.

The number of carriers at point x along the HEMT channel for the gate voltage V_G and the drain voltage V_D relative to the source is

$$n_s(x) = \frac{C}{e}[V_g - \varphi(x)]. \qquad (5)$$

Here, C is the gate capacitance; $\varphi(x)$ is the potential along the channel, which is induced by the drain current I_D; $V_g = V_G + V_T$; and V_T is the threshold transistor voltage, which is governed by the electron density n_{s0} in the channel and at the QDs for $V_G = V_D = 0$; i.e.,

$$\frac{C}{e}V_T = n_{s0}. \qquad (6)$$

By controlling the number of carriers in the HEMT channel using the gate and drain voltages, we control the Fermi level energy and, thus, the population of QDs with electrons.

4. THE DRAIN CURRENT IN A QD FIELD-EFFECT TRANSISTOR

With increasing drain voltage V_D, the electric field in the channel F increases. For a sufficiently strong field F, the QDs in the channel can be ionized. The escape of electrons from the QDs will increase their concentration in the QW and, correspondingly, the channel conductivity and the I_D current.

The known physical mechanisms of generation of electrons from the QDs, namely, the tunneling or impact ionization, lead to a very strong dependence of the rate of ionization on the field strength F above its critical value F_c. This allows us to assume that as soon as the field in a certain x_c point of the channel will exceed the critical value, i.e.,

$$\left.\frac{\partial\varphi(x)}{\partial x}\right|_{x_c} \geq F_c,$$

the complete ionization of QDs will occur in the region $x > x_c$.

If the field induced by the drain current in the channel is weak, i.e., $\partial\varphi/\partial x < F_c$, no ionization of QDs occurs anywhere in the channel and the density of conduction electrons in the channel will be equal to

$$n_w(x) = \frac{C}{e}[V_g - \varphi(x)] - n_d, \quad x < x_c. \qquad (7)$$

However, if the field F induced by the drain current is sufficiently strong and the conditions for ionization of QDs are met, the density of conduction electrons in the channel region at $x > x_c$ increases by the quantity n_d:

$$n_w(x) = \frac{C}{e}[V_g - \varphi(x)] \quad \text{for} \quad \left.\frac{d\varphi}{dx}\right|_{x \geq x_c} \geq F_c, \quad x \geq x_c. \qquad (8)$$

The drain current (see, for example, [11]) equals

$$I_D = \frac{d}{L}\int_0^{V_D} \sigma_w(x) d\varphi(x), \qquad (9)$$

where d is the width and L is the length of the channel from the drain to the source, which is equal to the gate length; $\sigma_w = e\mu n_w(x)$; μ is the mobility; and n_w is the density of electrons not trapped at $x < x_c$.

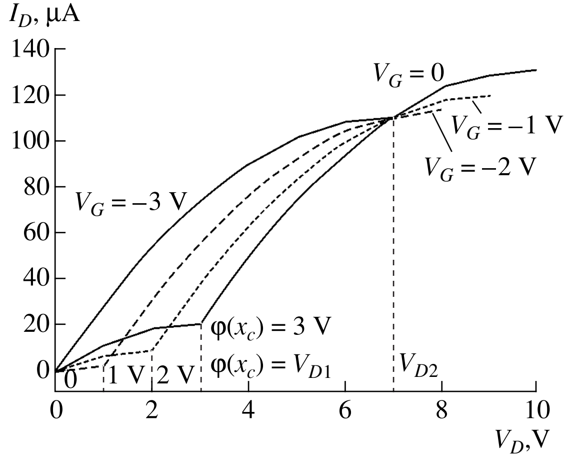

Fig. 1. Calculated $I_D(V_D)$ dependences for the QD transistor for several gate voltages V_G.

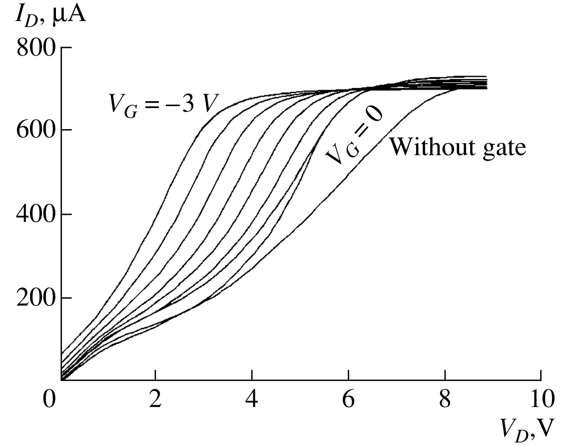

Fig. 2. Experimental $I_D(V_D)$ dependences for the QD transistor for various gate voltages V_G. The step of variation in the V_G equals –0.5 V.

Drain current (9) with allowance made for formulas (7) and (8) equals

$$I_D = \frac{e\mu d}{L}\left\{\int_0^{\varphi(x_c)}\left[\frac{C}{e}(V_g - \varphi(x)) - n_d\right]d\varphi + \int_{\varphi(x_c)}^{V_D}\frac{C}{e}(V_g - \varphi(x))d\varphi\right\}, \tag{10}$$

where $\varphi(x_c)$ is the potential induced by the drain current at the point x_c, at which

$$\left.\frac{\partial\varphi(x)}{\partial x}\right|_{x_c} = F_c.$$

For $V_D \le \varphi(x_c)$ (or $L < x_c$) over the entire channel length, the electrons associated with the QDs do not contribute to the conduction and the drain current equals

$$I_D = \frac{e\mu d}{L}\left\{\frac{C}{e}\left(V_g V_D - \frac{V_D^2}{2}\right) - n_d V_D\right\}, \quad L < x_c. \tag{11}$$

Taking into account the equality $(C/e)V_T = n_{w0} + n_d$, we can rewrite Eq. (11) as

$$I_D = \frac{e\mu d}{L}\frac{C}{e}\left\{\left(V_G + \frac{e}{C}n_{w0}\right)V_D - \frac{V_D^2}{2}\right\}, \quad L < x_c. \tag{12}$$

The current–voltage (I–V) characteristic of the transistor in the absence of excitation of electrons from the QDs differs from the I–V characteristic of a conventional transistor without QDs only by a smaller number of electrons contributing to the channel conductivity.

For $\varphi(x_c) \le V_D$ (or $x_c \le L$), according to Eq. (10), the drain current equals

$$I_D = \frac{e\mu d}{L}\left\{\frac{C}{e}\left(V_g V_D - \frac{V_D^2}{2}\right) - n_d\varphi(x_c)\right\}, \quad x_c < L. \tag{13}$$

The strongest fields, which are sufficient for ionization in the channel of the field-effect transistor, are formed in the undergate region depleted of electrons at the drain contact. The highest depletion is attained for $V_D = V_G + (e/C)n_{w0}$, when the saturation of the channel current occurs (see Eq. (12)). Therefore, as the condition for onset of ionization of QDs at the drain channel terminates, $x_c = L$, we take the drain voltage V_{D1}:

$$\varphi(x_c = L) = V_{D1} = V_g - \frac{e}{C}n_d. \tag{14}$$

For $V_d \ge V_{D1}$, the ionization of QDs radically affects the V_D dependence of I_D. Figure 1 shows the family of $I_D(V_D)$ dependences for various V_G under the assumption that $\varphi(x_c)$, according to expression (14), does not vary with increasing V_D. For the calculations of $I_D(V_D)$, it is assumed that $C/e = 10^{10}$ cm^{-2} V^{-1}, $\mu = 2.8 \times 10^3$ cm^2/(V s), $n_{s0} = 10^{11}$ cm^{-2}, $V_T = 10$ V, $d/L = 1.0$, $n_d = 7 \times 10^{10}$ cm^{-2}, and, consequently, $\varphi(x_c = L) = V_G + 3$ V.

The comparison of the calculated $I_D(V_D)$ curves with the I–V characteristics observed experimentally, which are shown in Fig. 2, shows that the calculation accounts for the following three characteristic features of the I–V characteristic of the QD transistor, which are observed experimentally.

First, in contrast with a conventional field-effect transistor, instead of one step, two steps are observed in the I–V characteristic. The first step corresponds to the I_D current when a fraction of electrons is trapped by a QD, and the second step corresponds to the escape of these electrons from a QD.

Second, the value of V_{D1} changes with variation in the gate voltage V_G by the magnitude of this variation. This corresponds to the shift of the kink in the *I–V* characteristics, which is observed experimentally as negative V_G increases, and to an anomalous increase in I_D on blocking the channel with increasing negative V_G (Figs. 1, 2).

Third, in the region of the second step, the *I–V* characteristics, which correspond to various V_G, intersect at the step fixed point, $V_D = V_{D2}$.

It follows from Eq. (13) that $I_D(V_D)$ is independent of the gate voltage V_G at the point $V_D = V_{D2}$ and has the form

$$I_{D2}(V_{D2}) = \frac{\mu C d}{2L}V_{D2}^2 \quad \text{for} \quad V_{D2} = \frac{e}{C}n_d. \tag{15}$$

In Fig. 1, $V_{D2} = 7$ V.

This permits one to determine experimentally the population of QDs n_d in 2D structures with QDs by measuring V_{D2} or I_{D2}/V_{D2}:

$$\frac{I_{D2}}{V_{D2}} = \frac{e\mu d}{2L}n_d. \tag{16}$$

The experimental *I–V* characteristics of the QD transistor (Fig. 2) yield $V_{D2} = 6$ V, which means that $n_d = 6 \times 10^{10}$ cm^{-2} for $C/e = 10^{10}$ V^{-1}.

In the absence of gate voltage ($V_G = 0$, $V_g = V_T$), the current in the structure channel takes the form

$$I_{D0} = \frac{e\mu d}{L}\left\{\frac{C}{e}\left(V_T V_D - \frac{V_D^2}{2}\right) - n_d V_D\right\} \quad \text{for} \quad V_D < V_{D10} = V_T - \frac{e}{C}n_d, \tag{17}$$

$$I_{D0S} = \frac{e\mu d}{L}\left\{\frac{C}{e}\left(V_T V_D - \frac{V_D^2}{2}\right) - n_d V_{D10}\right\} \quad \text{for} \quad V_D > V_{D10}. \tag{18}$$

For structures without gates, the population of QDs can be also determined from the first kink of the *I–V* characteristic (at the point of onset of the ionization of QDs) $V_D = V_{D10}$, and from the second kink at the onset of saturation, V_{D20}; i.e.,

$$V_{D10} = V_T - \frac{e}{C}n_d, \quad V_{D20} = \frac{e}{C}n_d. \tag{19}$$

Note that the quantities V_T and C, which determine the magnitude of the charge induced in the channel and trapped by the QDs, depend on the structure and conductivity of the surface layer over the channel. For a structure without a gate, i.e., with the free surface, a considerable variation in the $I_D(V_D)$ dependence was observed on etching off the surface layer [1].

The *I–V* characteristics of the transistor observed experimentally (Fig. 2) differ from those calculated for low V_D, $V_D < V_{D1}$ (Fig. 1). It is important that the I_D current is also observed experimentally for $V_D = 0$ if $V_G \neq 0$. This is indicative of the presence of the conducting layer, which is parallel to the channel between the source and the drain. The metal gate shunts this undergate layer, and the voltages V_G and V_D applied to the layer are concentrated at the segments gate–source and gate–drain. The concentration of the voltage at these segments can cause the ionization of QDs in the transistor channel. The parallel current through the conducting layer adds to the current through the channel. This is clear that the parallel current along the conducting layer is not equal to zero for $V_D = 0$, as observed experimentally.

Naturally, the conducting layer, which is parallel to the channel, also affects the current through a heterostructure without a gate. Such a layer affects not only the potential distribution along the channel but also the V_T and n_d quantities. It was observed experimentally that the etching off of this layer restores the transistor characteristic of the channel in a heterostructure without a gate.

5. THE GAIN OF THE QD FIELD-EFFECT TRANSISTOR

The gain in the absence of ionization of QDs ($V_D < V_{D1}$) is given by

$$g_m = \frac{dI_D}{dV_g}\frac{1}{d} = \frac{e\mu}{L}\frac{C}{e}V_D \tag{20}$$

at $V_D < V_g$ and

$$g_{mS} = \frac{e\mu}{L}\left(\frac{C}{e}V_g - n_d\right) \tag{21}$$

at $V_D \geq V_g$ (for the region of saturation of the current). The expression for the gain g_m for $V_D < V_{D1}$ coincides with the expression for g_m of the conventional transistor. In the case of ionization of QDs ($V_D > V_{D1}$), the gain, according to expression (13) is described by the expressions

$$g_m = \frac{e\mu}{L}\left(\frac{C}{e}V_D - \frac{dn_d\varphi(x_c)}{dV_g}\right) \tag{22}$$

at $V_D < V_g$ and

$$g_{mS} = \frac{e\mu}{L}\left(\frac{C}{e}V_g - \frac{dn_d\varphi(x_c)}{dV_g}\right) \tag{23}$$

in the region of saturation of I_D (at $V_D \geq V_g$).

If n_d is independent of V_g and $\varphi(x_c)$ is determined by expression (14), $dn_d\varphi(x_c)/dV_g = n_d$. In this case, for $V_D = V_{D2}$ (Eq. (15)), as has been already noted, $g_m = 0$.

For $V_D \geq V_{D1}$, the coefficient $g_m < 0$ if the number of free electrons in the channel is less than the number of electrons trapped at the QDs, i.e., $n_w < n_d$. If $n_d > 2CV_D/e$, the transconductance of the QD transistor

exceeds the transconductance of the conventional transistor.

Note that the coefficient g_m changes sign twice with increasing V_D: for $V_D < V_{D1}$ and $V_D > V_{D2}$, the coefficient g_m is positive, and for $V_{D1} < V_D < V_{D2}$, this coefficient is negative. This extends the functional capabilities of the field-effect QD transistor.

The transconductance of the QD transistor can be considerably increased by controlling the quantity n_d by the gate voltage and by increasing the second (negative) term in equality (23) due to $dn_d/dV_g \neq 0$.

In the carrier-depleted region of channel, ionization (variation in the population) of QDs can occur due to lowering of the Fermi level E_F relative to the E_D level in the QDs (see Section 3) with variation of the gate voltage V_g. This circumstance ensures $dn_d/dV_g \neq 0$ and an increase in the QD transistor gain.

6. CONCLUSIONS

The calculation model, which accounts for the specific features of characteristics of the high-field electron transport observed experimentally for the unipolar heterostructure QD transistor, is suggested. The specific features include the two-step shape of the drain *I–V* characteristic and anomalous dependence of the drain current I_D on the gate voltage V_G. It is shown that these specific features are caused by the effect of ionization of QDs in the strong electric field at the end of the drain gate. The ionization of QDs sets in for a drain voltage V_D that exceeds a certain value $V_{D1} = V_g - (e/C)n_d$, at which the onset of saturation of the $I_D(V_D)$ dependence occurs (the first step in the V_D dependence of I_D). Upon further increase in the drain voltage, for $V_D > V_{D1}$, the curve $I_D(V_D)$ again rises abruptly due to the effect of ionization of QDs. After this rise, the dependence I_D (V_D) levels off again for $V_D = V_{D2} > V_{D1}$, where $V_{D2} = (e/C)n_d$ (the second step in the output *I–V* characteristic). The use of this phenomenon is suggested for determining the population of QDs with electrons (by measuring V_{D2} or I_D/V_{D2}). The model suggested also describes the twice-repeated variation in the sign of the transistor transconductance $g_m = dI_D/dV_G$ as a function of V_G. It is shown that if the density of electrons trapped by QDs n_d exceeds the density of 2D electrons in the channel by a factor of more than two, the transconductance of the QD transistor can exceed the transconductance of the transistor without QDs. In this case, the population of QDs is easily controlled by varying the total electron density in the channel.

REFERENCES

1. V. G. Mokerov, Yu. V. Fedorov, L. E. Velikowski, and M. Yu. Scherbakova, in *Proceedings of 9th International Symposium on Nanostructures: Physics and Technology, St. Petersburg, 2001* (Ioffe Physicotechnical Inst., St. Petersburg, 2001), p. 453.
2. V. G. Mokerov, Yu. V. Fedorov, L. É. Velikhovskiĭ, and M. Yu. Shcherbakova, Dokl. Akad. Nauk **375**, 754 (2000) [Dokl. Phys. **45**, 649 (2000)].
3. V. G. Mokerov, Yu. V. Fedorov, L. É. Velikovskiĭ, and M. Yu. Scherbakova, Nanotechnology **12**, 552 (2001).
4. D. Bimberg, M. Grundmann, and N. N. Ledentsov, *Quantum Dot Heterostructures* (Wiley, New York, 1999), p. 122.
5. L. Jacak, P. Hawrylak, and A. Wojs, *Quantum Dots* (Springer, Berlin, 1998).
6. P. N. Brounkov, N. N. Faleev, Yu. G. Musikhin, *et al.*, in *Proceedings of 23rd International Conference on Physics of Semiconductors, Berlin, 1996* (World Sci., Singapore, 1996), p. 1361.
7. P. N. Brunkov, S. G. Konnikov, V. M. Ustinov, *et al.*, Fiz. Tekh. Poluprovodn. (St. Petersburg) **30**, 924 (1996) [Semiconductors **30**, 492 (1996)].
8. I. A. Karpovich, A. P. Gorshkov, S. B. Levichev, *et al.*, Fiz. Tekh. Poluprovodn. (St. Petersburg) **35**, 564 (2001) [Semiconductors **35**, 543 (2001)].
9. C. Lingk, W. Helfer, G. von Plessen, *et al.*, Phys. Rev. B **62**, 13588 (2000).
10. A. Patane, A. Polimeni, L. Eaves, *et al.*, Phys. Rev. B **62**, 13595 (2000).
11. V. A. Gergel', V. G. Mokerov, M. V. Timofeev, and Yu. V. Fedorov, Fiz. Tekh. Poluprovodn. (St. Petersburg) **34**, 239 (2000) [Semiconductors **34**, 233 (2000)].

Translated by N. Korovin

Semiconductors, Vol. 37, No. 10, 2003, pp. 1222–1228. Translated from Fizika i Tekhnika Poluprovodnikov, Vol. 37, No. 10, 2003, pp. 1253–1259.
Original Russian Text Copyright © 2003 by Naumova, Antonova, Popov, Nastaushev, Gavrilova, Litvin, Aseev.

PHYSICS OF SEMICONDUCTOR DEVICES

Silicon-on-Insulator Nanotransistors: Prospects and Problems of Fabrication

O. V. Naumova, I. V. Antonova, V. P. Popov, Yu. V. Nastaushev, T. A. Gavrilova, L. V. Litvin, and A. L. Aseev

Institute of Semiconductor Physics, Siberian Division, Russian Academy of Sciences, pr. Akademika Lavrent'eva 13, Novosibirsk, 630090 Russia

e-mail: naumova@isp.nsc.ru

Submitted January 8, 2003; accepted for publication January 13, 2003

Abstract—Basic problems encountered in the fabrication of nanosized transistors are considered. Field-effect transistors, which are based on silicon-on-insulator structures, have various gate configurations, and are an alternative to conventional metal–oxide–semiconductor (MOS) transistors, are tested. It is shown that the structures of multichannel transistors, which are based on uniformly doped layers of silicon-on-insulator and have a three-dimensional gate, are the most promising: these structures make it possible to solve the problems of both the short-channel effect for a conventional MOS transistor and the low current density in nanotransistors with a single channel. *© 2003 MAIK "Nauka/Interperiodica".*

1. INTRODUCTION

Progress in the technology of silicon-on-insulator (SOI) structures have stimulated an intensive search for new structural and technological approaches to the fabrication of nanoscale field-effect transistors (FETs). SOI transistors offer a number of advantages over their analogues based on bulk silicon even in the range of micrometer sizes; these advantages are related to perfect insulation in SOI structures and consist of a lower power consumption, higher breakdown voltages, and a higher response speed [1–3]. The advantages of SOI structures in the domain of nanometer sizes are caused first of all by the fact that these structures make it possible to solve a number of problems inherent to short-channel transistors and also to fabricate new devices based on quantum-mechanical size-related effects.

The aim of this study was to analyze the problems related to fabrication of nanosized transistors based on SOI structures and to test certain structures that are alternatives to the conventional metal–oxide–semiconductor (MOS) transistor.

2. EXPERIMENTAL

As the starting material, we used SOI structures fabricated by the Smart-Cut method [4]; the thickness of the top silicon layer was 480 nm, and the thickness of the buried oxide was 320–450 nm. The top silicon layer in the SOI structures was doped with boron or phosphorus to concentrations of 1×10^{16}–2×10^{19} cm^{-3} and was then thinned to a thickness of 40–8 nm by multiple oxidation at temperatures of 900–1000°C. The optical and electron-beam lithography methods [5] were then used to form device structures on the silicon film obtained. Specific structures will be described in more detail as the results are presented.

3. CONVENTIONAL MOS TRANSISTORS: LIMITING DIMENSIONS AND POSSIBLE ALTERNATIVE DESIGNS

In quite natural desire of manufacturers of integrated circuits (ICs) to increase the integration level (the number of transistors on a chip) and the IC response speed (the clock rate of microprocessors) is realized by reducing the linear dimensions of circuit components, the most important of which remains an MOS transistor. However, the Dennard scaling principle [6] is applicable only if the MOS-transistor gate dimension is no smaller than about 100 nm, so that the conventional complementary MOS technology for silicon can be used; in contrast, problems in fabrication of virtually any element of the transistor arise if the dimensions are smaller than 100 nm [7]. Some of the problems related to short-channel transistors and possible solutions to these problems are given in the table.

One of the main problems of short-channel transistors consists in the punch-through effect for depletion regions for the source and drain due to the reverse-biased drain–base junction (under certain conditions, the transistor-channel length becomes comparable to the width of the space-charge region (SCR) of the drain junction). As can be seen from the table, this problem can be solved by increasing the doping level in the base. However, heavier doping leads to a decrease in the charge-carrier mobility (and, consequently, to a decrease in the response speed); to an increase in the threshold voltage and, most important, in the leakage current; and to an increase in the probability of break-

1063-7826/03/3710-1222$24.00 © 2003 MAIK "Nauka/Interperiodica"

Main problems in the fabrication of nanometer-scale MOS transistors. The most important problems and most promising methods for solution are italicized

	Problems	Solutions
1	*The gate SiO_2 layer*:	
	leakage currents if the layer thickness is less than 2 nm	Replacement of SiO_2 by an insulator with a higher permittivity. Oxides of rare-earth metals are considered the most promising.
2	*Drain–source regions* (short-channel effects):	
	(i) drive-in diffusion of implanted impurity with subsequent activation (formation of shallow junctions);	(1) Preliminary amorphization, irradiation with an ion beam in the nonchanneling direction; (2) Rapid thermal annealing; (3) Rapid thermal gas-phase diffusion, rapid thermal solid-source diffusion, laser-assisted doping, and *immersion–plasma implantation*.
	(ii) punch-through effect for depletion regions for the source and drain due to the reverse-biased drain–base junction;	(1) An increase in the doping level of the base region; (2) *Fabrication of MOS transistors on the basis of SOI structures using completely depleted top silicon layers.*
	(iii) leakage currents between gate and drain at the drain junction at high electric-field strength in the region of the gate overlapping with the drain (tunneling, injection of hot electrons);	Introduction of additional, lightly doped drain regions.
	(iv) leakage currents, an increase in capacitance of the drain–base junction, and an increase in the threshold voltage at a high doping level in the base region; and	Formation of the regions which surround the drain–source layers and have the opposite conductivity type.
	(v) a decrease in the series resistance of drain–source regions.	Formation of “elevated” drain–source regions (for example, epitaxial overgrowth).
3	*Gate*:	
	(i) a decrease in the lithographic (topological) length of the gate; and	Electron-beam lithography, X-ray lithography in the region of extreme ultraviolet radiation (λ = 13 nm), and ion-beam lithography.
	(ii) depletion of polysilicon gate (parasitic capacitance).	The use of metallic gates for *n*- and *p*-Si.

down of the drain *p–n* junction. Therefore, if the length of the transistor channel is several tens of nanometers, an efficient method for suppressing the punch-through effect consists in redistribution of the potential in the transistor base by applying a voltage to an additional gate. This redistribution can be accomplished if transistors are fabricated on SOI structures with completely depleted films (the thickness of the top silicon layer is smaller than the width of the depletion layer induced by the voltage applied to one of the gates). In particular, the substrate can serve as an additional gate in SOI structures.

In order to suppress the short-channel effects, voltages of different polarity should be applied to the *n*- and *p*-MOS transistors; thus, the use of the substrate as the control electrode is not the optimal variant for ICs. It is more promising to use (i) the dual-gate structures of the SOI–MOS transistors, in which case the gates are located on both sides and in the plane of the channel; (ii) structures in which the platelike transistor body stands as if edgewise rather than lying in the horizontal plane on the substrate (the so-called dual-gate FinFET, with the channels being induced by the voltages applied to the gates on both sides of the plate); and (iii) the structures in which the gate encompasses the channel on three sides (inversion channels are now formed under the gate on three sides [1, 2, 8]), which makes it possible to increase the current-flow area with the total device area remaining unchanged. In addition, according to the estimates made by Intel Corp., the heat release becomes unacceptably high if an MOS transistor fabricated using the conventional technology has a dimension of about 30 nm. The three-dimensional (3D) technology makes it possible to appreciably reduce the losses by heat release.

Still, the question arises as to what extent the length of the channel in a conventional FET can be reduced. Japanese researchers ascertained that electrons tunnel directly from the source to the drain through the narrow conduction band of the *p*-Si substrate at a gate length of 8 nm in various MOS transistors with shallow junctions [9, 10]. Thus, a channel length of ~8 nm at room temperature is critical and represents the physical limit for conventional silicon MOS transistors. In order to obviate this difficulty, one can either form an insulating layer at both ends of the channel or search for other MOS-transistor designs alternative to the conventional MOS structure.

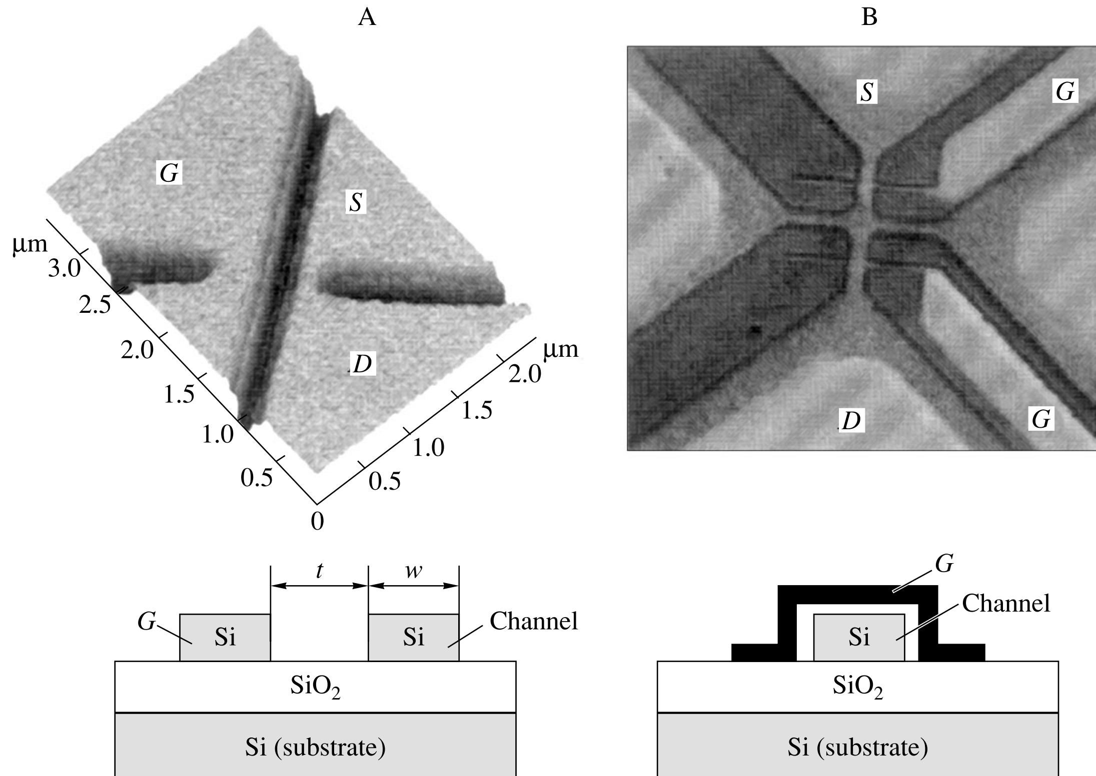

Fig. 1. Various designs of SOI–MOS transistors: structure A includes a single in-plane gate (the channel dimensions are 100×200 nm and structure B includes two three-dimensional gates (the gate width is 250 nm). Schematic representations of transistor cross sections are shown in the lower portion of the figure.

One of the designs of a device which is alternative to the conventional MOS transistor includes a heavily doped small silicon wire on an insulator; conduction of this wire is controlled by a field gate. Since the wire is doped uniformly, a number of problems related to shallow junctions are eliminated. The punch-through effect is eliminated. Thus, only one of the problems related to the drain–source regions (table) remains to be solved; this particular problem concerns the reduction of series resistance of the above layers.

In this study we tested the following MOS structures: structure A had the in-plane gate in the channel plane; structure B had a 3D gate that encompassed a single channel on three sides; and structure C had a 3D gate that encompassed each of the n channels in a multichannel structure (Figs. 1, 2). Figure 3 shows the drain–gate characteristics of structure B prior to deposition of the planar gate. The substrate served as the gate. Two special features of the characteristics can be seen in Fig. 3. At the voltage applied to the substrate $V_{sub} = 0$, the top p-Si layer can be nonconducting despite a high doping level. This circumstance is a consequence of a positive charge in the oxide (a buried SiO_2 layer, which passivates the structure). Owing to the positive charge in the oxide, conductance of the top n-Si layer is governed by both the quasi-neutral bulk and the accumulation layer in the vicinity of Si/SiO_2 interfaces. The conductance of the p-Si layer is controlled by the thickness of this layer minus the thickness of depletion layers near the Si/SiO_2 interfaces. If the thickness of the depletion layer and the film thickness are comparable, the conductance tends to zero. In this respect, it is better to use the n-Si layers. The second special feature consists in the fact that the same device (in contrast to a conventional MOS transistor) can operate on the basis of both electrons and holes if the conditions of either accumulation or inversion are provided by application of a voltage to an additional gate (the substrate or a lateral gate).

An SOI–MOS transistor with in-plane gates is fabricated in the course of so-called nanostructuring, in which case both the channel and the gates are formed of the same silicon layer, while the shape of the channel and gates are governed (if electron-beam lithography is used) only by the pattern formed by the electron beam (a particular case of a structure with a single in-plane gate is illustrated in Fig. 1). Such technology is basically inapplicable to bulk silicon and represents a new potential of SOI structures since etching off by (exposure to electron irradiation) of the silicon layer down to the insulator is used. Attractive features of SOI structuring consist primarily in the fact that simple scanning of the electron beam can be used to form multiple-gate structures with different shapes of gates [3, 5].

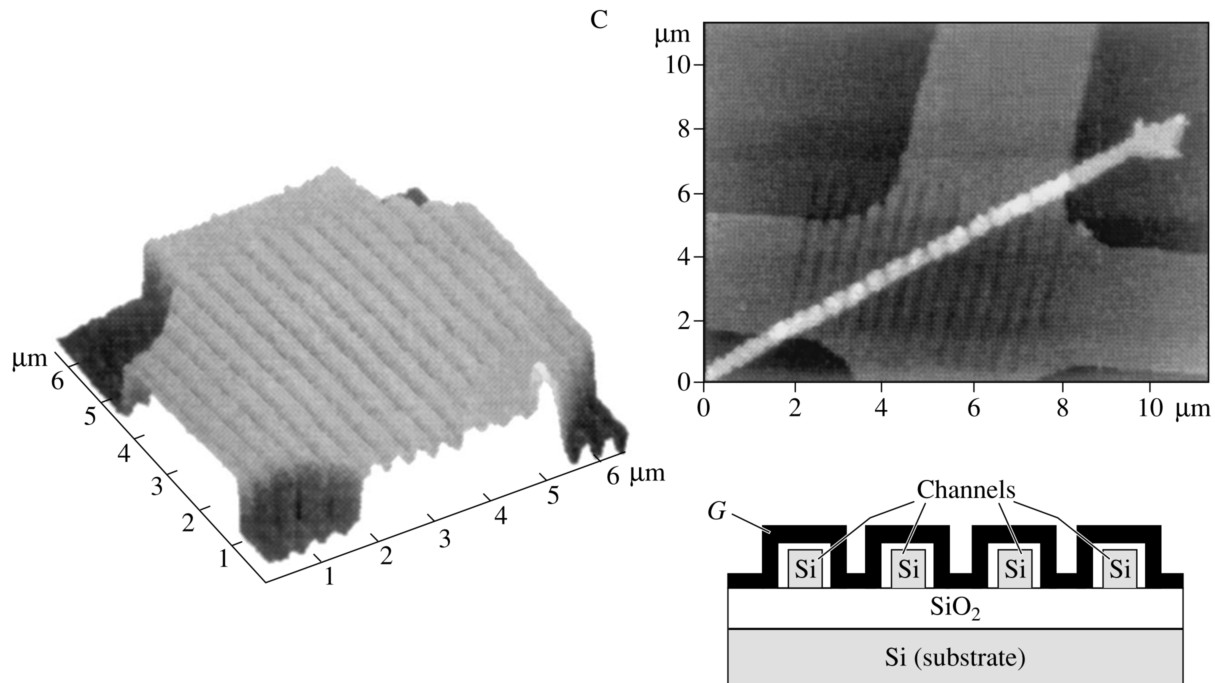

Fig. 2. The structure C of a multichannel SOI–MOS transistor with a three-dimensional gate; the central part of the transistor before and after deposition of the three-dimensional gate is depicted on the left and on the right, respectively. Schematic representation of the transistor cross section is shown in the lower right of the figure.

Although these devices seem simple, it is very difficult to fabricate them. In fact, in order to obtain a sufficiently high conductance of the channel (~500 μA/μm for a conventional MOS transistor), one has to ensure a high doping level N of the top silicon layer. This circumstance inevitably imposes a restriction on the channel width (the diameter of silicon wire) w and on the spacing t between the channel and the in-plane gate (t is equivalent to the thickness of the gate insulator for a conventional MOS transistor). For example, for a structure with two in-plane gates, the condition $w < 2d_{scr} \propto N^{-1/2}$ (d_{scr} is the thickness of SCR formed by a voltage applied to one of the gates) should be satisfied. The value of t is limited by the acceptable threshold voltage (<1 V). We can estimate that, at a concentration equal to 2×10^{20} cm^{-3}, the value of w should not exceed 5 nm, so that $t \approx 1.5$ nm if SiO_2 is used as the gate insulator.

Basically, such small values of t, which are difficult to attain in practice and are governed by the electron-beam diameter in the technology under consideration, can be increased by choosing an insulator with a larger permittivity.

One can increase the channel width w by decreasing the doping level for the SOI layer; however, two problems then arise. The first problem is related to an increase in the sensitivity to the charge fluctuations in oxide and at surface states in the vicinity of the Si/SiO_2 interface and to the charge fluctuations due to roughness of the SOI surface, the lithography-induced noise, and the impurity segregation as a result of thermal treatment. Figure 4 shows the source–gate characteristics of a transistor with structure A (see Fig. 1) when the voltage was multiply swept. Fluctuations of the transistor conductance are observed owing to unannealed recharging centers in the structure.

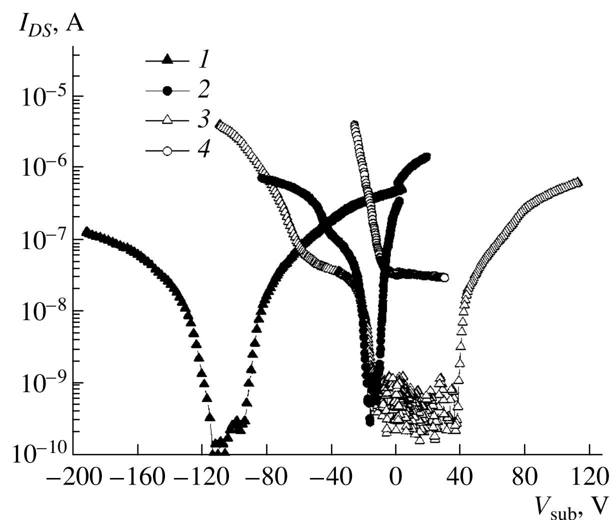

Fig. 3. The drain–gate characteristics of structure B at different conductivity types, doping levels, and thicknesses of the top silicon layer. The substrate was used as the gate. $V_{DS} = 0.15$ V; d_{Si} = (*1*) 20, (*2*) 44, (*3*) 9, and (*4*) 55 nm; N_D = (*1*) 10^{19} and (*2*) 10^{17} cm^{-3}; and N_A = (*3*) 2×10^{19} and (*4*) 10^{18} cm^{-3}.

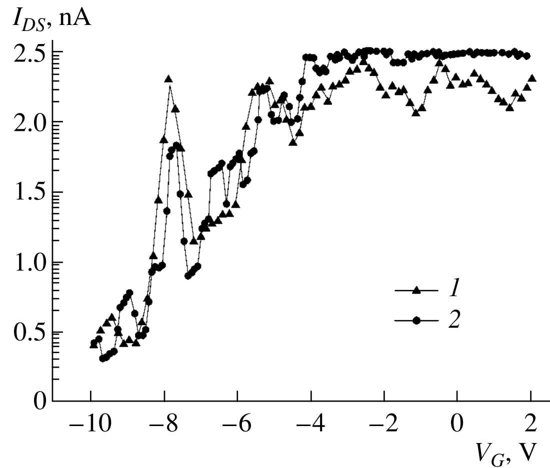

Fig. 4. The drain–gate characteristics of structure A under a repeated voltage sweep; d_{Si} = 17 nm, $N_A = 2 \times 10^{17}$ cm^{-3}, T = 1100°C, and V_{sub} = 50 V.

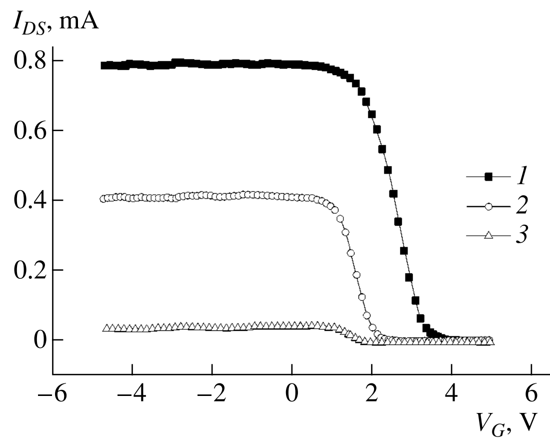

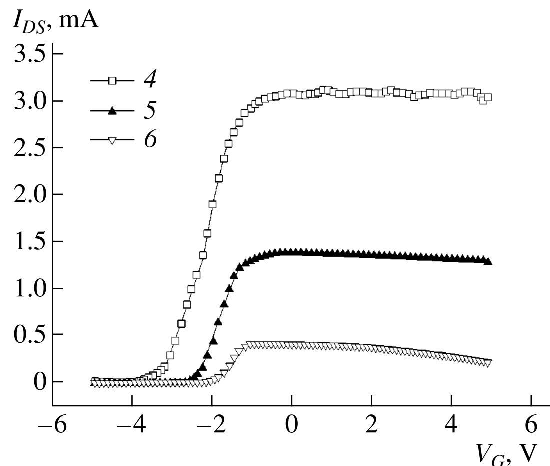

Fig. 5. The drain–gate characteristics of structure C at various voltages V_{sub} applied to the substrate: V_{sub} = (*1*) 100, (*2*) 70, (*3*) 50, (*4*) 50, (*5*) 25, and (*6*) 10 V. The structure parameters: the top 10-nm-thick SiO_2 film, a 44-nm-thick Si film, and the buried 327-nm-thick SiO_2 layer; N_D = 10^{17} cm^{-3} and V_{DS} = 0.15 V.

The second and evident problem arising when the doping level is lowered is related to a reduction of the current that flows through the transistor in its conducting state. Therefore, structures with in-plane gates can be used in circuits where there is no need for a high current density; however, these structures can be competitive with conventional MOS transistors if the following two conditions are satisfied: availability of (i) lithography, which can ensure component sizes on the order of nanometers, and (ii) the technology for producing insulators alternative to SiO_2 and introducing them into a nanometer-scale gap between the channel and gate.

A design of a multichannel transistor with parallel-connected silicon wires (Fig. 2) partly eliminates the problem related to low conductance of the channel. The 3D gate used in this design makes it possible to surround the channel on three rather on two sides. In Fig. 5, we show the source–gate characteristics, which indicate that the device is operable (it is noteworthy that structural and technological parameters of the transistor were not optimized with respect to the channel thickness and the dopant concentration). Apparently, the latter variant represents the most promising design based on SOI and is an alternative to the conventional MOS transistor; however, this structure does not eliminate the problem of using an insulator other than SiO_2 if heavily doped layers of SOI are used.

4. DESIGNS OF NANOMETER-SIZED TRANSISTORS WHICH ARE BASED ON SOI AND CAN OPERATE AT ROOM TEMPERATURE

One of the known variants of transistors whose operation is based on quantum-mechanical size effects is the single-electron transistor; the latter includes two series-connected tunneling junctions separated from each other by a nanometer-sized island [3]. This design represents the most promising device concerning low power consumption, very small capacitance, and, consequently, the highest integration density. The main problem related to a single-electron transistor (detection of a small charge captured at the island at room temperature) was overcome by Japanese scientists, who suggested using for this purpose a planar polysilicon gate (the so-called concept of the single-transistor one-electron memory) [11–13]. Owing to the unique ability to control the flux of separate electrons, a single-electron transistor is of interest primarily when used in the memory units of ICs. Indeed, the number of memory cells in a single chip is restricted by dissipated energy, which is proportional to the number of electrons in a cell. If a single electron in the limiting case is used to store the information, the dissipated energy in the course of recharging will be lower than in conventional memory cells by several orders of magnitude.

Fabrication of single-electron devices based on SOI involves the formation of nanometer-scale islands (in the limiting case, quantum dots) in the SOI wire; these islands are separated by tunneling barriers from the

remaining part of the wire. Basically, there are two approaches to the formation of such a structure. The first approach consists in self-formation.

Figure 6 shows dependences of the conductance $G = I_D/V_D$ on the gate voltage for structure B (the substrate served as the gate) [14]. The thickness of the top silicon layer was ~8 nm. The width of the SOI film was 2 μm. Quasi-periodic oscillations of conductance were observed in the structures at room temperature only in the accumulation mode (the oscillations were not observed when an inversion *n*-type channel was formed in the vicinity of the interface between the top *p*-Si layer and buried SiO_2). Therefore, the observed effect was related to the formation of tunneling barriers for the charge carriers of only one type (holes) within the top silicon layer (see the inset in Fig. 6); these barriers were formed owing to fluctuations of charge (in the oxide and at surface states) in combination with impurity segregation and microprofile of the SOI surface [14, 15].

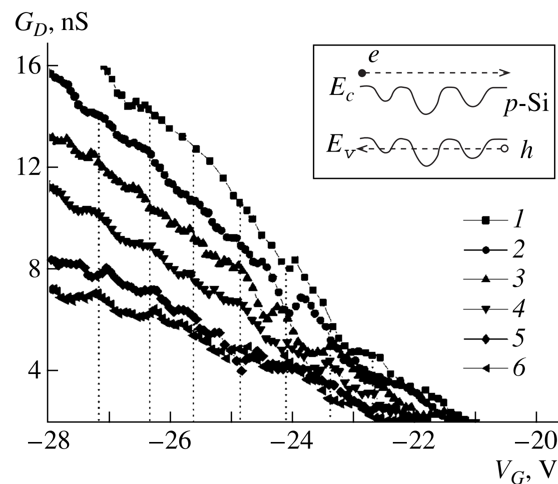

Fig. 6. The dependence of conductance on the gate (substrate) voltage of structure B with a top silicon layer ~8 nm thick. The curves were obtained at various drain voltages V_D at room temperature [14]. Schematic representation of the energy-band diagram for the situation where tunneling barriers for holes are formed owing to the charge fluctuations when the film is depleted of charge carriers is shown in the inset. V_D = (*1*) 1.6, (*2*) 1.4, (*3*) 1.2, (*4*) 1.0, (*5*) 0.8, and (*6*) 0.6 V. The structure parameters: the top 11-nm-thick SiO_2 film, an 8-nm-thick top Si film, and the buried 443-nm-thick SiO_2 layer; $N_A \approx 10^{17}$ cm^{-3}.

Figure 7 shows an atomic-force microscopy (AFM) image which illustrates the microprofile of the outer boundary of the top silicon layer thinned to 10 nm. In the method used for the formation of SOI structures (exfoliation over the layer the adhesion of which was weakened by hydrogen implantation [4]), the outer surface of the top silicon layer was formed owing to the development of a crack over the layer implanted with hydrogen. If no special efforts were made to polish the surface and the SOI structure was thinned using the operations of thermal oxidation and etching off of the oxide, a specific structure can be automatically formed at a certain thickness of silicon layer; this structure contains conducting channels and an array of nanoscale silicon islands separated from the channels by tunneling barriers and is equivalent to a system of single-electron transistors. This system is formed relatively easily, without the need for nanoscale lithography.

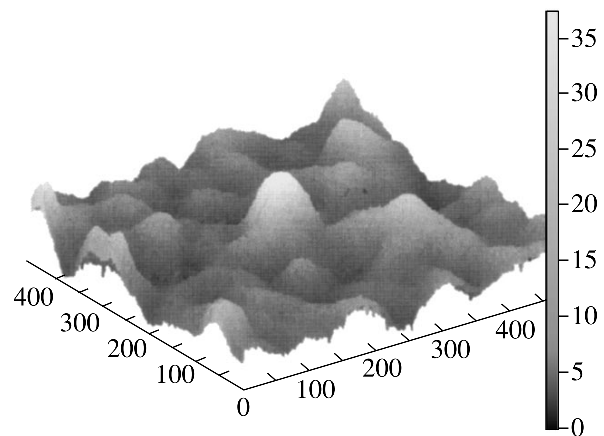

Fig. 7. Image of a 10-nm-thick top silicon layer on an insulator; the image was obtained using atomic-force microscope. The scanned area is 450 × 450 nm^2.

A drawback of such structures (as for all other structures based on self-formation of nanoscale objects) consists in the irreproducibility of electrical characteristics as a result of the fact that each silicon island has a specific set of localized energy states and the passage of electrons through tunneling barriers is a probabilistic process. Therefore, here, either efforts are required to form a homogeneous surface microprofile or the second approach should be used; this approach consists in the intentional (lithographic) definition of sizes of silicon islands and in electrostatic control of the potential-barrier heights. Using lateral structuring of SOI (Fig. 1), one can form controlling in-plane (fingerlike) gates of various configurations. However, in order to fabricate devices which operate at room temperature and have reproducible parameters, either the dimensions of the devices should be smaller than the sizes of self-forming quantum dots or the surface microprofile and variations in the width of the SOI wire should be almost eliminated; the lithography should ensure reproducibility of the device sizes at the level of several nanometers. For structures with dimensions smaller than 10 nm, this issue remains open at present. At the same time, since it is still required to form the memory units of transistors in an IC rather than fabricating a separate transistor, combination of single-electron transistors with the remaining part of the circuit (primarily, with an amplifier) is important. An indubitable advantage of single-electron SOI transistors is the possibility of fabricating hybrid circuits consisting of single-electron transistors and MOS transistors; the advantage of

SOI transistors with any structures is their compatibility with the existing silicon technology.

5. CONCLUSIONS

Transition from bulk silicon to SOI wafers represents one of the methods for solving the basic problems of fabricating transistors of nanoscale dimensions.

An alternative design to SOI nanotransistors (a structure with uniformly doped silicon film) makes it possible to overcome the problem of short-channel effects. Apparently, the most promising design of such a nanotransistor is that of a multichannel transistor with 3D gate formed on uniformly doped SOI structure. Due to the positive charge in the oxide surrounding the SOI wire, it is preferable to deal with *n*-type silicon layers.

The self-formation of nanometer-scale silicon islands in SOI layers with thickness smaller than 10 nm is, on the one hand, one of the methods for formation of single-electron devices and, on the other hand, an undesirable effect in lithographic definition of the device structure. Fabrication of single-electron devices controlled by lithographically defined in-plane gates represents the ideal variant for production of devices with reproducible characteristics. However, this issue concerns not only the lithography and structural quality of SOI; there is also a need for developing the technology for deposition of insulators, which are an alternative to SiO_2 and have a higher permittivity, on nanometer-sized gaps between etched areas of a silicon layer.

ACKNOWLEDGMENTS

This study was supported according to the program "Physics and Technology of Nanostructures" of the Russian Federation (project no. 204-9(00)-II).

We thank Professor A.V. Latyshev and D.V. Shcheglov for AFM measurements.

REFERENCES

1. S. Cristoloveanu and S. Li Sheng, *Electrical Characterisation of Silicon-on-Insulator Materials and Devices* (Kluwer Academic, Boston, 1995).
2. B. Doyle, R. Arghavani, D. Barlage, *et al.*, Intel Tech. J. **06**, 42 (2002).
3. K. K. Likharev, Proc. IEEE **87**, 606 (1999).
4. V. P. Popov, I. V. Antonova, V. F. Stas, *et al.*, Mater. Sci. Eng. B **73**, 82 (2000).
5. Y. V. Nastaushev, T. A. Gavrilova, M. Kachanova, *et al.*, Mater. Sci. Eng. C **19**, 189 (2002).
6. R. Dennard, F. Gaensslen, L. Kuhn, and H. Yu, in *Abstracts of IEEE International Electron Device Meeting* (1972).
7. G. Ya. Krasnikov, *Structural and Technological Features of Submicron MOS-Transistors* (Tekhnosfera, Moscow, 2002), p. 416.
8. M. G. Peters, S. G. den Hartog, J. I. Dijkhuis, *et al.*, J. Appl. Phys. **84**, 5052 (1998).
9. H. Kawaura, T. Sakamoto, and T. Baba, in *Extended Abstracts of International Conference on Solid State Devices and Materials* (Tokyo, 1999), p. 20.
10. N. Matsuo, J. Yamauchi, Y. Kitagawa, *et al.*, Jpn. J. Appl. Phys. **39**, 3850 (2000).
11. N. Ishikuro, N. Fujii, T. Saraya, *et al.*, Appl. Phys. Lett. **68**, 3585 (1996).
12. L. Zhuang, L. Guo, and S. Y. Chou, Appl. Phys. Lett. **72**, 1205 (1998).
13. K. Yano, T. Ishii, T. Sano, *et al.*, in *Abstracts of International Electron Device Meeting* (San Francisco, CA, 1998).
14. O. V. Naumova, I. V. Antonova, V. P. Popov, *et al.*, Microelectron. Eng. **66**, 442 (2003).
15. H. Ishikuro and T. Hiramoto, Appl. Phys. Lett. **74**, 1126 (1999).

Translated by A. Spitsyn

Semiconductors, Vol. 37, No. 10, 2003, pp. 1229–1233. Translated from Fizika i Tekhnika Poluprovodnikov, Vol. 37, No. 10, 2003, pp. 1260–1264.
Original Russian Text Copyright © 2003 by Kalinina, Kholuyanov, Davydov, Strel'chuk, Hallén, Konstantinov, Luchinin, Nikiforov.

PHYSICS OF SEMICONDUCTOR DEVICES

Effect of Irradiation with Fast Neutrons on Electrical Characteristics of Devices Based on CVD 4*H*-SiC Epitaxial Layers

E. V. Kalinina*^, G. F. Kholuyanov*, D. V. Davydov*, A. M. Strel'chuk*, A. Hallén, A. O. Konstantinov***, V. V. Luchinin****, and A. Yu. Nikiforov*****

**Ioffe Physicotechnical Institute, Russian Academy of Sciences, St. Petersburg, 194021 Russia*
^e-mail: evk@pop.ioffe.rssi.ru
***Royal Institute of Technology, Department of Electronics, Electrum 229, SE 16440 Kista, Sweden*
****Acreo AB, Electrum 236, SE 16440 Kista, Sweden*
*****St. Petersburg Electrotechnical University, Center of Microtechnology and Diagnostics, St. Petersburg, 107376 Russia*
******Specialized Electronic Systems, Moscow, 115409 Russia*
Submitted February 11, 2003; accepted for publication February 17, 2003

Abstract—The effect of irradiation with 1-MeV neutrons on electrical properties of Al-based Schottky barriers and p^+–n–n^+ diodes doped by ion-implantation with Al was studied; the devices were formed on the basis of high-resistivity, pure 4*H*-SiC epitaxial layers possessing *n*-type conductivity and grown by vapor-transport epitaxy. The use of such structures made it possible to study the radiation defects in the epitaxial layer at temperatures as high as 700 K. Rectifying properties of the diode structures were no longer observed after irradiation of the samples with neutrons with a dose of 6×10^{14} cm^{-2}; this effect is caused by high (up to 50 GΩ) resistance of the layer damaged by neutron radiation. However, the diode characteristics of irradiated p^+–n–n^+ structures were partially recovered after an annealing at 650 K. © *2003 MAIK "Nauka/Interperiodica".*

1. INTRODUCTION

Silicon carbide is one of the most promising wide-gap semiconductors, which feature high electric and mechanical strength, high thermal stability, and high radiation resistance. This unique combination of properties makes it possible to use SiC in the fabrication of electronic devices that can operate under extreme conditions, i.e., at high temperatures, at high radiation levels, and in reactive media.

Studies of the effects of neutron radiation on SiC properties have been mainly concerned with mechanisms of defect production [1–4]. Studies of radiation defects in finished device structures exposed to radiation are no less important; such studies provide information on mechanisms of failures and threshold radiation doses, which bring about variations in the device characteristics and degradation of devices, and also make it possible to develop models for the behavior of devices under irradiation [5]. Previous studies of the electrical characteristics of irradiated SiC rectifiers based on *p*–*n* junctions and Schottky barriers yielded diverse and contradictory results [6–9]. Such a diversity of experimental data can probably be attributed to differences in the characteristics of irradiated samples as a result of poor quality of the starting material. Recent progress toward commercial growth of pure SiC epitaxial layers made it possible to obtain new data on the effect of neutron irradiation on some characteristics of SiC device structures [10–14].

This study is concerned with the effect of neutron radiation both on the defect production in epitaxial layers of lightly doped *n*-type SiC and on some electrical characteristics of both Schottky diodes and ion-implantation-doped p^+–n–n^+ structures formed in these layers.

2. EXPERIMENTAL

The diode structures studied were fabricated on the basis of *n*-type 4*H*-SiC layers grown by chemical vapor deposition (CVD) on n^+-4*H*-SiC substrates with a concentration of uncompensated donors of $N_d - N_a \approx 10^{19}$ cm^{-3}. The 26-µm-thick CVD layers had an electron concentration of $N_d - N_a \approx (5–8) \times 10^{15}$ cm^{-3}. The diode p^+–n–n^+ structures were formed by implantation of 150-keV Al ions with a dose of 5×10^{16} cm^{-2}. In order to activate the implanted impurity, we annealed the implanted samples in an Ar atmosphere for 15 s at 1700°C; as a result, a p^+–n junction was formed at a depth of 0.6 µm [15]. Ohmic contacts were formed by deposition of Al and Cr/Al on the p^+- and n^+-type regions of diode structures, respectively (vacuum evaporation of the corresponding sources was employed). In addition, Al Schottky barriers were formed on preliminarily masked (unimplanted) areas of the epitaxial

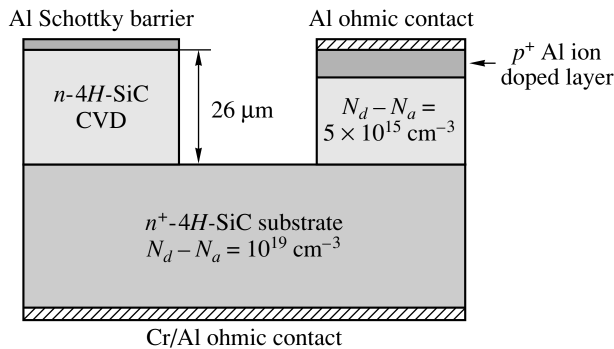

Fig. 1. Cross section of structures with either the Schottky barrier or the p^+–n junction formed by ion implantation of Al in a 4H-SiC epitaxial layer.

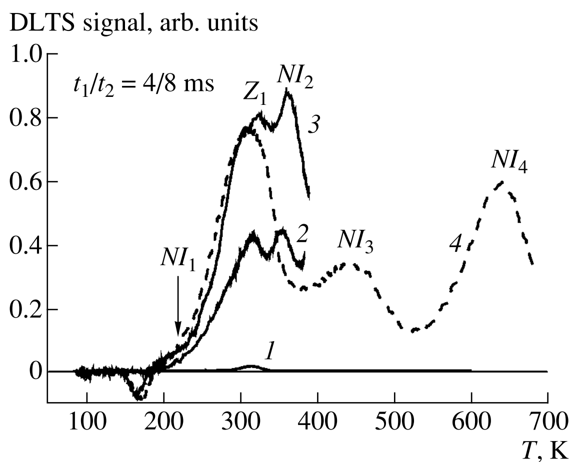

Fig. 2. The °C-DLTS spectra of (*1*, *2*) Schottky diodes and (*3*, *4*) p^+–n junctions formed by ion-implantation of Al; the spectra were measured (*1*) before and after irradiation with fast neutrons with doses (*2*) D_1 and (*3*) D_2. Spectra *1*–*3* were measured at temperatures no higher than 400 K, and spectrum *4* was measured after heating of the sample to 700 K.

layer. Thus, the base Cr/Al contacts to the n^+-type regions of all diode structures were formed in a single process. The diode mesa structures with either Schottky barriers or p^+–n junctions had an area of 10^{-3} cm^2 and a height of 30 μm and were formed by ion–plasma etching; the Al contact served as the mask (Fig. 1). We studied the diodes without special treatment of peripheral regions; this treatment is commonly used to eliminate surface breakdown.

The diode structures were irradiated sequentially with three doses of 1-MeV neutrons with accompanying doses of gamma-ray radiation. In parameters of irradiation are listed in Table 1. Prior to and after each irradiation of the diode structures, we carried out measurements and performed a comparative analysis of the electrical characteristics of these structures.

The concentration profile of electrically active impurities in the CVD layer in the vicinity of the Schottky barriers and p^+–n junctions was determined from capacitance–voltage (C–V) characteristics measured at a frequency of 10 kHz. The presence and number of deep levels in the 4H-SiC band gap were estimated using the data of deep-level transient spectroscopy (C-DLTS) in the temperature range of 80–700 K. The current–voltage (I–V) characteristics of the Schottky barriers and p^+–n–n^+ structures were measured at a direct current in the temperature range of 293–650 K.

3. RESULTS AND DISCUSSION

According to the measurements of C–V characteristics, a decrease in the $N_d - N_a$ concentration was observed in the space-charge region for both types of diode structures (Schottky diodes and p^+–n junctions doped with Al using ion implantation); this concentration decreased by a factor of 1.5 after the first irradiation with neutrons (D_1) and by a factor of 2 after the second irradiation (D_2). The voltage-independent values of capacitance for Schottky barriers and p^+–n junctions were equal to 0.2–0.3 pF after the third irradiation with an overall fast-neutron dose of $D_3 = 6.24 \times 10^{14}$ cm^{-2}. The above value of capacitance corresponds to an insulating layer with a thickness of 20–30 μm, which is comparable to the thickness of the high-resistivity CVD layer.

The DLTS measurements of unirradiated CVD layers revealed the presence of a single-type deep-level center Z_1 with an activation energy of 0.62 eV and a concentration of (2–3) $\times 10^{13}$ cm^{-3} (Fig. 2, curve *1*). After irradiation of the diode structures with a neutron dose D_1, the DLTS measurements were performed in the temperature range of 80–400 K. This irradiation brought about not only an increase in the concentration of Z_1 center but also the emergence of another deep-level NI_2 center with activation energy of 0.68 eV (curve *2*). The total concentration of Z_1 centers increased by an order of magnitude as compared with

Table 1. Parameters of irradiation with fast neutrons

Order of irradiation	Dose, cm^{-2}	Total dose, cm^{-2}	Accompanying dose of gamma-ray radiation, rad
First irradiation (D_1)	1.2×10^{14}	1.2×10^{14}	2.3×10^{14}
Second irradiation (D_2)	1.9×10^{14}	3.1×10^{14}	4.6×10^{14}
Third irradiation (D_3)	3.14×10^{14}	6.24×10^{14}	8.6×10^{14}

Table 2. Parameters of deep levels detected in CVD 4*H*-SiC layers after irradiation with fast neutrons with different doses

Order of irradiation	Center	$E_c - E_0$, eV	σ_n, cm^2	N, cm^{-3}
Starting sample	Z_1	0.63 ± 0.01	10^{-14}	$(2–3) \times 10^{13}$
First irradiation (D_1)	Z_1	0.63 ± 0.01	10^{-14}	4×10^{14}
	NI_2	0.68 ± 0.01	10^{-14}	4×10^{14}
Second irradiation (D_2), before annealing	NI_1	0.37 ± 0.01	10^{-16}	5.5×10^{13}
	Z_1	0.69 ± 0.01	10^{-14}	5.5×10^{14}
	NI_2	0.74 ± 0.03	5×10^{-15}	5.8×10^{14}
Second irradiation (D_2), after annealing at 700 K	NI_1	0.37 ± 0.01	10^{-16}	$<10^{13}$
	Z_1	0.68 ± 0.01	10^{-14}	5.3×10^{14}
	NI_2	0.74 ± 0.03	10^{-14}	$<10^{13}$
	NI_3	0.92 ± 0.1	5×10^{-15}	$\sim 2 \times 10^{14}$
	NI_4	1.56 ± 0.02	5×10^{-13}	8×10^{14}

that in unirradiated samples and was equal to 4×10^{14} cm^{-3} (Table 2).

After irradiation of the diode structures with a dose D_2, the DLTS measurements were performed using the ion-implantation-doped p^+–n junctions in two stages: first in the temperature range of 80–400 K in order to prevent annealing of unstable defects and then at temperatures as high as 700 K. Measurements performed at temperatures no higher than 400 K revealed Z_1 and NI_2 centers (Fig. 2, curve *3*) in the samples irradiated with dose D_2, similarly to the results obtained after irradiation of the samples with dose D_1. However, concentrations of these centers were appreciably higher than those after the first irradiation. In addition, repeated irradiation of the samples with neutrons gave rise to NI_1 centers with the level in the band gap at $E_c - E_0 =$ 0.37 eV below the bottom of the conduction band; these centers had a low concentration and were annealed out at 400 K (Table 2). Heating of the samples to 700 K brought about an insignificant decrease in the concentration of Z_1 centers, whereas the concentrations of deep-level NI_1 and NI_2 centers decreased appreciably. In addition, centers NI_3 and NI_4 with levels located at 0.92 and 1.56 eV, respectively, below the bottom of the conduction band were observed after annealing at temperatures higher than 400 K. The electron-capture cross sections (σ_n) for various deep levels were determined from intercepts of the Arrhenius curves with the horizontal axis (Fig. 3). Parameters of all observed deep levels are listed in Table 2; the total concentration of these levels was $\sim 2 \times 10^{15}$ cm^{-3} after the second (D_2) irradiation.

As was mentioned above, an insulating layer was formed as a result of irradiation of diode structures with fast neutrons with a dose D_3; the thickness of this layer was comparable to that of the lightly doped epitaxial layer (26 μm). We may assume that the total concentration of deep-level centers introduced by the third irradiation was comparable to the initial concentration of active donors in the CVD layer ($N_d - N_a = (5–8) \times 10^{15}$ cm^{-3}).

Taking into account that, according to the measurements of *C–V* characteristics, a decrease in the concentration of uncompensated donors in the epitaxial layer is insignificant in the course of neutron irradiation, we may assume that only a fraction of deep-level centers are compensating.

Initial portions of the forward *I–V* characteristics measured for the Schottky barriers and also for the ion-implanted diodes at voltages lower than the contact potential difference U_c featured an exponential dependence of the current on voltage and small leakage currents before irradiation (see the inset in Fig. 4; curves *1*, *4*). The small leakage currents in the unirradiated diode structures studied are indicative of a fairly high quality of starting semiconductor material and of proper treatment of the mesa-structure surface. Each neutron irradiation with doses D_1 (Fig. 4, curves *2*, *5*) and D_2 (curves *3*, *6*)

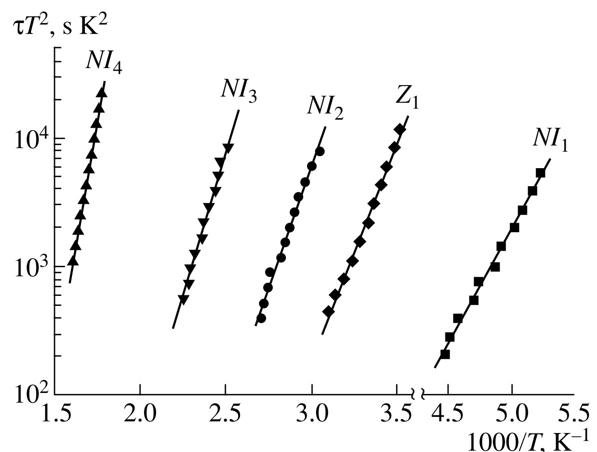

Fig. 3. The Arrhenius curves for deep-level centers detected by DLTS in the CVD 4*H*-SiC layers after irradiation with fast neutrons with dose D_2.

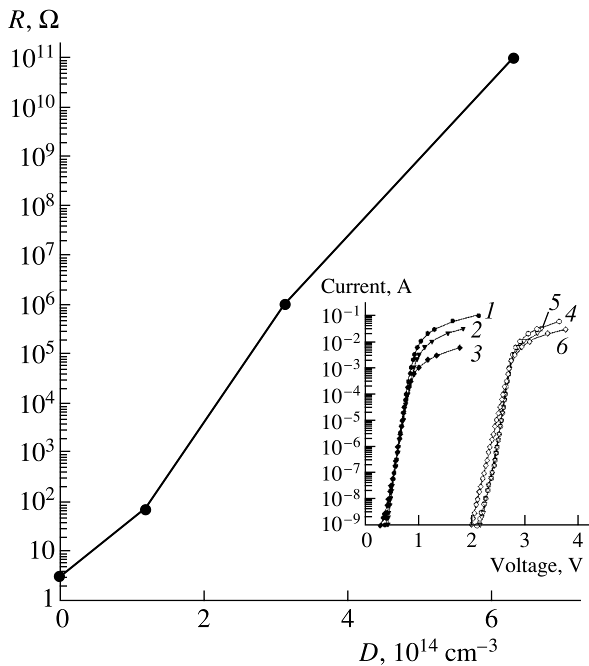

Fig. 4. The resistance of the 4*H*-SiC CVD layer as a function of the neutron-radiation dose (D). The low-voltage portions of the forward *I–V* characteristics of (*1–3*) Schottky barriers and (*4–6*) ion-implanted $p^+–n$ junctions are shown in the inset; these characteristics were measured (*1*, *4*) before and after irradiation with doses (*2*, *5*) D_1 and (*3*, *6*) D_2.

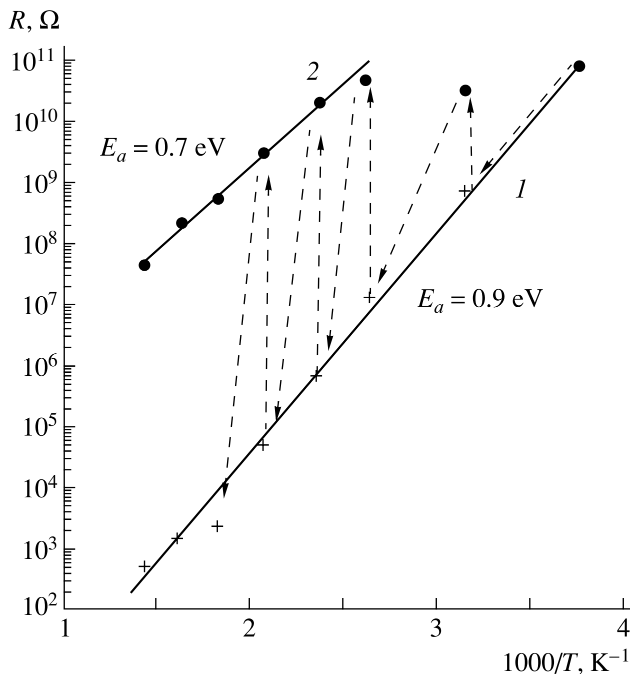

Fig. 5. Temperature dependences of the resistance of ion-implanted $p^+–n–n^+$ structures irradiated with neutrons with dose D_3. Dependence *2* was measured at 293 K after stage-by-stage heating with a step of 50 K with intermediate cooling to 293 K.

brought about a narrowing of the exponential portion of the *I–V* characteristic due to an increase in the resistance of diode structures.

Appreciable changes in the *I–V* characteristics were observed after neutron irradiation of the same diode structures at voltages which exceeded the values of the contact potential for both the Schottky diodes and $p^+–n$ junctions (Fig. 4). Irradiation with fast neutrons led to an appreciable increase in the resistance of rectifiers, which could be formally caused by changes in the resistances of the base Cr/Al ohmic contacts, low-resistivity substrate, and heavily doped ion-implanted thin (0.6 μm) p^+-type layer (or high-resistivity CVD layer). Measurements of contact resistances for the base contact after irradiations showed that the contact resistance was not affected by irradiation. According to the data on irradiation of SiC with fast neutrons [3, 16], the radiation doses should not affect the heavily doped n^+- and p^+-SiC regions. In this case, an increase in the structural resistance was governed only by an increase in the resistance of the high-resistivity CVD layer owing to the appearance of radiation defects as a result of irradiation. This structural resistance increased as a result of irradiation with dose D_2; the diode structures lost their rectifying properties after irradiation with dose D_3. The currents were on the level of nanoamperes at a forward voltage of 50 V; the total resistance of diode structures of both types exceeded 50 GΩ.

It was observed that the resistance of diode structures decreased significantly after illumination of neutron-irradiated diode structures with an incandescent lamp. Disregarding the accompanying factors (for example, current spreading), we can attribute the manifestation of the photoeffect in the structure under investigation to the introduction of radiation defects into the CVD layer as a result of irradiation with neutrons; these defects profoundly affect the resistance of the CVD layer.

Radical changes in the *I–V* characteristics of diodes subjected to irradiation with neutrons were observed as a result of heating of irradiated diodes. In Fig. 5, we show the temperature dependences of resistance of an ion-implanted diode structure irradiated with neutrons with dose D_3. The samples were heated in stages with a step of about 50°C with intermediate cooling to room temperature. Experimental points in curve *2* are obtained at room temperature and are shown in relation to the temperature of preliminary heating. As can be seen, the resistance of structures decreased by eight orders of magnitude (Fig. 5, curve *1*) as a result of partial annealing of radiation defects when the irradiated samples were heated to 650 K. An appreciable annealing of radiation defects was observed when the samples were heated to temperatures equal to or higher than 200°C. After heating the samples to 650 K with subsequent cooling, the resistance of the irradiated structure decreased by almost four orders of magnitude compared to the resistance before heating.

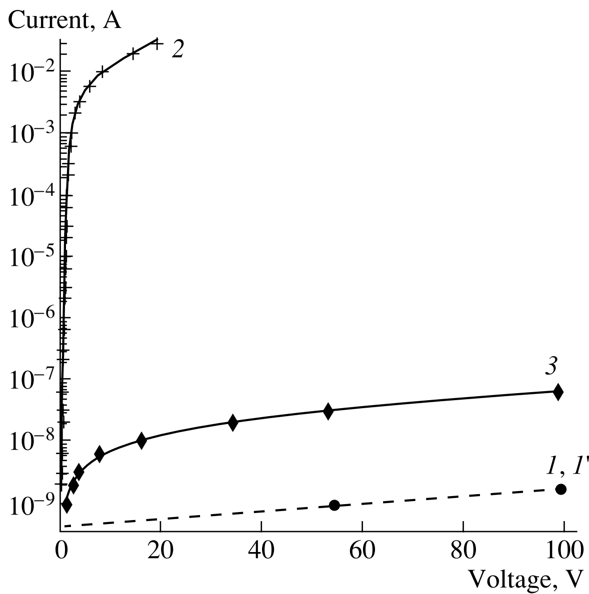

Fig. 6. The (*1*, *2*) forward and (*1'*, *3*) reverse portions of *I–V* characteristics for ion-implanted $p^+–n–n^+$ structures irradiated with neutrons with a total dose of 6×10^{14} cm^{-2}. Curves *1* and *1'* represent the results of measurements at $T = 293$ K and curves *2* and *3* correspond to measurements at $T = 650$ K.

Figure 6 shows the *I–V* characteristics of diodes fabricated using ion-implantation doping and then subjected to neutron irradiation with dose D_3 at $T = 293$ K (Fig. 6, curves *1*, *1'*). It can be seen that the rectifying properties of diode structures are partially recovered at a higher temperature (Fig. 6, curves *2*, *3*), so that the forward resistance was equal to ~200 Ω. The starting diode structures had a forward resistance of ~3 Ω.

The reverse voltages of the studied diode structures of both types were tested up to 300 V. Reverse currents at room temperature were in the range of nanoamperes both for starting diodes and the diodes irradiated with fast neutrons with doses D_1 and D_2. We may state that the irradiation did not give rise to additional channels for leakage currents and breakdown.

4. CONCLUSIONS

Our studies showed that the concentration of radiation defects introduced into the CVD 4*H*-SiC layers as a result of irradiation with fast neutrons with a dose of 6×10^{14} cm^{-2} became comparable to the net donor concentration $N_d - N_a = (5–8) \times 10^{15}$ cm^{-3} in the epitaxial layer. According to the measurements of the *C–V* and *I–V* characteristics, a fraction of radiation defects produced by neutron radiation were of compensating type. As a result, the CVD 4*H*-SiC layer was transformed into an insulator with a capacitance of 0.2–0.3 pF and a resistance of ~50 GΩ, which brought about a disappearance of rectifying properties of the diodes formed on the CVD layers. However, we observed that the diode structures, which degraded as a result of irradiation with fast neutrons, partially recovered their rectifying properties at a temperature of 650 K. Thus, we showed for the first time that the radiation resistance of devices based on SiC could be improved at higher operation temperatures.

ACKNOWLEDGMENTS

We thank G.N. Violina for her helpful participation in discussions and G.A. Onushkin for his assistance in preparation of the manuscript.

This study was supported by the Russian Foundation for Basic Research, project no. 01-02-17911.

REFERENCES

1. Yu. N. Nikolaev, Élektron. Tekh. **3**, 54 (1966).
2. V. V. Makarov, Fiz. Tverd. Tela (Leningrad) **13**, 2357 (1971) [Sov. Phys. Solid State **13**, 1974 (1971)].
3. A. I. Veĭnger, A. A. Lepneva, G. A. Lomakina, *et al.*, Fiz. Tekh. Poluprovodn. (Leningrad) **18**, 2153 (1984) [Sov. Phys. Semicond. **18**, 1256 (1984)].
4. V. Nagesh, J. W. Farmer, R. F. Davis, and H. S. Kong, Appl. Phys. Lett. **50**, 1138 (1987).
5. A. Yu. Nikiforov, P. K. Skorobogatov, and Yu. I. Syts'ko, in *Radiative Stability of Electroic Systems: Stability-2002* (Paims, Moscow, 2002), Vol. 5, p. 147.
6. L. W. Aukerman, H. C. Garton, R. K. Willardson, and V. E. Bryson, *Silicon Carbide*, Ed. by J. R. O'Connor and J. Smiltens (Pergamon, Oxford, 1959), p. 388.
7. E. W. J. Mitchell and M. J. Moore, *Radiation Damage in Semiconductors* (Dunod, Paris, 1965), p. 235.
8. C. E. Barnes, Appl. Phys. Lett. **20**, 86 (1972).
9. I. V. Ryzhikov, I. L. Kasatkin, and E. F. Uvarov, Élektron. Tekh., Ser. 2: Poluprovodn. Prib., No. 4 (147), 9 (1981).
10. V. V. Evstropov and A. M. Strel'chuk, Fiz. Tekh. Poluprovodn. (St. Petersburg) **30**, 112 (1996) [Semiconductors **30**, 52 (1996)].
11. A. Yu. Nikiforov, V. V. Luchinin, and V. S. Figurov, in *Radiative Stability of Electronic Systems: Stability-98* (SPELS–NIIP, Moscow, 1998), Vol. 1, p. 127.
12. S. Seshadri, A. R. Dulloo, F. H. Ruddy, *et al.*, IEEE Trans. Electron Devices **46**, 567 (1999).
13. A. Yu. Nikiforov, A. V. Afanas'ev, V. A. Il'in, *et al.*, in *Radiative Stability of Electronic Systems: Stability-2001* (Paims, Moscow, 2001), Vol. 4, p. 145.
14. A. Yu. Nikiforov, P. A. Ivanov, and V. V. Luchinin, in *Radiative Stability of Electronic Systems: Stability-2002* (Paims, Moscow, 2002), Vol. 5, p. 167.
15. E. Kalinina, G. Kholujanov, V. Solov'ev, *et al.*, Appl. Phys. Lett. **77**, 3051 (2000).
16. A. V. Afanas'ev, V. A. Il'in, and A. A. Petrov, Peterb. Zh. Élektron. **3–4**, 12 (2000).

Translated by A. Spitsyn

Semiconductors, Vol. 37, No. 10, 2003, pp. 1234–1238. Translated from Fizika i Tekhnika Poluprovodnikov, Vol. 37, No. 10, 2003, pp. 1265–1269.
Original Russian Text Copyright © 2003 by Maleev, Kovsh, Zhukov, Vasil'ev, Mikhrin, Kuz'menkov, Bedarev, Zadiranov, Kulagina, Shernyakov, Shulenkov, Bykovskiĭ, Solov'ev, Möller, Ledentsov, Ustinov.

PHYSICS OF SEMICONDUCTOR DEVICES

Design and Technology of Vertical-Cavity Surface-Emitting Lasers with Nonconducting Epitaxial Mirrors

N. A. Maleev*, A. P. Kovsh*, A. E. Zhukov*, A. P. Vasil'ev*, S. S. Mikhrin*, A. G. Kuz'menkov, D. A. Bedarev*, Yu. M. Zadiranov*, M. M. Kulagina*, Yu. M. Shernyakov*, A. S. Shulenkov, V. A. Bykovskiĭ**, Yu. M. Solov'ev***, C. Möller****, N. N. Ledentsov*, and V. M. Ustinov***

**Ioffe Physicotechnical Institute, Russian Academy of Sciences, St. Petersburg, 194021 Russia*

***Minsk Research Institute of Radio-Engineering Materials, Minsk, 220024 Belarus*

****AOZT Svetlana-Élektronpribor, St. Petersburg, 194021 Russia*

*****Heinrich-Hertz Institut für Nachrichtentechnik Berlin, 10587 Berlin, Deutschland*

Submitted March 11, 2003; accepted for publication March 18, 2003

Abstract—Design and technology problems in the fabrication of vertical-cavity surface-emitting lasers (VCSELs) equipped with nonconducting distributed Bragg reflectors (DBRs) and fabricated using molecular-beam epitaxy are considered. VCSELs with an active region were formed on the basis of InGaAs quantum wells and incorporated an AlGaAs/GaAs bottom DBR and an oxidized AlGaO/GaAs top DBR; the diameter of the oxidized aperture was equal to 7–12 μm. The devices exhibit a continuous-wave lasing at room temperature with threshold currents of 0.5–1.5 mA, a differential efficiency as high as 0.5 mW/mA, and a highest output power of 3 mW. © *2003 MAIK "Nauka/Interperiodica".*

Recently, vertical-cavity surface-emitting lasers (VCSELs) have found wide application in fast-response systems for transmission and processing of information [1]. The main advantages of these lasers as compared with conventional stripe-geometry injection lasers consist in lower angular divergence, a symmetrical directivity pattern for output optical radiation, and the possibility of batch technology for fabrication and testing of devices on the wafer [2]. In contrast to stripe-geometry lasers with cleaved faces, distributed Bragg reflectors (DBRs) are used in a VCSEL as cavity mirrors; these reflectors are formed on the basis of alternating layers of materials that have differing indices of optical refraction, with each layer thickness amounting to a quarter of the resonance wavelength (with allowance made for the refractive index). Semiconductor DBRs based on alternating $Al_xGa_{1-x}As$ layers with different compositions and dielectric DBRs have found the widest applications. Isolating hydrogen implantation or selective oxidation of buried AlGaAs layers are typically used to spatially confine the region of flowing current (in order to form the VCSEL aperture) [1, 2].

VCSELs can be classified into two large groups according to the schemes for accomplishing the charge-carrier injection into the active (emitting) region. Devices with conductive semiconductor mirrors belong to the first group. The design of VCSELs with conductive mirrors ensures relative simplicity of planar technology and is used with good results in the fabrication of commercial VCSELs for the wavelength region of 0.85 μm [1]. However, implementation of doped DBRs with low resistivity requires complicated profiles of both doping and solid-solution composition at the boundaries of the layers; these profiles should be controlled to a high accuracy [2]. A relatively high level of doping of conductive mirrors leads to an appreciable increase in optical losses due the free-carrier absorption, which is an important limiting factor in the fabrication of long-wavelength VCSELs, which have a comparatively low level of optical gain in the active region [3]. Furthermore, it is difficult to obtain small values of parasitic capacitance in the VCSEL designs with doped mirrors; this circumstance can limit the frequency range of the devices.

The aforementioned factors stimulate the development of VCSELs with nonconducting mirrors; in this design, one (or both) of the contacts are formed at the conductive layers immediately adjacent to the active (emitting) VCSEL region (the so-called intracavity-contacted VCSELs) [2, 4]. Since both contact areas in the case under consideration can be positioned on the front surface of the semiconductor structure, such devices are ideally suited to the flip-chip technology, with the emission being extracted through the substrate. This method is optimal for integration of both emitter arrays based on VCSELs and digital silicon integrated circuits [5]. In addition, undoped semiconducting or insulating mirrors ensure the lowest level of optical losses, which makes it possible to fabricate long-wavelength VCSELs [4]. Up to now, it has been shown conclusively that it is possible to develop VCSELs with nonconducting mirrors for various spectral regions; in this design, either two semiconducting DBRs or a bottom semiconducting DBR in combina-

tion with a top dielectric DBR are used as the mirrors [2–4]. Still another possibility is the use of mirrors based on AlGaO/GaAs, which are formed by selective oxidation of AlGaAs layers with a high Al content [6].

Oxidized DBRs ensure high levels of reflection in a wide wavelength range and a small depth of the optical-field penetration into mirrors [2]; this circumstance made it possible to successfully use the active region based on InAs/InGaAs quantum dots (QDs), which has a relatively low level of optical gain, and develop for the first time a VCSEL for a wavelength of about 1300 nm. Such VCSELs are based of GaAs substrates and operate in the continuous-wave mode at room temperature with a threshold current of ~1.5 mA, an output power as high as 1 mW, and an external differential quantum efficiency higher than 45% [7, 8]. However, a high series resistance of the devices under consideration (~200–300 Ω) [7], the necessity for careful calibration of the composition of the structure's layers in order to ensure the specified oxidation rates [6], and the problems related to mechanical strength of oxidized mirrors [6, 9] give rise to certain difficulties. In this context, it is urgent to search for the design and technology approaches that would make it possible to retain a high quality factor of vertical optical microcavity with simultaneous simplification of VCSEL technology and an increase in their reliability.

In this paper, we report the results of efforts to optimize the design and fabrication technology of VCSELs with nonconducting mirrors and active regions based on InGaAs quantum wells (QWs) grown by molecular-beam epitaxy (MBE) on GaAs substrates. We showed that it is possible to etch the structures of multiple-layer DBRs with high precision so that the slopes of the mesa walls are controlled and to form reliable, selectively oxidized mirrors. The produced VCSELs with an oxidized-aperture diameter of 7–12 μm exhibit lasing in the continuous-wave (cw) mode at room temperature with threshold currents of 0.5–1.5 mA, differential efficiency as high as 0.5 mW/mA, and the maximum output power as high as 3 mW.

As a result of theoretical analysis, we suggest a combined design of a VCSEL with a bottom undoped semiconductor DBR based on AlGaAs/GaAs and a top oxidized DBR (Fig. 1a). Since it is expected that radiation is extracted from the cavity through the substrate, the requirements on the reflectivity of the bottom mirror are not very stringent, so that the reproducible formation of a semiconductive DBR with the necessary characteristics can be accomplished with confidence using conventional epitaxial technology. In designing the optical-cavity structure, we took into account that it was necessary to use relatively thick contact *n*- and *p*-type layers in order to ensure both an acceptable value of the series resistance and reproducible selective etching of the multilevel VCSEL mesa structure. In order to reduce the internal optical losses caused primarily by the free-carrier absorption in the *p*-type layer,

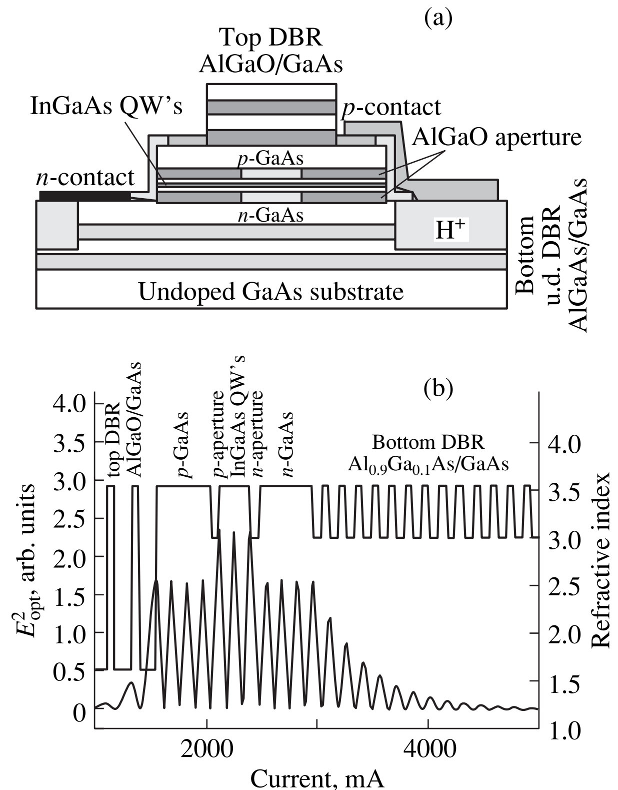

Fig. 1. (a) Schematic representation of a cross section of a VCSEL structure with a bottom semiconducting Bragg reflector and a top oxidized Bragg reflector; (b) calculated depth profiles for the refractive index and the optical-wave intensity in a vertical microcavity for the suggested laser design.

we used nonuniform doping of contact layers, so that the heavily doped interlayers were located at the calculated nodes of the standing optical wave. Two relatively thick, oxidized aperture layers make it possible to partially redistribute the optical field in the cavity (Fig. 1b), which leads to additional reduction of losses and an increase in the optical-confinement factor compared to a structure with a single thin aperture [10]. The contact areas of the *p* and *n* types are formed on the *n*-type contact layer. In order to eliminate the leakage currents and reduce the parasitic capacitances, we used an additional isolating implantation of protons. In the design we suggest, there is no need for etching off the third mesa (down to the substrate), which simplifies the VCSEL production technology appreciably.

In this study, the VCSEL structures with active layers based on InGaAs QWs were grown by MBE using a Riber 32 system. The epitaxial structure consisted of

(i) a top undoped DBR, which included seven pairs of $GaAs/Al_{0.97}Ga_{0.03}As$ layers;

(ii) a nonuniformly doped *p*-GaAs contact layer;

(iii) a top p-$Al_{0.98}Ga_{0.02}As$ aperture layer with gradient variation in the composition at boundaries;

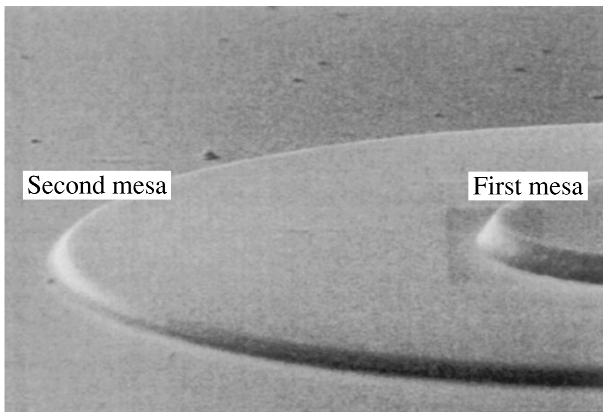

Fig. 2. Microphotograph of a VCSEL structure after dry etching off of the top Bragg reflector down to the contact *p*-type layer (the first mesa) and of the cavity down to the contact *n*-type layer (the second mesa).

(iv) an undoped active region with two $In_{0.15}Ga_{0.85}As$ QWs in the GaAs host;

(v) a bottom n-$Al_{0.98}Ga_{0.02}As$ aperture layer with gradient variation in the composition at boundaries;

(vi) an *n*-GaAs contact layer; and

(vii) a bottom DBR containing 19 pairs of $Al_{0.95}Ga_{0.05}As$/GaAs layers.

The thicknesses of AlGaAs and GaAs layers in the bottom DBR, aperture layers, and GaAs layers in the top DBR are approximately equal to one-quarter of the resonance wavelength λ_{Bragg} of the vertical microcavity. The total geometrical thickness of the resonator L_{cav} corresponds approximately to $5\lambda_{Bragg}$. The thicknesses of $Al_{0.97}Ga_{0.03}As$ layers in the top DBR are chosen so that these thicknesses amount to $(1/4)\lambda_{Bragg}$ after selective oxidation (with allowance made for both a variation in the refractive index and a certain mechanical compression of the layers as a result of oxidation).

The main problem in epitaxial growth of VCSEL structures is related to a necessity for precision control (to an accuracy no worse than 1%) of the thickness and composition of the layers [1, 2]. The optical-microcavity thickness L_{cav} is the most critical factor since it is this thickness that governs to the greatest extent the operating wavelength of a VCSEL. The use of preliminary calibrations does not necessarily ensures the required accuracy owing to possible fluctuations in both the growth rates and position of the substrate holder. However, the VCSEL design with undoped mirrors offers a possibility of intermediately controlling the structure parameters with subsequent correction of the cavity thickness. The essence of the suggested procedure consists in interruption of the growth at a nominal cavity thickness slightly smaller than that in the design. After this interruption, the sample is transferred to an auxiliary chamber of the MBE system; in this chamber, the reflection spectrum of the sample is measured and used to determine the thicknesses of the layers in the bottom DBR and the total cavity thickness (using the methods of inverse mathematical simulation [11]). The sample was then transferred back to the MBE growth chamber, and the growth of the structure was completed with allowance made for necessary corrections.

The precision etching of multilevel mesa structures is one of the most critical operations in VCSEL technology. Taking into account a large number of alternating AlGaAs layers which differ greatly in composition, the use of chemical etching is found to be hardly appropriate in this case. In this context, the methods of dry etching are widely used in VCSEL technology; as a rule, these methods ensure a nearly vertical wall of the mesa [2, 11]. This fact complicates connection of the *p*- and *n*-type contacts with corresponding contact areas (with allowance made for a characteristic mesa height of several micrometers). In the course of this study, we developed the dry-etching method, which employs the Ar^+ ion beam and makes it possible to reproducibly obtain a specified slope of the mesa-structure walls. This method is based on the use of a photoresist with increased ductility, the choice of optimal conditions of drying and exposure, and optimization of both the angle between the substrate and the ion flux and the ion energy (~1 eV). Figure 2 shows a microphotograph of a two-level VCSEL mesa structure fabricated using the dry-etching method developed by us.

Another critical operation in the fabrication of VCSELs is the formation of oxidized apertures and oxidation of the top mirror. A special feature of the developed technology consists in simultaneous selective oxidation of all layers in the structure. This feature requires the selection of a specific combination of mesa sizes and the corresponding choice of composition of layers in the structure. If the oxidation rate for the top mirror is lower than that for aperture layers, it is impossible to produce a normal device structure since the aperture closes (ceases to exist) before the formation of the top mirror is completed. Therefore, the thicknesses and compositions of oxidized layers are chosen so that complete oxidation is attained more rapidly for the top mirror than for the aperture layers. However, an excessively large difference in the oxidation rates causes the top DBR to be highly overoxidized. Overoxidation of the top DBR impairs the mechanical characteristics of the structure owing to excessive compression of the layers and reduces the reflection coefficient as a result of morphology degradation. Another difficulty is related to the fact that a low content of Ga (amounting to several percent) in the AlGaAs layers to be oxidized prohibits the efficient use of the methods for preliminary calibration of the composition, such as measurements of photoluminescence or X-ray diffraction [6]. Therefore, we used special test structures that made it possible to directly calibrate the oxidation rates for the layers with different composition and thickness (see Fig. 3a). It can be seen that the oxidation depth depends not only on composition but also on the thickness of the

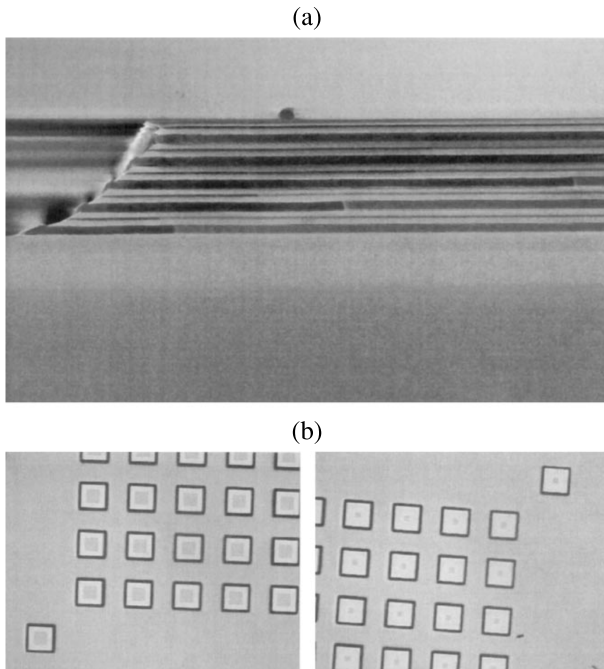

Fig. 3. (a) An SEM image of the cleaved surface of a test structure for calibrating the oxidation rates; (b) microphotographs of the test mesa structures with oxidized apertures.

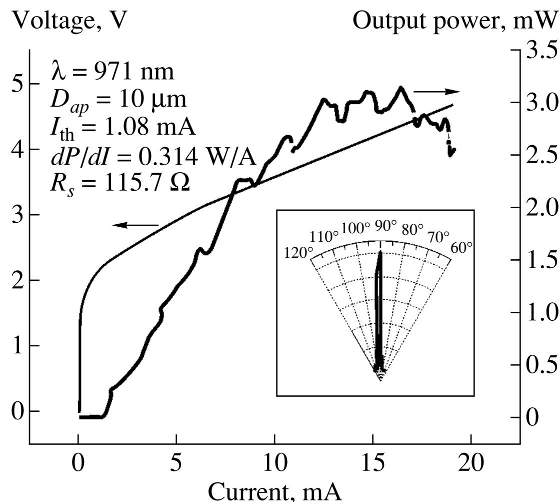

Fig. 4. Typical voltage–current and power–current characteristics for fabricated VCSELs. The directivity pattern of the output radiation is shown in the inset.

layers, which give rise to an additional degree of freedom in designing a VCSEL epitaxial structure. The choice of oxidation conditions plays a prominent part in the efforts to increase mechanical reliability of oxidized structures; it is especially important to ensure removal of residual products from oxidized layers [9]. Figure 3b shows the test mesa structures with formed apertures of various sizes after selective oxidation was completed and a rapid thermal annealing was performed; this annealing simulated the procedure for forming the contacts. The optimized technology ensures the uniformity of aperture sizes and the mechanical stability of the structures.

After etching of the mesas and selective oxidation, we carried out the formation of the *p*- and *n*-type ohmic contacts, passivation of the device structure with an insulator, isolating implantation, opening of contact windows, and formation of contact areas [12]. The voltage–current, output-power–current, and spectral characteristics were then measured directly from the wafer in the dc mode at room temperature of the surrounding medium without special cooling (radiation was extracted through the substrate). In order to measure the directivity pattern, we mounted separate laser-diode crystals on crystal holders.

Figure 4 shows typical voltage–current and power–current characteristics for produced VCSELs. The directivity pattern of output radiation (in polar coordinates) is shown in the inset. The best of the fabricated VCSELs, with a diameter of the oxidized aperture of D_{ap} = 7–12 μm, exhibit lasing in the cw mode at room temperature with threshold currents of I_{th} = 0.5–1.5 mA, a differential efficiency as high as dP/dI = 0.5 mW/mA, and a highest output power of no lower than 3 mW. The structures of the devices are mechanically stable, and their series resistance R_s ranges from 80 to 150 Ω.

Thus, in the course of this study, we experimentally tested the design and fabrication technology of VCSELs with combined mirrors (a bottom DBR based on $Al_{0.95}Ga_{0.05}As$/GaAs and a top DBR based on AlGaO/GaAs) and two oxidized apertures. We suggested the dry-etching technology for multiple-layer VCSEL structures using a beam of Ar^+ ions; this technology makes it possible to obtain reproducibly a specified slope of the mesa-structure walls. We also optimized the selective-oxidation technology, which ensures the mechanical stability of VCSEL structures. Recently reported significant improvement in the properties of the active region in the lasers based on InGaAs/GaAs QDs makes it possible to expect successful utilization of the suggested design for implementation of long-wavelength VCSELs on GaAs substrates.

REFERENCES

1. K. D. Choquette and H. Q. Hou, Proc. IEEE **85**, 1730 (1997).
2. *Vertical-Cavity Surface-Emitting Lasers*, Ed. by L. A. Coldren, H. Temkin, and C. W. Wilmsen (Cambridge Univ. Press, Cambridge, 1999).
3. L. A. Coldren, E. Hall, and S. Nakagawa, in *Proceedings of Electronic Components and Technology Conference, Lake Buena Vista, FL* (2001).
4. D. L. Huffaker and D. G. Deppe, IEEE Photonics Technol. Lett. **11**, 934 (1999).

5. R. Pu, C. Duan, and C. W. Wilmsen, IEEE J. Sel. Top. Quantum Electron. **5**, 201 (1999).
6. K. D. Choquette, K. M. Geib, C. I. H. Ashby, *et al.*, IEEE J. Sel. Top. Quantum Electron. **3**, 916 (1997).
7. J. A. Lott, N. N. Ledentsov, V. M. Ustinov, *et al.*, Electron. Lett. **36**, 1384 (2000).
8. V. M. Ustinov, A. E. Zhukov, N. A. Maleev, *et al.*, in *Technical Summary Digest of Conference on Optoelectronics-2002, San Jose, CA, USA, 2002* (SPIE's Photonics West, 2002); Proc. SPIE **4646**, 49 (2002).
9. H. Q. Jia, H. Chen, W. C. Wang, *et al.*, J. Cryst. Growth **223**, 484 (2001).
10. N. A. Maleev, A. Yu. Egorov, A. E. Zhukov, *et al.*, Fiz. Tekh. Poluprovodn. (St. Petersburg) **35**, 881 (2001) [Semiconductors **35**, 847 (2001)].
11. J. Kaindl, S. Stoier, and G. Franz, J. Electrochem. Soc. **142**, 2418 (1995).
12. N. A. Maleev, A. R. Kovsh, A. P. Vasil'ev, *et al.*, in *Proceedings of 4th Belarus–Russia Workshop on Semiconductor Lasers and Systems* (Minsk, 2002), p. 111.

Translated by A. Spitsyn

Semiconductors, Vol. 37, No. 10, 2003, pp. 1239–1242. Translated from Fizika i Tekhnika Poluprovodnikov, Vol. 37, No. 10, 2003, pp. 1270–1273.
Original Russian Text Copyright © 2003 by Novikov, Maksimov, Shernyakov, Gordeev, Kovsh, Zhukov, Mikhrin, Maleev, Vasil'ev, Ustinov, Alferov, Ledentsov, Bimberg.

PHYSICS OF SEMICONDUCTOR DEVICES

Temperature Characteristics of Low-Threshold High-Efficiency Quantum-Dot Lasers with the Emission Wavelength from 1.25 to 1.29 μm

I. I. Novikov*, M. V. Maksimov*, Yu. M. Shernyakov*, N. Yu. Gordeev*, A. R. Kovsh*, A. E. Zhukov*, S. S. Mikhrin*, N. A. Maleev*, A. P. Vasil'ev*, V. M. Ustinov*, Zh. I. Alferov*, N. N. Ledentsov*, and D. Bimberg**

**Ioffe Physicotechnical Institute, Russian Academy of Sciences, St. Petersburg, 194021 Russia*

e-mail: novikov@switch.ioffe.ru

***Institut fur Festkorperphysik, Technische Universitat Berlin, D-10623 Berlin, Germany*

Submitted March 27, 2003; accepted for publication April 1, 2003

Abstract—The temperature behavior of the operation characteristics of low-threshold (the threshold current density is below 100 A/cm^2) high-efficiency (differential quantum efficiency is as high as 88%) injection laser heterostructures is studied. The active region of structures emitting in the range from 1.25 to 1.29 μm included two, five, and ten layers of InAs–GaAs quantum dots. It is shown that both the threshold current density and the external differential quantum efficiency become N-shaped functions of temperature as the distribution of carriers in the active region changes from nonequilibrium to equilibrium one. © *2003 MAIK "Nauka/Interperiodica".*

INTRODUCTION

Semiconductor quantum-dot (QD) lasers are intensively studied today because of the promise they hold for showing better characteristics as compared to those of the existing quantum-well lasers, for example, higher temperature stability and lower threshold current density [1, 2]. At present, we already have semiconductor QD lasers with unprecedentedly low threshold current density [3, 4], high temperature stability [5], and high external quantum efficiency [6, 7]. However, it is expected that a detailed investigation of physical processes in lasers of such type will lead to still further improvement of their parameters.

It should be noted that the presence of defects and dislocations in the active region, as well as a considerable spread of parameters, make it difficult to interpret experimental data obtained for QD lasers. When they have a sufficiently high density, dislocations and defects can give rise to nonradiative recombination current that is comparable to or even exceeds the QD inversion current. If the size spread of QDs is considerably wide, it is usually difficult to determine whether generation occurs via the ground or an excited QD state. In this study, we investigate the temperature characteristics of laser heterostructures with an active region on the basis of InAs–GaAs QDs with a small size spread (the full width at half-maximum (FWHM) of the electroluminescence (EL) line is less than 50 meV at room temperature), low dislocation density in the active region (the "transparency" current density is below 6 A/cm^2 per a QD layer), and high external differential quantum efficiency (88%) [6].

EXPERIMENTAL

The laser heterostructures were grown by molecular-beam epitaxy (MBE) and had the active regions composed of 2, 5, or 10 InAs–GaAs QD layers formed by the activated decomposition of InGaAs [8]. A detailed description of the construction of laser structures can be found in [6].

The diode lasers were produced in stripe geometry with 100 μm-wide strips. A conductive adhesive was used to mount the samples on a copper heat sink with their epitaxial layers up. The lasers were driven by current pulses 500 ns in duration with a 1-kHz repetition rate.

Temperature dependences of the threshold current density (J_{th}) and differential quantum efficiency (η_{diff}) were measured in the temperature range from 20 to 300 K. By means of a helium cryostat, temperature stabilization was ensured to be as accurate as 1 K. A photodetector with an operation diameter of 10 mm was employed to detect laser power.

RESULTS AND DISCUSSION

The temperature dependences of the threshold current density (J_{th}) for all structures studied are shown in Fig. 1. It can be seen that, for structures with two and five QD layers, the value of J_{th} increases at low temper-

1063-7826/03/3710-1239$24.00 © 2003 MAIK "Nauka/Interperiodica"

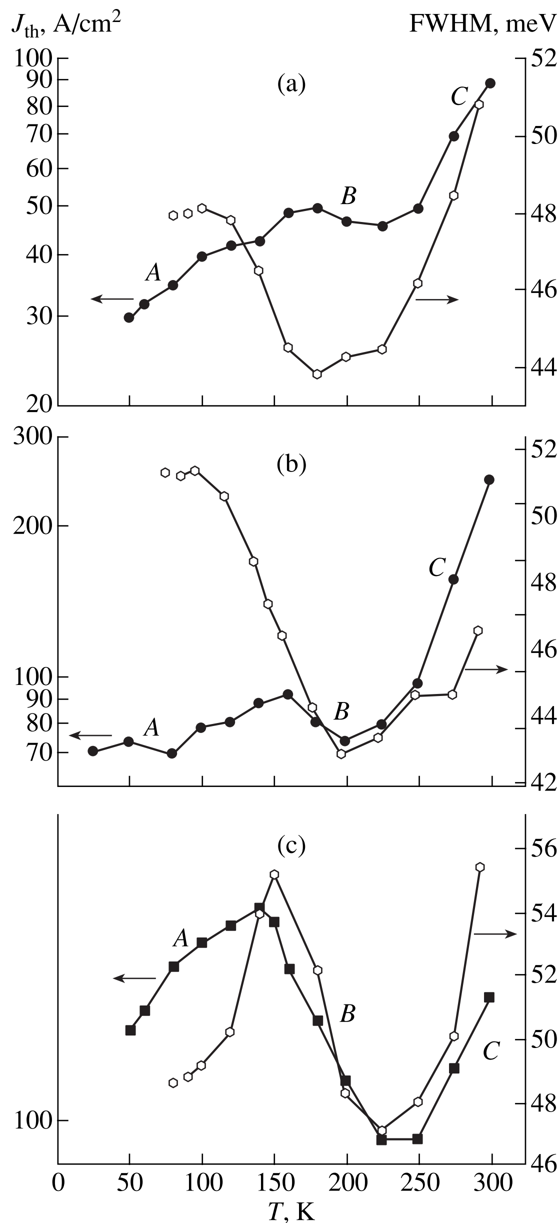

Fig. 1. Temperature dependences of the threshold current density J_{th} (cavity length $L = 2$ mm) and the FWHM of electroluminescence line (cavity length $L = 250$ μm) for laser heterostructures with an active region composed of (a) 2, (b) 5, and (c) 10 quantum-dot layers.

atures (section *A*). A flattening off and the following slight decrease in J_{th} are observed at 175 and 160 K for two- and five-layered structures, respectively (portion *B*). Steep growth of the threshold current density starts at 200–225 K (portion *C*). The temperature dependence of J_{th} for a ten-layered structure (Fig. 1c) is characterized by a more pronounced peak and minimum at ~140 and 225 K, respectively; the change in the value of J in the region with a negative characteristic temperature (T_0) is also more abrupt.

A decrease in the threshold current density of QD lasers with temperature had already been observed in a number of previous studies [9, 10]. In [9], the phenomenon of negative T_0 is explained by the thermal injection of electrons and holes from QDs with a low energy of carrier localization (small-size QD) and their subsequent recapture by QDs with a higher energy of localization (larger QD). This process corresponds to the transition from nonequilibrium to equilibrium distribution of carriers in the active region [11] and is characterized by a decrease in the effective width of EL and amplification spectra. Hence it follows that the current density required for the onset of lasing also decreases with temperature. In contrast to our results, no increase in J_{th} at low temperatures (Fig. 1, portion *A*) was observed in [9, 10]. This distinction may be due to the fact that a greater size spread of QDs and a lower energy of carrier localization were encountered in [9, 10]; therefore, the transition from nonequilibrium to equilibrium distribution should start at a lower temperature as compared to the result obtained in this study.

It seems likely that, for the lasers studied here, the region of negative T_0 (portion *B*) also corresponds to the transition from nonequilibrium to equilibrium distribution of carriers in a QD array. However, portions *A* and *C* in Fig. 1 correspond directly to nonequilibrium and equilibrium cases. This inference is also supported by the temperature dependences of the EL line FWHM (Fig. 1). For all structures, these dependences were measured in equal conditions: i.e., with a cavity length of 250 μm (such length provides high losses via the emission of radiation and considerably reduces the effect of reabsorption) and injection current density of 20 A/cm^2. It is clearly seen that the temperature range corresponding to line narrowing coincides with the range of negative characteristic temperature; especially good correlation is observed for the structures with 10 QD layers.

Another series of spectral measurements enabled the lasing wavelength λ to be determined within the entire temperature range. The results are shown in the inset to Fig. 2. The dependence is linear, suggesting that lasing occurs via the ground state of QDs.

The temperature dependences of differential quantum efficiency for 2-mm-long samples are shown in Fig. 2. All the curves have a pronounced minimum at 180–200 K. An unusual feature is that an increase in η_{diff} is also accompanied by an increase in the threshold current density (portion *C* in Fig. 1).

Figure 3 shows power–current characteristics for the structures with five layers of quantum dots at different temperatures. At room temperature, the power–current characteristic can be closely approximated by a well-known linear dependence of the output power *P* on injection current *I*:

$$P = \frac{\varepsilon\eta_{diff}}{q}(I - I_{th}), \quad (1)$$

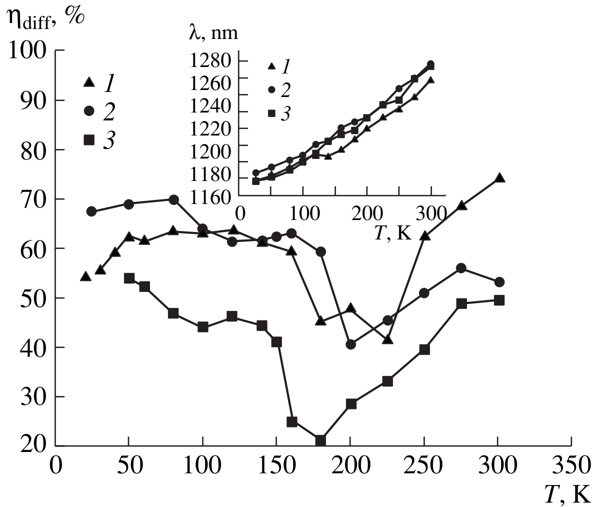

Fig. 2. Temperature dependences of the external differential quantum efficiency (η_{diff}) for heterostructures with (*1*) 2, (*2*) 5, and (*3*) 10 quantum-dot layers in the temperature range T = 20–300 K. The cavity length L = 2 mm. Inset shows the corresponding temperature dependences of the lasing wavelength.

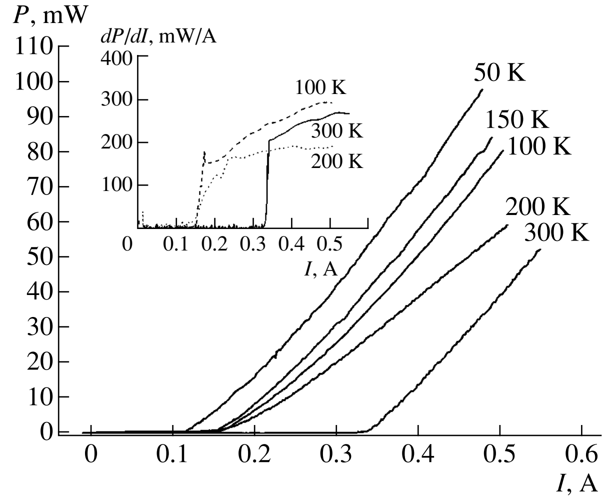

Fig. 3. Power–current characteristics of the structures with five quantum-dot layers and the cavity length L = 2 mm at different temperatures. Inset shows the derivative of power with respect to current (dP/dI) as a function of the injection current (I) at different temperatures.

where ε is the photon energy, q is the elementary charge, and I_{th} is the threshold current.

At low temperatures (for example, at 200 K), the dependence of lasing power on current is nonlinear near the threshold and formula (1) becomes applicable only for a still larger injection current. In view of this circumstance, the differential quantum efficiency at a fixed temperature was determined at a linear portion of the power–current characteristic, after the initial gradient growth has terminated. The inset to Fig. 3 shows the derivative of total luminous power with respect to current, which presents (to within a constant) the dependence η_{diff} on current at different temperatures. It is clearly seen that the value of derivative above the lasing threshold strongly depends on injection current.

An increase in the differential quantum efficiency of QD lasers with temperature had been already observed previously [12] and was explained by the temperature-induced increase in homogeneous broadening. According to study [13], such behavior of η_{diff} can be associated with multomode lasing threshold, which also increases with temperature. In the case when the spatial hole burning is the main factor leading to multimode lasing, the number of simultaneously excited modes decreases with temperature and, therefore, the dependence of the output power on current becomes closer to linear.

We also studied the threshold current density and the differential quantum efficiency at temperatures above 293 K, in the range from 20 to 80°C. Samples having a length of 2 mm were soldered by an indium solder to a copper heat sink with their epilayers facing down.

The temperature dependence of the lasing wavelength is shown in the inset to Fig. 4. For structures with five and ten QD layers, the dependence is linear, whereas, for the structures with two layers, the wavelength features a stepwise decrease at 70°C, which indicates that the transition to the lasing via excited state has occurred.

Temperature dependences of the differential quantum efficiency for all structures studied are shown in Fig. 4. In view of the specific features of the experi-

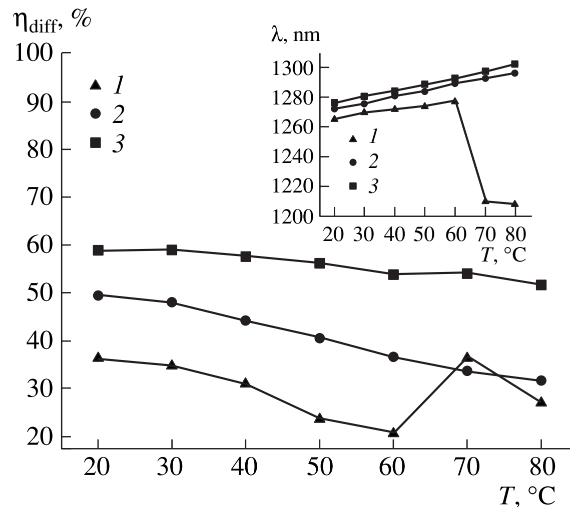

Fig. 4. Temperature dependences of the external differential quantum efficiency (η_{diff}) for heterostructures with (*1*) 2, (*2*) 5, and (*3*) 10 quantum-dot layers in the temperature range T = 20–80°C. The cavity length L = 2 mm. Inset shows the temperature dependences of the lasing wavelength.

ment, different samples were used in the measurements at temperatures above and below 293 K. Consequently, the curves in Fig. 4 cannot be considered as an extension of the dependences in Fig. 2. A special feature is the large value of differential quantum efficiency at 70°C as compared to that at 60°C. It should be noted that, in our previous experiments with similar structures, the lasing transition from the ground to the excited state was accompanied by a decrease rather than an increase in the differential quantum efficiency [14]. This phenomenon calls for further investigation.

CONCLUSION

For the first time, quantum-dot lasers with a small spread of QD sizes, high energy of the carrier localization in dots, low threshold current density, and low losses are demonstrated to have *N*-shaped temperature dependences of the threshold current density and the differential quantum efficiency. This form of temperature dependences is likely due to the transition from nonequilibrium to equilibrium distribution of carriers in the active region. We expect that comprehensive understanding of interrelations between the temperature dependences of lasing parameters and the characteristics of QD array (density, localization energy, size distribution) or the geometry of the laser structure (the number of QD layers, the width and the doping of the waveguide region) will allow one to optimize a QD laser structure and to realize its advantages predicted in theory.

ACKNOWLEDGMENTS

This study was supported by INTAS, the Russian Foundation of Basic Research, and the Ministry of Science of Russian Federation within the program "Physics of Solid Nanostructures."

REFERENCES

1. D. Bimgerg, M. Grundmann, and N. N. Ledentsov, *Quantum Dot Heterostructures* (Wiley, Chichester, 1998).
2. N. N. Ledentsov, IEEE J. Sel. Top. Quantum Electron. **8**, 1015 (2002).
3. O. B. Shchekin, G. Park, D. L. Huffaker, *et al.*, IEEE Photonics Technol. Lett. **12**, 1120 (2000).
4. G. T. Liu, A. Stinz, H. Li, *et al.*, IEEE J. Quantum Electron. **36**, 1272 (2000).
5. O. B. Shchekin, J. Ahn, and D. G. Deppe, Electron. Lett. **38**, 712 (2002).
6. S. S. Mikhrin, A. E. Zhukov, A. R. Kovsh, *et al.*, Fiz. Tekh. Poluprovodn. (St. Petersburg) **36**, 1400 (2002) [Semiconductors **36**, 1315 (2002)].
7. A. R. Kovsh, N. A. Maleev, A. E. Zhukov, *et al.*, Electron. Lett. **38**, 1104 (2002).
8. M. V. Maximov, A. F. Tsatsul'nikov, B. V. Volovik, *et al.*, Phys. Rev. B **62**, 16671 (2000).
9. A. E. Zhukov, A. Yu. Egorov, A. R. Kovsh, *et al.*, Fiz. Tekh. Poluprovodn. (St. Petersburg) **31**, 483 (1997) [Semiconductors **31**, 411 (1997)].
10. O. Shchekin, G. Park, D. Huffaker, and D. Deppe, Appl. Phys. Lett. **77**, 466 (2002).
11. L. V. Asryan and R. A. Suris, Semicond. Sci. Technol. **11**, 554 (1996).
12. M. Sugawara, K. Mukai, Y. Nakata, *et al.*, Phys. Rev. B **61**, 7595 (2000).
13. L. V. Asryan and R. A. Suris, IEEE J. Quantum Electron. **36**, 1151 (2000).
14. M. V. Maximov, L. V. Asryan, Yu. M. Shernyankov, *et al.*, IEEE J. Quantum Electron. **37**, 676 (2001).

Translated by A. Sidorova